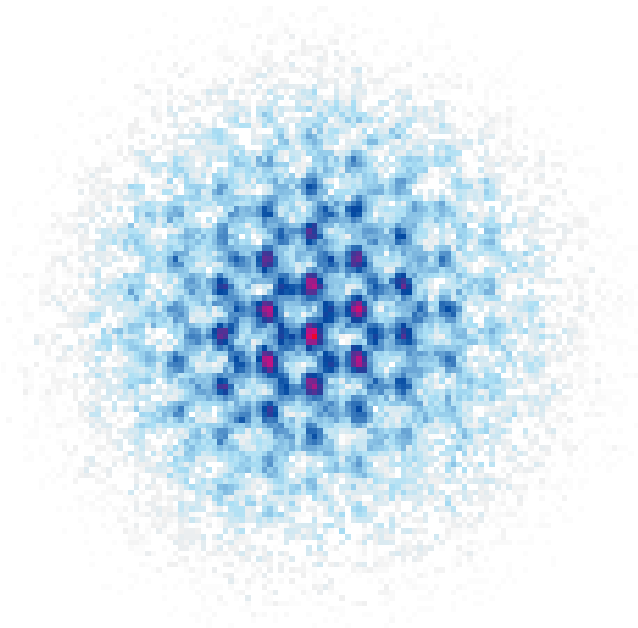


# Studying Quantum Gases in a Dynamically Tunable Lattice with Sub-Lattice-Site Resolution



Dissertation

zur Erlangung des Doktorgrades  
an der Fakultät für Mathematik, Informatik und Naturwissenschaften  
Fachbereich Physik  
der Universität Hamburg

vorgelegt von  
Marcel Nathanael Kosch  
aus Drestedt

Hamburg  
2022



# Gutachter

Gutachter der Dissertation:

Prof. Dr. Klaus Sengstock  
Prof. Dr. Henning Moritz

Zusammensetzung der Prüfungskommission:

Prof. Dr. Klaus Sengstock  
Prof. Dr. Henning Moritz  
Prof. Dr. Ludwig Mathey  
Prof. Dr. Markus Drescher  
Prof. Dr. Ralf Riedinger

Vorsitzender der Prüfungskommission:

Prof. Dr. Ludwig Mathey

Datum der Disputation:

07.07.2023

Vorsitzender des Fach-Promotionsausschusses PHYSIK:

Prof. Dr. Günter H. W. Sigl

Leiter des Fachbereichs PHYSIK:

Prof. Dr. Wolfgang J. Parak

Dekan der Fakultät für Mathematik,  
Informatik und Naturwissenschaften:

Prof. Dr.-Ing. Norbert Ritter

## **Erklärung zur Eigenständigkeit**

Hiermit erkläre ich an Eides statt, die vorliegende Dissertationsschrift selbst verfasst und keine anderen als die angegebenen Hilfsmittel und Quellen benutzt zu haben.

*Marcel Kosch*

*Hamburg – 05.05.2023*

# Abstract

Ultracold gases in optical lattices provide a versatile simulation platform of real solid-state quantum systems as they offer clean systems with a high degree of control over the systems parameters and access to additional observables. In this thesis, new methods to get access to the real space density distribution and a dynamic control of the systems geometry are presented and employed.

The first main result presented in this thesis is a new imaging approach, which uses matter wave optics to magnify the density distribution in an optical lattice by up to a factor of around 90. In combination with standard absorption imaging, this allows sublattice resolved access to the integrated real space density in our 2D optical lattice. At the heart of the method is a quarter period evolution time in a harmonic potential following the shut off of the optical lattice, transforming the initial atomic positions to their momenta. A subsequent free fall time transfers these momenta to a magnified image of the initial positions. In this way, the depth of focus of the imaging is very large, allowing to image 3D quantum systems. The method is characterized in detail and using the single site populations high precision thermometry of the system across the BEC phase transition is demonstrated. By utilizing magnetic resonance techniques, also the addressing of individual lattice sites is shown.

In the next part, the control over our quantum system is improved by employing a novel type of optical lattice. It uses different frequencies to allow for a dynamic geometry control while offering high passive stability. In the case of our hexagonal lattice beam arrangement, this allows to tune between honeycomb, boron nitride and triangular lattices within a few microseconds. The geometry for a given set of lattice wave vectors and beam balances is fully described by the newly introduced concept of a geometry phase. Its fundamental importance is highlighted by also appearing as a staggered flux in the corresponding momentum space lattices. Using the high tunability, atoms are transferred into higher Bloch bands and their dynamics measured in real space. The tunability can also be used as a tool for full state tomography measurements, which is presented in a set of preliminary measurements. Furthermore, exemplary realizations of a quasiperiodic and a 3D lattice in multifrequency design, both featuring tunable geometry phases, are proposed.

The last part of this thesis reports on real space pattern formations in tilted lattices of different geometries, resolved by using our quantum gas magnifier. This allows in particular the observation of a spontaneously forming density-wave breaking the underlying translational symmetry of the triangular lattice, which is ascribed to interaction-induced pair tunneling processes. Additionally, self-trapping and the formation of ring structures along equipotential lines are observed.



# Zusammenfassung

Ultrakalte Quantengase in optischen Gittern bieten eine vielseitige Plattform zur Simulation von Quantensystemen in echten Festkörpern, da sie der Erstellung reiner Systeme mit hoher Kontrolle über deren Parameter und Zugang zu zusätzlichen Observablen ermöglichen. In dieser Arbeit werden neue Methoden vorgestellt und eingesetzt, um Zugang zur Ortsraumdichteverteilung sowie dynamische Kontrolle der Geometrie des Systems zu erlangen.

Das erste zentrale Ergebnis dieser Arbeit ist ein neuer Abbildungsansatz, der basierend auf Materiewellenoptik die Dichteverteilung in einem optischen Gitter um bis zu einem Faktor von etwa 90 vergrößert. In Verbindung mit einer üblichen Absorptionsabbildung ermöglicht dies eine Auflösung unterhalb der Gitterkonstante und gibt Zugang zu der integrierten Ortsraumdichte unseres optischen 2D Gitters. Der wesentliche Baustein dieser Methode ist eine Entwicklungszeit von einer viertel Periode in einem harmonischen Potential im Anschluss an das Abschalten des optischen Gitters, die die anfänglichen Positionen der Atome auf ihre Impulse überträgt. Durch eine anschließende freie Fallzeit werden diese Impulse auf ein vergrößertes Bild der anfänglichen Positionen übertragen. Auf diese Weise ist die Tiefenschärfe der Abbildung sehr groß, wodurch 3D Systeme abgebildet werden können. Die Methode wird im Detail charakterisiert und mithilfe der Einzelplatzbesetzungen wird eine hochpräzise Thermometrie des Systems über den BEC Phasenübergang durchgeführt. Unter Einsatz von Magnetresonanzen wird zudem das Ansprechen einzelner Gitterplätze demonstriert.

Im folgenden Abschnitt wird die Kontrolle über das Quantensystem verbessert, indem ein neuer optischer Gittertyp eingesetzt wird. Dieser verwendet verschiedene Frequenzen um dynamische Kontrolle über die Geometrie bei gleichzeitig hoher passiver Stabilität zu erlangen. Im Fall unserer hexagonalen Gitterstrahlanordnung ermöglicht dies, innerhalb weniger Mikrosekunden zwischen Honigwaben-, Bornitrit- und Dreiecksgitter zu schalten. Die Geometrie eines gegebenen Satzes von Gittervektoren und relativen Strahltiefen wird vollständig von der neu eingeführten Geometriephase beschrieben. Deren fundamentale Bedeutung wird auch erkennbar durch ihr Auftauchen als gestaffelter Fluss im zugehörigen Impulsraumgitter. Unter Verwendung der hohen Durchstimmpbarkeit der Geometrie werden Atome in höhere Blochbänder übertragen und ihre Dynamik im Ortsraum gemessen. Die Durchstimmpbarkeit kann auch als Hilfsmittel für eine volle Zustandstomographie verwendet werden, was anhand einiger vorläufiger Messungen vorgestellt wird. Darüber hinaus werden beispielhafte Umsetzungen eines quasiperiodischen- und eines 3D-Gitters im Multifrequenzentwurf vorgeschlagen, die ebenfalls jeweils verstimmbare Geometriephasen aufweisen.

Der letzte Teil dieser Arbeit beschäftigt sich mit entstehenden Dichtestrukturen im Ortsraum in gekippten Gittern verschiedener Geometrien, die mittels unseres Quantengasvergrößerers aufgelöst werden. Dies erlaubt insbesondere die Beobachtung einer

sich ausbildenden Dichtewelle, die spontan die Translationssymmetrie des zugrundeliegenden Dreiecksgitters bricht, was über wechselwirkungsinduzierte Paartunnelprozesse erklärt wird. Weiterhin wird self-trapping und der Aufbau von Ringstrukturen entlang von Äquipotentiallinien beobachtet.

# Contents

<b>1. Introduction</b>	<b>1</b>
<b>2. Ultracold Atoms in Optical Lattices</b>	<b>5</b>
2.1. Preparation of the BEC	5
2.2. The Optical Lattice	8
2.3. Band Structure Description	10
<b>3. Quantum Gas Magnification</b>	<b>13</b>
3.1. Theoretical Description	14
3.2. Experimental Application	17
3.3. Characterization	20
3.3.1. Focusing of the Matter Wave Lens	20
3.3.2. Resolution Analysis	23
3.3.3. Single Particle Aberrations of the Imaging Protocol	25
3.3.4. Interaction Effects	27
3.4. Precision Thermometry	28
3.5. Sub-Lattice-Site Resolution	31
3.6. Local Addressing on the Single Site Level	34
3.6.1. Thermalization Dynamics after Shaping the System	37
3.7. Conclusion and Outlook	40
<b>4. Dynamic Lattice Geometry Control via a Multifrequency Optical Lattice</b>	<b>43</b>
4.1. Tunable Lattice Geometry	44
4.1.1. Derivation of the Geometry Phase	45
4.1.2. Characteristics of the Lattice Potential	45
4.1.3. Spatial Variation of the Lattice Geometry	50
4.1.4. Generalization to $N$ 1D Lattices in $d$ Physical Dimensions	50
4.2. Implementation	51
4.3. Characterization	53
4.3.1. Calibrating the Lattice Geometry	54
4.3.2. Stability of the Lattice Geometry	58
4.4. Staggered Flux in the Momentum Space Lattice	60
4.5. Excitations into Higher Bands	65
4.5.1. Preparation of Higher Bands	65
4.5.2. Dynamics in Real Space	67
4.6. Sublattice Modulation Spectroscopy	70

4.7. State Tomography with Interactions . . . . .	74
4.8. Extension of the Geometry Phase Concept to more complex Optical Lattices . . . . .	80
4.8.1. Quasiperiodic Optical Lattice with Geometry Phase . . . . .	80
4.8.2. Generalization to 3D Optical Lattices . . . . .	85
4.9. Conclusion and Outlook . . . . .	87
<b>5. Pattern Formation in dc Driven Lattices</b>	<b>91</b>
5.1. Transport Protocol . . . . .	93
5.2. Spontaneous Density-Wave Formation in the Triangular Lattice . . . . .	94
5.2.1. Effective Model . . . . .	94
5.2.2. Numerical Modeling of the Dynamics . . . . .	97
5.2.3. Spontaneous Symmetry Breaking . . . . .	98
5.2.4. Evolution of the Density-Wave . . . . .	101
5.2.5. Role of the Transverse Tunneling . . . . .	104
5.2.6. Incommensurate Tilt Direction . . . . .	107
5.2.7. Self-Trapping at the Edge of the System . . . . .	108
5.3. Transport in the Honeycomb Lattice . . . . .	110
5.4. Conclusion and Outlook . . . . .	113
<b>A. Quantum Walk in Triangular Momentum Space Lattice</b>	<b>115</b>
<b>B. PCA of Distorted Brillouin Zones</b>	<b>119</b>
<b>C. Derivation of Resonant Excitation Strengths</b>	<b>123</b>
<b>D. Dynamic Increase of the Tilt Strength in the Triangular Lattice</b>	<b>129</b>
<b>E. Transport in the Honeycomb Lattice</b>	<b>135</b>
<b>Bibliography</b>	<b>139</b>

# 1. Introduction

Ultracold atoms offer the possibility to very flexibly engineer artificial states of matter that can be used for the simulation of other, more complex or less accessible, quantum systems, realizing an idea first proposed by Feynman [1]. They are well suited to serve as a platform for such quantum simulations as they provide very versatile and controllable systems with good access to different important observables [2]. Utilizing quantum systems for the simulation themselves is necessary, because simulation of many-body problems on classical computers quickly gets unfeasible. Ultracold atoms allow both for clean realizations of interesting model Hamiltonians, important in the description of known physical systems, as well as new ones without real world counterparts. A crucial step for quantum simulation was to reach the quantum behavior of dilute atomic gases by cooling their temperature down close to absolute zero where quantum degeneracy is actualized. This was for the first time accomplished in 1995 for bosonic atoms leading to formation of Bose-Einstein condensates (BEC) [3–5] and in 1999 for fermionic atoms [6]. Using this new access to quantum systems many groundbreaking experiments have been performed ever since [7–9].

One fruitful direction is to load these ultracold quantum gases in optical lattices in order to simulate solid-state systems [10, 11] as this constitutes an ideal realization of the (Fermi)-Hubbard model [12] or Bose-Hubbard model [13], depending on the statistics of the utilized atomic species. Here the interference patterns of multiple laser beams are used to mimic the spatially periodic potential landscape of solid crystals with the neutral atoms taking the place of electrons in the material. The resulting potentials are defect free and the fundamental properties, the tunneling rate and the particle interaction strength, can be tuned strongly by the utilized lattice depth determined via the laser intensity and additionally by employing Feshbach resonances [14]. Another difference is the realized lattice constant, which is typically increased by several orders of magnitude compared to solid-state materials. The larger spacing, together with the much larger particle weight of the atoms compared to single electrons, also reduces the timescales of the dynamics in the system considerably and thus makes resolving such processes easier. At the same time, this is connected to very low energy scales in the system, demanding for correspondingly low temperatures of the atoms in the lattice.

In order to make best use of a simulator it is of fundamental importance to have access to the important observables of the investigated physical processes. To this end ultracold gases offer a very powerful measurement possibility in a straightforward way by performing a free expansion time, converting the atomic momenta into their final positions and thus allowing to image the momentum distribution of the

system under study. Another essential property is the spatial distribution, which gives access to central problems like transport phenomena, spontaneous formation of domains or edge states in topological systems. By employing sophisticated techniques, most notably quantum gas microscopy [15, 16] it is possible to reach single site resolution in optical lattices. In this thesis I present a new technique which we developed [17] following a different approach by increasing the spatial distribution using matter wave optics. This allows us to get single-shot images of the real space density of 2D lattices of tubes with high bosonic occupation numbers and sub-lattice resolution. The technique is well suited for high precision thermometry measurements with much less numerical effort than necessary from momentum space images [18–20] and to follow density dynamics within single lattice sites, contrary to superresolution microscopy [21, 22] within single shots and on a local level, i.e. for individual lattice sites. Another area which is explored in this thesis using the quantum gas magnifier are phenomena of pattern formation and transport measurements. This is an important field of research in quantum gas experiments [23–25] as transport properties are essential in the description of many important phases in solid-state materials. The new access to the single-shot real space density distribution of lattices with high occupation numbers in particular allows us to identify an interaction driven spontaneously symmetry breaking process far from equilibrium [26]. Such processes, resulting in patterns which spontaneously break the spatial symmetry of the underlying potential landscape are a very fundamental phenomenon in physics [27], found also for example in macroscopic systems like soliton trains in continuously driven water. The different interesting regimes attainable with the quantum gas magnifier illustrate its diverse possibilities as part of the toolbox of quantum gas simulation.

One part of the high versatility of ultracold gases in optical lattices comes from the possibility to shape the periodic potential very freely via the number, orientations, wavelengths and polarizations of the constituent lattice beams and thus simulate very different solid-state materials. Many different geometries have already been realized, in particular including complex nonseparable and bipartite lattices like for example superlattices [28, 29], honeycomb lattices [30–32], Lieb lattices [33], Kagome lattices [34] and quasicrystal lattices [35]. Interestingly, optical lattices also allow for dynamical geometry changes beyond the possibilities given by solid-state materials. I present a new concept for the design of optical lattices which we implemented [36]. By employing different frequencies in a passively stable way, we are able to dynamically tune the lattice geometry on the microsecond scale without the need for a phase lock. In the case of our hexagonal lattice beam setup this allows to continuously tune the geometry from the triangular lattice to the honeycomb lattice, which is for example promising as a tool for creating and detecting topological effects [37].

---

## Thesis Outline

Chapter 2 gives an overview of the experimental sequence employed to reach a condensed sample of  $^{87}\text{Rb}$  atoms, which is used as the starting step for all experiments throughout this thesis. It further introduces the concept of optical lattices and derives the theoretical description of our system.

Chapter 3 introduces the quantum gas magnifier [17]. First the theoretical concept and our realization of it, using a magnetic trap as the harmonic confinement and magnifying the density distribution in our optical lattice, are presented. Following this, characterization measurements are performed, showing the high resolution available and how, via the suppression of interaction effects during the magnification protocol, distortions only play a minor role in the final measurement. The technique is then used to perform several benchmarking experiments. It offers the possibility to perform thermometry measurements with very high precision and resolves density features well below the lattice spacing. Finally addressing on the single site level is demonstrated by targeting magnetic resonances.

Chapter 4 reports on our highly tunable multifrequency optical lattice setup [36]. The lattice geometry is described by the here introduced concept of the geometry phase, to which we have direct access in this new lattice design. Following the derivation of the lattice description, our implementation is presented and characterized in detail. In different measurements the possibilities given by our new setup are demonstrated by exciting atoms into higher Bloch bands, achieving a new type of spectroscopy and performing state tomography measurements. Furthermore the geometry phase concept is expanded to a general number of dimensions and lattice beams and multifrequency setups for a quasiperiodic and a 3D optical lattice are proposed.

Chapter 5 is dedicated to the measurement of different real space pattern formations, particularly the observation and investigation of a spontaneously symmetry breaking density-wave emerging in a strongly dc-driven triangular lattice [26]. The effect is described theoretically via an effective Hamiltonian as well as extensive  $c$ -field simulations. The spontaneousness of the emergent density-wave is established, its dynamics explored and the role of the effective tight-binding description studied by varying the forcing direction relative to the lattice vectors. Additionally, self-trapping effects are observed in a variety of regimes and an emergent ring structure in transport experiments in the honeycomb lattice is investigated.

## List of Publications

The following research articles have been published in the course of this thesis.

- **Quantum gas magnifier for sub-lattice-resolved imaging of 3D quantum systems**  
*L. Asteria, H. P. Zahn, M. N. Kosch, K. Sengstock, C. Weitenberg*  
Nature **599**, 571-575 (2021)  
DOI: 10.1038/s41586-021-04011-2
- **Formation of Spontaneous Density-Wave Patterns in dc Driven Lattices**  
*H. P. Zahn, V. P. Singh, M. N. Kosch, L. Asteria, L. Freystatzky, K. Sengstock, L. Mathey, C. Weitenberg*  
Physical Review X **12**, 021014 (2022)  
DOI: 10.1103/PhysRevX.12.021014
- **Multifrequency optical lattice for dynamic lattice-geometry control**  
*M. N. Kosch, L. Asteria, H. P. Zahn, K. Sengstock, C. Weitenberg*  
Physical Review Research **4**, 043083 (2022)  
DOI: 10.1103/PhysRevResearch.4.043083

---

## 2. Ultracold Atoms in Optical Lattices

In this chapter, I will give an overview of our quantum simulation machine. With it, we prepare ultracold bosonic atoms in optical lattices, which are the foundation of the methods and effects presented in this thesis.

The first section describes the preparation of a BEC of  $^{87}\text{Rb}$  atoms at our experimental apparatus, which was originally build as described in [38, 39]. It follows the by now well established pattern of firstly trapping and cooling atoms in a magneto-optical trap (MOT) [40], reducing their temperature further via an optical molasses [41] and finally loading them into a conservative potential, a magnetic trap in our case, to perform evaporative cooling [42] until the atomic cloud reaches the necessary temperature and phase space density for condensation.

In the following section I will introduce optical lattices, in particular our lattice geometries, which are used to simulate solid state Hamiltonians with ultracold gases. They consist of periodic potentials for the atoms, formed via interference of laser beams. The description of the resulting system by means of band structure calculation is presented in the final section.

### 2.1. Preparation of the BEC

At the heart of our experimental setup is the vacuum chamber, in which the condensation of an atomic sample of  $^{87}\text{Rb}$  and the subsequent studies of lattice Hamiltonians take place well-guarded from disturbances from background collisions. In order to simultaneously allow for efficient loading rates of  $^{87}\text{Rb}$  atoms and decrease background scattering as much as possible, the vacuum chamber is split in two parts. An upper part with a glass cell containing the atomic source and a 2D MOT in which the atoms are captured initially, held at a pressure of usually 2 to  $3 \times 10^{-10}$  mbar, and a lower part with a 2nd glass cell featuring a 3D MOT, the main magnetic trap and the optical lattice at a pressure below  $1 \times 10^{-11}$  mbar, leading to an increased lifetime of the atoms in the system. Both parts are connected via a differential pumping stage, i.e. a long and thin tube, able to conserve the pressure gradient.

The vapor of  $^{87}\text{Rb}$  atoms in the upper chamber is created by an electrically heated dispenser. From it, atoms are captured in the 2D MOT. It consists of two pairs of counterpropagating, red detuned and circularly polarized laser beams and a pair of magnetic coils in anti-Helmholtz configuration. In this way it makes use of the

Doppler effect to selectively excite those atoms moving towards one of the laser beams, leading to a net momentum transfer oppositely to them and hence a cooling of the atomic ensemble. A restoring force to the trap center is introduced via the magnetic field, which gives rise to the Zeeman effect, making photon absorptions more likely further away from the center. The plane of this 2D MOT is oriented perpendicular to gravity and the captured atoms are transferred through the differential pumping stage to the lower chamber via a blue detuned pushing beam along the direction of gravity. Here the atoms are accumulated in a 3D MOT, with three beam pairs covering all spatial directions. Depending on the performance of the machine this step usually takes between 5 to 10 s.

So far the achievable temperature is limited by the Doppler temperature  $T_{\text{Doppler}} = \hbar\Gamma/(2k_B)$  through the natural linewidth  $\Gamma$  of the targeted  $D_2$  transition. To further cool the atoms, a bright molasses is employed for a few milliseconds by switching off the magnetic field of the MOT and adjusting the laser beam detuning. The molasses uses polarization gradient cooling to get down near its theoretical limit of a single photon recoil temperature.

However, the phase space density still needs to be significantly higher than possible with the limitation from photon reemissions and thus evaporative cooling is necessary. Therefore, we ramp up a magnetic guiding field and bring in a short light pulse to pump the atoms to the hyperfine state  $F = 2$ ,  $m_F = 2$ , which has a nonzero magnetic moment  $\mu_F = -g_F m_F \mu_B$ . Here  $\mu_B$  denotes the Bohr magneton and  $g_F$  the Landé factor of the corresponding hyperfine state. This magnetic moment couples on the external magnetic field and as a result, the atoms experience a potential

$$V(\mathbf{r}) = -g_F m_F \mu_B |\mathbf{B}(\mathbf{r})|. \quad (2.1)$$

Accordingly, atoms with  $g_F m_F > 0$  experience potential minima at local minima of the magnetic field. These states are therefore called low-field seeking states. Our magnetic trap is a hybrid between a cloverleaf and a 4D trap, consisting of four pairs of inner coils, with half of them having a reduced winding number, and an outer pair of Helmholtz coils, which is also used in anti-Helmholtz configuration for the 3D MOT. A schematic of the design is shown in Fig. 2.1, for more details see [39, 43, 44]. It offers the full  $2\pi$  optical access in the plane between the coils and allows to work in a regime with a harmonic potential for low-field seeking atoms without a magnetic field of zero which would induce Majorana spin-flips to untrapped states and hence atom losses. The resulting magnetic field close to the center can be described by [44, 45]

$$\mathbf{B}(x, y, z) = B_0 \begin{pmatrix} 0 \\ 0 \\ 1 \end{pmatrix} + B' \begin{pmatrix} x \\ -y \\ 0 \end{pmatrix} + \frac{B''}{2} \begin{pmatrix} -xy \\ -yz \\ z^2 - 1/2(x^2 + y^2) \end{pmatrix}, \quad (2.2)$$

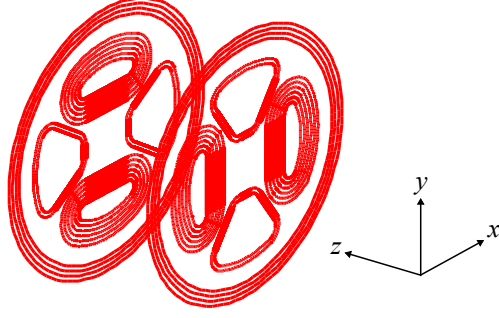


**Figure 2.1.: Winding scheme of our hybrid cloverleaf-4D magnetic trap.**

The inner coils mostly follow a cloverleaf pattern, but with half of them having significantly reduced windings causing axial curvature. Surrounding these is a pair of Helmholtz coils. Adapted from [44].

with the bias field  $B_0$ , the radial gradient  $B'$  and the axial curvature  $B''$ . From this the magnetic field can be approximated in Taylor expansion using cylindrical coordinates  $z$  and  $\rho = \sqrt{x^2 + y^2}$  to

$$B(\rho, z) \approx B_0 + \frac{1}{2}\rho^2 B''_{\text{rad}} + \frac{1}{2}z^2 B'', \quad (2.3)$$

with the curvature in radial direction given by

$$B''_{\text{rad}} = \left( \frac{B'^2}{B_0} - \frac{B''}{2} \right). \quad (2.4)$$

With the dependency of the trap frequency of an atom with mass  $m$  in a harmonic magnetic potential given by  $\omega = \sqrt{\frac{\mu_B}{m} \frac{d^2 B}{dr^2}}$ , the trap frequencies in axial and radial direction can be calculated using  $B''$  and  $B''_{\text{rad}}$  via

$$\omega_z = \sqrt{\frac{g_F m_F \mu_B}{m} B''} \quad (2.5)$$

$$\omega_{xy} = \sqrt{\frac{g_F m_F \mu_B}{m} B''_{\text{rad}}}. \quad (2.6)$$

Using the correct choice for the bias field the trap potential can be made isotropic, which is used for loading the atoms in the magnetic trap, as it optimizes the overlap with the symmetric cloud following the optical molasses. Subsequently the magnetic trap is compressed in  $x$ - and  $y$ -direction by lowering the bias field, which is mostly determined by the current through the Helmholtz coils, increasing the density and thus allowing for efficient thermalization during the evaporative cooling. Here we use the maximal current of 110.6 A through the inner coils, resulting in  $B' = 1.69 \cdot 10^4$  G/m and  $B'' = 7.12 \cdot 10^5$  G/m<sup>2</sup>. This maximal confinement in the radial direction, i.e. the  $xy$ -plane, allows together with a bias field of  $B_0 = 0.11$  G to reach a frequency of  $\omega_{xy} = 2\pi \cdot 649$  Hz. In the axial direction the confinement is much weaker, only leading

to a frequency of  $\omega_z = 2\pi \cdot 11$  Hz. For the evaporative cooling, radio frequency (RF) radiation is brought to the atoms, resonant to the energy difference between the different  $m_F$  states. Since the potential depth of the atoms in the magnetic field is proportional to  $m_F$  (Eq. 2.1), they are transferred to anti-trapped states and lost from the atomic cloud. At the same time the resonance condition is spatially dependent, as the magnetic field rises approximately harmonically around the trap center (Eq. 2.3). Using this, a cooling effect is reached by initially resonantly targeting a surface at high potential value, i.e. far away from the trap center, where almost exclusively atoms at highest temperatures are found. The remaining ensemble continually equilibrates while the RF signal is lowered exponentially over typically 20 s from 18 MHz to around 95 kHz. The chosen duration is a trade-off between the time needed to stay in thermal equilibrium and the finite lifetime of the atoms in the trap. This finally sufficiently increases the phase space density for the formation of a BEC.

## 2.2. The Optical Lattice

In a next step, the atoms are subjected to an optical lattice to simulate quantum effects in periodic potentials. Such lattices work using the optical dipole force acting on the induced atomic dipole moments in a light field [46, 47]. Its oscillating electric field results in a shift of the atomic energy levels, such that the atoms experience a conservative potential proportional to the light intensity  $I$  and inversely proportional to the detuning between the light field and the atomic resonance. In order to limit scattering events with the lattice laser beams providing the light field, their frequency is far detuned compared to the atomic resonance frequencies of  $^{87}\text{Rb}$ . This simultaneously decreases the potential depth, however only linearly whereas the scattering rate scales quadratically with the detuning, such that the desired potential depth can in turn be reached by using sufficient laser beam powers. The sign of the potential depends on the sign of the detuning. For light frequencies below the atomic resonance as in our case, which are called red-detuned, the induced dipole moment is in phase with the electric field, leading to an attractive force towards regions of high light intensity. Oppositely, blue-detuned light fields, having higher frequencies than the atomic resonance, feature repulsively interacting dipole potentials and hence have potential minima at regions of low light intensities.

We work with 2D hexagonal optical lattices, constructed by overlapping three laser beams with wavelength  $\lambda = 1064$  nm, originating from a joint laser source, and wavevectors  $\mathbf{k}_i = \frac{2\pi}{\lambda}$  ( $i = 1, 2, 3$ ) in a single plane ( $xy$ -plane) under  $120^\circ$  angles between each other. The beams are brought to the experimental chamber via three polarization maintaining fibers and focused on the position of the atomic cloud with Gaussian waists of  $160 \mu\text{m}$  [48, 49]. The laser beam polarizations can be set individually by combinations of a  $\lambda/4$  and a  $\lambda/2$  waveplate in two beams and a  $\lambda/2$  waveplate in the third beam. This allows to realize arbitrary ratios between polarizations in the lattice plane, called p-polarization, and perpendicular to the lattice plane, called

s-polarization, for all laser beams and additionally to tune their respective phases for two of the laser beams. This is interesting, because with such a beam geometry and red-detuned laser beams the s-polarization results in a triangular lattice potential for the atoms, whereas the p-polarization results in the opposite potential landscape, which has a honeycomb geometry with two lattice sites per unit cell. Thus for the correct relative position between the two polarizations, which are set via their relative phase delay, also boron nitride lattices are attainable. These feature the two minima per unit cell of the honeycomb lattice, but with an energy offset between the two, given by the ratio of the polarizations. More details on this setup and its possible lattice geometries can be found in [49]. Throughout this thesis the polarizations are set perpendicular to the lattice plane and the lattice geometry varied instead using our new multifrequency approach, which is described in detail in chapter 4.

The optical dipole potential seen by the atoms is proportional to the intensity of the summed electrical fields of the three lattice beams, which result from the complex electrical fields as the absolute values squared. Consequently, the lattice potential is described by [36]

$$V_{\text{pot}}(\mathbf{r}, t) = \kappa \left| \sum_{i=1}^3 \mathbf{E}_i(\mathbf{r}, t) \right|^2 = \kappa \sum_{i=1}^3 \left| \mathbf{E}_i(\mathbf{r}, t) \right|^2 + \kappa \sum_{i=1}^3 2\Re(\mathbf{E}_i(\mathbf{r}, t) \mathbf{E}_{i+1}^*(\mathbf{r}, t)) \quad (2.7)$$

$$= V_0 + \kappa \sum_{i=1}^3 2\Re(\mathbf{E}_i^{(0)} \mathbf{E}_{i+1}^{*(0)} e^{i(\mathbf{k}_i - \mathbf{k}_{i+1})\mathbf{r}}) = V_0 + \kappa \sum_{i=1}^3 2\Re(I_i^{(0)} e^{i\phi_i} e^{i(\mathbf{k}_i - \mathbf{k}_{i+1})\mathbf{r}}) \quad (2.8)$$

$$= V_0 + \kappa \sum_{i=1}^3 2I_i^{(0)} \cos((\mathbf{k}_i - \mathbf{k}_{i+1})\mathbf{r} + \phi_i). \quad (2.9)$$

Here  $\mathbf{E}_4(\mathbf{r}, t) = \mathbf{E}_1(\mathbf{r}, t)$  and  $\kappa$  is the proportionality constant. In the second line we used as definition of the complex fields  $\mathbf{E}_i(\mathbf{r}, t) = \mathbf{E}_i^{(0)} e^{i(\mathbf{k}_i\mathbf{r} - \omega t)}$ , which also shows that the first summand is independent of position and time and is thus abbreviated to  $V_0$ . The products  $\mathbf{E}_i^{(0)} \mathbf{E}_{i+1}^{*(0)}$  determine the intensities and phases of the three 1D lattices and thus are replaced by  $I_i^{(0)} e^{i\phi_i}$ . Lastly, when defining the single 1D lattice depths as  $V_i = \kappa I_i^{(0)}$  and the corresponding reciprocal lattice vectors as  $\mathbf{b}_i = \mathbf{k}_i - \mathbf{k}_{i+1}$ , with  $\mathbf{k}_4 = \mathbf{k}_1$ , the potential is expressed by

$$V_{\text{pot}}(\mathbf{r}) = V_0 + 2 \sum_{i=1}^3 V_i \cos(\mathbf{b}_i \cdot \mathbf{r} + \phi_i). \quad (2.10)$$

In total this gives an optical potential composed of an energy offset  $V_0$  and three 1D lattices with depths  $V_i$ , reciprocal lattice vectors  $\mathbf{b}_i$  and phases  $\phi_i$ , which are generally given by the relative phases and polarizations of pairs of lattice beams. With our lattice beams enclosing angles of  $120^\circ$  the length of the reciprocal lattice vectors is  $|\mathbf{b}_i| = \sqrt{3} \frac{2\pi}{\lambda}$  and their scalar products  $\mathbf{b}_i \cdot \mathbf{b}_j = -\frac{6\pi^2}{\lambda^2}$  for  $i \neq j$ . As derived

in section 4.1.1 the lattice potential can be written in terms of the geometry phase  $\phi_g = \phi_1 + \phi_2 + \phi_3$ , which directly determines the lattice geometry:

$$V_{\text{pot}}(\mathbf{r}) = V_0 + 2 \sum_{i=1}^3 V_i \cos(\mathbf{b}_i \cdot \mathbf{r} + \phi_g/3). \quad (2.11)$$

The potential depth  $V$  in the following is stated in units of the recoil energy of a lattice photon

$$E_{\text{rec}} = \frac{h^2}{2m\lambda^2}, \quad (2.12)$$

with Planck constant  $h$  and atomic mass  $m$ , which is given by  $E_{\text{rec}}/h = 2.03$  kHz for our  $^{87}\text{Rb}$  atoms and refers to the balanced case  $V = V_1 = V_2 = V_3$ , if not stated differently. We usually determine it via Kapitza-Dirac scattering, as described in [50].

In order to load the atoms to the ground state of the optical lattice, its power is ramped up exponentially within up to 600 ms. Then, following the desired operations in the lattice potential, we either realize the momentum distribution of the atoms by performing standard time-of-flight free expansion or the real space distribution using our quantum gas magnifier as described in chapter 3. Finally the realized atomic distribution is measured via absorption imaging [51]. For this a resonant laser beam is brought to the atoms along the  $z$ -direction, i.e. perpendicular to the lattice plane, and its intensity distribution imaged on a CCD camera, such that the shadow cast by the atoms due to photon absorption and reemission over the whole solid angle can be compared to a subsequent unperturbed image of the intensity profile. Using Lambert-Beers law this allow to reconstruct the integrated optical density along the  $z$ -direction.

### 2.3. Band Structure Description

The physical systems we study are determined by the periodic potentials of our optical lattice, mimicking solid-state systems. We can thus use the same successful framework of Band theory, resulting in a dispersion of energy bands and corresponding eigenstates, to describe our system. We limit the calculation of the energies and eigenstates of the atoms in our optical lattice to the single particle case. Working with bosonic atoms, a more thorough description would need to be based on the many-body Hamiltonian and include interactions between the particles. In practice however, interaction effects are typically relatively small corrections on the band structure of our systems and a good approximation of the energies and band gaps can be inferred from the single-particle Hamiltonian. The important exception within this thesis is found in the experiments in chapter 5 where interaction effects become dominant due to large energy offsets between lattice sites mostly freezing out single particle tunneling.

The eigenstates in the non-interacting case follow from the time-independent Schrödinger equation applied to the single-particle Hamiltonian  $\hat{\mathcal{H}}$

$$\hat{\mathcal{H}}\psi(\mathbf{r}) = \left( -\frac{\hat{p}^2}{2m} + V_{\text{pot}}(\mathbf{r}) \right) \psi(\mathbf{r}) = E\psi(\mathbf{r}), \quad (2.13)$$

with the periodic potential  $V_{\text{pot}}$  in our case given by Eq. 2.11. The discrete translational symmetry of the systems allows to use Blochs theorem [52], stating that the eigenstates of the Hamiltonian can be written as the product of a lattice periodic function  $u_k(\mathbf{r})$  with plane waves,

$$\psi(\mathbf{r}) = u_k(\mathbf{r})e^{i\mathbf{k}\cdot\mathbf{r}}. \quad (2.14)$$

In order to diagonalize the Hamiltonian we project it on the plane wave basis set and numerically calculate the energies and eigenstates by restricting the system to an  $N \times N$  reciprocal lattice, as described in detail in [49, 53]. Following the notation in [49], we get as the matrix representation of  $\hat{\mathcal{H}}$  in the plane wave basis

$$\mathcal{H}_{\mathbf{k}\mathbf{k}'} = \langle \mathbf{k} | \hat{\mathcal{H}} | \mathbf{k}' \rangle = \int d^3r e^{i\mathbf{k}\cdot\mathbf{r}} \hat{\mathcal{H}} e^{-i\mathbf{k}'\cdot\mathbf{r}}. \quad (2.15)$$

By making use of the periodicity of the lattice potential we can substitute the momentum vectors  $\mathbf{k}^{(i)}$  in terms of the reciprocal lattice vectors. These are the only coupled momenta and are mediated via Bragg scattering processes in the optical lattice. Thus, the momentum vectors are substituted by

$$\begin{aligned} \mathbf{k} &= m_1 \mathbf{b}_1 + m_2 \mathbf{b}_2 + \mathbf{s} \\ \mathbf{k}' &= n_1 \mathbf{b}_1 + n_2 \mathbf{b}_2 + \mathbf{q} \end{aligned} \quad (2.16)$$

with integers  $m_{1,2}$ ,  $n_{1,2}$  and the quasimomenta  $\mathbf{s}$  and  $\mathbf{q}$ , which are defined within the unit cell of the reciprocal lattice, the 1st Brillouin zone (BZ). However, neglecting the effect of the external harmonic trap, there is no coupling between different quasimomenta included in the systems Hamiltonian. As such in the following we can restrict to the case  $\mathbf{s} = \mathbf{q}$  given by

$$\mathbf{q} = \beta_1 \mathbf{b}_1 + \beta_2 \mathbf{b}_2, \quad (2.17)$$

with  $0 \leq \beta_{1,2} < 1$ . By plugging in the different parts of the Hamiltonian  $\hat{\mathcal{H}}$  into Eq. 2.15 the matrix elements can be computed. This results in

$$\int d^3r e^{i\mathbf{k}\cdot\mathbf{r}} \frac{\hat{p}^2}{2m} e^{-i\mathbf{k}'\cdot\mathbf{r}} = 3E_{\text{rec}} \delta_{m_1, n_1} \delta_{m_2, n_2} \delta_{\mathbf{s}, \mathbf{q}} \left( (n_1 + \beta_1)^2 + (n_2 + \beta_2)^2 - (n_1 + \beta_1)(n_2 + \beta_2) \right) \quad (2.18)$$

for the kinetic part, which has to be described by a diagonal matrix ( $m_1 = n_1$ ,  $m_2 = n_2$ ), because it does not couple different momenta. The matrix elements from

the lattice potential conversely are off-diagonal terms as they are associated with a change in momentum by  $\pm\mathbf{b}_1$ ,  $\pm\mathbf{b}_2$  or  $\pm\mathbf{b}_3 = \pm(-\mathbf{b}_1 - \mathbf{b}_2)$ . Using Eq. 2.11 for  $V_{\text{pot}}$  this gives

$$\begin{aligned} \int d^3r e^{i\mathbf{k}\cdot\mathbf{r}} V_{\text{pot}}(\mathbf{r}) e^{-i\mathbf{k}'\cdot\mathbf{r}} &= V_1 \left( e^{i\phi_g/3} \delta_{m_1, n_1+1} \delta_{m_2, n_2} \delta_{\mathbf{s}, \mathbf{q}} + e^{-i\phi_g/3} \delta_{m_1, n_1-1} \delta_{m_2, n_2} \delta_{\mathbf{s}, \mathbf{q}} \right) \\ &+ V_2 \left( e^{i\phi_g/3} \delta_{m_1, n_1} \delta_{m_2, n_2+1} \delta_{\mathbf{s}, \mathbf{q}} + e^{-i\phi_g/3} \delta_{m_1, n_1} \delta_{m_2, n_2-1} \delta_{\mathbf{s}, \mathbf{q}} \right) \\ &+ V_3 \left( e^{i\phi_g/3} \delta_{m_1, n_1-1} \delta_{m_2, n_2-1} \delta_{\mathbf{s}, \mathbf{q}} + e^{-i\phi_g/3} \delta_{m_1, n_1+1} \delta_{m_2, n_2+1} \delta_{\mathbf{s}, \mathbf{q}} \right). \end{aligned} \quad (2.19)$$

Overall the energies and eigenstates of the system for one quasimomentum  $\mathbf{s} = \mathbf{q}$  can hence be obtained by solving the eigenvalue problem for a  $N \times N$  matrix  $\mathcal{H}_{\mathbf{k}\mathbf{k}'}$ , with the band structure following from the eigenvalues  $E_{\mathbf{q}}^{(n)}$  as a function of the quasimomentum  $\mathbf{q}$  throughout the 1st BZ and the band index  $n \in \{1, \dots, N^2\}$ . The eigenstates result in the plane wave basis, weighted by the Bloch coefficients:  $|\psi_{\mathbf{q}}^{(n)}\rangle = \sum_{k=1}^{N^2} c_k^{(n)} |k\rangle$ . From them the real space orbitals for atoms in a certain band with some specified quasimomentum can be computed. At the position  $\mathbf{r}$  in the  $xy$ -plane the real space density  $\rho$  is proportional to

$$\rho_{\mathbf{q}}^{(n)}(\mathbf{r}) = \left| \langle \mathbf{r} | \psi_{\mathbf{q}}^{(n)} \rangle \right|^2 \propto \left| \sum_{k=1}^{N^2} c_{k, \mathbf{q}}^{(n)} e^{i\mathbf{k}\mathbf{r}} \right|^2 \quad (2.20)$$

### 3. Quantum Gas Magnification

For the experimental study of complex quantum mechanical processes, it is essential to have access to the relevant observables, with one particularly fundamental observable being the real space density of the system. However, due to the small scales at which the quantum nature of matter takes over, imaging such systems has proven to be a challenging task. In the context of ultracold quantum gases this has been made possible most prominently by quantum gas microscopes [15, 16], which offer single atom sensitivity and single site resolution of optical lattices allowing even for the study of quantum correlations [54, 55]. Despite their potency there are several limitations connected to their approach. Besides the very high technical complexity, they suffer from a narrow depth of focus, due to the high numerical aperture that is necessary for the high optical resolution, restricting the systems under study to 2D planes. Additionally, light-assisted collisions lead to parity projections during the imaging times. Similarly, alternative approaches come with their own strengths and drawbacks. With electron [56] or ion microscopes [57] it is possible to avoid the strong limitation of the depth of focus at the cost of a low single atom detection fidelity, preventing the study of correlations. Using super-resolution microscopes [21, 22] even sublattice density information is accessible, but they use scanning techniques to do so. Generally, these approaches focus on increasing the resolution of the measurement to reach the density information.

In contrast, our technique [17] works by magnifying the quantum system thus increasing its length scale and making it easily resolvable using standard absorption imaging. In this way, we realize sublattice resolution of 3D systems with a 2D lattice structure, imaged by integrating along the third direction. In order to magnify the density distribution we use matter wave optics, analogous to lenses leading to optical magnification.

The matter wave lens is realized by a harmonic potential with a trap frequency  $\omega_{\text{ho}}$  in which the atomic distribution evolves for a quarter period. This maps the initial position  $X_0$  to the momentum  $P$ . Via a subsequent free expansion time, the so-called time-of-flight, another Fourier transform takes place, resulting in the final position being determined by the initial position  $X = M X_0$ , with a magnification  $M \approx \omega_{\text{ho}} t_{\text{ToF}}$  reaching up to around 90 in our case. The concept is illustrated in Fig. 3.1, where the initial triangular lattice is strongly magnified using two different harmonic confinements, allowing to image the complete density distribution with sublattice resolution in single shots.

In the next sections, I will present our quantum gas magnifier, starting with the derivation of the focusing condition and our experimental realization of the concept.

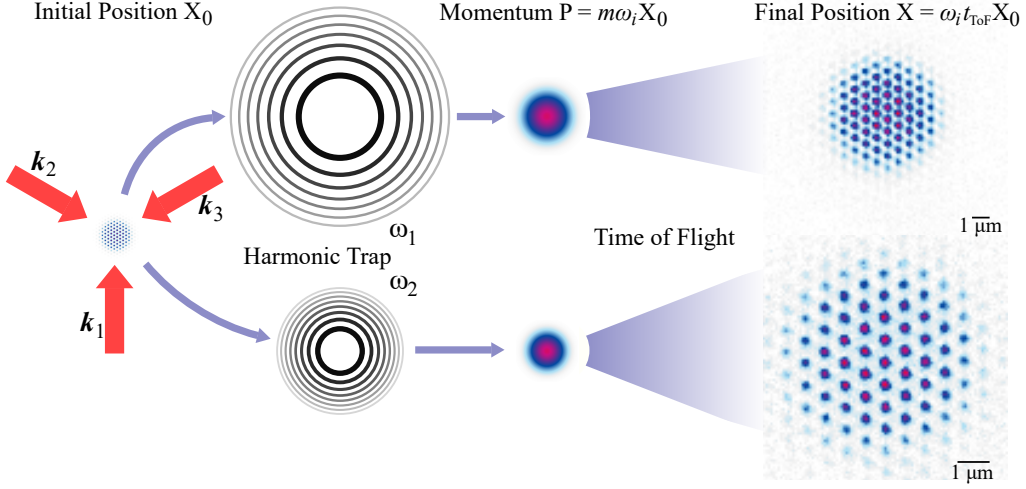


**Figure 3.1.: Working principle of the quantum gas magnifier.** The density distribution in the optical lattice is magnified using matter wave optics. Starting from the left, the ultracold atoms are loaded in a hexagonal optical lattice and suddenly released in a harmonic trap of variable confinement  $\omega_i$ . The result of different confinements is highlighted by the two rows, with  $\omega_1 < \omega_2$ . After a  $T/4$  duration in the harmonic trap the initial position distribution is converted into the momentum distribution. Following this, the atoms are released and after a free expansion time  $t_{\text{ToF}}$  the final position of the atoms is given by  $X = M X_0$  with a magnification  $M = \omega_i t_{\text{ToF}}$ . The magnified distribution is measured via absorption imaging. The two exemplary images of a triangular lattice on the right are done using  $M = 46(1)$  and  $M = 84(1)$ .

Following this, the method is characterized by investigating the realized resolution and imaging aberrations from atomic interactions and the trap anharmonicity. As a next step, the possibility for high precision measurements is demonstrated by measuring the thermal-to-BEC phase transition and using the very high resolution available, dynamics within a single unit cell are studied. Finally, preparation options are discussed using magnetic resonance techniques.

The concept was implemented and the measurements taken together with my PhD colleagues Luca Asteria and Henrik Zahn under the supervision of Klaus Sengstock and Christof Weitenberg.

### 3.1. Theoretical Description

In the following, the focusing condition of the matter wave optics will be derived, i.e. the evolution time necessary in the harmonic oscillator to reach faithful imaging of the initial position distribution without influence of the initial momenta of the

particles. As will be seen, this importantly can be done with finite free expansion times by correctly adjusting the time in the harmonic potential.

For the derivation, we will use the Heisenberg picture and limit the system to 1D. However, the results can straightforwardly be expanded to 2D and 3D for  $\omega_x = \omega_y = \omega_z$ . We start with the Hamiltonian of the harmonic oscillator with angular frequency  $\omega_{\text{ho}}$  and a particle mass of  $m$ :

$$\hat{H}_{\text{ho}} = \frac{\hat{p}^2}{2m} + \frac{m\omega_{\text{ho}}^2 \hat{x}^2}{2}. \quad (3.1)$$

This leads to the equations of motions given by

$$\dot{\hat{x}} = \frac{i}{\hbar} [\hat{H}, \hat{x}] = \frac{\hat{p}}{m} \quad (3.2)$$

$$\dot{\hat{p}} = \frac{i}{\hbar} [\hat{H}, \hat{p}] = -m\omega_{\text{ho}}^2 \hat{x}. \quad (3.3)$$

These equations are solved after an evolution time  $t_{\text{ho}}$  in the harmonic oscillator by the operators  $\hat{x}$  and  $\hat{p}$  defined as

$$\hat{x}(t_{\text{ho}}) = \hat{x}(0) \cos(\omega_{\text{ho}} t_{\text{ho}}) + \frac{\hat{p}(0)}{m\omega_{\text{ho}}} \sin(\omega_{\text{ho}} t_{\text{ho}}), \quad (3.4)$$

$$\hat{p}(t_{\text{ho}}) = \hat{p}(0) \cos(\omega_{\text{ho}} t_{\text{ho}}) - m\omega_{\text{ho}} \hat{x}(0) \sin(\omega_{\text{ho}} t_{\text{ho}}). \quad (3.5)$$

Subsequently the potential is turned off and the atoms experience a free expansion time at fixed momenta. The resulting position operator is thus given by

$$\begin{aligned} \hat{x}(t_{\text{ho}} + t_{\text{ToF}}) &= \hat{x}(t_{\text{ho}}) + \hat{p}(t_{\text{ho}}) \frac{t_{\text{ToF}}}{m} \\ &= \hat{x}(0) \left( \cos(\omega_{\text{ho}} t_{\text{ho}}) - \omega_{\text{ho}} t_{\text{ToF}} \sin(\omega_{\text{ho}} t_{\text{ho}}) \right) \\ &\quad + \hat{p}(0) \left( \frac{1}{m\omega_{\text{ho}}} \sin(\omega_{\text{ho}} t_{\text{ho}}) + \frac{t_{\text{ToF}}}{m} \cos(\omega_{\text{ho}} t_{\text{ho}}) \right). \end{aligned} \quad (3.6)$$

The focusing condition is now met for

$$\tan(\omega_{\text{ho}} t_{\text{ho}}) = -\omega_{\text{ho}} t_{\text{ToF}}, \quad (3.7)$$

allowing to simplify  $\hat{x}(t_{\text{ho}} + t_{\text{ToF}})$  to

$$\begin{aligned} \hat{x}(t_{\text{ho}} + t_{\text{ToF}}) &= \hat{x}(0) \left( \cos(\omega_{\text{ho}} t_{\text{ho}}) + \tan(\omega_{\text{ho}} t_{\text{ho}}) \sin(\omega_{\text{ho}} t_{\text{ho}}) \right) = \hat{x}(0) \frac{1}{\cos(\omega_{\text{ho}} t_{\text{ho}})} \\ &= \hat{x}(0) \frac{1}{\cos(\arctan(\omega_{\text{ho}} t_{\text{ToF}}))} = \hat{x}(0) \sqrt{1 + (\omega_{\text{ho}} t_{\text{ToF}})^2}. \end{aligned} \quad (3.8)$$

The magnification of the density distribution after the sequence is hence given by  $M = \sqrt{1 + (\omega_{\text{ho}} t_{\text{ToF}})^2} \approx \omega_{\text{ho}} t_{\text{ToF}}$ . The approximation holds for  $\omega_{\text{ho}} t_{\text{ToF}} \gg 1$ , which is very well fulfilled in our typical realizations. The error from the approximation in the perceived effectively realized confinement  $\omega_{\text{ho}}$  in the upper image of Fig. 3.1 for example is only 0.03%.

In Fig. 3.2 the focusing condition is demonstrated graphically. It shows the time-dependent coefficients  $c_x(t)$  and  $c_p(t)$  of the decomposed position operator  $\hat{x}(t) = c_x(t)\hat{x}(0) + c_p(t)\hat{p}(0)$ . In this diagram the time evolution in the harmonic potential leads to a circular trajectory around  $(c_x, c_p) = (0, 0)$  from the starting point  $A$  to point  $B$  after  $t_{\text{ho}}$ . The angle spanned by this evolution is given by  $\omega_{\text{ho}} t_{\text{ho}}$ . With the onset of the time-of-flight the momentum operator  $\hat{p}(t)$  stays constant, leading to a straight line tangentially touching the circle at point  $B$  with length  $\omega_{\text{ho}} t_{\text{ToF}}$ . Here the focusing condition (Eq. 3.7) appears via the 2nd angle,  $\theta_{\text{ToF}} = \arctan(\omega_{\text{ho}} t_{\text{ToF}}) = -\omega_{\text{ho}} t_{\text{ho}} + n\pi$  with  $n \in \mathbb{Z}$ , since  $\omega_{\text{ho}} t_{\text{ho}} + \theta_{\text{ToF}} = \pi$  must be fulfilled in order to end up at point  $C$  with  $c_p = 0$ . The magnification can be read out as the hypotenuse of the triangle  $OBC$  yielding the expected  $M = \sqrt{1 + (\omega_{\text{ho}} t_{\text{ToF}})^2}$ . The graphic also connects back to the intuitive picture with the evolution time in the harmonic potential simply being  $T/4$ . This is reached in the far field limit, since  $\omega_{\text{ho}} t_{\text{ToF}} \rightarrow \infty$  leads to  $\omega_{\text{ho}} t_{\text{ho}} \rightarrow \pi/2$ . Additionally, the graphic shows that the magnified position is actually also inverted for every second odd multiple of  $T/4$ , because  $\cos(\omega_{\text{ho}} t_{\text{ho}} + \theta_{\text{ToF}})$  is negative for  $t_{\text{ho}} \approx (1 + 4n)T/4$  and positive only for  $t_{\text{ho}} \approx (3 + 4n)T/4$ . As this has no importance for our images, we conventionally always state  $|M|$ .

The derivation can of course be performed in the Schrödinger picture as well, illustrating that the matter wave can be magnified faithfully [58]. When reaching

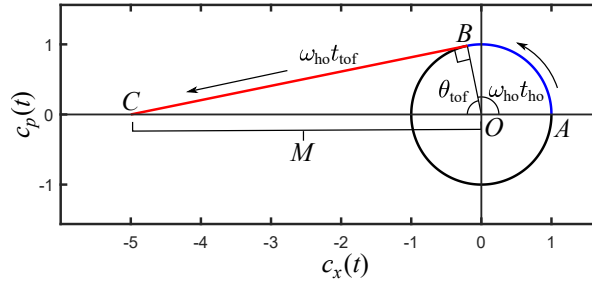


**Figure 3.2.: Visualization of the focusing condition.** Depicted is the time evolution of the operator  $\hat{x} = c_x(t)\hat{x}(0) + c_p(t)\hat{p}(0)$  during the matter wave magnification protocol. Starting from  $A$  the particle follows a circle in the coefficient space during the evolution in the harmonic potential until  $B$ . The arc between  $A$  and  $B$  encompasses an angle  $\omega_{\text{ho}} t_{\text{ho}}$ . At that point the confinement is switched off, resulting in a straight line until the end of the free expansion and thus of length  $\omega_{\text{ho}} t_{\text{ToF}}$  ending at point  $C$ . The corresponding angle being  $\theta_{\text{ToF}}$  ensures the focusing condition is met, i.e.  $C$  is placed at  $c_p = 0$ . The magnification  $M$  can be found as the distance of  $C$  from the origin. Adapted from [58].

single-atom resolution, this method would thus also give access to the study of quantum correlations. Furthermore, it can be expanded to a time dependent confinement during the matter wave lensing. As long as the confinement remains harmonic, there exists a time  $t_{\text{ho}}$  in the harmonic trap that is not dependent on  $\hat{p}(0)$  and faithfully reproduces the initial density distribution [58].

Alternatively, by choosing  $\cot(\omega_{\text{ho}}t_{\text{ho}}) = \omega_{\text{ho}}t_{\text{ToF}}$ , the final distribution is independent of the initial position and instead determined solely by the initial momentum:  $\hat{x} = M\hat{p}_0$ . This allows to compensate for the finite free expansion time  $t_{\text{ToF}}$  and results in a freely tunable magnification in between 1 in the case of pure  $T/4$  evolution in the harmonic confinement [59–61] and around  $\omega_{\text{ho}}t_{\text{ToF}}$  in the limit of pure free expansion time. Although this avoids deviations from the far-field approximation, one would need to check for aberrations during the matter wave part, especially from interactions between the particles, for the trade-off in a concrete system under consideration.

## 3.2. Experimental Application

With the theoretical concept of the quantum gas magnifier established, I now want to introduce the concrete realization and typical experimental sequence in our system.

As described in section 2.1, we reach condensation of  $^{87}\text{Rb}$  atoms, previously pumped to the stretched  $|F = 2, m_F = 2\rangle$  state, via evaporative cooling in a magnetic trap. Since it is in very good approximation harmonic with equal frequencies  $\omega_x = \omega_y$  within the lattice plane, it serves as the matter wave lens. We thus keep the BEC in the magnetic trap while typically the 2D optical lattice is adiabatically ramped up. The system overall is 3D, since the confinement out-of-plane is much weaker,  $\omega_x \gg \omega_z$ , leading to a hexagonal array of 1D tubes with up to around 1,000 atoms per tube. The magnifier protocol is started by suddenly switching off the optical lattice via acousto-optic modulators (AOMs). This is effectively instantaneous with regard to the atoms, as it only takes on the order of  $10^2$  ns for the RF signal to travel the refractive material. Then the atoms evolve for approximately a quarter period in the harmonic potential,  $t_{\text{ho}} \approx T/4 = 2\pi/(4\omega_{\text{ho}})$ . Following this, the magnetic trap is switched off within around  $40 \mu\text{s}$  using IGBTs. With only gravity left, the atomic distribution, Fourier transformed via the matter wave lens, freely expands during the time-of-flight such that the momentum distribution is mapped to the position once again. After some 20 ms of free expansion we perform standard absorption imaging. The imaging pulse has a duration of only  $50 \mu\text{s}$  as to limit the distance the atoms fall down during the imaging. Finally the shadow of the atomic cloud gets imaged after an optical magnification of  $M_{\text{opt}} = 2.04$ , on a CCD camera.

Additionally, we have the option to tune both the system size and the magnification by varying the current send through the coils generating the magnetic potential. In order to have efficient evaporation, we always start with the BEC in a tight  $xy$ -confinement of  $\omega_{\text{sys}} = 2\pi \times 610$  Hz, realized for a current of 110.6 A. As depicted

in Fig. 3.3 we vary the system size by exponentially ramping the current within 100 ms to a desired value. Due to the changing gravitational sag this induces dipole oscillations of the BEC, which are damped by long loading times of the optical lattice of up to 600 ms. If we want to once more change the confinement directly prior to the imaging, to usually get  $\omega_{\text{ho}} > \omega_{\text{sys}}$ , i.e. a larger magnification, we need to fix the atomic distribution during the ramp of the magnetic trap. This is done by quenching the lattice depth to around the deepest value attainable, typically  $V = 6 E_{\text{rec}}$ , which corresponds to a tunnel coupling of only around  $J \approx 0.001$  Hz in the triangular lattice, and quickly ramping the current in 1 ms to realize the desired magnetic confinement.

Freezing the atoms in a deep lattice not only allows to more freely tune the harmonic confinement, but also effects another property of high importance to the matter wave dynamics, which is the coherence of the atoms. If the atoms are coherent across the system they will form interference patterns of reincreased density, so-called Talbot revivals [62], periodically during expansion [58, 63]. This results in many instances of high atomic density, in particular at the start of the dynamics in the harmonic trap. In addition, when realizing the momentum distribution at the end of the  $T/4$  pulse, the atoms reassemble in small regions at the Bragg peaks. Because we are working with interacting particles these times of high density lead to changes in the trajectories, significantly reducing the lattice signal at the end of the magnifying sequence. For the measurements, we typically thus either end by freezing out the

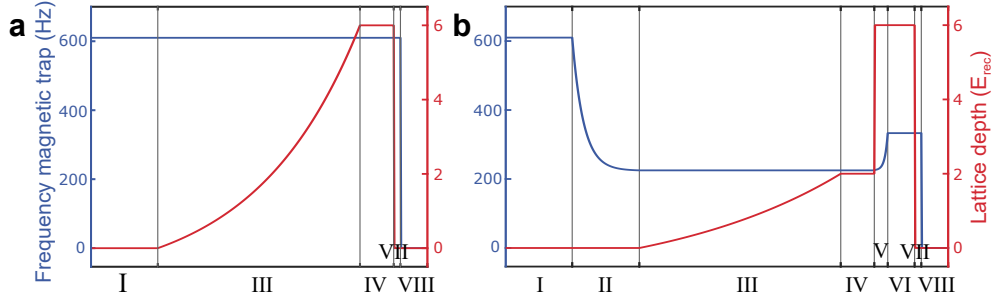


**Figure 3.3.: Experimental sequences of the quantum gas magnifier.**

**a** Sketches of the magnetic trap frequency in Hz (blue, left axis) and the lattice depth in  $E_{\text{rec}}$  (red, right axis) for the most straightforward magnifying sequence. Region I is the ending of the evaporative cooling, followed by an adiabatic loading into a lattice of  $V = 6E_{\text{rec}}$  (III). After some measurement in this lattice (IV) it is switched off for the  $T/4$  pulse in region VII, while the harmonic confinement stays constant at 610 Hz. Finally, this is switched off as well, starting the time-of-flight (VIII). **b** Experimental protocol including in addition to the previous steps an increase of the system size by ramping down the magnetic trap after the evaporation (II), freezing of the atoms combined with a second ramp of the confinement to increase the magnification (V) and a final hold time before the matter wave lensing (VI). For more details on step VI see section 3.3.4. The  $x$ -axis is not to scale to better visualize the shorter time steps.

coherence of the system since this does not change the lattice site populations or immediately load with the corresponding lattice depth to also image the sublattice density distribution of the system. Suppressing the tunneling can be done relatively easily in the case of the triangular lattice, which is characterized by all three 1D lattices which make up the optical lattice having overlapping potential minima (see section 4.1.2). The potential barriers of the honeycomb lattice on the other hand only have 1/8 the height for the same lattice beam intensities. Thus we have to use the deepest lattice available to freeze out coherence in honeycomb and boron nitride lattices. It is however insufficient to keep the atomic distribution unaltered during a ramp of the magnetic trap, limiting our studies on such lattice structures with sub-lattice resolution to comparatively small systems of around 20 to 50 lattice sites.

Some exemplary images of  $^{87}\text{Rb}$  atoms in the 2D optical lattice taken with the quantum gas magnifier are shown in Fig. 3.4. For a and b triangular lattices are used, while c has images from a honeycomb and a boron nitride optical lattice. In Fig. 3.4a the system size is kept constant at a confinement of  $\omega_{\text{sys}} = 2\pi \times 225 \text{ Hz}$  by always ramping the current through the coils down to 100 A in step II, whereas the harmonic confinement is varied from 362 to 543 and 641 Hz, resulting in magnifications of  $M = 46(1)$ ,  $69(1)$  and  $84(1)$ . The confinements are simple approximations supposing  $\omega_{\text{ho}} = 2\pi/(4T/4)$  exactly and the magnifications are obtained by fitting the imaged lattice constants together with the known pixel size of  $13 \mu\text{m}$  and the separately confirmed optical magnification of  $M_{\text{opt}} = 2.04$ . For Fig. 3.4b the system size is

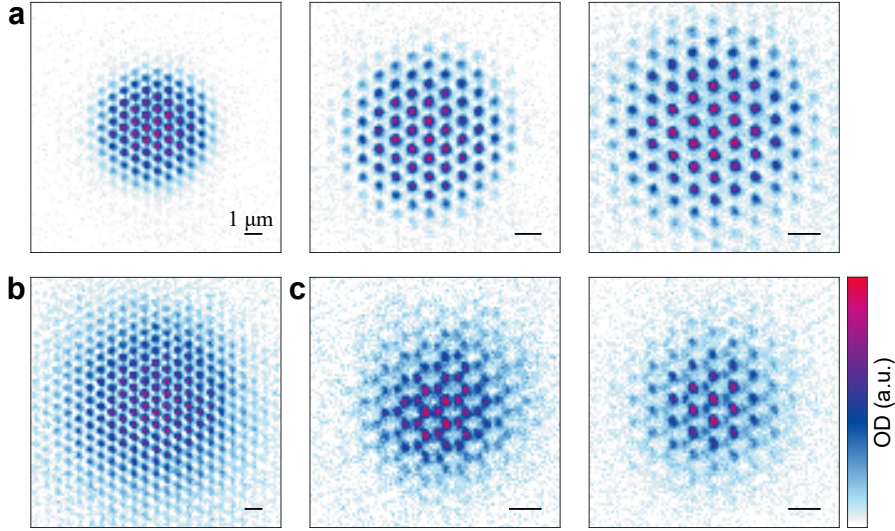


**Figure 3.4.: Example images after quantum gas magnification.** **a** Ultracold  $^{87}\text{Rb}$  atoms in a triangular lattice with system size given by a harmonic confinement of  $\omega_{\text{sys}} = 2\pi \times 225 \text{ Hz}$  and magnifications of  $M = 46(1)$ ,  $69(1)$  and  $84(1)$ . **b** Image of a triangular lattice with  $\omega_{\text{sys}} = 2\pi \times 89 \text{ Hz}$  and  $M = 46(1)$ . **c** Images of a honeycomb lattice and a boron nitride lattice with  $\omega_{\text{sys}} = 2\pi \times 610 \text{ Hz}$  and  $M = 83(1)$ . Adapted from [17].

strongly increased to  $\omega_{\text{sys}} = 2\pi \times 89$  Hz and the magnification set again to  $M = 46(1)$  by appropriately ramping the confinement. Finally the images in Fig. 3.4c have  $\omega_{\text{sys}} = \omega_{\text{ho}} = 2\pi \times 610$  Hz leading to  $M = 83(1)$ . Such magnifications allow us to easily resolve the two lattice sites within the unit cell for the depicted lattice geometries. The first image features a graphene or honeycomb lattice with equal on-site energies and the second one a boron nitride lattice with an energy offset between the A- and B-sites of 4.3 kHz, leading to strong population differences in the ground state.

### 3.3. Characterization

In the following section, the characteristics and limitations of our realization of the quantum gas magnifier will be examined more closely. For this, we experimentally verify the optimal focusing of the matter wave lens and check the resolution, particularly in dependence of the strength of the interaction effects. We also confirm aberrations due to anharmonicity to only have a very minor contribution to the magnified density and discuss how to experimentally lower the effect of the interactions.

#### 3.3.1. Focusing of the Matter Wave Lens

We start the characterization by looking at the precise focusing conditions in the experiment depending on the systems parameters. To quantify the focusing we define the lattice contrast of the quantum gas magnifier as the integrated strength of the peaks in the 2D Fourier transformations of the measured density distribution normalized to the total atom number. The strength is determined by integrating the signal in three circular masks, with each including the signal at one of the reciprocal lattice vectors. The resulting contrast as a function of the evolution time in the harmonic trap  $t_{\text{ho}}$  for different atom numbers is depicted in Fig. 3.5. An independent measurement of the trapping frequency utilized here results in  $\omega_{\text{ho}} = 2\pi \times 305$  Hz. In order to get a sharp image of the initial real space distribution it is necessary to finely adjust the evolution time in the trapping potential to its effective frequency during the evolution pulse  $\omega_{\text{pulse}}$ . In Fig. 3.5a are four images each for atom numbers of roughly 30,000 and 120,000 atoms in the lattice. The evolution times are changed from the focusing times by up to several percent, severely worsening the lattice resolution. In our case, using tens of thousands of interacting atoms, we have a noticeable influence on the exact focusing time and the possible lattice contrast from interaction effects. As shown in Fig. 3.5b, the maximal contrast decreases to about 60% when changing the atom number from 30,000 to 120,000. Additionally, we observe a shift of the focusing time towards longer times, which can be explained by an effectively lower trapping potential seen by the individual atoms due to mean field repulsion. This is displayed for varying atom numbers in Fig. 3.5c, where the focusing time is determined for each 1D direction separately.

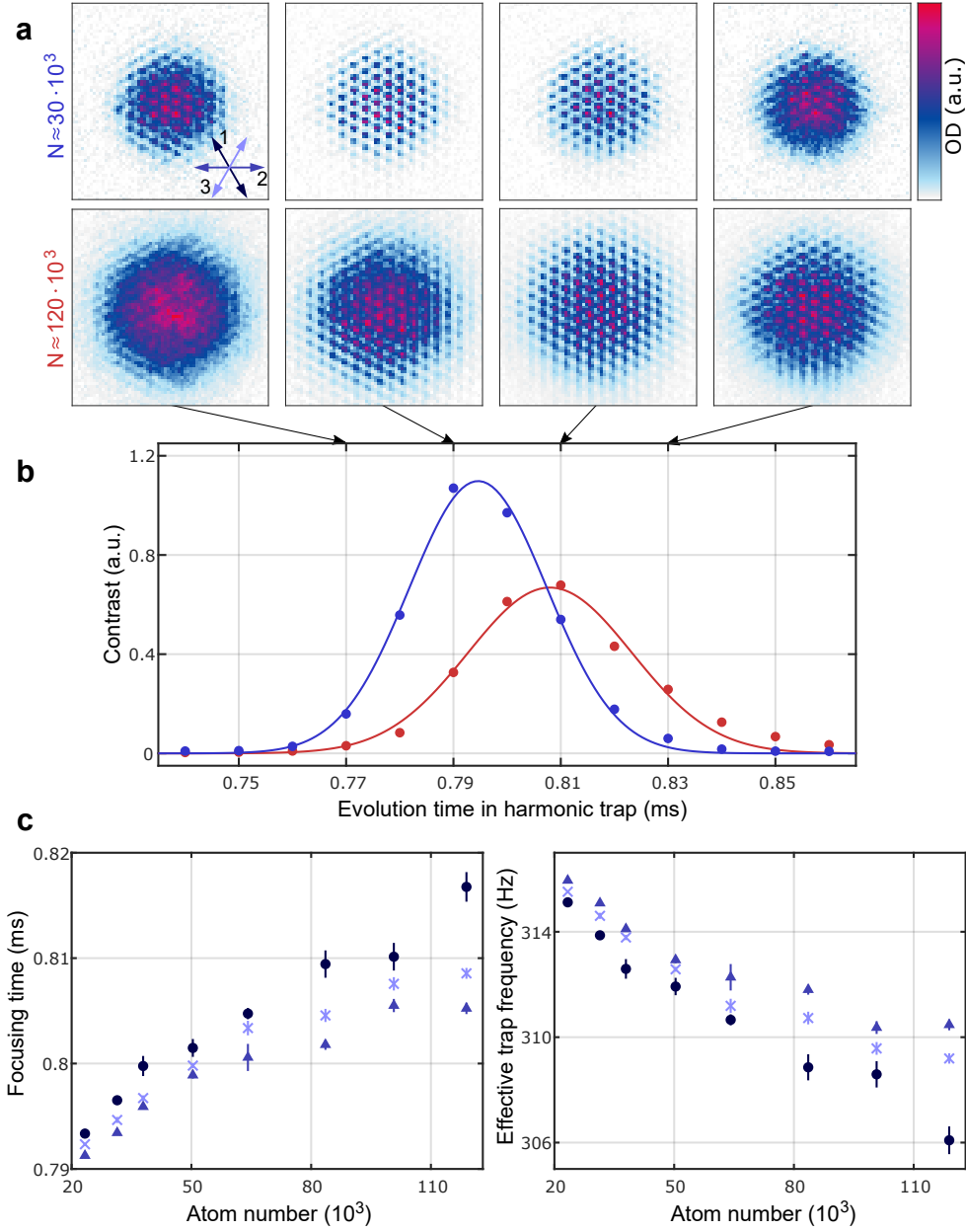


**Figure 3.5.: Lattice contrast of the quantum gas magnifier.** **a** Shown are example images at four evolution times in the harmonic trap,  $t_{\text{ho}} = 0.77, 0.79, 0.81, 0.83$  ms, for a low (30,000) and a high (120,000) number of atoms in the triangular lattice. Every time a system size of  $\omega_{\text{system}} = 2\pi \times 134$  Hz, a harmonic trapping frequency of  $\omega_{\text{ho}} = 2\pi \times 305$  Hz and a time-of-flight of  $t_{\text{ToF}} = 18.5$  ms are used. The inset in the first panel defines the three 1D lattice directions. **b** Contrast of the lattice structure for both atom numbers from **a** as a function of  $t_{\text{ho}}$ . Blue (red) symbols represent measurements with around 30,000 (120,000) atoms. The lines are Gaussian fits, yielding a difference in focusing times of  $13.4 \pm 1.5 \mu\text{s}$  and widths of  $12.8 \pm 0.5$  and  $15.3 \pm 1.4 \mu\text{s}$ . **c** Evolution times of maximal contrast and corresponding effective trap frequencies as a function of the atom number. The symbols correspond to the focusing times of the three directions marked in **a** (direction 1: dark blue circles, direction 2: middle blue triangles, direction 3: light blue crosses). The error bars denote the 68% confidence interval of the centers of Gaussian fits as those depicted in **a**. Adapted from [58].

The effect of the harmonic trap on the final lattice contrast can be increased by comparing the situation at different odd multiples of  $T/4$ . Since the harmonic potential transforms position to momentum or momentum to position for every quarter period, this results repeatedly in images of the magnified spatial distribution. However the impact of aberrations during the hold time increases, leading to a decrease in signal quality (Fig. 3.6a). At  $3T/4$  for example, the maximal contrast ratio between 120,000 and 30,000 atoms has already dropped to below 10%. When increasing the interaction effects further by keeping the coherence between different tubes, we can barely recover the lattice structure after evolution times of  $3T/4$  even for low atom numbers.

Using more relay imaging steps, we also find increased differences in the focusing times for the three 1D lattice directions (Fig. 3.6b). In particular the two directions partially along gravity (1 and 3 in the inset of Fig. 3.5a) have longer times, i.e. see a weaker harmonic potential, than the 1D lattice perpendicular to gravity. We attribute this to the gravitational sag, leading to a small flattening of the potential along gravity. However, since the effect is very minor, with a resulting ellipticity on the order of 1%, this does not prohibit us from simultaneously focusing the lattice both in  $x$ - and  $y$ -direction.

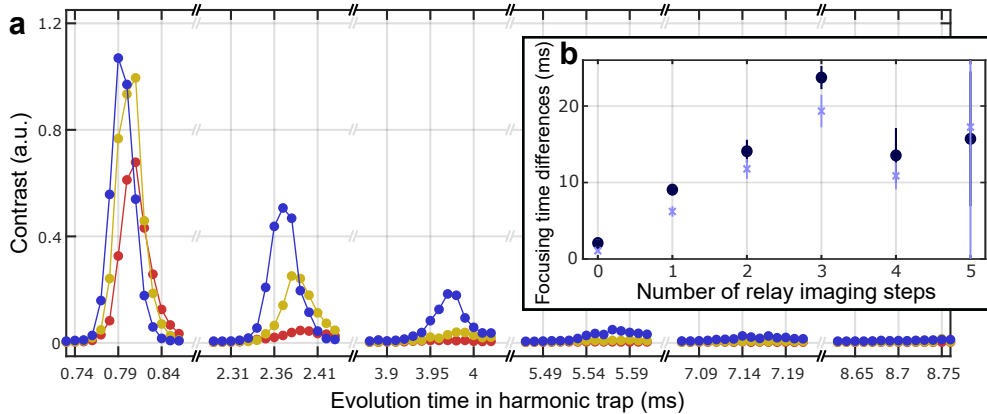


**Figure 3.6.: Image contrast for different number of relay imaging steps.**

**a** The lattice contrast is shown around the expected times for  $(2n+1)T/4$  with  $n = 0, \dots, 5$ , for 30,000 (65,000, 120,000) atoms in blue (yellow, red). **b** Differences in focusing times in directions 1 (dark blue circles) and 3 (light blue crosses) compared to direction 2 (definitions in the inset in Fig. 3.5a). The focusing times result from Gaussian fits to the blue data of **a** for the shown relay imaging steps. For  $n = 5$  the fit fails, as there is no sufficient recovery of the lattice contrast. Adapted from [58].

### 3.3.2. Resolution Analysis

In a second characterization step, we will investigate the resolution we reach using the quantum gas magnifier more quantitatively. For this, we fit a grid of 1D Gaussians with a global width and individual amplitudes to central cuts along all the three 1D directions of the magnifier images. To account for atoms scattered during the  $T/4$  evolution and general imperfections the fit also includes a much broader background Gaussian and a constant offset. The fit function of the optical density  $\rho_{\text{OD}}$  is hence described by

$$\rho_{\text{OD}}(x) = c_0 + c_{\text{bg}} \exp\left(-\frac{(x - x_{\text{bg}})^2}{2\sigma_{\text{bg}}^2}\right) + \sum_{n=1}^N c_n \exp\left(-\frac{(x - x_n)^2}{2\sigma_{\text{site}}^2}\right), \quad (3.9)$$

with  $x_n = x_0 + a_{\text{lat}}(n - \frac{N+1}{2})$ . Here  $\sigma_{\text{site}}$  is the desired global  $1/\sqrt{e}$  width of the lattice sites,  $a_{\text{lat}}$  is the fitted lattice constant and  $N$  is the number of Gaussians in the grid. In the following we choose  $N = 21$ , which is sufficient to include all relevant lattice sites in single lines at the utilized system sizes. A set of example images with the fitted cuts for three different magnifications are plotted in Fig. 3.7a.

From this we determine the lattice site widths as a function of the magnification and the number of atoms in the system as shown in Fig. 3.7b and c. According to the Rayleigh criterion, the lattice sites are well resolved if  $\sigma_{\text{site}} < 0.35 a_{\text{lat}}$  is fulfilled, which ensures the distance of two sites  $a_{\text{lat}}$  to be larger than the radius of the first minimum of the diffraction patterns of the sites. The experimentally observed widths can in first approximation be described as a convolution of the magnified size of the wave function at a lattice site  $\sigma_{\text{wf}}$  and the optical resolution of the absorption imaging  $\sigma_{\text{opt}}$ , resulting in

$$\sigma_{\text{site}}(M) = \sqrt{\sigma_{\text{opt}}^2 + (M\sigma_{\text{wf}})^2}. \quad (3.10)$$

This functional dependency is fitted to the measured widths, averaged over all different atom numbers, in Fig. 3.7b (solid brown line), leading to  $\sigma_{\text{opt}} = 5.2(2) \mu\text{m}$  and  $\sigma_{\text{wf}} = 118(3) \text{ nm}$ . The graph also contains the Rayleigh criterion in blue, showing that according to the fit, a resolution of around 23 would already be sufficient to reach single site resolution. With a standard time-of-flight duration at our setup of 20 ms this would require a trapping frequency of  $\omega_{\text{ho}} = 2\pi \times 183 \text{ Hz}$ .

In a next step, we further include interaction effects in the resolution analysis by measuring the site widths for different atom numbers. As discussed in the previous section, the aberrations due to atomic interactions can also be enhanced by taking higher odd multiples of  $T/4$  into account. This is shown in Fig. 3.7c for atom numbers between around 20,000 and 130,000 using two different magnifications via trapping frequencies of  $\omega_{\text{ho}} = 2\pi \times 633$  and 305 Hz and by including the 0th, 1st and 2nd relay imaging steps. For an analytical description we use a heuristic model, introducing an interaction-induced broadening  $\sigma_{\text{int}}$  and matter wave aberrations of single particles  $\sigma_{\text{lens}}$  to Eq. 3.10:

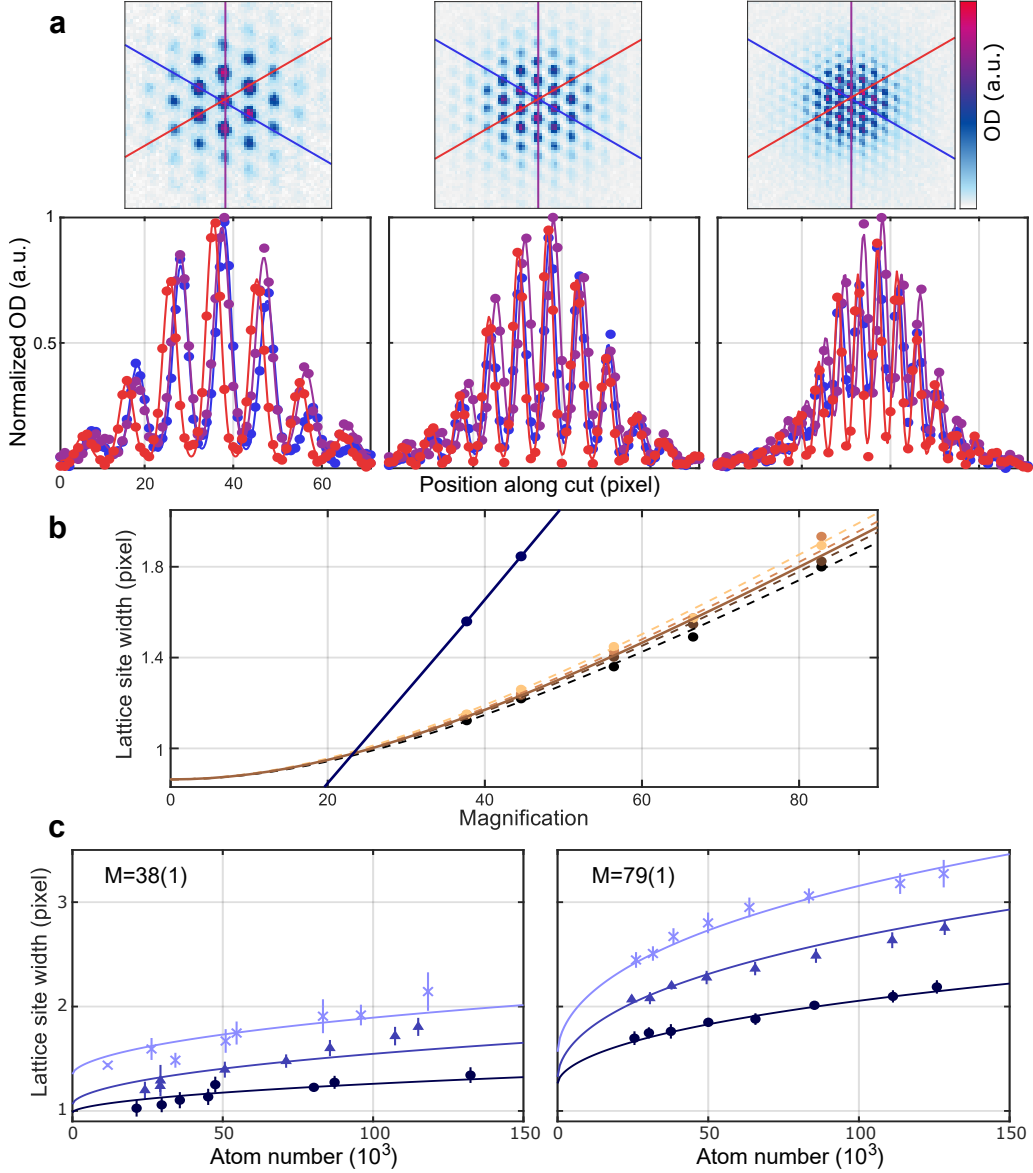


**Figure 3.7.: Resolution of the quantum gas magnifier.** **a** Exemplary images together with central cuts through the distribution using magnifications of  $M = 83(1)$ ,  $56(1)$ ,  $38(1)$ . The position of the cuts are marked by the lines through the images in the corresponding colors. The lines to the data points result from fits of Eq. 3.9. **b** Shown are the fitted lattice site widths for varying magnifications and atom numbers (from black to light brown:  $N = 45(2)$ ,  $54(3)$ ,  $64(3)$ ,  $72(2) \times 10^3$ ). The brown line is the simplified theoretical description of Eq. 3.10 using averages over the four atom numbers, whereas the dashed lines result from fits using Eq. 3.11. Additionally, the Rayleigh criterion, i.e. the widths with  $\sigma_{\text{site}} < 0.35 a_{\text{lat}}$ , is represented by the blue line. **c** Fitted lattice widths for magnifications  $M = 38(1)$  (left panel) and  $M = 79(1)$  (right panel) and three different odd multiples of  $T/4$  (dark blue circles:  $n = 0$ , middle blue triangles:  $n = 1$ , light blue crosses:  $n = 2$ ) versus the number of atoms in the lattice. The lines come from a common fit to all data points using Eq. 3.11. The error bars provide the 68% confidence interval of the three 1D directions (as marked in **a**). Adapted from [58].

$$\sigma_{\text{site}}^2(M, N, n) = \sigma_{\text{opt}}^2 + (M\sigma_{\text{wf}})^2 + ([2n + 1]^{p_1} N^{p_2} M\sigma_{\text{int}})^2 + ([2n + 1]^{p_3} \sigma_{\text{lens}})^2. \quad (3.11)$$

A single Fit to the data of Fig. 3.7c yields  $\sigma_{\text{opt}} = 5.3(3) \mu\text{m}$ ,  $\sigma_{\text{wf}} = 68(24) \text{ nm}$ ,  $\sigma_{\text{int}} = 4.2(4) \text{ nm}$ ,  $\sigma_{\text{lens}} = 0.42(46) \mu\text{m}$  and for the exponents  $p_1 = 0.29(5)$ ,  $p_2 = 0.33(5)$  and  $p_3 = 1.6(7)$ . We compare these results to the more detailed magnification dependence from Fig. 3.7b, using the stated values for  $\sigma_{\text{lens}}$  and  $p_{1,2,3}$ . Fitting the other parameters to these data points leads to  $\sigma_{\text{opt}} = 5.2(1) \mu\text{m}$ ,  $\sigma_{\text{wf}} = 75(10) \text{ nm}$ ,  $\sigma_{\text{int}} = 3.6(3) \text{ nm}$ , in good agreement with the previous fit. Since the values for  $\sigma_{\text{opt}}$  are stated as  $1/\sqrt{e}$ -widths they correspond to a Rayleigh resolution of about  $r_0 = \sigma_{\text{opt}}/0.35 = 15 \mu\text{m}$ .

In conclusion, we find the measured optical density of the real space distribution to be well described by a convolution of the original wave function and a good optical resolution, with comparatively minor additions from single particle aberrations and atomic interactions, provided the coherence across the lattice is frozen in a sufficiently deep lattice. Thus, via the quantum gas magnification the density distribution can be enlarged far beyond the single site resolution.

### 3.3.3. Single Particle Aberrations of the Imaging Protocol

In the following, I will discuss single particle aberrations that occur during the matter wave optics in our magnetic trap. Most importantly, anharmonicities in the trapping potential used to realize the Fourier transform of the initial atomic distribution could severely limit the accuracy of the magnified image of the lattice.

In this regard, a magnetic trap is especially well suited to serve as the harmonic potential, because it can be very smooth and isotropic and also comparatively broad, as the potential region is not limited to the typically smaller waist of an optical dipole trap. Nevertheless, the potential does get more anharmonic at larger distances from the trap center. This gets visible for very large magnifications and populated lattice sites far from the center, as depicted in Fig. 3.8a. Here we shift the atomic distribution away from the trap center and utilize a trap frequency of  $\omega_{\text{ho}} = 2\pi \times 641 \text{ Hz}$  in the image plane. In this way, the populated lattice sites reach the outer part of the potential where the slope gets more linear.

As presented in section 2.1, the magnetic trap can be described by Eq. 2.2. The parameters are given by  $B_0 = 0.11 \text{ G}$ ,  $B' = 1.69 \cdot 10^4 \text{ G/m}$  and  $B'' = 7.12 \cdot 10^5 \text{ G/m}^2$ . Extending the Taylor expansion of  $B(\rho)$  from Eq. 2.3 to the quartic term, i.e. including the main anharmonicities of the magnetic trap, the potential is given by

$$V_{\text{trap}}/h = 78.4 \text{ kHz} + 1.78 \text{ kHz} \left(\frac{\rho}{\mu\text{m}}\right)^2 - 7.2 \text{ Hz} \left(\frac{\rho}{\mu\text{m}}\right)^4. \quad (3.12)$$

The constant term gives the resonance to the  $m_F = 1$  state at the trap center. For small distances from the center, the slope is dominated by the quadratic term and gets

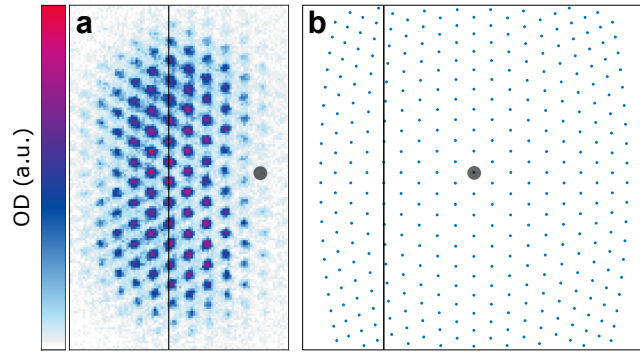


**Figure 3.8.: Aberrations from the trap anharmonicity.** **a** Sum of two images with different displacements between the atomic cloud and the magnetic trap center (gray circle). The harmonic confinement is set to  $\omega_{\text{ho}} = 2\pi \times 641$  Hz. The straight black line is a guide to the eye, highlighting the distortion of the lattice site positions far from the center. **b** Simulation using classical point particles leading to the same lattice distortion. Adapted from [58].

increasingly more anharmonic via the quartic term. To compare our measurement to the expected distortion from the magnetic trap, Fig. 3.8b shows the velocity distribution after a quarter period evolution time in the magnetic trap for classical particles initially located at the lattice sites in a  $19 \times 19$  region. The resulting distortion fits well to the measured lattice site positions.

In conclusion, imaging aberrations due to anharmonicity are negligible in our system. We do however notice deviations when comparing the realized magnification of the distribution with the expectations resulting from the independently measured angular frequency of the harmonic confinement  $\omega_{\text{ho}}$  and the experimentally optimized evolution time in the trap  $t_{\text{ho}}$ . The differences are shown in Fig. 3.9, with Fig. 3.9a referencing to the actually measured magnifications and Fig. 3.9b referencing the different observables to the frequency of the harmonic confinement measured by exciting dipole oscillations of a cold atomic cloud via shifting the trap with respect to the atoms. The expected magnification  $M = \omega_{\text{ho}} t_{\text{ToF}}$  from  $\omega_{\text{ho}}$  is consistently around 15% smaller than the observed one and the expectation from the optimized evolution time in the trap  $M = 2\pi t_{\text{ToF}} / (4t_{\text{ho}})$  is around 10% smaller. The changes with the atom number included in Fig. 3.9b reveal, that the deviations from interactions are significantly smaller than this, with the extrapolation to zero interactions even increasing the discrepancy, as our repulsive interaction leads to an effective lowering of the trap frequency. The origin of these mismatches is not fully understood. The best candidate is the ramp of the confinement during the switch-off, which takes approximately  $40 \mu\text{s}$ , bringing the trap frequency from the optimal evolution time more in line with the independent measurement of the frequency.

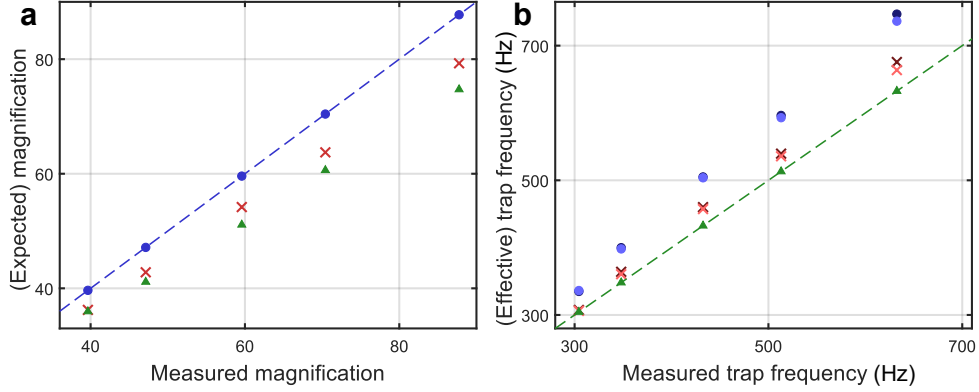


**Figure 3.9.: Comparison of different accesses to magnification and trap frequency.** **a** Shown are the magnifications determined in three ways for five different systems as function of the actually measured magnification. Thus the measured magnification from the fitted lattice constant  $a_{\text{lat}}$  via  $M = \frac{a_{\text{lat}} l_{\text{pixel}}}{2/3\lambda M_{\text{opt}}}$  (blue circles) lie on the dashed angle bisector. Here  $l_{\text{pixel}}$  is the camera pixel side length of  $13 \mu\text{m}$ . Additionally, the magnification obtained via the evolution time  $t_{\text{ho}}$ , used to yield a focused image, calculated as  $M = 2\pi t_{\text{ToF}}/(4t_{\text{ho}})$  (red crosses) and the magnification following ideally from the independent trap frequency measurement as  $M = \omega_{\text{ho}} t_{\text{ToF}}$  (green triangles) are plotted. **b** Comparison of the same methods by their respective expectations of the trap frequency as function of the independent frequency measurement. The different colors for the two other cases demonstrate the comparatively low influence from mean-field repulsion, showing the cases for around 45,000 atoms (dark blue circles and dark red crosses) and around 75,000 atoms (light blue circles and light red crosses).

### 3.3.4. Interaction Effects

In order to correctly transfer the initial positions of the atoms to their momenta at the end of the quarter period evolution time, they should only be accelerated through the harmonic trap. As we are working with interacting particles, we thus have to avoid high densities during the dynamics. A first significant density reduction is achieved by switching off the optical lattice at the start of the evolution time. As stated previously, we then suppress subsequent appearances of high densities due to Talbot revivals during the evolution time by removing the coherence between the lattice sites. We find the typically very fast increase of the lattice depth to  $V = 6 E_{\text{rec}}$  for the freezing to induce breathing oscillations along the  $z$ -direction, changing the lengths of the tubes. The resulting changes in the density have a significant influence on the observed lattice contrast, as shown in Fig. 3.10. The lattice contrast is optimal for large widths along the  $z$ -direction during the dynamics, when the density is minimal. This corresponds to small cloud widths in Fig. 3.10, because in this direction we only have a confinement of up to  $\omega_z = 2\pi \times 11 \text{ Hz}$ , and thus measure the momentum width

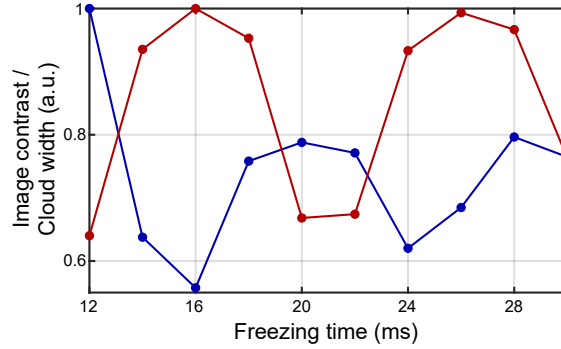


**Figure 3.10.: Contrast oscillation after freezing.** Shown is the contrast of the image via the relative strength of the Fourier peaks of the lattice structure in blue and the measured cloud width along the  $z$ -direction in red. Broader clouds have a smaller width during the quarter period evolution time and hence enhanced interactions, leading to a smaller contrast of the quantum gas magnifier. Adapted from [58].

instead of the real space one. In our typical parameter regime we find a hold time of 12 ms after the increase of the lattice depth to yield the best image contrast.

In the future, it would be very interesting to perform the magnification protocol with an atomic species featuring Feshbach resonances, such that interaction effects could be entirely switched off. This would allow getting sharp images also of coherent systems.

### 3.4. Precision Thermometry

Having investigated the different characteristics and aberrations of our quantum gas magnifier and especially checked the reliability of the access to the single lattice sites, we will now make use of it to perform a first benchmark experiment. The idea is to study the well-known thermal-to-BEC phase transition in real space images, as they allow for an easier identification of the systems temperature compared to standard momentum space images.

For this measurement we prepare the system at different temperatures and atom numbers, by changing both the final frequency of the evaporation ramp from 80 to 140 kHz, which acts correlatedly on the resulting temperature and atom number, and the duration of the subsequent hold time from 1 ms to 5 s. During the latter the RF signal is still active, 15 kHz above the respective final frequency, to act as a RF shield, preventing heating and thus mainly acting on the atom number. Following this, the magnetic confinement is ramped to  $\omega_{ho} = 2\pi \times 305$  Hz and then the atoms are adiabatically loaded into a triangular lattice of  $V = 1 E_{rec}$  depth, corresponding to a tunneling energy, approximated in tight-binding description as nine times the width of the 1st band, of  $J/h = 13$  Hz. Alternatively put, the bandwidth of the 1st

band is  $k_B \times 5.4 \text{ nK}$  and the following 1st band gap has a width of  $k_B \times 290 \text{ nK}$ . Prior to the magnifying sequence, i.e. the switch off of the lattice potential, the coherence is removed by a 15 ms hold time at a lattice depth of  $V = 6 E_{\text{rec}}$ , i.e.  $J/h = 1 \text{ mHz}$ . From the resulting density distributions we then extract the single lattice site populations by overlapping the images with a lattice of Wigner-Seitz cells and integrating the optical density over each of them (see Fig. 3.11a). This is done by firstly finding the currently realized lattice constant via fitting a periodic function to the integrated density profiles. Subsequently the position of the lattice sites with respect to the camera is determined by maximizing the signal in an array of circular masks placed on top of the measured density. For more details on the read-out of the lattice site populations see [17, 50].

The resulting data can be modeled by a bimodal density distribution, consisting of a condensed part in the center of the system, to find the ratio of atoms in the BEC, and a thermal part, from which the cloud temperature can be extracted. The density of the condensed part of the cloud can be described in Thomas-Fermi approximation, leading to an inverted parabolic shape given by the confinement of the system  $\omega_{\text{sys}}$  in the lattice plane. For the thermal part, we use a semi-ideal approach, describing the atoms as an ideal gas in a potential composed of the harmonic trap and a repulsive term from the condensed fraction, which is necessary because of the high atomic density in the condensate. From a combined fit we extract the ratio of condensed atoms  $f_0$  and the temperature of the thermal part  $T$  with high precision as demonstrated by the very good description of the data depicted as projections versus the radial position in Fig. 3.11c and d.

Using the varying temperatures and atom numbers, this allows us to quantitatively study the BEC phase transition. When plotting the BEC fractions as a function of the measured temperature (Fig. 3.11e) the different realizations are spread in the 2D plane and do not fall on a single line, because the critical temperature for condensation  $T_c^0$  depends on the atom number of the atomic cloud. In order to normalize the temperature to the critical temperature we calculate the latter analytically in non-interacting approximation. As a result, the data points collapse onto a single curve, as depicted in Fig. 3.11f. However, we find a shift of the critical temperature  $T_c$  towards lower values compared to the non-interacting theoretical description. The non-interacting case is approximated by a power law for the density of states  $g(E) = C_\alpha E^{\alpha-1}$ , which leads to a dependency  $f_0 = 1 - (T/T_c^0)^\alpha$  with  $\alpha = 2.69(1)$ , shown as the green line in Fig. 3.11f. This value of  $\alpha$  reflects our system being in a complex regime in between a lattice, which is relevant for the density of states only for energies smaller than the 1st band gap, and a 3D harmonic oscillator. The error, as usual, gives the 68% confidence interval of the fitted coefficient. From this we extract the interaction shift by fitting a scaled critical temperature  $T_c$  to the data points with  $f_0 > 0.1$ , using  $f_0 = 1 - (T/T_c)^{2.69}$ . This results in  $T_c/T_c^0 = 0.901(4)$ . The high precision of the thermometry measurement is reflected by the small statistical error found by the fit. On top of the statistical error we have an estimated error on the determined total atom number of 3%, leading to a systematic error on  $T_c$  of 1%. The

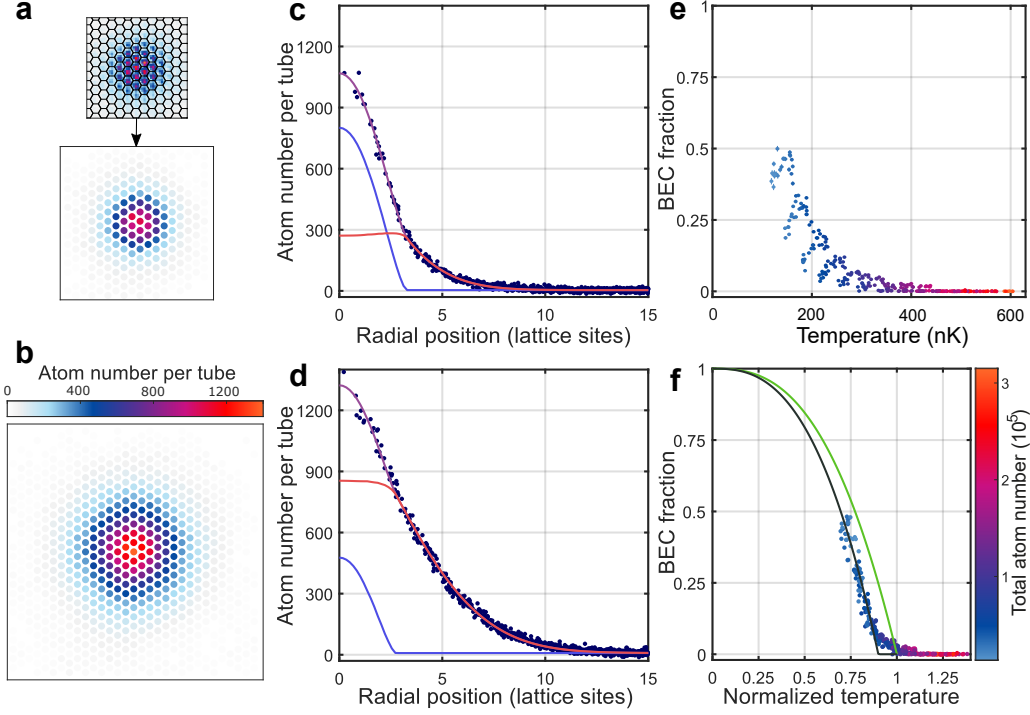


**Figure 3.11.: Thermal-to-BEC phase transition in an optical lattice using real space images.** **a** Read-out of the lattice site populations by overlapping the optical density images with a grid of Wigner-Seitz cells. The system has a temperature of  $T = 171(1)$  nK and 37,000(400) atoms. **b** Shown are the atoms numbers per lattice site at  $T = 310(1)$  nK and a total atom number of 106,000(600). **c,d** Atom number per tube projected to the distance from the clouds center corresponding to the measurements shown in **a** and **b**, respectively. The lines represent the bimodal fit (purple) and its components, the BEC part (blue) and the thermal part (red). **e,f** Condensate fraction as a function of the temperature and the normalized temperature, originating from bimodal fits as depicted in **c** and **d**. The color encodes the total atom number and the error bars denote the 68% confidence interval of the fits. In **f** the green line gives the non-interacting power law approximation and the black line the fit to the data by rescaling the critical temperature. Adapted from [17].

data points with less than 10% of the atoms in the BEC are disregarded in the fit, because of the strong smoothing at the phase transition.

The shift we find is expected in a system of finite-size and including interactions [64] and similar yet less pronounced shifts were already measured in 3D harmonic traps [65, 66]. However, so far there is no full theoretical description available of our crossover regime between the 2D lattice and the overall 3D system, including the relevant contribution from the external harmonic confinement. These peculiarities might also explain the strong smoothing of the phase transition we observe. For

more details on the modeling of our system and effects on the shift of the critical temperature see [17, 50].

### 3.5. Sub-Lattice-Site Resolution

Owing to the strong harmonic confinement achievable in our setup we can magnify the real space density of the atoms in the lattice by almost two orders of magnitudes. This allows going beyond the single site occupation numbers and resolving features well within single lattice sites. To demonstrate this we measure the dynamics initialized via a quench of the lattice potential from a deep balanced boron nitride lattice to a lattice of dimers with energy offset and compare it to a non-interacting simulation of the density  $\rho$  based on Eq. 2.20.

The atoms are adiabatically loaded in a boron nitride lattice with  $V = 32 E_{\text{rec}}$  and a large energy offset between the A- and B-sites of  $\Delta_{AB} = 12 \text{ kHz}$ , such that initially all atoms are located on the lower A-sites. Then the dynamics is started by setting the intensities of two beams to half the balanced value:  $I_2 = I_3 = I_1/2$ . This displaces pairs of lattice sites towards each other, such that they form dimers, as visualized in Fig. 3.12. As a consequence, the tunneling barriers between the sites within dimers are lowered significantly and the lattice site positions are slightly displaced which induces a dynamic between the sites of the dimers and also oscillations in the positions of the atoms within lattice sites. Due to the feedback control of the laser beams the lowering of the intensities is not just given by a step function, but by an exponential decrease with a small overcorrection, in total taking around  $70 \mu\text{s}$  until the final situation is reached.

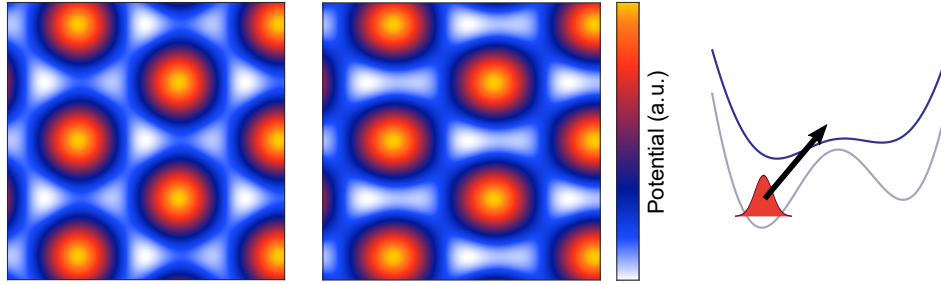


**Figure 3.12.: Initializing the dynamics.** The potential landscapes show the initial balanced boron nitride lattice and the dimerized case with two lattice beams at half the intensity. On the right cuts through a pair of A- and B-sites are shown before (light blue line) and after (dark blue line) the lattice depth quench. It changes both the position of the minima and lowers the potential barrier between them.

We measure the density distribution after a magnification of  $M = 93(1)$  in  $10 \mu\text{s}$  steps from  $10 \mu\text{s}$  to  $390 \mu\text{s}$ , taking six repetitions each, and determine the lattice position in each shot separately. To follow the dynamics, cuts of one pixel width through the center of each dimer are taken. With our magnification we have  $a_{\text{lat}} =$

10.9 pixel and thus one pixel corresponds to 65 nm. Then the resulting distribution is calculated as the average over all single dimers with a summed optical density larger than half the maximal optical density in each respective single shot. These density distributions are plotted underneath each other as a function of the evolution time in Fig. 3.13b. This clearly reveals both an oscillation of the position of the lower lattice site and tunneling processes to the second site.

To the left of the experimental results in Fig. 3.13b the simulated results are shown, which agree well when including a broadening of the distribution via a Gaussian filter of 76 nm. In the simulation we include the evolution of the lattice beam depths as measured on the photo diodes of the feedback control in steps of  $\delta t = 5 \mu\text{s}$ . For this we perform a band structure calculation with the actually realized lattice depths for each time step as described in section 2.3, with the short time scale of the measurement justifying the use of a non-interacting simulation. The resulting instantaneous band energies  $E_{\mathbf{q},m}^{(n)}$  and eigenstates  $|\tilde{\psi}_{\mathbf{q},m}^{(n)}\rangle$  at the  $m$ th time step are then used to obtain the time evolution of the initially realized wave function given by the eigenstate  $|\psi_0^{(1)}\rangle = \sum_k c_k^{(1)} |k\rangle$  in the 1st band ( $n = 1$ ). As simplification the calculation can be restricted to the quasimomentum at the  $\Gamma$  point in the center of the BZ ( $\mathbf{q} = 0$ ), since the dimers are effectively decoupled, leading to flat bands and hence no influence from the quasimomentum. Thus the wave function at the  $m$ th time step is given by

$$|\psi_m\rangle = \sum_n \langle \tilde{\psi}_m^{(n)} | \psi_{m-1} \rangle e^{-\frac{iE_m^{(n)}\delta t}{\hbar}} |\tilde{\psi}_m^{(n)}\rangle. \quad (3.13)$$

Using Eq. 2.20 with the wave function for each time step we calculate the real space density distribution and cut out the signal across one dimer to get the left image in Fig. 3.13b. In the simulation, the external trap is not included, as we see no dependence of the dynamics on the position of a dimer within the cloud in the experiment.

The good agreement between the measured and simulated time evolution demonstrates that the large magnification of our setup indeed allows to faithfully image the real space density well within the unit cell.

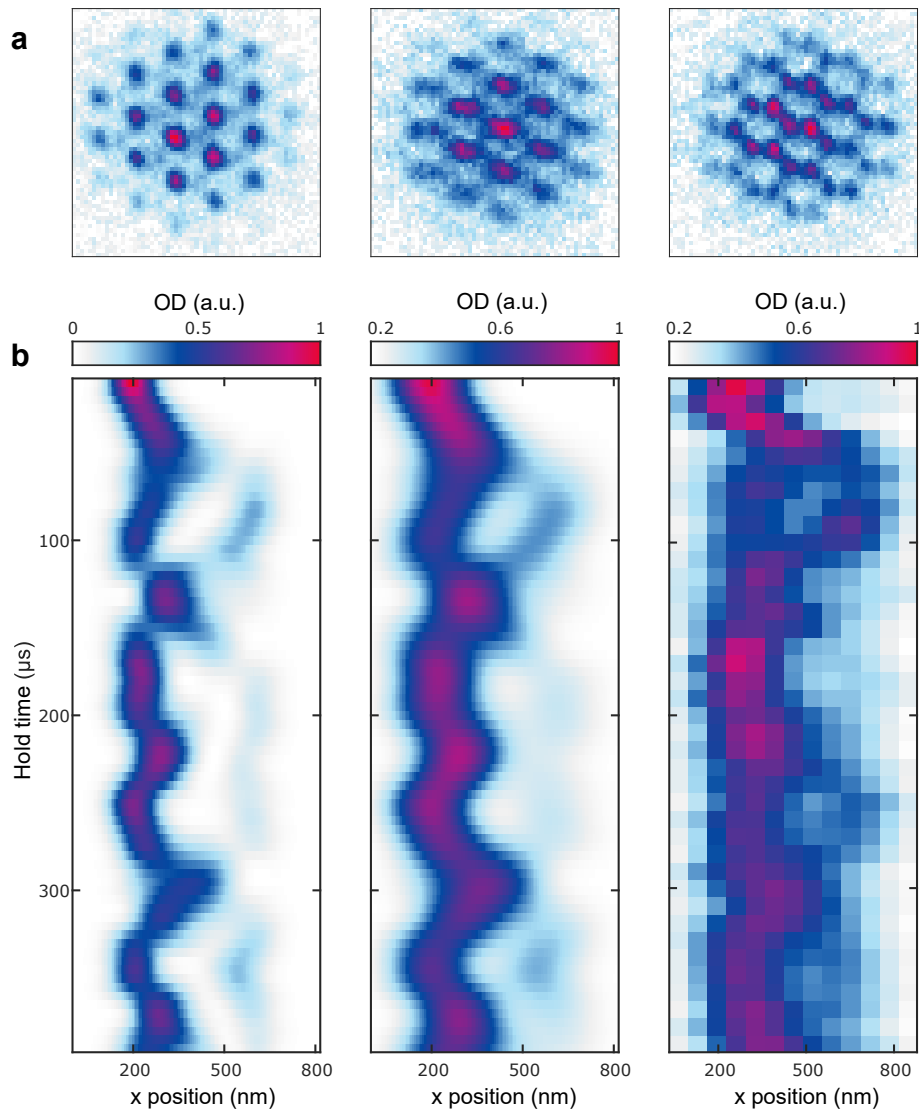


**Figure 3.13.: Nanoscale dynamics in an optical boron nitride lattice.** **a** Shown are three exemplary images 10, 50 and 90  $\mu\text{s}$  after the quench revealing the onset of a tunneling dynamic between the different types of lattice sites. The images are taken with a magnification of  $M = 93(1)$  **b** Time evolution of the density distribution within the dimers. The left images are from the simulation described in the text with the middle one having a Gaussian filter of 76 nm width and a background added for the comparison to the experimental results on the right. The latter are extracted by averaging cuts of single pixel width through all dimers with above 1/2 of the maximal dimer signal, resulting in on average 6.5 utilized dimers per single shot. Adapted from [17].

### 3.6. Local Addressing on the Single Site Level

To make use of the quantum gas magnifier as a general tool for quantum simulation, it is also beneficial to achieve local addressing for the preparation of specific desired states. In quantum gas microscopes this is done using the high-resolution objectives for the imaging, which also allow to get light beams focused onto the system with waists on the order of the lattice constant [67]. Similarly, single sites can be targeted and depleted by using electron beams [68] or by constructing the lattice potential via spatial light modulators with single site resolution [69]. We achieve single site addressing by means of magnetic resonance techniques [70] via the RF antenna used for the evaporative cooling. The local addressing is possible due to the magnetic trap shifting the resonance between the different  $m_F$  levels depending on the distance from the trap center.

The mechanism is visualized in Fig. 3.14. With our  $^{87}\text{Rb}$  atoms in the  $F = 2$  state, there are five  $m_F$  states connectable via the RF signal. According to Eq. 2.1 the magnetic potential depth is proportional to the  $m_F$  state of the atom, resulting in different slopes of the potential as a function of the radius from the trap center. At different lattice sites the resonance condition to drive atoms away from the initial  $m_F = 2$  state thus varies. Atoms brought into the  $m_F = 1$  state are subject to a loss channel, as they can collisionally decay to the  $F = 1$  manifold. Additionally, the RF radiation leads to the population of the lower  $m_F$  states which do not see a trapping potential from the magnetic field, further increasing the loss of such atoms from the system. However, it does still take typically tens of ms to fully deplete a lattice site. Addressing large regions of the lattice by ramping the frequency of the signal thus takes up to several hundreds of ms. In order to suppress tunneling between the sites during this process, which would wash out the addressing resolution, we thus freeze the atoms in a deep lattice.

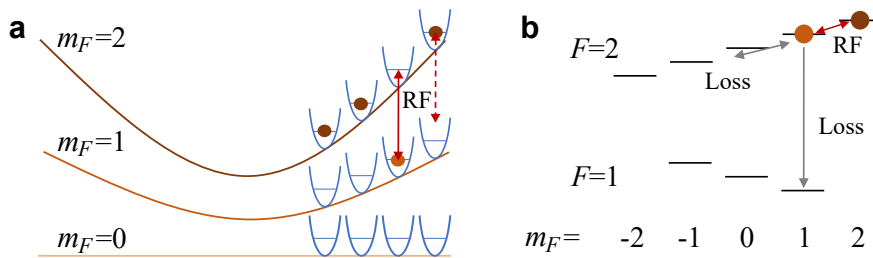


**Figure 3.14.: Scheme of local addressing using magnetic resonance. a** Potential depth of different  $m_F$  levels in the magnetic trap. The transition frequency differs, depending on the distance from the trap center. **b** Sketch of the  $F = 1$  and 2 manifolds of  $^{87}\text{Rb}$  in the presence of a magnetic field. The RF radiation couples the stretched  $m_F = 2$  level to the others, leading to collisional losses. Adapted from [17].

As stated above, the resonance is dependent on the distance of a certain lattice site from the magnetic trap center. In principal, the resonance condition is of course fulfilled over an entire iso-magnetic field surface in 3D space. Due to the strong ellipticity of our magnetic trap, with much weaker confinement along the  $z$ -direction vertical to the lattice plane, compared to the 3D lattice system where the 1D tube lengths are dominated by the lattice beams with waists of around  $160\ \mu\text{m}$ , the iso-magnetic surface can be as thin as a single lattice site over the entire lengths of the tubes. We can thus target ring structures in the lattice, without at the same time addressing all lattice sites within such a ring by crossing the outer parts of their 1D tubes. The form of the magnetic trap now allows for two basic shapes of the targeted region. By keeping it centered on the populated lattice sites, we can address ring-like areas. This is shown in the upper row of Fig. 3.15, where we used a sweep to deplete all lattice sites outside a three-site radius and single frequencies, to either target a ring of sites or, when going to the resonance in the magnetic trap center, a single lattice site. It is also possible to very rapidly shift the position of the magnetic trap away from the atoms via offset fields. When shifting the trap far enough, the curvature of an iso-magnetic surface across the atomic cloud becomes negligible, allowing to target straight lines across the system, as depicted in the middle row of Fig. 3.15. Here we shifted the trap center perpendicular to one of the lattice vectors by around  $14$  to  $16\ \mu\text{m}$ , which at a trap confinement of  $543\ \text{Hz}$ , is equivalent to approximately two system sizes. As a result, we can address regions with straight borders by again sweeping the utilized frequency, to e.g. cut away half of the system or only leave a single populated line of lattice sites. Alternatively, using only a single frequency allows targeting a single line. The resonance and thus the targeted region also is sharper when shifted away from the center than directly around the center. This is due to the slope of the resonance frequency rising linearly away from the center making the neighboring lattice sites increasingly more off resonant. On top of that the ratio between the system size in  $z$ -direction and the extent of the iso-magnetic surface in  $z$ -direction is more favorable, as the latter increases away from the center, while the size of atomic cloud stays unchanged. The width of the targeted region is, however, still on the scale of a lattice constant and hence it is not possible to only target a single lattice site by shifting the trap under an incommensurate angle. Lastly, images 7 and 8 give the situation for a much faster addressing time of  $11\ \text{ms}$ , while the RF signal is ramped to be resonant for around  $3/4$  of the system. The magnetic field is chosen such that the atoms in the usual  $m_F = 2$  level experience a trapping potential of  $\omega_{\text{ho}}^{m_F=2} = 2\pi \times 472\ \text{Hz}$ , leading to a sharp image of their spatial distribution for  $T/4 = 530\ \mu\text{m}$  (image 7). At the same time, there is a significant amount of atoms in the  $m_F = 1$  state, which experience a weaker confinement of  $\omega_{\text{ho}}^{m_F=2} = \omega_{\text{ho}}^{m_F=1}/\sqrt{2} = 2\pi \times 334\ \text{Hz}$ . We can image their spatial distribution by accordingly reducing the pulse time of the magnetic trap, as done for image 8. The lattice contrast is much lower, because of the large background of unfocused  $m_F = 2$  atoms.

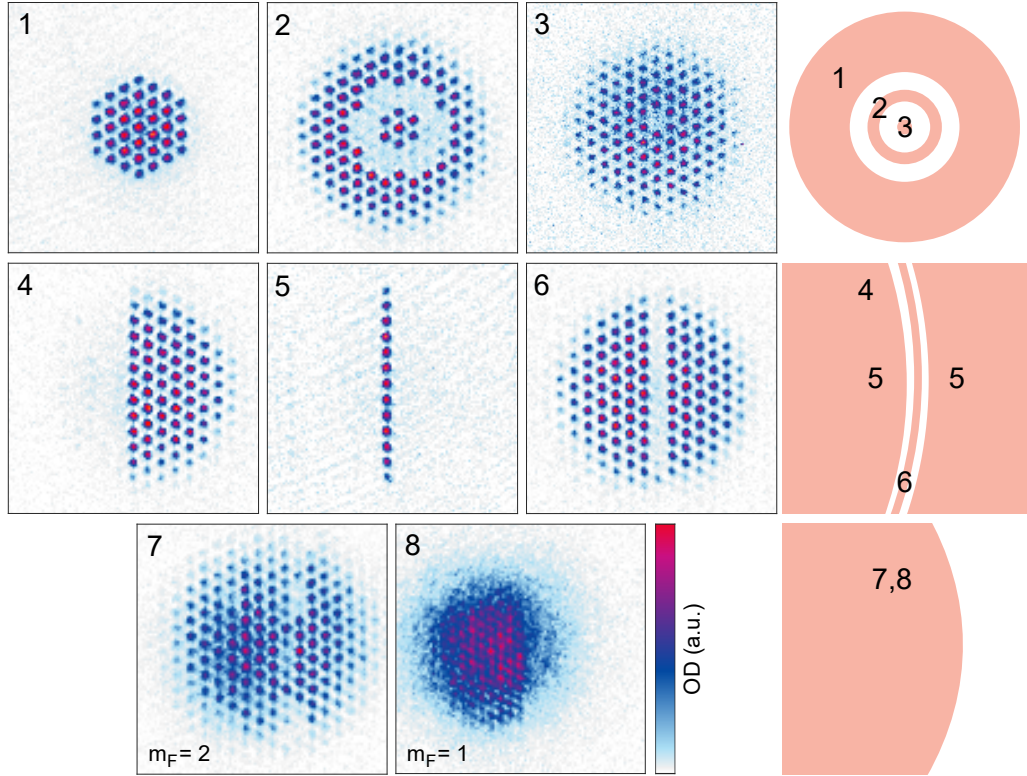


**Figure 3.15.: Example images of the RF addressing.** In the upper row the magnetic trap is centered on the atomic cloud and has a frequency of 543 Hz (658 Hz) in image 1 and 2 (3). The RF signal duration is 100 ms in each case, being ramped from 150 to 110 kHz in image 1 and held constant at 108.5 kHz (67.2 kHz) in image 2 (3). On the right, the corresponding regions targeted by the RF signal are sketched. In the middle row the magnetic trap always has a frequency of 543 Hz and is shifted to the right by  $14.1 \mu\text{m}$  ( $15.7 \mu\text{m}$ ) in image 4 and 6 (5). The RF signal duration is 200 ms in each case. For image 4 it is ramped from 360 to 290 kHz, while it is held constant at 360 kHz for image 6. For image 5 two ramps are used, going from 420 to 486 kHz and from 494 to 540 kHz. On the right a simplified sketch of the targeted regions is shown, which omits the  $1.6 \mu\text{m}$  shift difference. In the bottom row are two images which are prepared with the same RF sweep covering the left part of the cloud as sketched on the right side of the images. Different to the previous images, the RF signal here only has a duration of 11 ms. In the region covered by the sweep some of the atoms are thus transferred to different  $m_F$  states and not yet lost. Image 7 is as usual focused on the  $m_F = 2$  atoms and image 8 on the  $m_F = 1$  atoms, which are magnified by a factor of  $1/\sqrt{2}$  less due to the smaller magnetic moment. Adapted from [17].

These localized cuts into the system also allow for the appraisal of the realized position stability. On the one hand, the fact that we reliably see such sharp patterns after shining in RF radiation for 200 ms (Fig. 3.15 image 5) gives a hard upper limit for the movement within this time. On the other hand, since the lattice beams are not phase locked, the position of the lattice sites differs from shot to shot. As a result, when trying to prepare a single line, in a sizeable ratio of the images the position does not match the gap in between the two RF ramps, leading to defects in the final pattern, exemplified in Fig. 3.16.

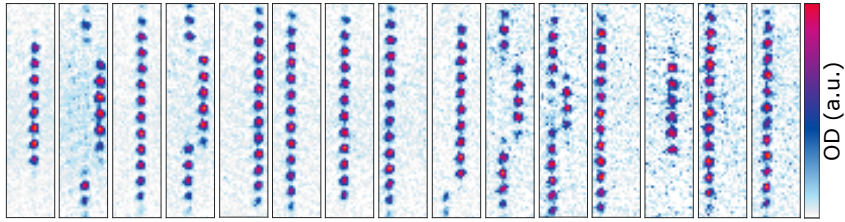


**Figure 3.16.: Repeated preparations of single populated lines.** The system parameters are as for image 5 of Fig. 3.15 for all 15 consecutively measured realizations. The RF ramps always leave out the region between 486 and 494 kHz. We reliably find regions of around one lattice constant populated. However, due to position instabilities of the lattice between shots, the populated region can be split between two neighboring lines of lattice sites.

Apart from this, the combination of shifting the relative positions of the trap center and the atomic cloud as well as targeting single sites by going to the resonance at the trap center, would generally allow for the preparation of arbitrary density patterns. In practice however, the long depletion times necessary due to the waiting for the collisional losses, make this approach unfeasible. It would therefore be promising to instead use microwave radiation to directly transfer the atoms to the  $F = 1$  manifold in combination with an optical push-out beam, which should significantly lower the depletion time.

### 3.6.1. Thermalization Dynamics after Shaping the System

Using the RF addressing, we now want to exemplarily investigate the relaxation dynamics of a system as prepared in image 4 of Fig. 3.15. This starting situation is reminiscent of the one used in [71], where an addition of disorder to the lattice system above a critical threshold was found to result in many-body localization, meaning the interacting system does not thermalize. Making use of the 3D character of our system, we investigate the situation with large bosonic filling on individual lattice sites prepared in a highly nonequilibrium state, monitoring its thermalization.

In order to quantify the asymmetry of the density distribution between the initially depleted left side and the populated right side we calculate the imbalance  $\mathcal{I}$ , defined as

$$\mathcal{I} = \frac{N_{\text{R}} - N_{\text{L}}}{N_{\text{R}} + N_{\text{L}}}, \quad (3.14)$$

with  $N_{\text{R}}$  being the number of atoms in the right half of the trap and  $N_{\text{L}}$  the one in the left half. We measure this as a function of the hold time after the preparation and for different temperatures of the atomic cloud. In between the preparation, where the magnetic trap is shifted by  $14.1 \mu\text{m}$  to target a straight line through the system and the varying hold time, the magnetic trap is shifted back to the previous center of the cloud, so the energy offsets between neighboring sites during the relaxation dynamics are negligible. Fig. 3.17a shows the resulting density distribution integrated along the edge cut by the RF radiation for an initial temperature of  $T_{\text{init}} = 0.76(2) \mu\text{K}$ , where the imbalance decays to zero within around 1.3 s. The extracted imbalances for all starting temperatures of the system are depicted in Fig. 3.17b, revealing that the imbalance does also decay for much lower temperatures, but on a much longer time scale, not going to zero within the experimental observation time of 3.2 s.

The temperatures of the different initial realizations are determined by fitting a bimodal model to the lattice site populations in the right half of the trap, consisting of an inverted parabola, which accounts for the condensed fraction and a Gaussian function modeling the thermal part and giving the sought-after temperature. Here we omit the interaction between the two parts, as its effect on the thermal wings of the distribution is significantly below the fit error. From the Gaussian width  $\sigma$  the temperature is given by  $T = m\omega_{\text{sys}}^2\sigma^2/k_{\text{B}}$ . An example of this is shown in Fig. 3.17c in blue, projected to 1D by only giving the radii of the lattice sites, but including a sign which encodes the position of a site being on the left or right side. We also use this fitting routine to verify the thermalization of the final situation for clouds which reach  $\mathcal{I} = 0$  within the observation time, in this case using the lattice site populations in both halves of the system. Indeed, we find very good agreement with the model demonstrating that the system did reach thermal equilibrium (see red curve of Fig. 3.17c).

Next we extract the thermalization rate  $\Gamma$  as a function of the initial temperature, by fitting an exponential decay  $\mathcal{I}(t) = \mathcal{I}_0 \exp(-\Gamma t)$  to every curve of Fig. 3.17b. We find an almost constant rate for temperatures below 350 nK followed by an increasingly steep growth for higher temperatures. This behavior can be modeled by the Arrhenius law, usually used to describe chemical reactions, but also suitable to model thermal hopping in optical lattices [72]. In this case, it describes the excitation to states beyond the trapping in the optical lattice. In our case of a triangular lattice, this barrier can either be identified with  $8/9$  of the total potential depth, which is the potential depth between different sites, or with the total potential depth, enabling the atoms to freely move over long distances across the lattice system. With our definition of the lattice depth, independently calibrated to  $V = 3 E_{\text{rec}}$  in this case, this results in a potential barrier of  $V_{\text{B}}/k_{\text{B}} = 2.3$  or  $2.6 \mu\text{K}$ . The hopping rate  $\Gamma_{\text{h}}$  of the Arrhenius law is determined as the product of an attempt rate  $\Gamma_{\text{a}}$  and the probability  $P(E > V_{\text{B}})$  for the energy to be larger than the barrier. We modify the formula by

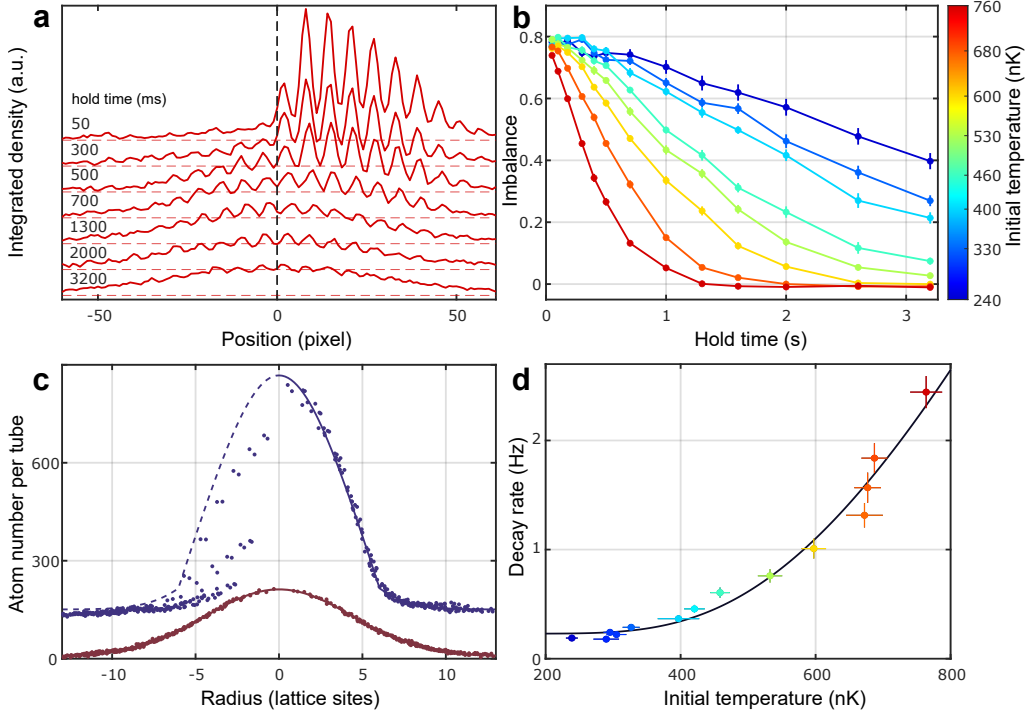


**Figure 3.17.: Thermalization dynamics after preparation of a nonequilibrium state.** **a** Shown is the optical density integrated along the edge cut through the system for an initial temperature of  $T_{\text{init}} = 0.76(2) \mu\text{K}$  and seven hold times, which are offset from each other for clarity. **b** Measured imbalances versus the hold time after the preparation for eight different initial temperatures. **c** The blue (red) symbols denote the lattice site populations averaged over 27 iterations after 50 ms (3.2 s) hold time, with the blue data shifted upwards for clarity. A bimodal fit to the right half of the blue data (solid blue line) yields  $T_{\text{init}} = 0.68(5) \mu\text{K}$ . The fit to the second set of populations, corresponding to  $T_{\text{init}} = 0.76(2) \mu\text{K}$ , gives  $T_{\text{init}} = 1.25(4) \mu\text{K}$  (solid red line). **d** Decay rate  $\Gamma$  of the imbalance for different initial temperatures (color-coding as in **b**), with the error bars denoting the 68% confidence intervals. The data is modeled by a fit of the modified Arrhenius law of Eq. 3.15. Adapted from [17].

adding an offset rate  $\Gamma_0$  to represent quantum tunneling. This leads to a hopping rate given by

$$\Gamma_h \approx \Gamma_a P(E > V_B) + \Gamma_0 = \frac{\Gamma_a}{k_B T} \int_{V_B}^{\infty} e^{-\frac{E}{k_B T}} dE + \Gamma_0 = \Gamma_a e^{-\frac{V_B}{k_B T}} + \Gamma_0. \quad (3.15)$$

Fitting this expression to the data of Fig. 3.17d yields an attempt rate of  $\Gamma_a = 52(44) \text{ Hz}$ , an offset rate of  $\Gamma_0 = 0.23(8) \text{ Hz}$  and an activation barrier of  $V_B = 2.4(6) \mu\text{K}$  in good agreement with the expected barrier height from the independent lattice depth calibration.

To summarize we find that the initial highly excited state of a half-filled system of interacting bosonic atoms in a triangular lattice does decay to equilibrium, although the thermalization happens on a similar time scale as the lifetime in our lattice. Thus, thermal equilibrium is only reached for comparatively hot atomic clouds which give rise to thermal hopping.

### 3.7. Conclusion and Outlook

In conclusion, we realized a novel imaging technique, which uses matter-wave optics to magnify the density distribution, gaining single-shot access to the 2D integrated real space density of 3D systems. We used it to image different 2D lattice geometries, including the first real space measurements of atoms in honeycomb and boron nitride optical lattices, with high occupation numbers, making it a promising tool for the simulation of many-body effects. By choosing sufficiently large magnification factors, this allows us to extract information of the density distribution with sub-lattice resolution. In comparison to other real space imaging methods it features a lower degree of technical complexity.

The concept is based on a Fourier transform of the matter wave by means of a quarter period evolution time in a harmonic trap. We derived theoretically that in this way the quantum mechanical wave function of the system can be faithfully magnified. Through the precise adjustment of the evolution time in the harmonic trap also errors arising from the finite free expansion time can be compensated and the concept also holds for dynamically varying confinements as long as the harmonicity is conserved [58].

We implemented the quantum gas magnification via an elliptical magnetic trap, isotropic in the lattice plane of our 2D optical lattice and performed extensive characterization measurements, verifying the high harmonicity in the trap center and showing the importance of suppressing interaction effects during the evolution time in the harmonic trap.

Using the real space access, we performed several benchmarking experiments. By extracting the lattice site populations in a triangular lattice we were able to perform very precise temperature measurements of the system and to map out the thermal-to-BEC phase transition, allowing determining the interaction shift of the critical temperature with a very small error. The sublattice resolution was shown by following the oscillation and tunneling dynamics across single unit cells initialized by quenching a balanced boron nitride lattice to a lattice of dimers. With a further increase of the magnification, also the differences in the real space distributions of different on-site orbitals could be imaged. Beyond reliable access to important observables like the real space density, another important part for a versatile quantum simulator is the possibility to precisely prepare and manipulate the system under study. To that end we implemented an addressing scheme in our optical lattice for targeting single lattice sites via magnetic resonance. This allows us to depopulate targeted lattice sites and

prepare for example small defects in the system or single occupied lines, which we used to exemplarily follow the rethermalization of a cloud in a triangular lattice after cutting away all atoms on one half of the system.

Additionally, since the quantum wave function is magnified, our imaging technique gives access to density fluctuations. A detailed analysis on this, showing both thermal and quantum fluctuations, can be found in [50]. For further studies on density fluctuations and correlations with the quantum gas magnifier it would be very important to reach single-atom sensitivity by means of free-space fluorescence imaging [73, 74], which is estimated in [58]. This would allow to measure correlation functions in strongly interacting systems also with atomic species, which cannot be used in quantum gas microscopes. Another very interesting prospect is the study of position dependent and short-range coherence properties within the system. One option is to make use of the Talbot effect [62]. It leads to revivals of the lattice structure at regular time intervals due to interference, which could be measured in real space to gain access for example to the coherence length. By acting on the atoms after the evolution time in the harmonic trap it would also be possible to apply masks in Fourier space [75]. More information on these possibilities can be found in [58, 63]. The single-shot, real space access is also very helpful for studying pattern formation and transport properties in optical lattices, which is the subject of chapter 5.

A promising further route is to use a smooth optical dipole trap with sufficiently large harmonical region in the center for the harmonic evolution pulse as it offers faster switching times than a magnetic trap. This would also make the study of spin mixtures much more straightforward, because one could omit complicated spin changing protocols before the harmonic trap evolution time, which in general are necessary for a magnetic trap to have the same frequency for all atoms in all states.



---

## 4. Dynamic Lattice Geometry Control via a Multifrequency Optical Lattice

Optical lattices for ultracold atoms offer a versatile tool for the study of quantum phases, allowing for an alternative approach compared to their solid-state counterparts due to the high degree of control over the system [11, 76]. In particular, the possibility of dynamic tuning of the lattice potential provides interesting benefits. At the same time the tunability typically comes with great challenges in the realization, as such setups include intrinsic instabilities making the lattice geometry dependent on phase noise and adding heating sources to the system. Contrarily, optical lattices build by only  $d + 1$  laser beams in  $d$  dimensions have an intrinsically stable lattice geometry [77]. The realized geometry is then solely determined by the lattice beam polarizations, which severely limits the tuning possibilities due to the typically slow adjustments. In the case of the triangular [30, 78] to honeycomb optical lattice [31, 32], tunability was previously realized by turning the magnetic quantization axis of the atoms in a near-detuned optical lattice [79] and by including a phase lock between different underlying lattices [31, 80, 81].

Our approach of the multifrequency lattice [36] offers an alternative way to realize dynamic geometry control, including tuning on the single microsecond scale and thus much faster than the typical atomic time scales in our lattice, in combination with passive geometry stability. The basic idea is to realize the three 1D lattices which make up the hexagonal optical lattice with independent phases from one another. This allows defining and directly targeting what we call the geometry phase, which is a single periodic parameter, defining the lattice geometry from honeycomb over boron nitride to triangular lattice.

In the following sections, I will explain the concept of the multifrequency lattice by deriving the mentioned geometry phase and presenting our lattice potential and its dispersion relation versus this phase. Then the concrete experimental realization and characterization are presented and the relevance of the geometry phase in the corresponding momentum space lattice is discussed, where it determines a staggered flux. This is followed by the discussion of several measurements highlighting the possibilities of the dynamic geometry tunability.

The multifrequency lattice was set up and characterized and the subsequent measurements taken together with my PhD colleagues Luca Asteria and Henrik Zahn under the supervision of Klaus Sengstock and Christof Weitenberg.

## 4.1. Tunable Lattice Geometry

Now I want to introduce our concept of constructing a 2D hexagonal nonseparable optical lattice via three different laser frequencies. The basic design is depicted in Fig. 4.1. It consists of three laser beams with relative angles of  $120^\circ$  in a single plane, which contain two different laser frequencies each. The resulting 1D lattices from pairwise interference can be accessed independently, leading to a highly tunable geometry of the total 2D lattice potential.

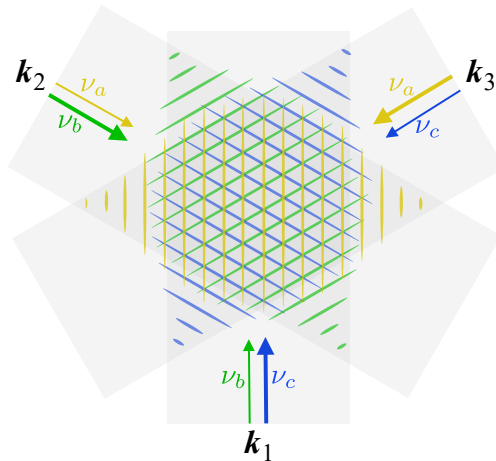


**Figure 4.1.: Concept of the multifrequency lattice.** Three laser beams with relative angles of  $120^\circ$  are superimposed. Every beam consists of two frequencies, leading to pairwise interference. This results in three independently tunable 1D lattices. Adapted from [36].

To start the discussion of our tunable multifrequency optical lattice, I will first derive the geometry phase as the central concept of the design. It follows directly from the general expression of the lattice potential and is the single tuning parameter between the triangular lattice, which is the hexagonal Bravais lattice and the geometrically frustrated honeycomb lattice with its two distinguishable lattice sites per unit cell. Following this, the precise behavior of the lattice potential and the corresponding energy bands as a function of the geometry phase will be presented.

### 4.1.1. Derivation of the Geometry Phase

The total lattice potential resulting from our three laser beams, as described in section 2.2, results in

$$V_{\text{pot}}(\mathbf{r}) = V_0 + 2 \sum_{i=1}^3 V_i \cos(\mathbf{b}_i \cdot \mathbf{r} + \phi_i). \quad (4.1)$$

The three independent relative phases of this potential result in three degrees of freedom. Two are defining the position of the lattice in 2D space and the third determines the shape of the potential, which we call the geometry phase  $\phi_g$ . Its dependence on the three 1D lattice phases can be derived by considering a translation  $\mathbf{r} \rightarrow \mathbf{r} + \delta\mathbf{r}$  of the potential. Using Eq. 4.1 it immediately follows, that this is equivalent to a transformation of the 1D lattice phases given by  $\phi_i \rightarrow \phi_i + \mathbf{b}_i \delta\mathbf{r}$ . Generally, such a change of the phases would vary both the lattice position and its geometry. However, by choosing the correct basis, two linear combinations of the 1D phases lead to two orthogonal translations, whereas the third independent linear combination only effects the lattice geometry. With the choice of the beam vectors under  $120^\circ$  towards each other, we have  $\sum_{i=1}^3 \mathbf{b}_i = 0$ . The linear combination of phase transformations

$$\sum_{i=1}^3 n_i \phi_i \rightarrow \sum_{i=1}^3 n_i \phi_i + \delta\mathbf{r} \cdot \sum_{i=1}^3 n_i \mathbf{b}_i, \quad (4.2)$$

is thus independent of  $\delta\mathbf{r}$  for  $n_1 = n_2 = n_3$ . The most fundamental choice of  $n_i = 1$  leads to the definition of the geometry phase:

$$\phi_g = \sum_{i=1}^3 \phi_i. \quad (4.3)$$

### 4.1.2. Characteristics of the Lattice Potential

Having established the definition of the lattice potential (Eq. 4.1) and the tuning parameter, the geometry phase (Eq. 4.3), I will now present the resulting optical lattices for equal 1D lattice depths (Fig. 4.2). As derived previously, the lattice geometry is given by the relative positions of the three 1D lattices. If the potential minima of all three lattices intersect in single points, the minima of the sum form a triangular pattern, which corresponds to  $\phi_g/(2\pi) = (m + 0.5)$ ,  $m \in \mathbb{Z}$ , and is depicted in the first and last images of Fig. 4.2a. This also naturally results in the configuration with the deepest potential wells. When we now vary the geometry phase  $\phi_g$ , we equally shift the minima position of the 1D lattices along their respective lattice vectors. The potential wells thus are static in position and flatten as the intersections enclose increasingly larger triangles. In the center between the triangular configurations, i.e. at  $\phi_g/(2\pi) = m$ , the potential maxima of all 1D lattices coincide in single points and the 1D lattices form a honeycomb lattice. The two distinguishable

lattice sites per unit cell are marked in the central image of Fig. 4.2a. Close around this symmetric situation the potential energies of the two sites move away from each other, forming boron nitride lattices. This is shown in Fig. 4.2b in cuts through the potential along the symmetry points for different lattice geometries. Thus in total we can tune the lattice geometry via  $\phi_g$  very rapidly from a triangular across a boron nitride to a honeycomb lattice. From Fig. 4.2b it is also apparent, that the effective depth of these different geometries vary significantly. In the triangular lattice 8/9 of the total depth account for the barriers between different lattice sites, while in the honeycomb lattice, which is actually just the sign inverted triangular lattice, the barriers are only 1/9 of the total depth. Together with the smaller distance between neighboring sites this explains the much larger tunneling couplings in the honeycomb case compared to the triangular one for a given lattice depth  $V$ .

To gain a better insight on the effect on the atoms in this lattice structure, we now investigate the band structure of the system as a function of the geometry phase. The integrated energy bands over the entire 1st BZ versus the geometry phase are plotted in Fig. 4.3a and b and for certain values of  $\phi_g$  the band structures are shown quasi-momentum resolved along a high-symmetry path through the 1st BZ in Fig. 4.3c. For the honeycomb lattice this yields relatively broad bands and a closed band gap between the two s-bands, the 1st and 2nd band, at the K and K' points. The triangular lattice however only has a single site per unit cell and hence only a single s-band. Due to the constant depth, the lower bands are almost completely flat in this case. In between these two configurations, their different order of even and odd bands enforces a series of band crossings between higher bands. Starting from  $\phi_g = 0$ , the lowest band gap increases in good approximation linearly, until the system reaches the first triple band crossing. Here the higher s-band hybridizes with the p-bands located at the energetically lower sites. When calculating the band structure across the 1st BZ for this  $\phi_g$ , the 2nd, 3rd and 4th bands show dispersion relations as known from the three s-bands of the Lieb lattice with a flat dispersion of the middle band. Beyond this geometry phase, the 4th band increases linearly in energy up to the next triple band crossing, in this case between the 4th, 5th and 6th band, which form dispersion relations reminiscent of the three s-bands of the Kagome lattice, where the highest band of the triplet is flat. This sequence of band crossings continues until the system reaches the triangular phase. The exact geometry phases at which the different higher band crossings happen depend on the lattice depth. This can be explained by different scalings with  $V$  for different bands. The lower scaling of higher bands compared to the 2nd band leads to earlier crossings for deeper lattices. The well-known band structures that appear at these crossings usually require more complex optical lattice designs, as they result from lattices with three sites per unit cell. By choosing the correct geometry phase of this comparatively simple design, their geometric properties could then be studied using wave packet dynamics [82].

For completeness it should be added that this setup allows to realize all configurations of a three beam, single frequency, triangular lattice conventionally set via the ratio of s- and p-polarizations and the phases between them in every lattice beam

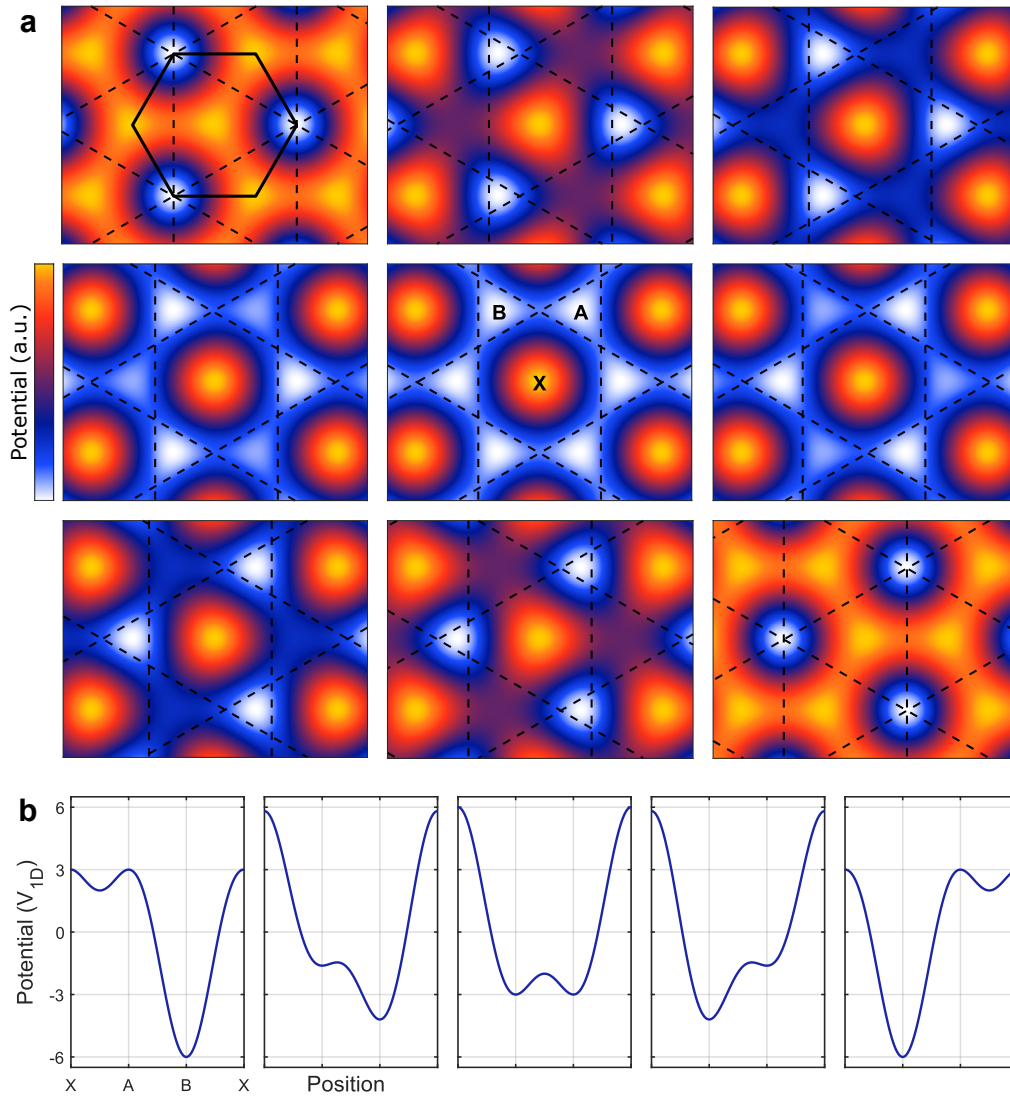


**Figure 4.2.: Lattice potential tuned via the geometry phase.** **a** Potential landscapes for nine different geometry phases ( $\phi_g/(2\pi) = -0.5, -0.25, -0.12, -0.03, 0, 0.03, 0.12, 0.25, 0.5$ ). The potential minima of the three underlying 1D lattices are marked by dashed lines. The hexagon in the top left shows a possible choice of the unit cell. **b** Cuts along a triangle through the potentials for  $\phi_g/(2\pi) = -0.5, -0.12, 0, 0.12$  and  $0.5$ . The corners of the triangles are marked in the central image of **a**.

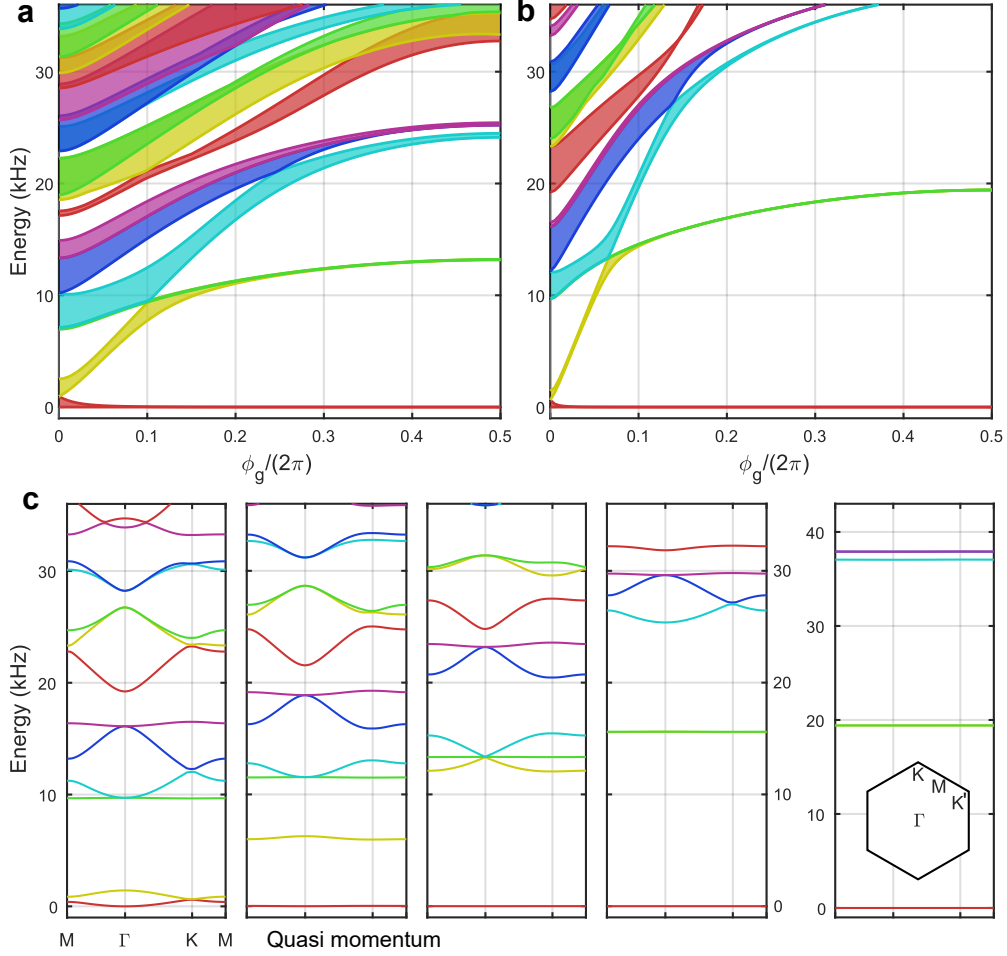


**Figure 4.3.: Band structure from honeycomb to triangular lattice tuned via the geometry phase.** **a** Shown are the band structures from numerical calculation corresponding to Eq. 4.1 with lattice depth  $V = 3 E_{\text{rec}}$ . The colors mark the different bands and the widths are given by integration over the 1st BZ. The band structure is symmetric under reflection around  $\phi_g/(2\pi) = 0$  and  $0.5$  (not shown). The honeycomb lattice on the left is connected to the triangular lattice on the right by a series of higher band crossings as a function of the geometry phase. **b** Same numerical calculations at  $V = 6 E_{\text{rec}}$ . The energy difference between the two sites is higher, leading to a larger band gap. Furthermore the band crossings appear at smaller  $\phi_g$  due to the lower dependence on the lattice depth of the higher bands compared to the 2nd band. **c** Band structures at  $V = 6 E_{\text{rec}}$  along a high symmetry path in the 1st BZ for  $\phi_g/(2\pi) = 0, 0.03, 0.066, 0.138$  and  $0.5$ . The 3rd and 4th panels show the triple band crossings between the 2nd to 4th and the 4th to 6th bands, respectively. The inset in the 5th panel shows the 1st BZ of the lattice system. Style adapted from [36].

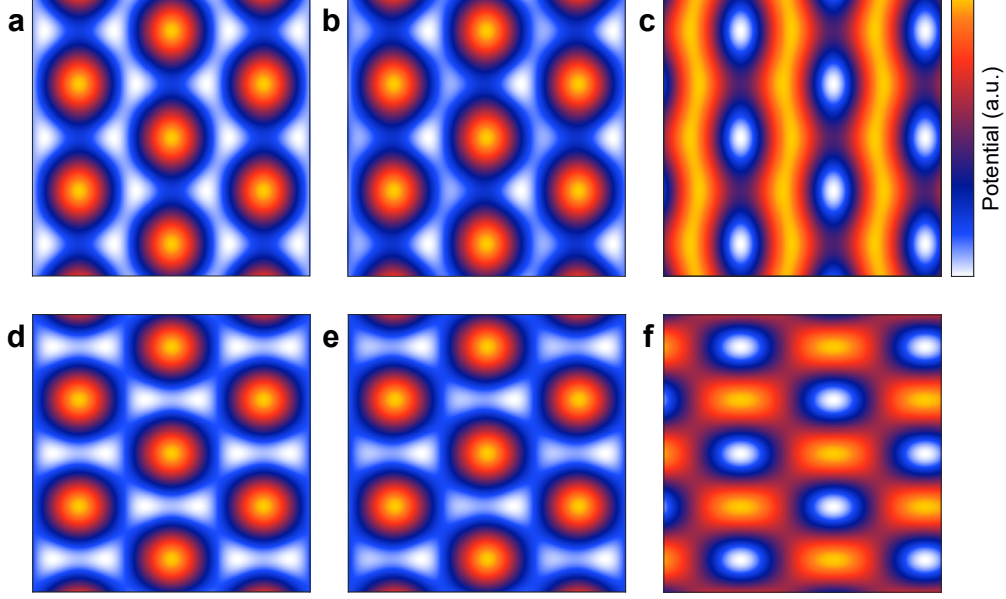


**Figure 4.4.: Further attainable lattice geometries.** Shown are different geometries realized by changing the balancing of the three underlying 1D lattices and the geometry phase  $\phi_g$ . **a** 1D chains using  $V_1 = V_3 = 4/3V_2$  with  $\phi_g = 0$ . **b** Staggered 1D chains with  $V_1 = V_3 = 4/3V_2$  and  $\phi_g/(2\pi) = 0.03$ . **c** 1D chains using  $V_1 = V_3 = 1/0.3V_2$  at  $\phi_g/(2\pi) = 0.5$ . **d** Balanced dimers using  $V_1 = V_3 = 4/5V_2$  and  $\phi_g = 0$ . **e** A-B-dimers using  $V_1 = V_3 = 4/5V_2$  and  $\phi_g/(2\pi) = 0.02$ . **f** Distorted square lattice with  $V_1 = V_3 = 1/5V_2$  and  $\phi_g/(2\pi) = 0.5$ .

(see e.g. [49]). Here we can realize them by using beam imbalances and the geometry phase while keeping the polarizations constant. These include several effectively 1D systems and a distorted square lattice, shown in Fig. 4.4. In the upper line are 1D chains, realized by having one dominant 1D lattice. For  $\phi_g = 0$  neighboring sites are strongly coupled, whereas for  $\phi_g/(2\pi) = 0.5$  and a stronger imbalance the sites of the chains consist of much deeper potential wells. Staggered chains can be realized using a boron nitride configuration with this type of imbalance. By alternatively lowering one 1D lattice compared to the other two, dimers can be created around  $\phi_g = 0$ , with the energy offset between the two sites again given by the precise value of the geometry phase. Going towards a stronger imbalance at  $\phi_g/(2\pi) = 0.5$  leads to a potential wall forming between two of the six nearest neighbors of the triangular lattice, resulting in a distorted square lattice.

In total, the analysis of the optical lattice potential and its band structure illustrates the high degree of tunability possible, when attaining direct control over the geometry phase.

### 4.1.3. Spatial Variation of the Lattice Geometry

A consequence of using different laser frequencies in order to construct the total optical lattice are slight differences in the 1D lattice constants. Put differently, the property  $\sum_{i=1}^3 \mathbf{b}_i = 0$ , used in the derivation of the geometry phase, is not actually met exactly. Thus the precise value of  $\phi_g$  is spatially dependent. Following Eq. 4.2, the geometry phase at position  $\mathbf{r}$  is defined by

$$\phi_g(\mathbf{r}) = \phi_g(0) + \sum_{i=1}^3 \mathbf{b}_i \cdot \mathbf{r}. \quad (4.4)$$

However, with our system parameters of  $\lambda = 1064 \text{ nm}$  and frequency differences of some MHz (see section 4.2) this deviation is completely negligible. For  $|\sum_{i=1}^3 \mathbf{b}_i|$  this results in  $0.33 \text{ rad/mm}$ , which only is a change of some  $\mu\text{rad}$  over our system size.

It might be interesting though to increase this effect on purpose. By going to a setup with frequency differences in the GHz regime, the geometry phase would vary by tens of rad over the system size. By choosing appropriate parameters, this could be used to engineer topological interfaces in the system and thus have access to domains of different topology. The width of the interface region would depend both on the selected frequencies and the lattice depth. Due to the linear change in  $\phi_g$  with position it would be expected to be comparatively broad, although the topology would of course still have to change at some point in space.

### 4.1.4. Generalization to $N$ 1D Lattices in $d$ Physical Dimensions

After presenting the concrete case of the multifrequency lattice potential we realized, I now want to briefly present the extension of the derivation of  $\phi_g$  to the general case of any number  $N$  of 1D lattices in  $d$  physical dimensions. This includes the general option of the potential to be periodic in  $D$  dimensions with  $D > d$ , such that its incommensurate projection to the physical dimensions results in a quasiperiodic lattice.

The dimensionality  $D$  is defined as  $D = N - N_{\text{iis}}$ , with  $N_{\text{iis}}$  the number of rationally independent integer sequences  $n_i^{(c)}$ ,  $\dots$ ,  $n_N^{(0)}$  and  $c = 1, \dots, N_{\text{iis}}$  which yield

$$\sum_{i=1}^N n_i^{(0)} \mathbf{b}_i = 0. \quad (4.5)$$

From this the number of components of the geometry phase  $\phi_g$  follows as the difference between the  $N$  distinct phases  $\phi_i$  and the number of translations of the  $D$  periodic potential, meaning  $N - D = N_{\text{iis}}$ . To get the description of any component of  $\phi_g$ ,  $\phi_{g_c}$ , we again perform a translation, here in the general  $D$ -dimensional space:  $\mathbf{r}' \rightarrow \mathbf{r}' + \delta \mathbf{r}'$ . This directly leads to

$$\phi_{g_c} \rightarrow \phi_{g_c} + \delta \mathbf{r}' \cdot \sum_{i=1}^N n_i^{(c)} \mathbf{b}'_i = \phi_{g_c}, \quad (4.6)$$

which gives the components  $\phi_{\mathbf{g}_c}$  analogous to Eq. 4.3 as

$$\phi_{\mathbf{g}_c} = \sum_{i=1}^N n_i^{(c)} \phi_i. \quad (4.7)$$

In Eq. 4.6 we used that from  $\sum_{i=1}^N n_i^{(c)} \mathbf{b}_i = 0$  follows  $\sum_{i=1}^N n_i^{(c)} \mathbf{b}'_i = 0$ . This also holds in the dimensions beyond the physical ones, because only  $D$  of the  $\mathbf{b}'_i$  are independent, with the remaining ones being defined by integer sums of the independent vectors.

## 4.2. Implementation

In the following, I will describe our realization of a hexagonal multifrequency optical lattice as depicted in Fig. 4.1.

We start from a single laser source, a COHERENT 25 W Mephisto, resulting in a laser beam at  $\lambda = 1064$  nm. It is split via  $\lambda/2$  waveplates and polarizing beam splitters into three beams used to construct the hexagonal 2D lattice structure at the position of the cold atomic cloud. Each of the beams is then guided through an electro-optic modulator (EOM) (Qubig, resonant high-Q electro-optic phase modulator with adjustable resonance frequency), run at different frequencies to add sidebands to the laser spectrum at positive and negative multiples of  $\nu_\alpha = 2.22$  MHz,  $\nu_\beta = 7.77$  MHz,  $\nu_\gamma = 9.99$  MHz, respectively. Afterwards, each laser beam is shifted to the +1st order of an AOM, adding the frequencies  $\nu_c = \nu_0 + \nu_\gamma$ ,  $\nu_b = \nu_0 + \nu_\beta$  and  $\nu_a = \nu_0$ , with  $\nu_0 = 105.005$  MHz, to the carriers and sidebands (Fig. 4.5a). In this way every pair of lattice beams has, in very good approximation, only one frequency in common (Fig. 4.5b).

The frequencies are chosen as multiples of 1.11 MHz, hence this 1.11 MHz is the smallest frequency difference, besides perfect resonance, that is present between the different beams. This is much higher than the kinetic energy scale of the  $^{87}\text{Rb}$  atoms in our lattice given by  $E_{\text{rec}}/h = 2.03$  kHz, so they cannot follow the very fast movement of such optical lattices. Additionally, the desired frequencies of every AOM stay within a window of 10 MHz. This allows us, despite the limited efficiency range of the AOMs, to use the same ones as we did in the past with the conventional approach of running all of them at the same frequency (110 MHz).

Another very important aspect is to ensure the fixed difference between the three EOM frequencies, as this is the condition for a constant geometry phase of the optical lattice. To show this, we derive the time dependencies of the 1D lattice phases including the modulations from the AOMs and EOMs. For  $\phi_1$ , corresponding to the 1D lattice with  $\mathbf{b}_1 = \mathbf{k}_1 - \mathbf{k}_2$ , this follows from  $\nu_b = \nu_c - \nu_\alpha$  in beam one and  $\nu_b$  directly from beam two (see Fig. 4.5b). With analogous considerations for  $\phi_2$  and  $\phi_3$  the time dependencies of the  $\phi_i$  are thus given by

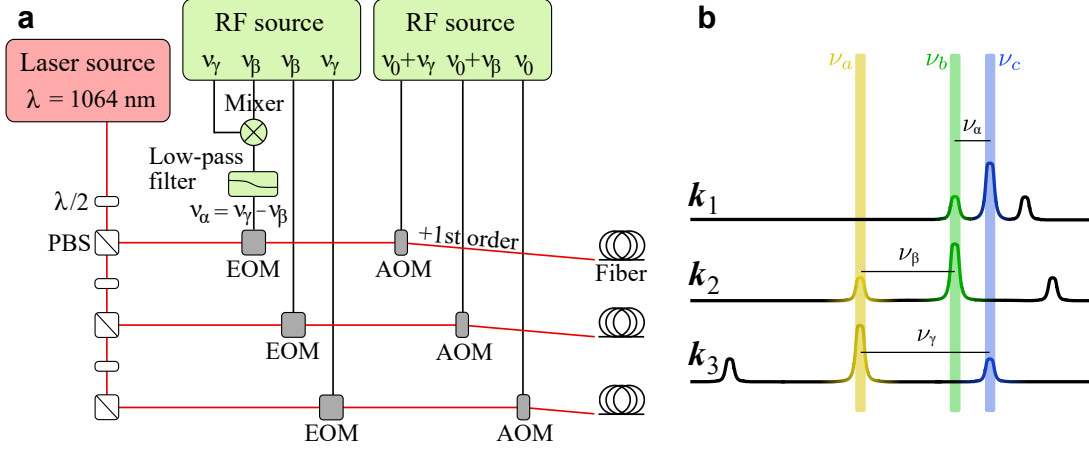


**Figure 4.5.: Experimental realization of the multifrequency approach.** **a** Schematic depiction of the optical lattice setup. The laser beam is split into three parts, with each passing through an EOM to add a sideband and an AOM to get the necessary frequency shift and amplitude tunability. The RFs used by the EOMs are generated by a single 4-channel source and  $\nu_\alpha$  in particular is derived via mixing the other two frequencies. **b** Frequency spectra of the three lattice beams resulting from the setup in **a**. Every pair of beams has one frequency in common, a carrier of one beam with a 1st sideband of the other beam. Adapted from [36].

$$\begin{aligned}
 \partial_t \phi_1 &= (\nu_c - \nu_\alpha) - \nu_b \\
 \partial_t \phi_2 &= (\nu_b - \nu_\beta) - \nu_a \\
 \partial_t \phi_3 &= (\nu_a + \nu_\gamma) - \nu_c.
 \end{aligned} \tag{4.8}$$

In the overall time dependence of  $\phi_g$  the contributions of the AOMs thus cancel out:

$$\partial_t \phi_g = \sum_{i=1}^3 \partial_t \phi_i = \nu_\gamma - \nu_\alpha - \nu_\beta, \tag{4.9}$$

leading to a constant  $\phi_g$  if  $\nu_\alpha = \nu_\gamma - \nu_\beta$ .

To do so, we derive all three RF signals from a single digital source, which was developed and custom-made in our group [53, 83]. The finite frequency resolution however would result in a phase drift between the different RF signals, consequently varying the geometry phase. We avoid this by mixing  $\nu_\beta$  and  $\nu_\gamma$  and filtering out the sum of both frequencies via a low-pass filter. The remaining frequency  $\nu_\gamma - \nu_\beta = \nu_\alpha$  then ensures the stability condition is met. The same considerations also hold for the frequency source of the AOMs, although in this case a phase difference between the RF signals acts on two 1D lattices in opposite directions, canceling out the effect on the geometry phase and leading to a movement of the lattice in space. However, we find this effect to be negligible in our case, since in stability measurements with hold

times in the lattice of up to six seconds the average magnified center position of the cloud only changes by less than one lattice constant.

A consequence of this setup is that we lose lattice depth for constant lattice beam powers as compared to the single frequency case. Every 1D lattice is now made by the interference of a carrier from one beam ( $i$ ) with a 1st sideband from another beam ( $j$ ), so its depth is proportional to  $J_0(n_i)J_1(n_j)$ , with  $J_{0,1}$  being Bessel functions of the first kind and  $n_{i,j}$  the modulation indices used for the corresponding beams. In order to maximize all 1D depths simultaneously, we maximize the product  $J_0(n)J_1(n)$ , which results in  $n = n_\alpha = n_\beta = n_\gamma \approx 1.08$ . This modulation index is then set by coupling every lattice beam in a Fabry-Pérot cavity and tuning the RF amplitude until the corresponding ratio of carrier to sidebands is met. Still, the maximal lattice depth is then reduced by a factor of  $J_0(1.08)J_1(1.08) \approx 0.34$ . On the other hand, since the geometry is not set by the ratio of the polarizations in-plane and out-of-plane anymore (see section 2.2), we use fully out-of-plane polarized beams as their interference term is twice as strong and hence the resulting optical potential is a factor of two deeper than with in-plane polarization. Thus, especially for the graphene-like region which otherwise needed in-plane polarization and where the tunneling couplings per lattice beam power are the highest, we gain a factor of two and have an overall depth of around 0.68 compared to the old realization. The out-of-plane polarization also ensures that there is no  $m_F$  dependency in our potential, which would otherwise be the case for a red-detuned honeycomb lattices [84].

The concrete choice for the carrier frequencies of 2.22, 7.77 and 9.99 MHz where done, because in this configuration undesired resonances between higher order sidebands only occur for especially high combinations of EOM orders and can safely be neglected. The first such resonance is between the +6th order with  $\nu_\alpha$  and the +2nd order with  $\nu_\beta$  both resulting in 128.315 MHz, yielding a product of the Bessel functions around 5 orders of magnitude below the carrier with 1st sideband product at their optimal modulation index of 1.08.

### 4.3. Characterization

At this point, we have three 1D optical lattices rotated by  $120^\circ$  with respect to each other in the 2D lattice plane. The next step is to measure the actually realized lattice geometry, i.e. to calibrate the geometry phase and to analyze its stability. Due to delays in the RF setup the geometry phase has an ab initio unknown offset  $\phi_{\text{off}}$  with respect to the phases of the three EOM RF signals in the form:

$$\phi_g = \phi_a + \phi_b - \phi_c + \phi_{\text{off}}. \quad (4.10)$$

The sign difference for  $\phi_c$  originates from the fact that it uses a sideband of opposite sign compared to the 1D lattices with  $\phi_a$  and  $\phi_b$ . In order to calibrate and regularly check the phase offset we have different options. I will describe the three ways we typically use in the following and afterwards analyze the systems stability.

### 4.3.1. Calibrating the Lattice Geometry

The first one is the method best suited to roughly find the RF phase for  $\phi_g = 0$ , if its value is completely unknown, as the parameters can easily be chosen such that it is sensitive over the entire  $2\pi$  range of a RF phase. The other two we found to be more precise as the observables strongly change by slightly deviating from the symmetric situation at  $\phi_g = 0$ , so we used these in order to routinely measure and account for small changes in the exact RF phase. In all of these measurements we only vary the phase of  $\phi_a$ , or more precisely the phase of a single RF signal with frequency  $\nu_\gamma$  used to derive  $\nu_\alpha$  via the mixer depicted in Fig. 4.5a.

The first rough calibration is done by adiabatically loading a BEC in an unbalanced lattice. For this, we lower the intensity of one of the three lattice beams via its AOM to about half the symmetric case, resulting in weaker momentum couplings along two directions compared to the third one. The situation is measured by quenching off all confinements and imaging the momentum distribution of the atoms formed after standard time-of-flight free expansion. The resulting Bragg peaks then of course are not 6-fold symmetric. However, the strength of the imbalance of the three pairs of Bragg peaks depends on the underlying lattice geometry. By repeating the measurement for different RF phases we find a broad maximum in the imbalance around the honeycomb phase  $\phi_g = 0$  (Fig. 4.6). The approximate RF phase offset  $\phi_{\text{off}}$  can then easily be determined by fitting heuristic Gaussian functions to the different Bragg peak populations. As shown by the dashed lines in Fig. 4.6 though, the measurements also agree well with a single particle theoretical expectation. These lines are given by the normalized absolute value squared of the eigenvectors of the different 1st order momentum modes from exact diagonalization, with the three 1D lattice depths as fit parameters.

This response to the geometry phase can be explained by a staggered magnetic flux appearing in the momentum space lattice. Due to different phases attained by changing from one momentum mode to another, the momentum plaquettes have a staggered flux of  $\Phi = \pi + \phi_g$  (for more details on this see section 4.4). As a result, two competing effects weigh in differently depending on the geometry phase. On the one hand the Bragg peaks with  $\pm\mathbf{b}_2$  tend to get higher populations due to higher intensity of the corresponding 1D lattice. On the other hand the energy is lowered by delocalization over all momentum modes, i.e. similar populations for all Bragg peaks. The latter effect is most prominent for the triangular lattice with  $\Phi = 0$ , whereas for the honeycomb lattice with  $\Phi = \pi$  the system is frustrated and the delocalization less energetically favorable.

In addition, this measurement can easily be tuned from being responsive across the entire  $2\pi$  range of  $\phi_g$ , enabling one to quickly get a good guess on the phase offset, to being more precise and giving a more reliable calibration. For relatively weaker lattices, the delocalization is more prominent for all phases, broadening the imbalance peak further. Going to deeper lattices however gives a larger and narrower peak. Due to the relatively smaller tunneling couplings for the triangular lattice at

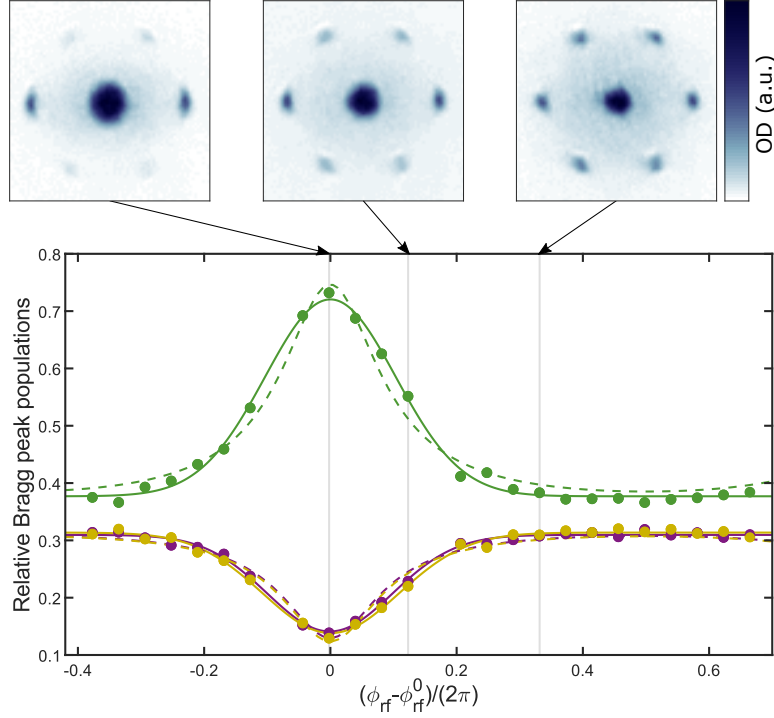


**Figure 4.6.: Relative strengths of the Bragg peaks of an imbalanced lattice as a function of the geometry phase.** Shown is the ratio of the populations in the three different pairs of Bragg peaks, denoted by the three colors and three exemplary time-of-flight distributions at the top. The symbols follow from the integrated OD in masks around the six 1st order peaks, with one experimental shot per data point. The center is determined by three heuristic Gaussian fits to the data (solid lines), which yield  $\delta\phi_{\text{rf}}^0 = 0.00153 \times 2\pi = 9.58 \text{ mrad}$ . Additionally, the theory curves from single particle description are shown (dashed lines), fitted to the data using the determined  $\delta\phi_{\text{rf}}^0$  and yielding 1D lattice depths of  $(V_1, V_2, V_3) = V \cdot (0.5, 1, 1)$ ,  $V = 1.6(1) E_{\text{rec}}$ . Adapted from [36].

the same lattice intensity, the coherence is easily removed for most phases in deep lattices and the Bragg peaks only appear closely around the honeycomb lattice.

As a final remark to this measurement, it is also apparent that balancing the three lattice beams is best being done in the honeycomb lattice, since it is the most sensitive to deviations from perfect balance.

Another calibration method is to use band spectroscopy and measure the ratio of atoms excited to the 2nd band by band mapping, i.e. lowering the lattice depth adiabatically in between the spectroscopy and time-of-flight such that the higher bands are mapped to higher BZs. By choosing a modulation frequency resonant to a small sublattice offset  $\Delta_{\text{AB}}$  we get a double-peaked response, as most atoms get excited at the corresponding geometry phases  $\phi_g = \pm\phi_\Delta$ , symmetric around  $\phi_g = 0$

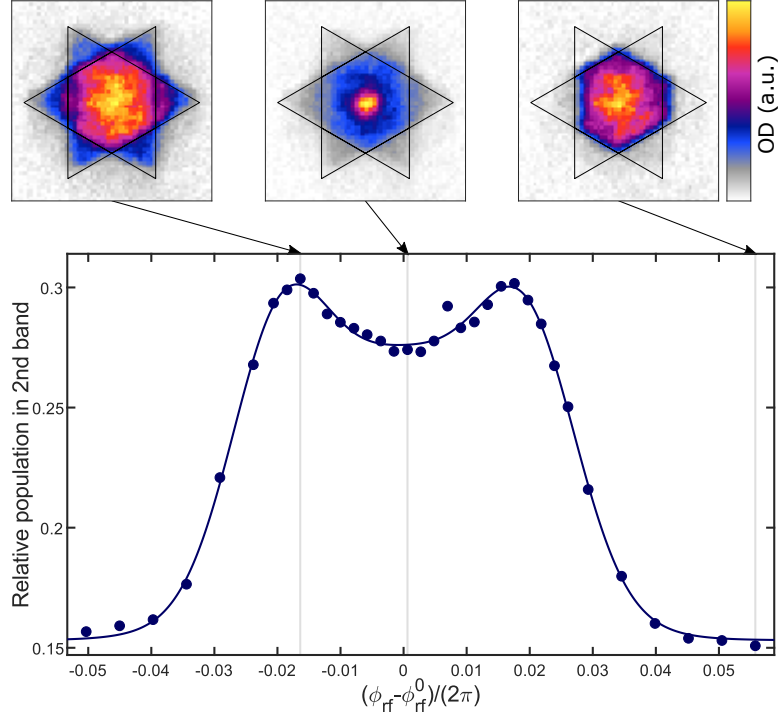


**Figure 4.7.: Population of the 2nd band after spectroscopy as a function of the geometry phase.** Shown is the relative 2nd band population after sublattice modulation spectroscopy of a boron nitride lattice at a fixed frequency of 2.8 MHz. The different Bloch band populations are read out from band mapping images. In the top row are three exemplary images overlapped with the 1st and 2nd BZs. The symbols in the graph are experimental data with 3 to 4 images per data point. The center is determined by fitting eq. 4.11 to the data (solid line), yielding  $\delta\phi_{\text{rf}}^0 = 0.00016 \times 2\pi = 0.98 \text{ mrad}$ . Adapted from [36].

(Fig. 4.7). Again we extract the center of the signal by fitting a heuristic function, here given by

$$n_{2\text{nd}}(\phi) = a_1 \exp\left(\frac{(\phi - \phi_0 - \phi_\Delta)^2}{2\sigma_1^2}\right) + a_2 \exp\left(\frac{(\phi - \phi_0)^2}{2\sigma_2^2}\right) + a_3 \exp\left(\frac{(\phi - \phi_0 + \phi_\Delta)^2}{2\sigma_3^2}\right) + c \quad (4.11)$$

with the relative population of the 2nd band  $n_{2\text{nd}}$  and a constant offset  $c$ . The chosen modulation type for the spectroscopy here is sublattice modulation (for more details on this see section 4.6). We found this calibration method to be very precise, however comparatively costly in measurement time, as both resonances need to be resolved well to give a small error in  $\phi_{\text{rf}}^0$ . This also includes that the chosen spectroscopy frequency needs to be finely adjusted to the utilized lattice depth.

Finally, our most typically used calibration method is to image the atoms in the lattice in real space via our quantum gas magnifier. In this way, the A- and B-site populations can be imaged directly, with both being equal in the honeycomb lattice and diverging approximately linearly for small energy offsets. The measurement consists of loading the atoms in a comparatively deep lattice, in order to freeze out the coherence for sharp real space images, and magnifying the distribution by a factor of 80 to 90. Since we have no phase lock, the position of the lattice is then determined for every image individually to read out the populations of the A- and B-sites. By simultaneously fitting two heuristic linear functions to the two relative populations we get a stable and precise result for the RF phase offset with comparatively few data points needed (Fig. 4.8).

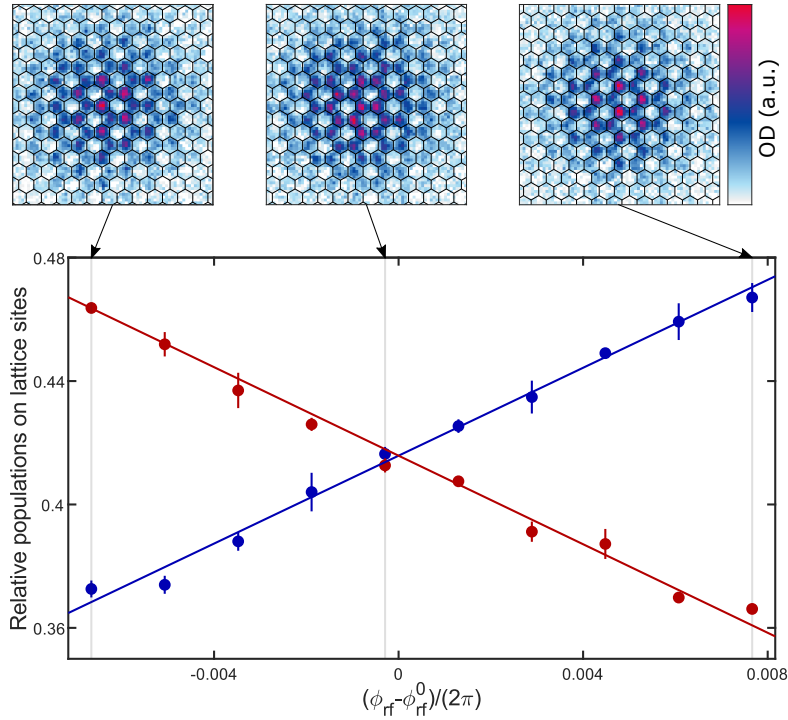


**Figure 4.8.: Populations of the A- and B-sites as a function of the geometry phase.** Shown are the relative populations of the two lattice sites in masks as depicted in the three exemplary images in the top row. The remainder to 100% is located at the areas corresponding to the potential maxima. The symbols are experimental data with the error bars denoting the standard deviation of 2 iterations. The center is determined as the crossing of two heuristic linear functions, which yield  $\delta\phi_{\text{rf}}^0 = 0.00011 \times 2\pi = 0.68$  mrad. Adapted from [36].

For comparison, the numerically calculated A- and B-site populations across  $\phi_g = 0$  are shown in Fig. 4.9. The curves are calculated by performing single particle band structure calculations for all lattice depths and geometry phases. The real space images of the ground state follow by Fourier transformation of the eigenstates cor-

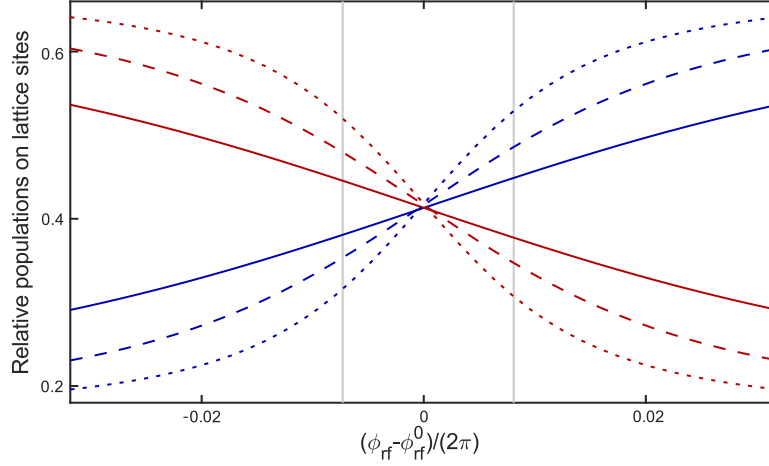


**Figure 4.9.: Theoretical expectation of A- and B-site populations.** Shown are the simulated single particle population ratios on the A- and B-sites across the honeycomb phase. The solid (dashed, dotted) lines corresponds to a lattice depth of  $V = 2$  ( $3, 4$ )  $E_{\text{rec}}$  respectively. A constant background is added to the real space density distribution to give a better comparison to the experimental data. The gray bars denote the region in  $\phi_{\text{rf}}$  shown in Fig. 4.8.

responding to the lowest Bloch band at zero quasimomentum (see section 2.3). Afterwards the images are treated the same way as the experimental images, meaning the different populations are read out by using masks as depicted in the top row of Fig. 4.8. Of course, for large energy differences between the two sites, the ground state is located only at the lower lattice site. By the same consideration, the slope of the lattice site change around  $\phi_{\text{g}} = 0$  depends on the depth of the lattice, with a stronger localization at the lower lattice site for a given geometry phase in a deeper lattice. It is important to note that between the modeled slope and our experimental observations there is a systematic shift. Due to the repulsive interaction between the atoms at our lattice sites, the energetically higher site has a larger population than the non-interacting theory. By independently calibrating the utilized lattice depth, this can be used to estimate the interaction shift. However, as the atom number per site changes over the system, the analysis should be limited to a small region within the lattice, which is possible using the real space information given by the magnifying approach.

### 4.3.2. Stability of the Lattice Geometry

After having found the phase offset, i.e. calibrated the lattice geometry, we can investigate its stability on different time scales. In order to perform precise measurements using the multifrequency design it is of course necessary to have a constant lattice geometry from shot to shot. This is especially important around the honeycomb lat-

tice, where the band energies depend strongly on the exact value of  $\phi_g$ . In order to characterize the stability we repeatedly performed calibration measurements via the magnifier (as shown in Fig. 4.8). Each calibration contains 44 images, four iterations of eleven RF phases, and took approximately 26 min. The resulting  $\phi_{\text{rf}}^0$  versus time are presented in Fig. 4.10a. We find as the standard deviation of the different measurements  $\delta\phi_{\text{rf}}^0 = 0.0004 \times 2\pi = 3 \text{ mrad}$ . In the most critical case of the honeycomb lattice, an unwanted shift to  $\phi_g = 3 \text{ mrad}$  would lead to a band gap of around 76 Hz or 11% of the 1st band width for a lattice depth of  $V = 5 E_{\text{rec}}$ . As this ratio has an approximately quadratic dependence on the lattice depth, the deviations for deeper lattices can become significant. When working in the boron nitride regime however, this error in  $\phi_g$  is already very minor, leading to an almost depth independent change in  $\Delta_{\text{AB}}$  of around 1% for  $\phi_g/(2\pi) = 0.04$ . For precision measurements in deep honeycomb lattices, it might be advisable to replace the current RF source by a possibly more stable one and also thoroughly check the following components of the RF setup for instabilities. On the single-shot scale we measure average fluctuations around the fitted curves of usually roughly 9 mrad. This is however rather an upper boundary for the actual  $\phi_g$  fluctuations, as the exact A to B ratio of the populations measured in a single shot is quite susceptible to noise.

Additionally, Fig. 4.10b shows the long term stability over around four months. We only find minor shifts of tens of mrad for up to around two months and occasionally isolated jumps from one day to another, most likely due to some external influence on the RF setup. An important part of reaching this level of stability is the temperature stabilization of the crystals in the EOMs, which is done using Peltier elements.

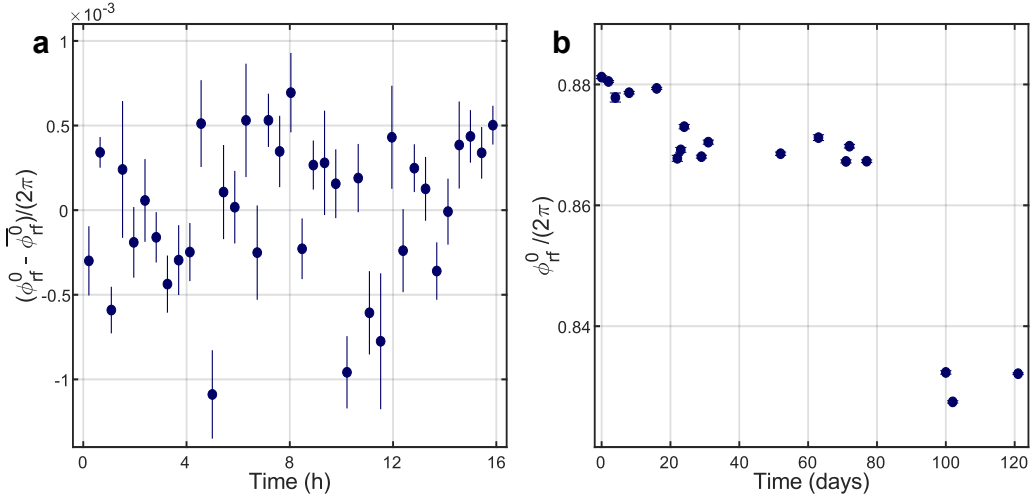


**Figure 4.10.: Stability of the geometry phase.** **a** Consecutive  $\phi_{\text{rf}}^0$  calibration results over a span of 16 hours, with one result every 26 minutes. They yield a standard deviation of  $\delta\phi_{\text{rf}}^0 = 0.0004 \times 2\pi = 3 \text{ mrad}$ . **b** Long term evolution of  $\phi_{\text{rf}}^0$ . Every point in both graphs results from a calibration measurement as in Fig. 4.8 and the error bars describe the 68% confidence interval of  $\phi_{\text{rf}}^0$ . Adapted from [36].

This is necessary, because the resonance frequency of the EOMs depends on their temperature. Thus, a drift would directly change the balancing of the lattice, as the precisely chosen carrier-to-sideband ratio would change. In addition, due to slight variations in the accumulated phase, this would also change the geometry phase.

As a last point, we need to ensure a reasonable short term stability of the geometry phase, referring to the hold times within the lattice of typically tens to hundreds of milliseconds. However, as  $\phi_g$  is by construction only determined by the sidebands of the laser beams, all sorts of e.g. mechanical noise on the fibers would simply move the lattice as a whole. We thus do not expect relevant noise on  $\phi_g$ , which is in line with the absent of worryingly large heating of the atoms when held in our lattice.

## 4.4. Staggered Flux in the Momentum Space Lattice

In the following, I will address another consequence of the geometry phase, showing its relevance in the description of our hexagonal lattice structure. As already mentioned in subsection 4.3.1 we see the effect of a staggered flux in the momentum space interpretation of our lattice, only dependent on the realized value of  $\phi_g$ . I will first define the staggered flux of our system and then investigate its effect on the dynamics in the momentum space lattice by looking at Kapitza-Dirac scattering.

In momentum space the system has a triangular lattice geometry for all  $\phi_g$ , with the different "sites" differing by multiples of the reciprocal lattice vectors. By "tunneling" between the sites, i.e. Bragg reflections, the atoms acquire the relative phase of the two lattice beams forming the corresponding 1D lattice. Accordingly, the phases imprinted in momentum space are given by the three 1D lattice phases  $\phi_{1,2,3}$  and by tunneling around one plaquette the sum of these Peierls phases is thus given by the geometry phase. We follow the convention of tunneling couplings in tight-binding Hamiltonians to include a minus sign. The couplings  $J_i$  are thus given by

$$\begin{aligned} J_i &= -\langle \mathbf{q} + \mathbf{b}_i | V_{\text{pot}}(\mathbf{r}) | \mathbf{q} \rangle = -\langle \mathbf{q} + \mathbf{b}_i | 2 \sum_{i=1}^3 V_i \cos(\mathbf{b}_i \cdot \mathbf{r} + \phi_i) | \mathbf{q} \rangle \\ &= -V_i e^{i\phi_i} = |V_i| e^{i(\pi - \phi_i)}. \end{aligned} \quad (4.12)$$

With that the staggered flux through the triangular plaquettes  $\Phi$  is given by

$$\Phi = \sum_{i=1}^3 (\pi + \phi_i) = \pi + \phi_g \quad (4.13)$$

as depicted in Fig. 4.11a. It is thus independent of the choice of the origin, in contrast to the Peierls phases. The flux in this system has to be staggered, because time reversal symmetry is not broken.

Because of the starting situation, with all atoms on a single site of the momentum space lattice, it is very well suited to study dynamics. Important to note is, that in

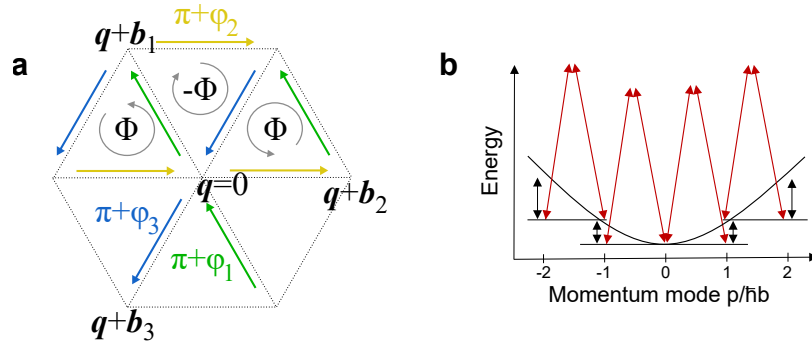


**Figure 4.11.: Momentum space lattice with staggered flux.** **a** Shown is the triangular momentum space lattice built up by the reciprocal lattice vectors  $\mathbf{b}_{1,2,3}$ , with the Peierls phases assigned to the different couplings in colors. The resulting flux is staggered. **b** Coupling of one 1D lattice by its wave vector  $\mathbf{b}_i$  (red arrows). Higher momentum modes are coupled increasingly off resonant (black arrows). Adapted from [36].

our realization of single frequencies for every coupling direction, an important part of the dynamics arise from the increasing energy mismatch between the momentum modes, due to the higher kinetic energy of the higher momentum modes (Fig. 4.11b).

We realize a quantum walk in the momentum space lattice by Kapitza-Dirac scattering, i.e. pulsing the lattice on for times short enough for the real space movement of the atoms to be negligible. In order to do so, we start by detuning two of the AOMs of our lattice by several hundred Hz and turning on the lattice beam intensities. The resulting beam frequencies are sufficiently off resonant for the atoms to only see a dipole confinement. After the feedback control has stabilized the lattice beam intensities at the desired values, we change the RF frequencies back on resonance for the Kapitza-Dirac pulse to start. The pulse is ended by turning off the RF signals, which is again much faster than the pulse times of some microseconds. In this way the feedback control of the lattice beams does not change the shape and duration of the lattice pulses. The choice to use the AOMs and not the EOMs for the control of the pulses is made for stability purposes, because thermal phase drifts of the EOMs would vary the geometry phase. Finally, the atomic distribution is measured after time-of-flight. Some example images at a constant pulse duration of  $t_p = 4.7 \mu\text{s}$  with varying geometry phases are shown in Fig. 4.12. As an effect of the staggered flux we detect the breaking of inversion symmetry for all  $\phi_g$  except the special cases of the triangular and honeycomb lattices, which both yield  $\Phi = -\Phi$ . In the former this is due to the staggered flux vanishing completely, in the latter because  $-\Phi = -\pi = \pi$ . In all other cases the system thus either favors tunneling against (2nd image from left) or along (4th image from left) the reciprocal lattice vectors  $\mathbf{b}_{1,2,3}$ , depending on the sign of the flux. We read out the effect by integrating the signal in circular masks around the six 1st order peaks and averaging over the three related ones. The result-

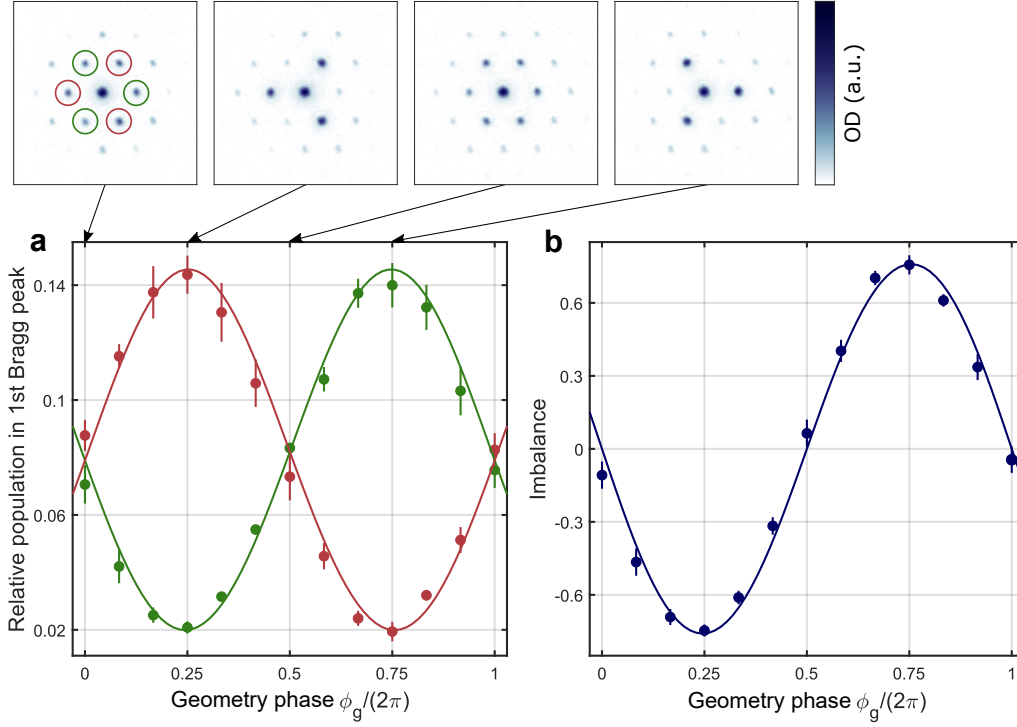


**Figure 4.12.: Inversion symmetry breaking via staggered flux.** **a** The relative populations of the 1st order Bragg peaks are shown as a function of the geometry phase. The symbols are the average of the three related peaks, as highlighted in the 1st image in the top row, from a single experimental shot, with the colors denoting the populations in the peak along the reciprocal lattice vectors  $p_a$  (green) and opposite to them  $p_o$  (red). The error bars give the standard deviation of the mean of the three related peaks. **b** Shown is the imbalance between the populations of panel **a** according to eq. 4.14. The lines in **a** and **b** are numerically calculated for a lattice depth of  $V = 6.5 E_{\text{rec}}$ . Adapted from [36].

ing average relative populations  $p_a$  and  $p_o$  are shown in Fig. 4.12a and the imbalance between the two, defined as

$$I = \frac{p_a - p_o}{p_a + p_o}, \quad (4.14)$$

in Fig. 4.12b.

The theoretical modelling is done by numerically calculating the energies  $E_n$  and eigenstates  $|\psi_n\rangle$  of the static, non-interacting lattice Hamiltonian in plane wave basis considering a reciprocal lattice of  $N \times N$ ,  $N = 11$ , sites. With the pulse time  $t_p$  and the unperturbed state with  $\mathbf{k} = 0$  as initial state, the relative population of the plane wave  $\mathbf{k}$  is then given by

$$n_{\mathbf{k}}(t) = \left| \sum_{n=1}^{N^2} \langle \mathbf{k} | \psi_n \rangle e^{-iE_n t / \hbar} \langle \psi_n | \mathbf{k} = 0 \rangle \right|^2. \quad (4.15)$$

Because the imbalance of the two triplets of Bragg peaks is sensitive over the entire  $2\pi$  range of  $\phi_g$  it can be used similarly to the measurements of the ground-state Bragg peak populations in subsection 4.3.1. However, an important difference is, that the observable in this case, the imbalance, disappears both for the honeycomb and for the triangular lattice.

The interpretation of the inversion symmetry breaking via the staggered flux also gives a physical picture for previous Kapitza-Dirac measurements performed in honeycomb optical lattices [85, 86].

In another measurement, we follow the dynamics of the atoms for three different geometry phases ( $\phi_g/(2\pi) = 0, 0.25, 0.5$ ). The quantum walks show complex behavior of positive and negative interference on certain sites and times (Fig. 4.13a and full data set in Appendix A). The width of the distributions is shown in Fig. 4.13b. The increasing energy mismatch causes an effective harmonic trap for the momentum space lattice, leading to a halting of the expansion and oscillating behavior afterwards. Underneath the dominating effect of the harmonical trap confinement, the distribution expands and oscillates slightly stronger in the case without the staggered flux.

This approach of inducing a quantum walk in a momentum space lattice visualizes the Bloch coefficients of the real space lattice, as these determine the populations of the different momentum modes. Thus the difference of the Bloch coefficients of the different lattice geometries from honeycomb to triangular lattice can, in this picture, be interpreted as a consequence of the staggered flux  $\Phi$ . Contrarily, in other setups where the momentum space was used as artificial dimensions, the different transitions were realized by using several different frequencies, to account for the increasing kinetic energy and stay resonant for higher momentum modes [87, 88]. This method can also be used to create rectified magnetic fluxes [89, 90].

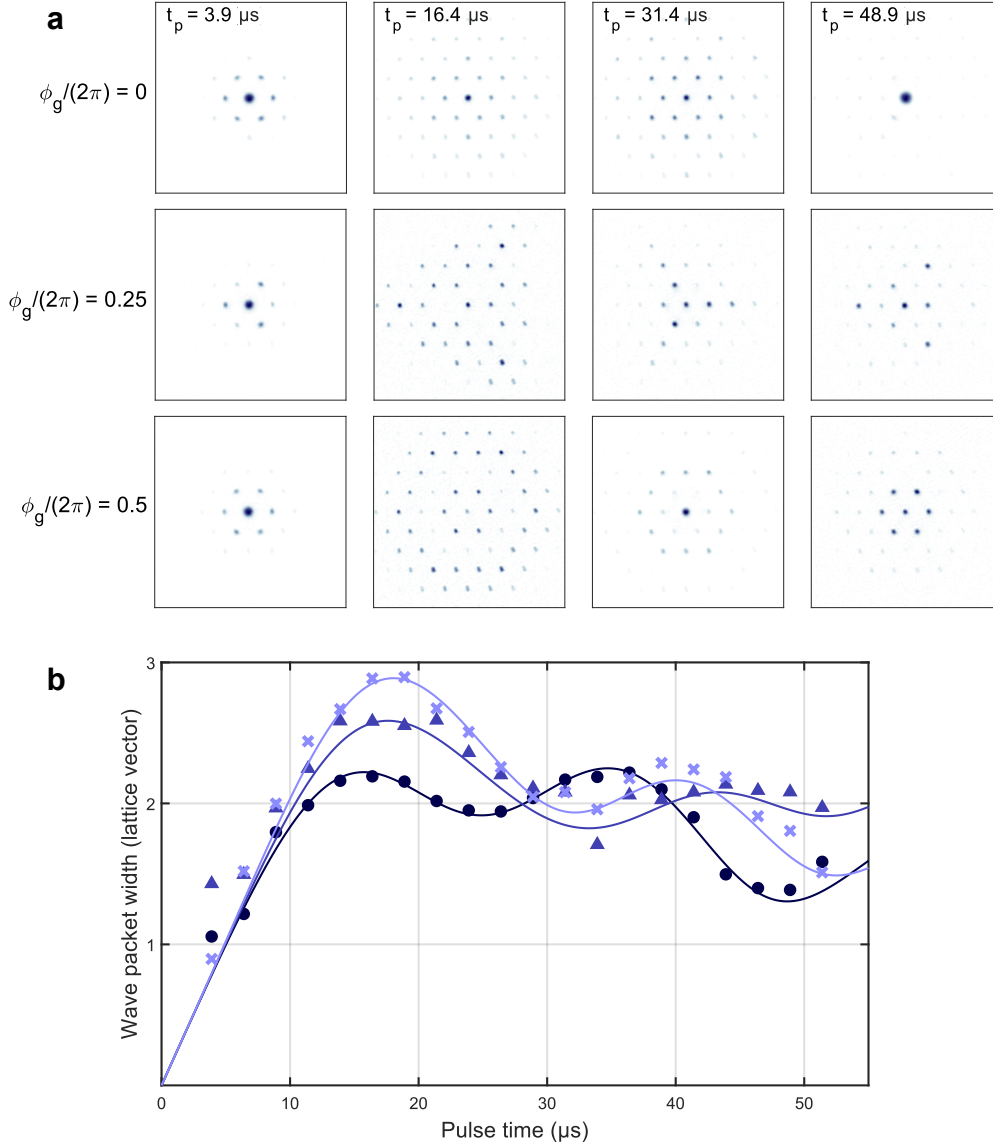


**Figure 4.13.: Time dynamics of quantum walk in momentum space lattice.** **a** Shown are exemplary atomic distributions for four pulse durations  $t_p$  and three geometry phases  $\phi_g$ . **b** Time evolution of the root mean square with of the distribution from experimental data (symbols) and numerical calculation (lines) for  $\phi_g/2\pi = 0$  (dark blue, circles),  $\phi_g/2\pi = 0.25$  (middle blue, triangles) and  $\phi_g/2\pi = 0.5$  (light blue, crosses). The calculation is done using  $V = 6.5 E_{\text{rec}}$ . Adapted from [36].

## 4.5. Excitations into Higher Bands

After having established the concept of the geometry phase as the parameter directly controlling the geometry of our lattice, i.e. the size of the energy offset between the two sites, I now want to present some options that arise from the high dynamic control of our multifrequency lattice design. In the following I will start by looking into the effects of rapidly changing  $\phi_g$ , in particular inverting its sign, both in momentum- and in real space.

### 4.5.1. Preparation of Higher Bands

First I will discuss the possibility of transferring the atoms into higher bands of the lattice, as done previously for checkerboard [91–94] and hexagonal lattices [80, 86, 95]. For this we use a lattice depth of  $V = 6.3 E_{\text{rec}}$  and start at  $\phi_g/(2\pi) = -0.048$ , where all condensed atoms are localized at the energetically lower lattice site and fill up the entire 1st band thermally. We then perform a rapid sweep of the geometry phase of typically around  $60 \mu\text{s}$  across  $\phi_g = 0$  to excite the atoms into certain higher bands, depending on the final geometry phase at the end of the sweep. In order to do so, we vary the frequencies of the sidebands for a time  $t_{\text{sweep}}$  according to

$$\Delta\nu_{(\alpha/\beta/\gamma)} = (+/+/-) \frac{\Delta\phi_g/3}{2\pi t_{\text{sweep}}}. \quad (4.16)$$

The minus sign for  $\nu_\gamma$  is necessary because it uses an opposite sideband compared to the other two. By equally detuning all 1D lattices, we ensure that only the geometry phase changes, whereas the position of the lattice sites remains constant. Afterwards we keep the system in the final configuration for  $500 \mu\text{s}$  and then image the resulting band populations via band mapping, which is shown in Fig. 4.14. By inverting the offset to  $\phi_g/(2\pi) = 0.048$  (leftmost situation in Fig. 4.14) we run through one band crossing, between the 1st and 2nd band, and stop the sweep with still a considerable energy offset to the next higher bands. Thus, most of the atoms are transferred to the 2nd band. For shorter sweep times the situation corresponds increasingly to a phase quench and the ratio of atoms projected to even higher bands grows. For longer sweep times of hundreds of  $\mu\text{s}$  this effect vanishes, however the ratio of the 1st band increases, as more tunneling events to the other lattice site occur. This tunnel coupling is of course much higher when ending at a resonance between bands at the different lattice sites as shown in the next column of Fig. 4.14. Here the geometry phase is swept up to  $\phi_g/(2\pi) = 0.064$ , so that it stops at the 2nd band crossing, where the 2nd, 3rd and 4th band touch at the  $\Gamma$  point. As a consequence, these three bands are populated roughly equally in this case. By increasing the energy offset of the final configuration even further, the atoms can be transferred to e.g. the 4th and 7th bands (right part of Fig. 4.14).

In our system we find lifetimes in the 2nd band of several hundreds of milliseconds, but were so far not able to see recondensation in the 2nd band when starting

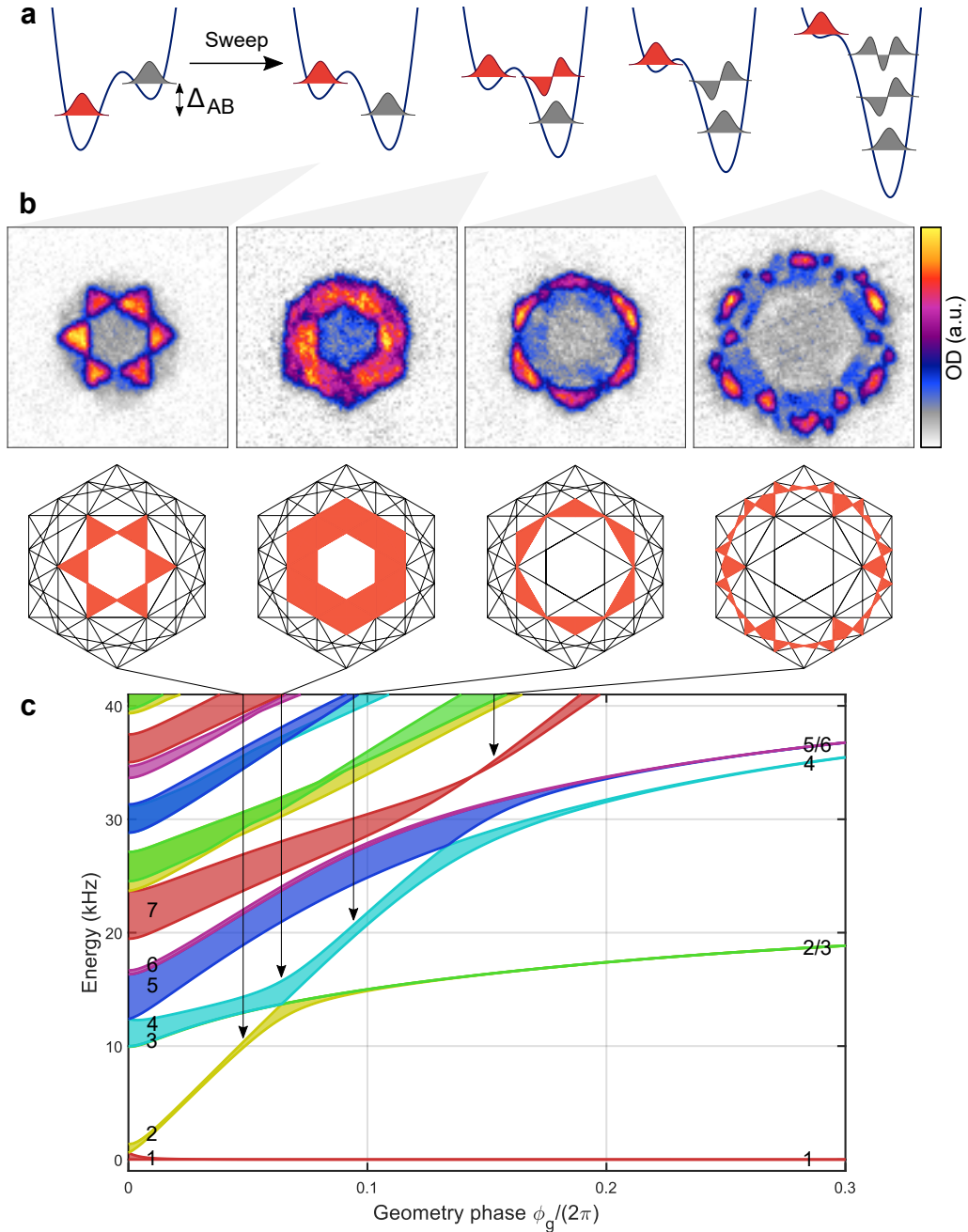


**Figure 4.14.: Preparation of higher bands by sweeping the geometry phase.**

**a** Cuts through the potential of one A-B-site pair before and after four different sweeps. The populated orbitals are marked in red. **b** Band mapping images, corresponding to the final situation in **a**, after linear sweeps from  $\phi_g/(2\pi) = -0.048$  to  $\phi_g/(2\pi) = 0.048, 0.064, 0.095, 0.153$  and a subsequent hold time in the final geometry of  $500 \mu\text{s}$ . The sweeps are done in  $60 \mu\text{s}$  for the 1st to 3rd image and  $20 \mu\text{s}$  for the 4th. The atoms are found in the 2nd band, 2nd+3rd+4th bands, 4th band and 7th band, respectively. These BZs are highlighted in the sketches below. **c** Band structure of the hexagonal lattice as a function of the geometry phase. The lattice depth is  $V = 6.3 E_{\text{rec}}$  as in **b** and the final values of  $\phi_g$  are marked by the arrows. Adapted from [36].

with a BEC. The recondensation would occur at the K points, which are the potential minima of the 2nd band. This would be an important step for studying exotic higher-band physics, like for example chiral superfluids [80]. In combination with the quantum gas magnifier, this could be used to directly image the on-site vortices of the chiral superfluid.

### 4.5.2. Dynamics in Real Space

In addition to measuring the different band populations via band mapping, we can also investigate the populations on the A- and B-sites in real space. The following measurements were done by performing a quench of the geometry phase, directly inverting the energy offset  $\Delta_{AB}$ .

Here we use a lattice depth of  $V \approx 3 E_{\text{rec}}$  with different initial geometry phases. After adiabatic loading of the lattice we proceed by an almost instantaneous inversion of the energy offset  $\Delta_{AB}$ . This is done by changing the phase offsets of the EOM RF signals from  $\Delta\phi_{(\alpha/\beta/\gamma)}^{\text{init}} = (-/-/+)\Delta\phi_g/3$  to  $\Delta\phi_{(\alpha/\beta/\gamma)}^{\text{final}} = (+/+/-)\Delta\phi_g/3$ . The resulting dynamics is then captured by imaging magnified real space densities after hold times in the final situation between  $10 \mu\text{s}$  and up to 6 ms. The single site populations are read out as described for the real space calibration in subsection 4.3.1 and plotted in Fig. 4.15 for  $\Delta\phi_g = 0.6$  and  $0.8$ . In the semi logarithmic plot, we find three distinct behaviors for three different time scales. The A-site population, now localized at the energetically higher potential minimum, quickly diminishes, while the B-site population rises. After around  $10^2 \mu\text{s}$  the populations are relatively static with some signs of damped oscillations. Then beyond around  $10^3 \mu\text{s}$  the dynamics is dominated by a slow reassembling on the now energetically lower B-sites, until after several ms the starting ratio between the sites is reached with the energy presumably going into excitations in the tubes and being carried away by the loss of around 30% of the atoms during the dynamics.

The theoretical description is done starting with the same numerical approach as in the case of the quench to a lattice of dimers in section 3.5, for now also including the restriction to quasimomentum 0, i.e. the  $\Gamma$  point. In this quench protocol however, the final potential is reached much faster than via a lattice depth quench and thus the evolution can be simulated by directly projecting the wave function of the ground state to the eigenstates of the final situation. In the case of a non-interacting particle without energy losses for such relatively small final offsets this results in an oscillation between the A- and B-sites dominated by the frequency given by the band gap between the 1st and 2nd band. The first half period fits well to the initial dynamic with the used lattice depth of  $3 E_{\text{rec}}$ , as this yields band gaps at the  $\Gamma$  point of 5 kHz ( $\phi_g = 0.3$ ) and 6.3 kHz ( $\phi_g = 0.4$ ). To get a quantitative agreement also in the relative populations, the numerically calculated density distributions have an added background once again, increasing the signal on the third of the Wigner-Seitz cell not associated with either the A- or the B-sites to the experimental level of roughly 25%. Due to repulsive interactions of our atoms leading to larger populations on

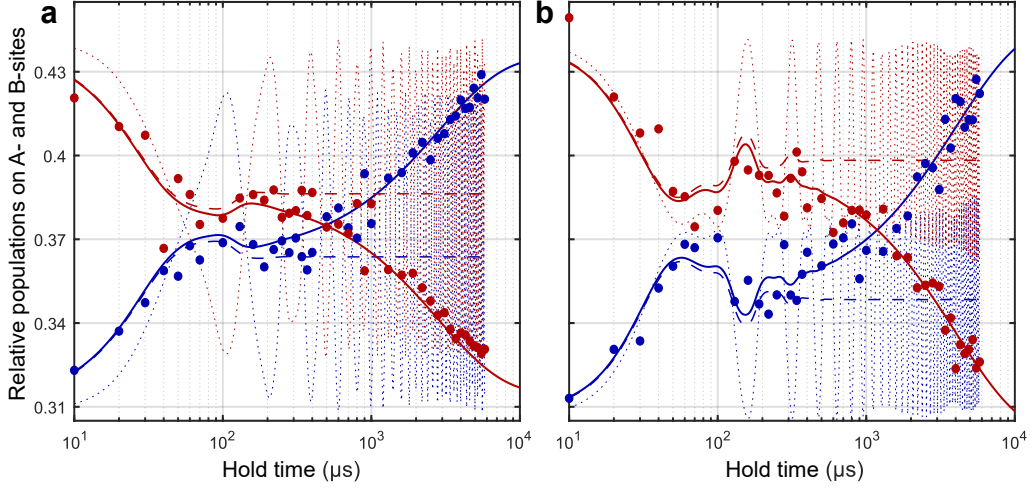


**Figure 4.15.: Dynamics between A- and B-sites following an offset inversion.** Shown are the measured population (symbols) on the A-sites (red) and the B-sites (blue) after quenching the geometry phase from  $\phi_g = -0.3$  to  $\phi_g = 0.3$  (**a**) and from  $\phi_g = -0.4$  to  $\phi_g = 0.4$  (**b**) at a lattice depth of  $V = 3 E_{\text{rec}}$ . The solid lines are a heuristic model following numerical calculation and the corresponding parameters are listed in table 4.1. Additionally the intermediate steps of the simulation are shown. The dotted lines follow from the adjusted populations  $\tilde{n}_A$  and  $\tilde{n}_B$  (Eq. 4.17) and the dashed lines give the effective populations of Eq. 4.18 for  $a_{\text{dec}} = 0$ , i.e. without the long term decay. The number of iterations per hold time is three (**a**) and two (**b**), respectively.

the energetically higher lattice sites, it is also necessary to decrease the A-site populations and increase the B-site populations of the numerical calculations by several percentage points. For longer times, the data does not follow the simple oscillation anymore. This is accounted for by a damping term, freezing the oscillations and an exponential decay from the A-sites to the B-sites, describing a de-excitation of the atoms from 2nd to 1st band. The unaltered populations from numerical calculation  $n_{A,B}$  are thus first adjusted and renormalized (not shown) to

$$\begin{aligned}\tilde{n}_A(t) &= n_A(t) + d_{\text{bg}} - d_{\text{AB}} \\ \tilde{n}_B(t) &= n_B(t) + d_{\text{bg}} + d_{\text{AB}},\end{aligned}\tag{4.17}$$

with  $d_{\text{bg}}$  giving an overall background and  $d_{\text{AB}}$  describing the interaction-induced population offset between the sites during the dynamic oscillations. From this the plotted lines in Fig. 4.15, including the damping and decay to the lower sites, follow as

$$\begin{aligned}
n_{\text{A}}^{\text{eff}} &= (\widetilde{n}_{\text{A}} - \overline{\widetilde{n}_{\text{A}}})e^{-\lambda_{\text{damp}}t} + \overline{\widetilde{n}_{\text{A}}} - a_{\text{dec}}(1 - e^{-\lambda_{\text{dec}}t}) \\
n_{\text{B}}^{\text{eff}} &= (\widetilde{n}_{\text{B}} - \overline{\widetilde{n}_{\text{B}}})e^{-\lambda_{\text{damp}}t} + \overline{\widetilde{n}_{\text{B}}} + a_{\text{dec}}(1 - e^{-\lambda_{\text{dec}}t}),
\end{aligned} \tag{4.18}$$

with  $\overline{\widetilde{n}_{\text{A}}}$  ( $\overline{\widetilde{n}_{\text{B}}}$ ) being the mean values of  $\widetilde{n}_{\text{A}}$  ( $\widetilde{n}_{\text{B}}$ ).

Thus in total there are five free fit parameters, two for adjusting the relative populations of the simulation to the experimental ones, the background  $d_{\text{bg}}$  and the A-B redistribution  $d_{\text{AB}}$ , and three to account for the differences on longer times scales, the oscillation damping via the damping constant  $\lambda_{\text{damp}}$  and the long time decay to the lowest band via the decay constant  $\lambda_{\text{dec}}$  and the decay amplitude  $a_{\text{dec}}$ . Since the band structure calculation takes significantly longer, it is kept outside of the fit and the lattice depth is instead roughly optimized by hand to be  $V = 3 E_{\text{rec}}$ , which is around 15% below the result of an independent calibration via Kapitza-Dirac scattering. The fitted values used for the lines in Fig. 4.15 are stated in table 4.1.

**Table 4.1.: Parameters used for the simulations in Fig. 4.15.**

Sub figure	$\lambda_{\text{damp}}$ (1/ms)	$\lambda_{\text{dec}}$ (1/ms)	$a_{\text{dec}}$	$d_{\text{bg}}$	$d_{\text{AB}}$
<b>a</b> ( $\Delta\phi_{\text{g}} = 0.6$ )	24(4)	0.35(6)	0.072(5)	0.96(1)	0.160(5)
<b>b</b> ( $\Delta\phi_{\text{g}} = 0.8$ )	10(2)	0.25(5)	0.098(11)	0.98(2)	0.170(6)

Using the heuristic model, we thus can describe the observed relative populations of the A- and B-sites and find a strong suppression of the energy conserving single-particle oscillations as well as a short lifetime on the energetically higher sublattice site. Interestingly, the extracted damping constant is smaller for the larger offset quench. This should however be taken with caution, because the available data set only had two iterations and high noise on the signal during the intermediate times between roughly  $10^2$  and  $10^3 \mu\text{s}$ , which mostly determine the fitted damping, could be interpreted by the fitting routine as oscillations and thus lower the damping constant. In order to get reliable dependencies of the damping and decay times on the system parameters like the geometry phase, larger data sets should be measured. A simplification used here is to limit the band structure calculation to the  $\Gamma$  point. In practice, the quasimomentum distribution is a Gaussian including a considerable part of the 1st BZ. Because the dispersion is not flat, this leads to a small damping of the oscillation already without the damping term in the heuristic model. Assuming the extreme case of a constantly filled 1st BZ for Fig. 4.15a for example decreases the damping constant  $\lambda_{\text{damp}}$  found by the fitting algorithm by around 15%. To lower the systematic error on  $\lambda_{\text{damp}}$  the realized momentum distribution could be extracted by a time-of-flight measurement and used for the calculation. The relatively short decay times are most likely due to the low lattice depth compared to the parameters in section 4.5.1, leading to a significantly smaller energy offset between the A- and B-sites.

Measuring the higher band excitations in real space would be especially interesting if a position dependent analysis is necessary, as the relative populations can be compared locally. In this exemplary measurement the distance from the trap center does not seem to make a difference, however, with the very few repetitions available no solid conclusions can be made.

## 4.6. Sublattice Modulation Spectroscopy

The dynamical control of the geometry of our lattice can also be used for a new type of periodic modulation of the optical lattice. By periodically changing the geometry phase, the two distinct lattice sites per unit cell are subject to opposite, linear changes in energy. This driving, which breaks inversion symmetry, can be used to perform spectroscopy measurements of atoms in the optical lattice potential and we refer to it as sublattice modulation spectroscopy. In the following, the sublattice modulation will be compared to different modulation techniques, namely symmetric amplitude modulation and circular shaking of the lattice potential.

We realize the sublattice modulation by periodically changing the detuning of the sideband frequencies, yielding a symmetric phase shift of all the 1D lattices with frequency  $\nu_{\text{spec}}$  described by

$$\phi_{1,2,3}(t) = \phi_{1,2,3}(0)(+/+/-)\frac{\delta\phi_g}{3}\sin(2\pi\nu_{\text{spec}}t). \quad (4.19)$$

For the circular lattice shaking we also periodically vary the frequency, however in this case of the RF signals for the AOMs. As explained previously, this changes the lattice position without changing the geometry phase. The amplitude modulation is simply realized by periodically changing the intensity setpoint of the feedback control system with frequency  $\nu_{\text{spec}}$ . In all cases, we start by loading the BEC in our lattice and fill up the entire 1st band thermally. At that point, we start one of the different modulation types using relatively low modulation amplitudes, i.e. staying in the linear response regime. The duration of the modulation is chosen as a tradeoff between a small Fourier broadening for small spectroscopy frequencies and avoidance of heating for long times. Here we used 10 ms at a given modulation strength, however we find the qualitative behavior to not depend strongly on the duration or modulation strength. The modulation indices are set to  $\epsilon_{\text{sm}} = 0.02$  (sublattice modulation),  $\epsilon_{\text{am}} = 0.05$  (amplitude modulation) and  $\epsilon_{\text{cs}} = 600 \text{ Hz}/\nu_{\text{spec}}$  (circular shaking), chosen to give a good signal for all frequencies at the selected modulation time of 10 ms. Lastly we image the different band populations by band mapping. For larger bands, we find the corresponding BZs to be strongly distorted, which we attribute to the harmonical confinement, gravity effects during the band mapping and experimental imperfections. Thus we calculate BZ masks using a principal component analysis (PCA), instead of the ideal ones (for more details see Appendix B).

The resulting band populations for the three spectroscopy types, using  $\phi_g/(2\pi) = 0.024$ , are shown in Fig. 4.16. Additionally, the expected transition frequencies for a lattice depth of  $V = 9.3 E_{\text{rec}}$  are marked as red shaded region. The widths of these is determined by the smallest and largest band gap to the 1st band for the full 1st BZ, i.e. all quasimomentum preserving transition frequencies. For the 2nd band and the higher bands the transition frequencies via 2-photon processes are also marked. The population peaks in the higher bands roughly fit these numerically calculated transition frequencies despite the relative simplicity of the model, assuming a single particle in a perfect lattice. For a precise quantitative description it would probably need to include the complete dynamics imprinted by the modulation pulses, possible finite-size effects on the band structure, the overlaying harmonical confinement seen by the atoms and of course interaction effects.

In all three cases we find a population peak in the 2nd band at around 7 to 8 kHz spectroscopy frequency, although there is an unexpected shift of some 500 Hz between the peak position from sublattice modulation and the two other methods. The relative excitation strength is clearly stronger to the 2nd band for sublattice modulation, as we also find a pronounced two-photon resonance to the 2nd band at approximately 3.7 kHz in this case, despite the signal at the higher bands being smaller than with amplitude modulation or shaking. These excitations, to the 3rd and 4th band at around 16 to 17.5 kHz and to the 5th band broadly around 22 kHz, are again found in all the spectra. Additionally though, we see excitations to different higher bands at around 15 kHz for amplitude modulation and circular shaking, which are absent using sublattice modulation. They might be explained by stronger higher order processes to the 7th band and partial decays from there to the 3rd band. Such processes could also explain the much broader resonance around 22 kHz, where especially amplitude modulation results in a wide plateau of excitations to different higher bands from 20 to 23 kHz. Given the significantly cleaner spectrum via sublattice modulation, it might be better suited for selectively coupling higher bands and off resonant preparation of Floquet systems, as we would expect comparatively lower heating rates.

For an interpretation of these results we calculate the transition matrix elements and integrate them over the 1st BZ to get an estimation of the different resonant excitation strengths. This is done for the three types of perturbations in linear response theory. The resulting excitation strengths up to the 7th band are depicted in Fig. 4.17 for three lattice geometries: honeycomb lattice, boron nitride lattice at  $\phi_g/(2\pi) = 0.024$  as used in the spectroscopy measurements in Fig. 4.16 and triangular lattice. The derivations are presented in Appendix C.

As expected, they show strong differences towards one another and also depend significantly on the lattice geometry. Especially the results for circular lattice shaking exhibit strongly different behavior, as the calculated excitation strengths are mostly independent of the targeted band. This can be explained by the simple analogy to a harmonic oscillator, in which also all levels are coupled via shaking the system, whereas the levels have to have the same parity, in order to be coupled via amplitude modulation. The suppression of certain excitations following from that argument can

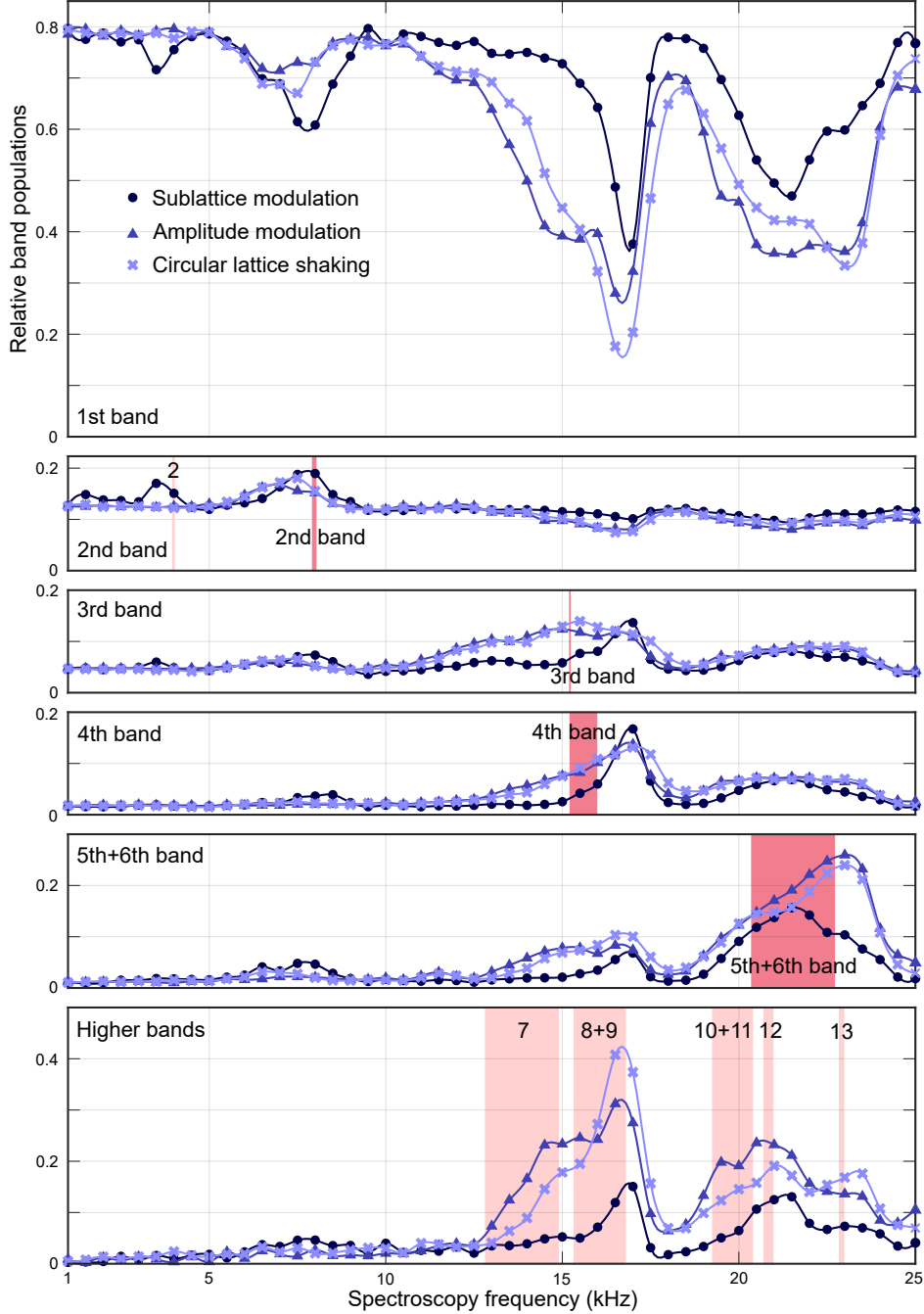


**Figure 4.16.:** Band resolved excitation spectra of a boron nitride lattice with  $\phi_g/(2\pi) = 0.024$  for three different types of modulation. The relative population of the 1st, 2nd, 3rd, 4th, 5th+6th and higher bands are shown as a function of the spectroscopy frequency. The symbols and colors mark the different modulation methods: sublattice modulation (dark blue circles), symmetric amplitude modulation (middle blue triangles) and circular lattice shaking (light blue crosses). The lines are spline interpolations of the data as guides to the eyes. The modulation indices are set to 0.02, 0.05 and  $600 \text{ Hz}/\nu_{\text{spec}}$ , chosen to yield a good signal at the modulation time of 10 ms. The dark red shaded regions indicate the resonance frequencies to different higher bands from numerical calculation at a lattice depth of  $V = 9.3 E_{\text{rec}}$  and the light red regions indicate resonance frequencies via two-photon processes. Adapted from [36].

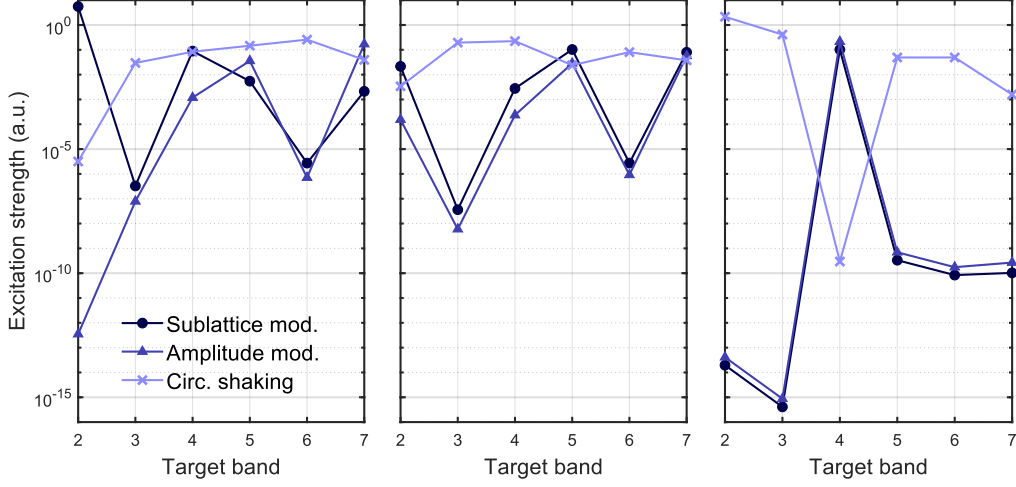


**Figure 4.17.: Resonant excitation strengths to higher bands.** The transition matrix elements from the 1st band for sublattice modulation (dark blue circles), amplitude modulation (middle blue triangles) and circular lattice shaking (light blue crosses) are integrated over the 1st BZ and logarithmically plotted as a function of the targeted band. The modulation strengths are taken from the measurement, meaning  $\epsilon_{sm} = 0.02$ ,  $\epsilon_{am} = 0.05$  and for the frequency dependent case of circular shaking:  $\epsilon_{cs} = 0.08$  (resonance to 2nd band), 0.035 (resonance to 3rd and 4th band), 0.028 (resonance to 5th and 6th band), 0.021 (theoretical expectation for resonance to 7th band). A lattice depth of  $V = 9.3 E_{rec}$  is used and the three panels correspond to the geometry phases of  $\phi_g/(2\pi) = 0, 0.024$  and  $0.5$  from left to right. Adapted from [36].

be found to the 3rd and the 6th band, both for amplitude modulation and sublattice modulation. For amplitude modulation, the same holds for excitations of the 2nd band. However, in the case of sublattice modulation it is very pronounced for geometry phases close to the honeycomb lattice.

Despite the theoretical descriptions of the excitation strengths suffering the same drawbacks as the numerically calculated transition regions, as they again exclude the full dynamics and any interaction effects, we do find similar qualitative features to the experimental measurements. Especially when comparing the relative excitation strengths to the 2nd and 4th band with the different methods in boron nitride lattices we find the strongest 2nd band ratio via sublattice modulation, as observed in the experiment. The strong differences in excitation strengths to the 3rd and 6th band are hard to compare, because the band gaps to the 4th and 5th band respectively are closed, which in practice would populate these bands anyway. Another accordance between theory and experiment is the pronounced 2nd order excitation of the 2nd band via sublattice modulation, as this term appears as a higher-order process in the perturbation operator.

A possible further application of sublattice modulation might be to probe the bond order wave in the ionic Hubbard model. Here the conceptually related superlattice modulation spectroscopy is predicted to be beneficial, as it allows accessing both the finite charge and spin gaps [96]. It also has similarities to phasonic modulation, where an additional, incommensurate optical lattice is moved through the system, which proved to be very effective in coupling via higher-order multiphoton transitions [97].

## 4.7. State Tomography with Interactions

Another application of the very fast lattice geometry change possible with our setup is to use this as a projection for Bloch state tomography measurements in order to extract topological properties of the system. In the following this is demonstrated in a set of preliminary measurements using the same approach as proposed in [37] and implemented in [32, 98, 99], which were done at this experimental apparatus as well. Further information on the experiment and the theoretical description allowing to reconstruct the Berry curvature can also be found in [49, 53]. Recently also a full Bloch state tomography was realized with bosons in a Raman lattice by targeting the atomic spin polarizations [100].

The main idea is to prepare a topologically interesting state in the boron nitride lattice with the Bloch states for every quasimomentum being given by a superposition of states purely situated on either the A- or the B-sites and to project it for the measurement onto decoupled flat bands. Here the eigenstates are associated only with one sublattice site and can be written  $|\mathbf{q}, A\rangle$  and  $|\mathbf{q}, B\rangle$ . To achieve such a projection, they prepared the initial system via Floquet engineering by circularly shaking the lattice potential. This shaking amplitude was adiabatically ramped up for the preparation and quenched off to project back on the static system, which had a large energy offset between the A- and B-sites and hence a flat band structure. This is visualized in Fig. 4.18a and b, taken from [32]. The situation can be nicely described on the Bloch sphere, with the decoupled states  $|\mathbf{q}, A\rangle$  and  $|\mathbf{q}, B\rangle$  pointing to its two poles. As shown in Fig. 4.18c, the prepared superimposed state is characterized by being oriented under some angle compared to the pole-axis, such that the projection back to decoupled states initializes a precession around this axis with a frequency  $\nu_{\mathbf{q}}$  determined by the band gap at the corresponding quasimomentum of the static system. This oscillation can then be measured in time-of-flight images by varying the precession time and measuring the resulting interference density from the A- and B-sites for every quasimomentum. The time-dependent density is given by

$$n(\mathbf{q}, t) = f(\mathbf{q}) \left( 1 - \sin(\theta_{\mathbf{q}}) \cos(\phi_{\mathbf{q}} + 2\pi\nu_{\mathbf{q}}t) \right), \quad (4.20)$$

with the polar angle  $\theta_{\mathbf{q}}$ , the azimuthal angle  $\phi_{\mathbf{q}}$  and the Wannier envelope  $f(\mathbf{q})$ . In practice, the amplitude of the modulation  $a = \sin \theta_{\mathbf{q}}$  is measured and the modulation is damped, such that the population of every quasimomentum versus the hold time in the decoupled system is fitted via

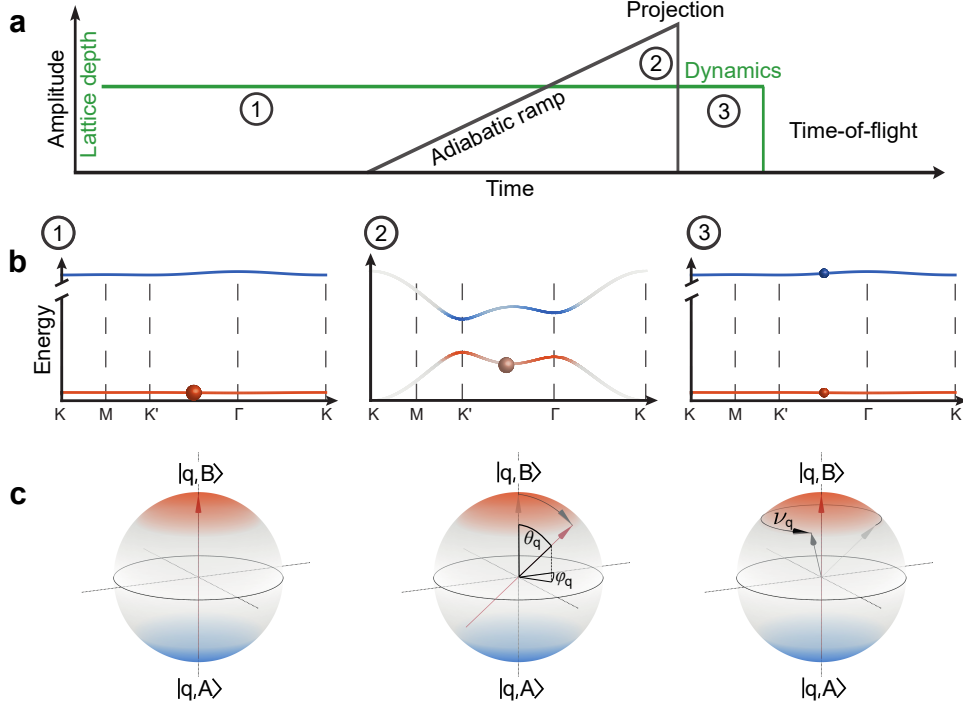


**Figure 4.18.: Bloch state tomography via dressing.** **a** Sketch of the experimental protocol used in [32]. The driving amplitude is ramped up for the system preparation and quenched off to project onto the static system, which has flat s-bands. **b** Band structures of the two band system at the different time steps of **a**. **c** Bloch sphere representation during the protocol, starting at  $|\mathbf{q}, B\rangle$  and being brought into a quasimomentum-dependent superposition of  $|\mathbf{q}, B\rangle$  and  $|\mathbf{q}, A\rangle$  by the ramp-up of the driving strength. With the subsequent projection to flat bands the states rotate on the Bloch sphere at the frequency of the final band gap  $\nu_{\mathbf{q}}$ . Adapted from [32].

$$n(\mathbf{q}, t) = f(\mathbf{q}) \left( 1 - ae^{-t/\tau} \cos(\phi_{\mathbf{q}} + 2\pi\nu_{\mathbf{q}}t) \right), \quad (4.21)$$

with the damping time  $\tau$ .

With the tunability of the multifrequency lattice, we now avoid having to start from decoupled bands in order for the projection to work. This allows to independently choose the preparation and precession parameters, which should be beneficial in taking tomography measurements of topologically nontrivial systems. Beyond this change in the sequence we now also changed the atomic species compared to the measurements in [32, 99], from spin-polarized fermionic  $^{40}\text{K}$  to bosonic  $^{87}\text{Rb}$  atoms. This makes following the density oscillation across the entire 1st BZ harder, because it is not equally filled. To reach a sufficient population of all quasimomenta for resolving the oscillations and being able to fit Eq. 4.21 to the data, we employ thermal atoms by increasing the temperature of the cloud. This is done by increasing the

final frequency of the RF-knife used for the evaporative cooling. The strongly different populations at different quasimomenta can then be compensated by the Wannier envelope  $f(\mathbf{q})$ . Another drawback is the significantly larger mass of the Rubidium atoms, which reduces the reciprocal lattice vector length to less than one half and thus lowers the quasimomentum resolution. A very interesting difference is the addition of interaction effects from our weakly interacting bosons compared to the spin-polarized fermions, which might allow us to effectively perform tomography measurements of the system's Bogoliubov modes. In the first preliminary measurements presented here, we simplified the situation by studying static lattices.

The measurement results and analysis for the tomography of one initial system is visualized in Fig. 4.19. Here the atoms are loaded adiabatically in a lattice very close to the honeycomb case with  $\phi_g/(2\pi) = 0.003$  and projected to a large energy offset between the A- and B-sites at  $\phi_g/(2\pi) = 0.077$ . The resulting momentum resolved density oscillations are imaged in  $20 \mu\text{s}$  steps from 20 to  $400 \mu\text{s}$  and fitted using Eq. 4.21. From the measured oscillation frequencies across the 1st BZ from roughly 8 kHz at the  $\Gamma$  point to around 6 kHz at the M points a lattice depth of  $V = 3.3 E_{\text{rec}}$  is concluded. When looking at the corresponding band structure this system only has a very small band gap between the 2nd and the higher bands, yet at the same time still a considerable band curvature, as evidenced by the varying oscillation frequencies found. This is due to experimental limitations preventing the use of deeper optical lattices at the time. However, we found no significant differences in the results when using smaller A-B-offsets for the projection. The higher bands might not be very impactful, because the atoms are for symmetry reasons mostly projected to the two s-bands.

The initial state for every quasimomentum, except for the knowledge of the hemisphere on the Bloch sphere it points to, is described by the fitted oscillation amplitude  $a = \sin \theta_{\mathbf{q}}$  and the azimuthal phase  $\phi_{\mathbf{q}}$ , which are depicted in the left column of Fig. 4.20. The phase profile fits to the expectation of a graphene or boron nitride lattice with topological defects at the K and K' points, where the Dirac cones are situated in the graphene lattice. They manifest as vortices in the phase, with opposite winding on the K and K' points. For the amplitude one would in first approximation expect a very strong amplitude modulation throughout the 1st BZ except for the regions around the K and K' points, since every state is a superposition located both on the A- and B-sites. Instead we surprisingly find a ring-shaped feature around the  $\Gamma$  point, i.e. the region of highest density. With all coefficients freely determined via the fitting routine this ring actually reaches  $a = 1$ , implying that the state points to the equator of the Bloch sphere and thus might reach into the other hemisphere going towards the  $\Gamma$  point. This value of  $a = 1$  has to be taken with caution though, as it depends on the damping constant varying significantly across the 1st BZ. This can be seen from Fig. 4.19b, where panel 4 presents the oscillation at the  $\Gamma$  point and panel 5 the situation on the amplitude ring. The latter only reaches unit amplitude due to extrapolation of the modulation to zero because of the comparatively strong damping. For now, it is not clear that this full modulation is indeed physical and not

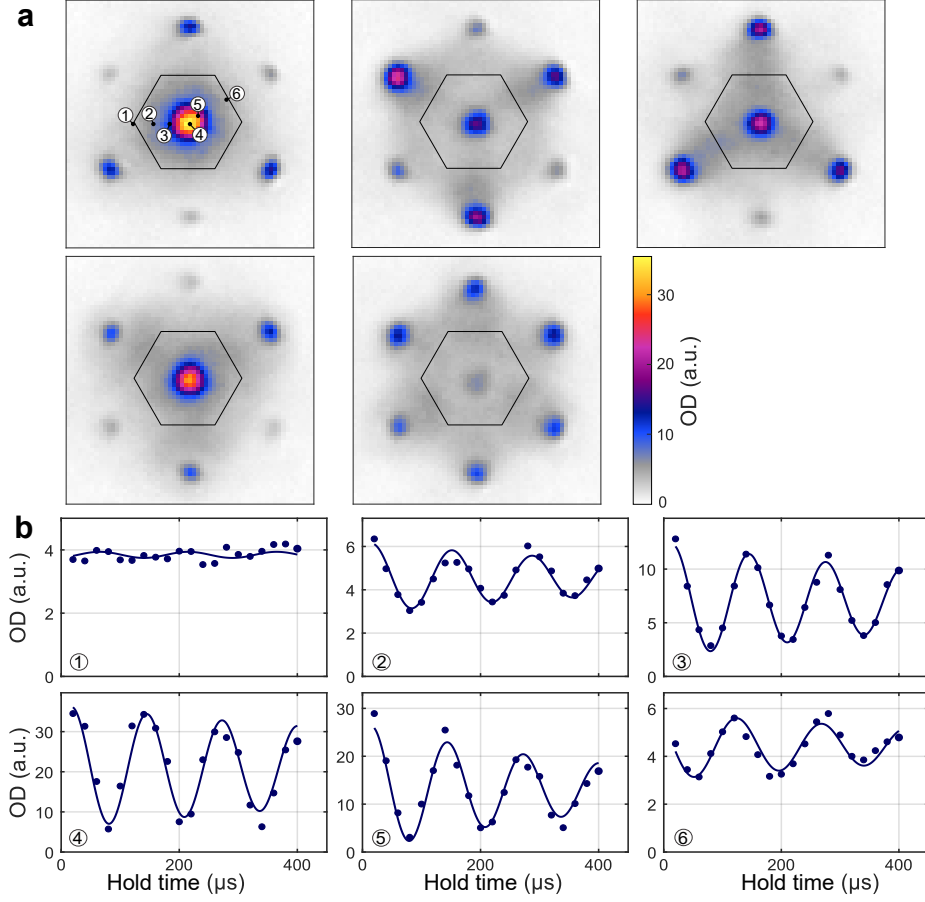


**Figure 4.19.: Visualization of density oscillations in the momentum distribution.** **a** Shown are five exemplary density distributions after 20, 100, 180, 260 and 340  $\mu\text{s}$  hold time after the projection to flat bands. Each distribution is averaged over around nine iterations. Initially the system has a very small energy offset at around  $\phi_g/(2\pi) = 0.003$  and is projected to  $\phi_g/(2\pi) = 0.077$  at a lattice depth of  $V = 3.3 E_{\text{rec}}$ . The hexagons mark the 1st BZ. **b** Population on single pixels as function of the hold time from experimental images as in **a** (symbols) and fits to the data using Eq. 4.21 (lines). The position of the pixels are marked in the first image of **a**.

an artifact from the measurement. However, even when forcing a constant intermediate damping constant across the entire 1st BZ, the amplitude ring persists as a local maximum, although not reaching  $a = 1$  anymore. Using the full state tomography, the topological properties can be attained via the Berry curvature [32, 37], which is dependent on the amplitude  $a$  and the derivatives of  $\theta_q$  and  $\phi_q$ . The result is plotted in Fig. 4.20c under the assumption that  $\theta_q$  folds back to the same side of the Bloch sphere within the ring structure. By integrating the Berry curvature over the 1st BZ the Chern number of the populated Bloch band can be calculated, which is a topo-

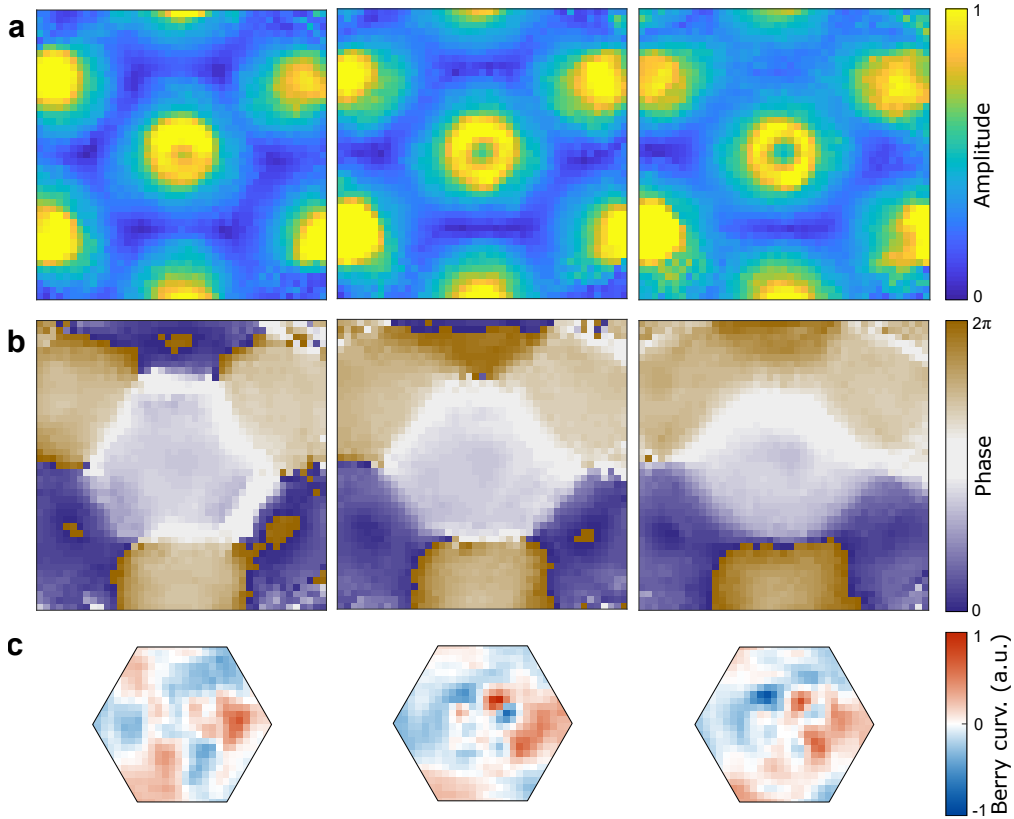


**Figure 4.20.: State tomography across the merging transition.** Visualization of the momentum resolved fitted coefficients for the system used in Fig. 4.19. From left to right the lattice is increasingly imbalanced:  $V_1 = V_2 = V_3$ ,  $V_1 = 0.94V_2 = 0.94V_3$  and  $V_1 = 0.88V_2 = 0.88V_3$ . **a** Depicted is the amplitude  $a = \sin \theta_q$  of the oscillation. In a ring around the  $\Gamma$  point it reaches 1, meaning the signal on the corresponding pixels is fully modulated. Close to the  $K/K'$  points almost no modulation of the signal is measured. **b** Azimuthal phase  $\phi_q$  across the merging transition. The increasing imbalance of the lattice moves the phase vortices at pairs of  $K$  and  $K'$  points towards each other until they merge at the halfway positioned  $M$  points. **c** From the fitted angles  $\phi_q$  and  $\theta_q$  the Berry curvature in the 1st BZ is calculated as described in [32]. The distribution is quite irregular, but the sum is at most 0.1% away from the expected quantized value of Chern number 0.

logical invariant. As expected for the static system, it has a quantized value of 0 with only a small error of 0.05%. For the sake of completeness, it should be noted that the measured Chern number also is 0 when folding the amplitude within the ring on the opposite hemisphere. As a first test to the robustness of our measurement protocol we map out the merging transition of the two Dirac points in the 1st BZ by varying the beam imbalance (Fig. 4.20) as proposed in [101] and previously demonstrated in [31, 102, 103]. As expected the phase vortices follow the Dirac points, which are brought closer to each other until pairs from a  $K$  and a  $K'$  point merge at an imbal-

ance of around 0.9. Thus the topological defects annihilate and we see a continuous phase profile in the right column as well as a merging of the amplitude  $a = 0$  regions associated with the phase vortices.

Returning to the extracted amplitude ring, we want to study its dependence on the interaction strength in the system, since the change to interacting atoms is the most important change compared to the earlier tomography measurements as described in Fig. 4.18 ([32, 99]). With  $^{87}\text{Rb}$  not offering Feshbach-resonances to deliberately tune the interaction strength, we instead lower its impact on the system in two different ways. Firstly by starting with a hotter cloud and secondly by lowering the

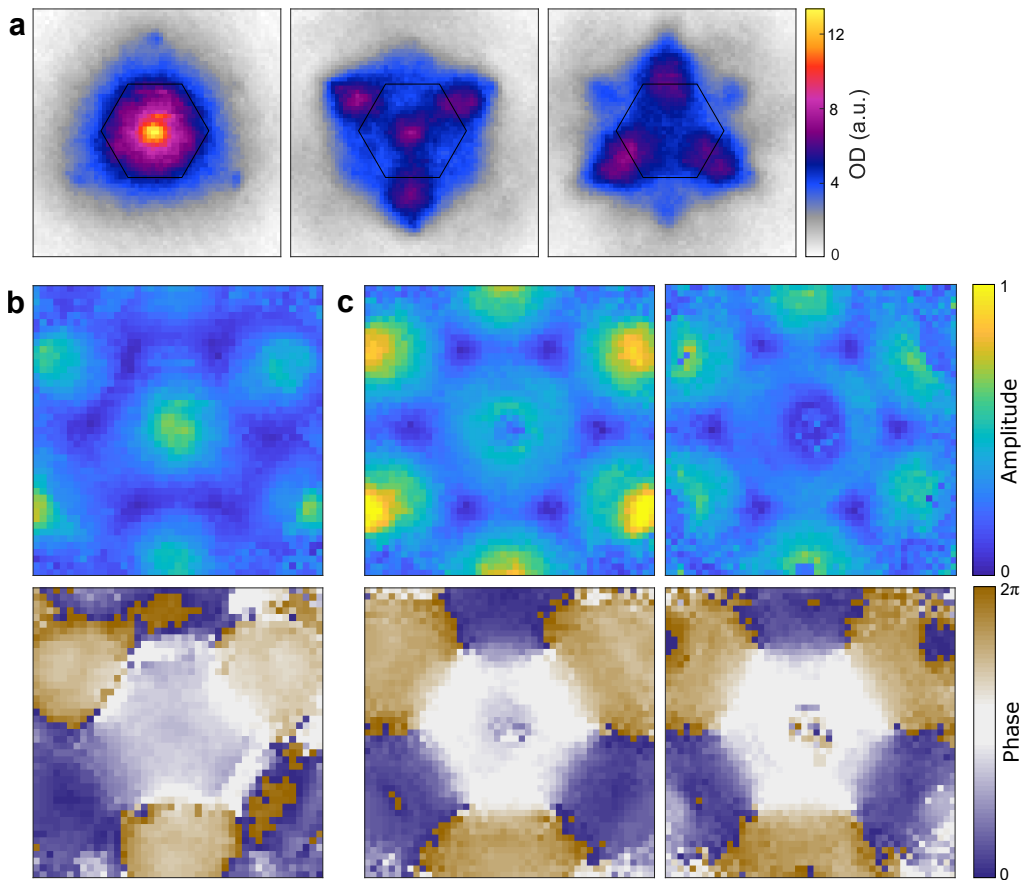


**Figure 4.21.:** **a** Exemplary momentum distributions at a higher temperature, but otherwise identical parameters to the first line of Fig. 4.19a. **b** Momentum resolved amplitude  $a$  and azimuthal phase  $\phi_q$  using the higher temperature demonstrated in **a**. Instead of the amplitude ring a hill around the  $\Gamma$  point is found. **c** The temperature is again lowered to be roughly equal to Fig. 4.20 and the lattice depth is lowered to around  $V = 0.5 \times 3.3 E_{\text{rec}}$  (left column) and  $V = 0.3 \times 3.3 E_{\text{rec}}$  (right column). At half the original lattice depth the amplitude ring around the  $\Gamma$  point is already significantly weaker and at 30% it has disappeared. The phase profiles are not qualitatively affected by these changes.

lattice depth such that in both cases the atomic density gets lowered. The resulting fitted amplitudes  $a$  are plotted in Fig. 4.21 and feature much weaker to no ring structures, suggesting that this feature does indeed originate from interaction effects. The amplitude distributions of the outer-lying copies of the  $\Gamma$  point are neglected in the analysis because of the vastly lower signal to noise ratio.

In conclusion, these first preliminary measurements demonstrate the usefulness of the tunability of the multifrequency setup for performing a full state tomography in the optical lattice. Regarding the amplitude ring, further studies are necessary to confirm it as arising from interaction effects and develop a theoretical understanding. Especially the measurements should be repeated in a deeper lattice, allowing to reach decoupled flat bands while at the same time keeping a large band gap to the higher bands, to work in a more clean system. To further investigate interaction effects it would be beneficial to change the atomic species, to be able to tune the interaction strength via Feshbach-resonances. Additionally, building on these measurements, it would be very interesting to include periodic driving to the initial system, in order to engineer and measure topologically nontrivial states [104, 105].

## 4.8. Extension of the Geometry Phase Concept to more complex Optical Lattices

In the last section, I want to show the relevance of the geometry phase concept also for more complex types of lattice potentials. Using the multifrequency design, similar phases, which invert the potential landscape and target the energies of single sublattice sites, can be tuned also for various kinds of lattice potentials. In the following subsections, the examples of quasiperiodic lattices and 3D lattices will be presented.

### 4.8.1. Quasiperiodic Optical Lattice with Geometry Phase

Quasiperiodic lattices are defined by possessing long-range order without actually being translationally symmetric, meaning they do not originate from translations of some unit cell. Since quasiperiodically ordered potentials can be interpreted as incommensurate projections of a periodic structure in higher dimensions, studying quasicrystals allows to address the physics in such high-dimensional objects, including for example their topology [106, 107].

To investigate the role of the geometry phase in a quasicrystal lattice, we chose a fivefold rotationally symmetric potential, as it is the most straightforward symmetric 2D quasicrystal with a geometry phase. The situation can be described very similarly to our realized setup, but using five equally distributed lattice beams, i.e. under  $72^\circ$  to their nearest neighbors, instead of three. The resulting potential can be written as

$$V_{\text{pot}}(\mathbf{r}) = 2 \sum_{i=1}^5 V_i \cos(\mathbf{b}_i \cdot \mathbf{r} + \phi_i). \quad (4.22)$$

When realizing this geometry in a multifrequency approach, there are two equally valid options. One can either bring frequencies from neighboring lattice beams on resonance, or frequencies from next-nearest neighboring beams. The potential shape is of course the same in both cases, but the 1D lattice constants and thus the entire potential landscape are a factor  $\frac{\sin(36^\circ/2)}{\sin(72^\circ/2)} = 0.526$  smaller in the latter case. For the same intensity, this would increase the energy scale of the band structure by a factor of 2.6, allowing to reach effectively cooler atomic ensembles in the lattice since the temperature is smaller compared to the eigenenergies. Both versions with the corresponding reciprocal lattice vectors are schematically shown in Fig. 4.22. In the following I will assume the situation from the right side of Fig. 4.22.

For the choice of the frequencies, we start with the same limiting considerations as in our hexagonal multifrequency lattice. On the one hand, the lowest running waves in the system must be much faster than the energy scales of the atoms in the lattice potential and on the other hand it would help in the realization to stay within several MHz. Thus in the examples of Fig. 4.22 there are three lattice beams using

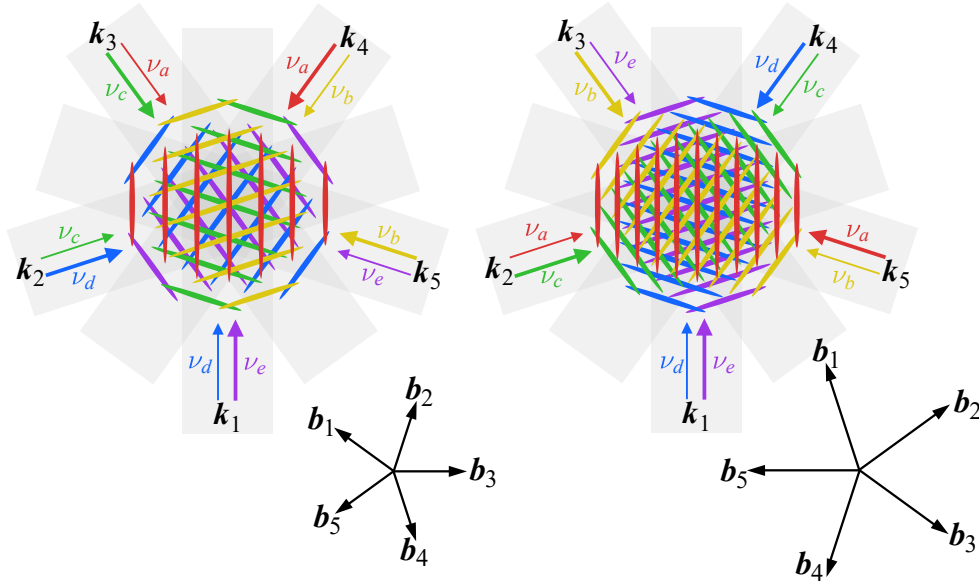


**Figure 4.22.:** Sketch of a fivefold quasicrystal lattice in two realizations.

Five laser beams with relative angles between neighboring beams of  $72^\circ$  are superimposed. Every beam consists of two frequencies with overall five unique frequencies. Depending on whether the resonant frequency components are in neighboring (left) or next-nearest neighboring (right) beams, the lattice vectors and corresponding reciprocal lattice vectors change. The reciprocal lattice vectors are defined as  $\mathbf{b}_i = \mathbf{k}_i - \mathbf{k}_{i+1}$  with  $\mathbf{k}_6 = \mathbf{k}_1$  (left) and  $\mathbf{b}_i = \mathbf{k}_i - \mathbf{k}_{i+2}$  with  $\mathbf{k}_6 = \mathbf{k}_1$  and  $\mathbf{k}_7 = \mathbf{k}_2$  (right).

the -1st order sidebands ( $\mathbf{k}_1, \mathbf{k}_2, \mathbf{k}_4$ ) and two lattice beams using the +1st order sidebands ( $\mathbf{k}_3, \mathbf{k}_5$ ). There are plenty possible sideband frequency combinations to fulfill the pairwise resonance requirement without the opposite sideband coming into resonance with any of the other main frequencies. In order to simultaneously stay within a small frequency region and of course to also suppress higher order resonances as much as possible, a good combination we found is:  $+\nu_\alpha = 4$  MHz,  $+\nu_\beta = 13$  MHz,  $-\nu_\epsilon = -10$  MHz,  $-\nu_\delta = -2$  MHz,  $-\nu_\gamma = -5$  MHz (Fig. 4.23). Here  $\nu_{\alpha/\beta/\gamma/\delta/\epsilon}$  is the sideband used on the carrier frequency with the corresponding latin letter which are ordered in frequency and the modulation frequencies are chosen as multiples of 1 MHz. In this case the first unwanted resonance appears between the +4th order of  $\nu_\delta$  and the +2nd order of  $\nu_\gamma$ , forming a 1D lattice of only 0.1% the relative depth of the five desired ones. Its impact is very limited, because its wave vector is oriented parallel to one of the five desired ones, such that it only leads to a very minor change in the depth of this 1D lattice. The first resonance between two beams that are not supposed to interfere and that hence leads to an additional 1D lattice not included in the quasiperiodic geometry is even weaker at a relative depth of 0.05%.

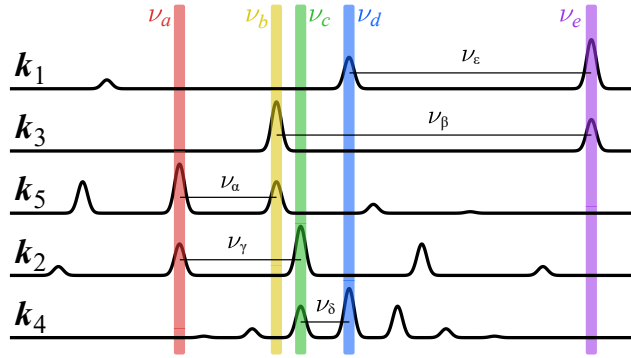


**Figure 4.23.: Possible choice of frequency spectra for a fivefold quasicrystal.**

As in the simpler case of a three beam lattice (Fig. 4.5) every lattice beam contains two relevant frequencies, a carrier and a 1st order sideband, which are each in resonance with a different 1st order sideband and carrier in two different lattice beams, respectively. The sideband frequencies are chosen as  $\nu_\alpha = 4$  MHz,  $\nu_\beta = 13$  MHz,  $\nu_\gamma = 5$  MHz,  $\nu_\delta = 2$  MHz and  $\nu_\epsilon = 10$  MHz. The spectra are numbered according to the right configuration of Fig. 4.22.

The set of reciprocal lattice vectors  $\mathbf{b}_i$  has four incommensurate vectors, since only one at a time can be described by the negative sum of the other four. This means that the realized 2D potential can be described as an incommensurate projection of a 4D periodic potential. In this special case of the argumentation from section 4.1.4 with  $D = N - N_{\text{iis}} = 4$  and  $d = 2$ , the five independent phases  $\phi_i$  thus give control over two translational degrees of freedom in the physical space, two phasonic degrees of freedom, which are translations in the not physically accessible space, and additionally a geometry phase. Analogous to the hexagonal case, the geometry phase is given by

$$\phi_g = \sum_{i=1}^5 \phi_i, \quad (4.23)$$

as this expression acts symmetrically on all 1D lattices and hence does not couple to any translations in the 4D space of the potential.

Consequently, the other degrees of freedom can be accessed by changing the 1D lattice phases while keeping their sum constant. With symmetry considerations and phase shifts of  $\pi/2$  between the two orthogonal directions for both types of translations, this can be written as

$$V_{\text{pot}}(\mathbf{r}) = 2 \sum_{i=1}^5 V_i \cos\left(\mathbf{b}_i \cdot \mathbf{r} + t_1 \cos\left(\frac{2\pi i}{5}\right) + t_2 \sin\left(\frac{2\pi i}{5}\right) + p_1 \cos\left(\frac{4\pi i}{5}\right) + p_2 \sin\left(\frac{4\pi i}{5}\right) + \frac{\phi_g}{5}\right). \quad (4.24)$$

Here the two orthogonal translations in physical space are set by the parameters  $t_1$  and  $t_2$  and the two phasons by  $p_1$  and  $p_2$ .

We find the geometry phase to have a similar effect on the quasiperiodic potential as on the hexagonal potential. For  $\phi_g/(2\pi) = m$ , with integer  $m$ , the potential features many relatively shallow local minima, akin to the honeycomb lattice, whereas for  $\phi_g/(2\pi) = m + 1/2$  there are less yet more pronounced local minima, resembling the triangular lattice. Around  $\phi_g/(2\pi) = m$ , the tenfold symmetric patterns are broken with offsets appearing between even and odd minima, as in the boron nitride phase. The difference in the potential minima are illustrated in Fig. 4.24c and d. When all occurring potential values from the landscapes plotted above are normalized and plotted as histograms, we find, that for  $\phi_g = 0$  the slope of the lowest potential values is higher than for  $\phi_g/(2\pi) = 0.5$ . Similarly, when restricting the analysis to local minima of the potentials, they only start to appear at higher potential depths, but more quickly at  $\phi_g = 0$ . Again the different local minima distributions can be attributed to a flux in momentum space given by  $\Phi = \pi + \phi_g$  through a pentagonal plaquette (Fig. 4.24b), which is maximal in the frustrated case  $\phi_g = 0$ .

To give a more conclusive picture of this quasiperiodic potential, a phasonic degree of freedom,  $p_1$  from Eq. 4.24, is changed in Fig. 4.25. The lattice geometry is unchanged and thus the local minima distribution is unchanged as well.

Following this scheme would allow realizing for the first time a quasiperiodic optical lattice with tunable geometry. In the first setup using ultracold atoms in a quasicrystal, the latter was constructed by four 1D lattices with  $45^\circ$  angles between neighboring ones [35]. The resulting four degrees of freedom thus correspond to two translations and two phasons and do not contain a geometric degree of freedom. In addition to accessing phasonic degrees of freedom, as done for phasonic spectroscopy [97] and as part of charge pump protocols [107–109], a multifrequency realization of a quasicrystal would allow to use further dynamic tuning possibilities. This could be used to quench the lattice geometry to perform tomography of the eigenstates, or to excite the atoms into higher states via geometry sweeps. It might also be promising to

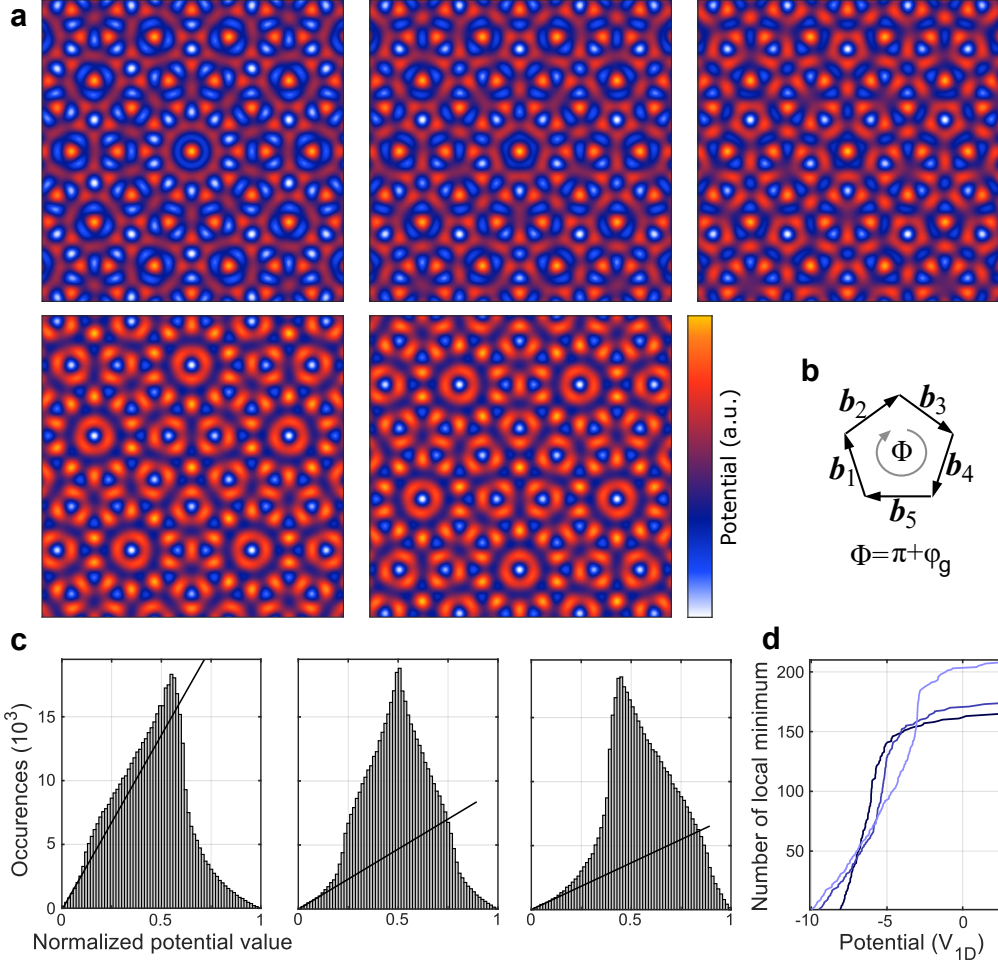


**Figure 4.24.: Fivefold quasiperiodic potential tuned via the geometry phase.** **a** Potential landscapes for five different geometry phases ( $\phi_g/(2\pi) = 0, 0.12, 0.25, 0.5, -0.5$ ). **b** Pentagonal plaquette in momentum space constructed by the reciprocal lattice vectors  $b_i$  with a flux  $\Phi = \pi + \phi_g$ . **c** Histograms of the normalized potential values from the potentials in **a** for  $\phi_g = 0, 0.25$  and  $0.5$ . The lines are fitted to the lowest 10%, emphasizing the larger number of lattice sites of similar energy at  $\phi_g = 0$ . **d** All local minima in the regions shown in **a** shown with their potential energy. The color denotes the geometry phases:  $\phi_g = 0$  (dark blue),  $\phi_g/(2\pi) = 0.25$  (middle blue),  $\phi_g/(2\pi) = 0.5$  (light blue). This also shows the higher amount of lattice sites at a similar energy for  $\phi_g = 0$ , while at  $\phi_g/(2\pi) = 0.5$  there are fewer but deeper lattice sites. Adapted from [36].

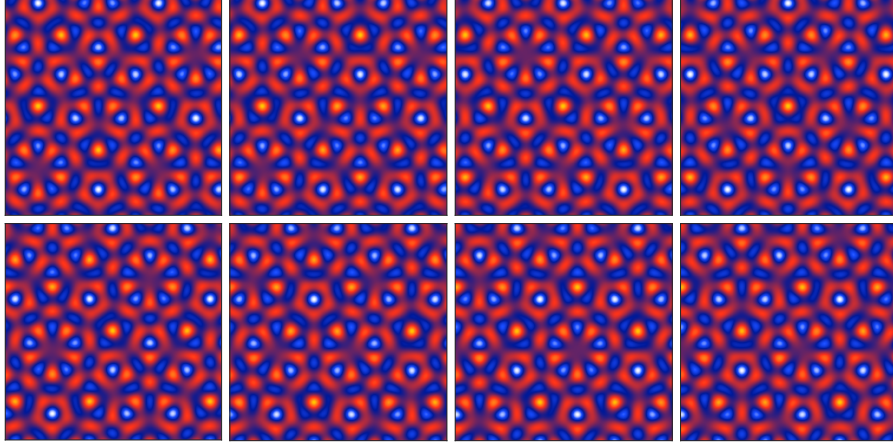


**Figure 4.25.: Fivefold quasiperiodic potential tuned via a phason.** For  $\phi_g/(2\pi) = 0.25$  the value of the phason  $p_1$  from Eq. 4.24 is varied from  $p_1 = -0.9$  (top left) in steps of 0.3 to  $p_1 = 1.2$  (bottom right). The potential landscape stays self-similar; it is neither translated in physical space nor is its geometry changed. Adapted from [36].

study the phase diagram as a function of the lattice geometry, since the local variation in the number of nearest neighbors was shown to strongly impact the phase diagram by theoretically studying an eightfold quasicrystal [110]. Similarly, controlling the width of the distribution of on-site energies via  $\phi_g$  could help by introducing an important tuning parameter in the investigations of Bose glasses [111] and many-body localization [112].

### 4.8.2. Generalization to 3D Optical Lattices

In the following, I will show how the multifrequency concept can also be used to generate dynamically tunable 3D optical lattices for the special case of a nonseparable lattice with three sites per unit cell. The realization of 3D nonseparable optical lattices for ultracold atoms would allow for the simulation of more complex solid state materials, featuring for example topological phenomena like in Weyl semimetals [113, 114] or higher-order topological insulators [115, 116]. With the fastly tunable geometry this would also enable Floquet engineering of new topological phases [117].

Here we consider a 3D lattice constructed by four lattice beams, such that phase noise once again would only couple to the position of the resulting interference pattern, not its geometry [77]. The four noncoplanar wave vectors  $k_i$  give rise to six 1D lattices defined via their reciprocal lattice vectors  $b_i$ , which are given by  $b_i = k_i - k_{(i \bmod 3)+1}$  for  $i \in \{1, 2, 3\}$  and  $b_i = k_4 - k_{i-3}$  for  $i \in \{4, 5, 6\}$ . To again have direct control over each 1D lattice individually every lattice beam would now contain three frequencies of which one would uniquely appear in one additional beam. The resulting potential can be written as

$$V_{\text{pot}}(\mathbf{r}) = V_0 + 2 \sum_{i=1}^6 V_i \cos(\mathbf{b}_i \cdot \mathbf{r} + \phi_i), \quad (4.25)$$

offering the six phases  $\phi_i$  as degrees of freedom. These comprise three degrees of freedom defining the position of the lattice potential in space and three for the geometry of the lattice, following from the generalization in section 4.1.4 for  $N = 6$  1D lattices forming a  $D = 3$  periodic potential. In general the components are defined as in Eq. 4.7, yielding as an independent triplet for example

$$\boldsymbol{\phi}_g = \begin{bmatrix} \phi_{g_1} \\ \phi_{g_2} \\ \phi_{g_3} \end{bmatrix} = \begin{bmatrix} \phi_1 + \phi_2 + \phi_3 \\ \phi_1 + \phi_4 - \phi_5 \\ \phi_2 + \phi_5 - \phi_6 \end{bmatrix}. \quad (4.26)$$

The individual components each define the geometry of a 2D lattice build by three of the four wave vectors. In the case of  $\phi_{g_1}$  these are  $k_{1,2,3}$ , for  $\phi_{g_2}$  the three corresponding reciprocal lattice vectors are construct from  $k_{1,2,4}$  and for  $\phi_{g_3}$  from  $k_{2,3,4}$ . Accordingly, each component could be calibrated individually as demonstrated in our 2D multifrequency lattice.

One possible realization would be to add a perpendicular lattice beam to our setup, i.e. along the  $z$ -direction,  $k_4 = 2\pi/\lambda\hat{z}$  and ensure interference between all beams by using linear in-plane polarization for the 1st to 3rd beam and circular polarization for the 4th beam. This allows to write the total potential as sum of a 2D and a 3D lattice:

$$V_{\text{pot}}(\mathbf{r}) = V_0 + V_{2\text{D}}(\mathbf{r}) + V_{3\text{D}}(\mathbf{r}) = V_0 + 2V_{2\text{D}} \sum_{i=1}^3 \cos(\mathbf{b}_i \cdot \mathbf{r} + \phi_i) + 2V_{3\text{D}} \sum_{i=4}^6 \cos(\mathbf{b}_i \cdot \mathbf{r} + \phi_i). \quad (4.27)$$

Here for simplification the balanced situations  $V_{2\text{D}} = V_1 = V_2 = V_3$  and  $V_{3\text{D}} = V_4 = V_5 = V_6$  are assumed. Using a stronger  $z$  dependent part, e.g.  $V_{3\text{D}} = 1.9 V_{2\text{D}}$  for  $\phi_{g_1}/(2\pi) = 0.29$  the 1D tubes resulting from  $V_{2\text{D}}$  can be split into separate minima. This results in a 3D lattice of trimers in  $xy$ -planes, which are nontrivially coupled to trimers in neighboring layers along the  $z$ -direction as visualized in Fig. 4.26. By appropriately choosing the ratio of  $V_{2\text{D}}$  and  $V_{3\text{D}}$  the tunnel coupling to the four nearest neighbors could also be balanced. Additionally, the multifrequency approach allows to shift the two parts of the potential,  $V_{2\text{D}}(\mathbf{r})$  and  $V_{3\text{D}}(\mathbf{r})$ , with respect to each other via  $\phi_{g_2}$  and  $\phi_{g_3}$  and thus to engineer energy offsets between the three sites per unit cell. This can be done arbitrarily by combining a change of one site with respect to the other two by shifting along the  $y$ -direction and an increasing change between all sites by shifting along the  $x$ -direction. This proposal would expand on the previous realization of an optical lattice of tunable trimers [118], which is 2D and does not possess passive stability.

Beyond the example presented here, there is a very large parameter space of possible 3D lattice geometries with four noncoplanar lattice beams, including all 14 3D Bravais

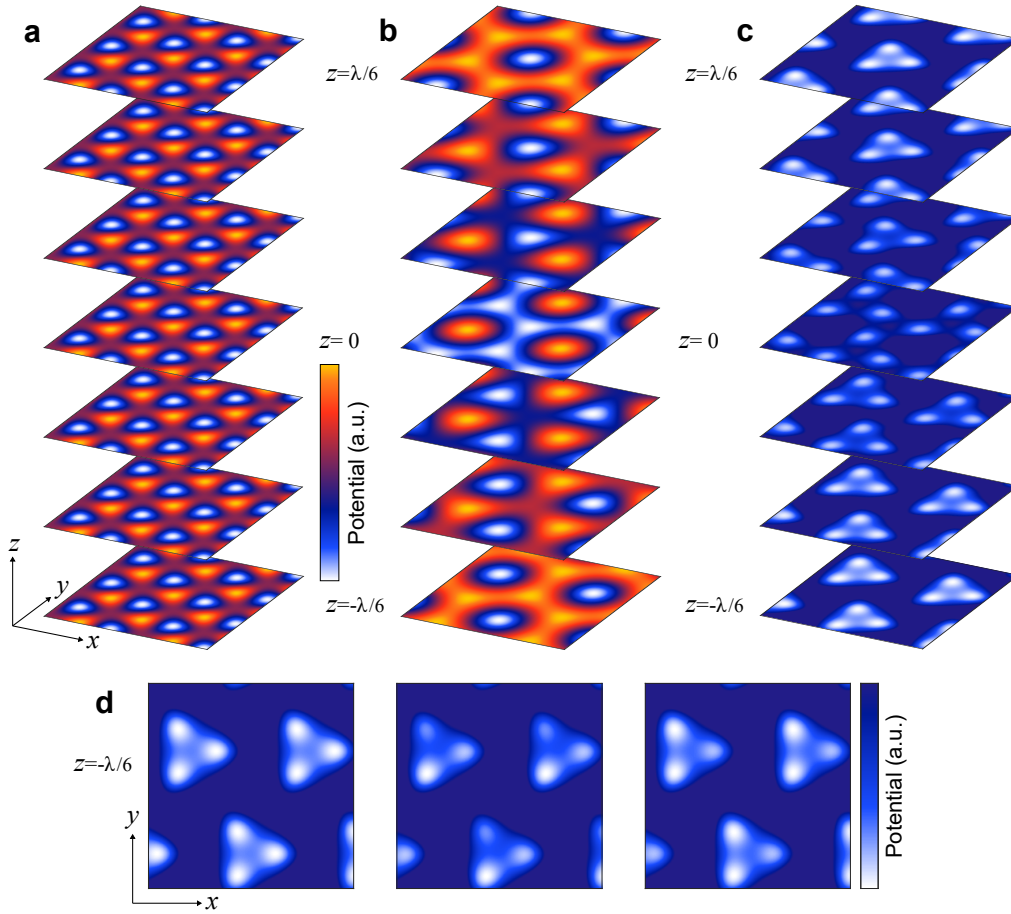


**Figure 4.26.: 3D multifrequency lattice of nonseparable trimers.** The first three subplots show potential landscapes in the  $xy$ -plane of size  $2\lambda \times 2\lambda$  for seven different values of  $z$ . **a** Balanced 2D potential  $V_{2D}(\mathbf{r})$  with  $\phi_{g_1}/(2\pi) = 0.29$ . **b** Balanced 3D potential  $V_{3D}(\mathbf{r})$  with  $\phi_{g_2} = \phi_{g_3} = \phi_{g_1}/3$  and  $V_{3D} = 1.9V_{2D}$ . **c** Resulting total potential  $V_{\text{pot}}(\mathbf{r})$  featuring layers of trimers with distances of  $\lambda/3$  in  $z$ -direction. The color map is cropped to emphasize the potential minima. **d** Shown is the same  $2\lambda \times 2\lambda$  region at  $z = -\lambda/6$  with different energy offsets between the three minima set by shifting  $V_{3D}(\mathbf{r})$  along the  $y$ - (2nd image) and  $x$ -direction (3rd image) via combinations of  $\phi_{g_2}$  and  $\phi_{g_3}$ . Adapted from [36].

lattices [119] and more multisite lattices, e.g. the diamond lattice [77, 120], which could also be considered in a multifrequency design.

## 4.9. Conclusion and Outlook

In this chapter I presented our new optical lattice setup based on a multifrequency design, which features a full dynamical control of the lattice geometry via the direct access to the newly introduced lattice geometry phase  $\phi_g$ . In this way, we can

rapidly tune the geometry from a triangular lattice over a boron nitride lattice with adjustable sublattice offset to a honeycomb lattice. By construction, phase noise on the lattice beams does not couple on the geometry phase, making the lattice geometry passively stable. In different calibration measurements, we demonstrated both the high precision achievable in determining and varying the geometry as well as its stability on different time scales.

The relevance of the introduced geometry phase is further supported by appearing as a staggered flux in the complementary momentum space lattice, where we measured it to break inversion symmetry in Bragg scattering experiments in excellent agreement with the numerical prediction.

Making use of the dynamic tunability we illustrated the possibility of this setup to excite the atoms into higher Bloch bands. The next step here would be to achieve condensation in the higher bands, as they feature many exotic quantum states [121]. In particular boron nitride optical lattices are under study [122, 123] and recently the realization of a chiral superfluid in the 2nd Bloch band was reported [80]. In this context a combination with our quantum gas magnifier would be fascinating, to achieve real space imaging of the higher orbitals. In the case of the chiral superfluid these exhibit vortices which could then be observed directly. The combination of higher band excitations with quantum gas magnification demonstrated in this thesis enabled us to follow the real space dynamics after the excitation, giving a complementary access to the system.

Furthermore, it allows to utilize a new lattice modulation type by modulating the energies of the A- and B-sites with opposite signs, which we found to couple less to higher bands than the other modulation techniques. It could therefore be an interesting method for novel Floquet protocols, since heating of the atoms is one of the primary practical problems in Floquet engineering [124, 125]. In combination with the already successfully implemented driving approaches of lattice shaking [32, 104] and amplitude modulation [126], it would also allow for more complex Floquet protocols and give access to more complex systems possibly featuring new topological phases.

Another very interesting application of the dynamic geometry control are state tomography measurements [32, 37, 99], where a quench to a different lattice geometry allows to independently prepare a physical system of interest from the measurement geometry, giving access to a larger range of systems to study. This was demonstrated in a set of preliminary measurements for a static system, where the merging transition was measured and an interaction strength dependent ring in the oscillation amplitude was found. For more comprehensive studies of interacting topological systems it would be promising to combine a multifrequency setup with an atomic species featuring a Feshbach resonance and as such a tunable interaction strength and also to go beyond static initial systems to prepare topologically nontrivial states. Similarly, quenching onto a different lattice geometry is an important part of proposed schemes for the detection of many-body phases [127, 128].

By setting the geometry via the relative positions of three independent 1D lattices, we avoid the dependence on the lattice beam polarization and can thus completely

---

avoid vector light shifts [46] by using out-of-plane polarization as done throughout this thesis. On the other hand this decoupling of the lattice geometry and the beam polarizations gives the opportunity to employ the vector light shift deliberately and vary the dependence of the lattice potential on the  $m_F$  state of the atom. Additionally, one could think of realizing a in-situ Stern-Gerlach separation of different spin states by dynamically tuning the lattice geometry to introduce a 2nd site within the unit cell and allowing a spin resolved measurement in a triangular lattice, as done using 1D chains in [129].

Finally, proposals of a quasiperiodic and a 3D optical lattice using the multifrequency approach were presented, which also feature dynamically tunable geometry phases. Such complex geometries would be interesting for the possibility to engineer new topological phases [117] and the tunable lattice geometry would again allow for interesting options like excitations of atoms into higher states and quenches onto different dispersions. Such changes in the energy spectrum would for example be interesting when studying Bose glasses in quasicrystals [111].



## 5. Pattern Formation in dc Driven Lattices

In this chapter, I will present measurements of various dynamical effects of interacting quantum systems in optical lattices. Due to the high measurement precision and tunability, optical lattices have proven to be a valuable platform for the study of dynamics and transport properties in closed quantum systems [47, 130–132]. As an additional tool for the observation, we make use of our quantum gas magnifier to investigate the dynamics in our 2D lattice of tubes with high bosonic occupation numbers. One area of particular interest within the wider realm of out of equilibrium phenomena is the emergence of patterns spontaneously breaking the symmetry of the underlying Hamiltonian of the system [133–136]. I report on our experimental finding of such a process as a transient state during the equilibration process in a system dominated by a constant driving force.

For all of these measurements the system is brought out of equilibrium by tilting it to apply a force to the atoms. The subsequent dynamics can then be measured in real space with single-shot access to the entire density distribution within the 2D lattice plane, revealing the spontaneous formation of a symmetry breaking density-wave. The quantum gas magnifier allows to investigate this effect compared to other detection methods. The patterns we induce would not be detectable using interference images in momentum space as the coherence is almost fully destroyed during the dynamics and even with coherence, the spontaneously forming domains within the density-wave would not be accessible. Similarly the averaging over multiple realizations that is part of scanning techniques, would not give access to the dynamics, since it breaks the translational symmetry of the optical lattice and washes out the emergent density pattern. Finally, large single-site populations are necessary to trigger the dynamically induced higher order processes which give rise to the density-wave, preventing it from forming in 2D systems with parity projection. It should be noted that this effect is distinctly different from previous observations in tilted lattices, which find suppressed decay of initially prepared density-waves in the unit occupation regime [137, 138].

An overview of the observed dynamics in a tilted triangular lattice is shown in Fig. 5.1, revealing different phenomena in the different regimes of the tunneling strength compared to the applied force and its orientation relative to the primitive lattice vectors. Applying a strong tilt perpendicular to one of the lattice vectors for example leads to the formation of a density-wave on top of the lattice structure (Fig. 5.1a,b), which as will be demonstrated in the following happens spontaneously. We find the same spontaneous symmetry breaking also for different tilt angles, though

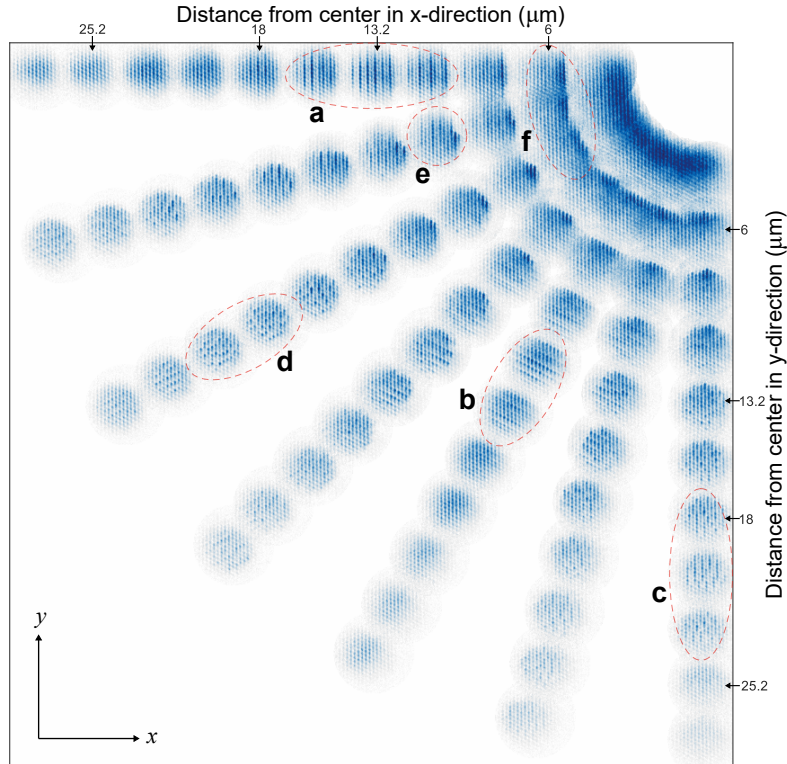


**Figure 5.1.: Various tilt strengths and directions in a triangular lattice.**

Shown are ultracold atomic clouds in a triangular lattice of depth  $V = 1 E_{\text{rec}}$  after a hold time of 80 ms at varying energy offsets between adjacent lattice sites, determined by the shift distance of the cloud from the center of the magnetic trap, and at different shift angles, covering one quadrant in  $15^\circ$  steps. The different images are separated more strongly in the figure to avoid overlaps. Single clouds have a diameter of around  $8 \mu\text{m}$ . We find large parameter regimes supporting the emergence of density-waves with spontaneous symmetry breaking. The dashed red ellipses mark parameter regimes looked at more closely in the following sections. **a,b** Tilt perpendicular to a lattice vector leading to an especially noticeable density-wave order (see section 5.2.3). **c,d** Tilt along a lattice vector yielding a more irregular density-wave (see section 5.2.5). **e** Incommensurate tilt with the density-wave forming outside the initial position (see section 5.2.6). **f** Small tilts lead to more significant mass transport within the cloud and an accumulation of atoms at the lower edge due to self-trapping (see section 5.2.7).

resulting in more irregular density patterns. One special case among these is a parallel orientation between the tilt and one lattice vector (Fig. 5.1c,d). As I will present in the following, the much stronger irregularity of the density-wave in this case arises from the suppression of tunneling perpendicular to the tilt. Another interesting observation is a change in the center-of-mass perpendicular to the tilt at incommensurate angles in between the previous two special orientations (Fig. 5.1e), which I will present in the subsequent section. A very different behavior can be observed for smaller tilt strengths where the atoms accumulate at the lower edge of the system independently of the tilt angle (Fig. 5.1f), exhibiting interaction-induced self-trapping of the atoms in the tilted system [139]. By changing to a strongly tilted honeycomb optical lattice, the buildup of a ring structure by atoms tunneling along equipotential lines around the external trap center, as numerically predicted in [140], is analyzed. The dynamics can also be altered by slowly increasing the tilt via detuning the lattice beams, such that the atoms are dragged upwards the slope of the external confinement instead of tilt quenches. An outlook into such transport measurements in triangular lattices, featuring strong self-trapping edges and further rich dynamics is provided in Appendix D.

The measurements were taken and the data analyzed together with my PhD colleagues Henrik Zahn and Luca Asteria under the supervision of Klaus Sengstock and Christof Weitenberg. The theoretical description was developed in collaboration with Ludwig Mathey, Lukas Freystatzky and Vijay Singh, who also performed the numerical simulations.

## 5.1. Transport Protocol

In the following I will describe our experimental protocol to add a dc drive to the system via displacing the external magnetic confinement with respect to the atoms and introduce the parameters we used to discover the dynamically forming density-wave. We initialize the dynamics by switching off Helmholtz-like offset coils placed in three sets of three pairs of coils, with one set each for the  $x$ -,  $y$ - and  $z$ -direction. More details on the magnetic trap setup can be found in section 2.1 and [39, 44]. To reduce the time scale of the switching as much as possible the coils are run with the desired currents starting from the evaporative cooling and switched off via MOSFETs to shift the position of the magnetic trap very fast compared to our typical tunneling time scales. For the measurements in the triangular lattice as summarized in Fig. 5.1 we always use a lattice depth of  $V = 1 E_{\text{rec}}$ , which results in a tunnel coupling  $J = 13$  Hz. Depending on the desired angle of the tilt with respect to the lattice vectors we use corresponding combinations of  $x$ - and  $y$ -coils, i.e. shift within the 2D lattice plane. At the slope of the magnetic trap the atoms in the lattice experience a constant force for varying evolution times. Subsequently we increase the lattice depth to around  $V = 6 E_{\text{rec}}$ , effectively freezing the distribution, and switch off a second set of  $x$ - and  $y$ -coils with opposite wiring to bring the atoms back into the center of the harmonic trap,

which is necessary to minimize imaging aberrations during the harmonic evolution of the magnifier protocol. On top of that the magnetic confinement is increased following the freezing to combine a larger system size using  $\omega_{\text{sys}} = 2\pi \times 135$  Hz with a magnification sufficient for single site resolution via  $\omega_{\text{ho}} = 2\pi \times 305$  Hz. The resulting shift in the gravitational sag is taken into account and leads to a difference in coil currents for the initial shift to the slope and the final shift to the new trap center for the imaging.

Due to the relevant tunnel coupling in the initial system we start these dynamics experiments with coherence throughout the system and find it to be a necessary ingredient for the pattern formation to take place [26, 50].

Alternatively we can add a tilt in a continuous way through a detuning of the lattice beams, because a frequency offset  $\Delta\nu$  between two interfering lattice beams leads to a running wave of velocity  $v = a_{\text{lat}}\Delta\nu$ . Thus, the atoms in the lattice are, depending on the velocity, lattice depth and strength of the external confinement, dragged upwards the slope or have to move through the lattice to stay in the trap center. Slow shifts are used in section 5.2.7 where they lead to strong self-trapping effects.

## 5.2. Spontaneous Density-Wave Formation in the Triangular Lattice

One of the most striking features found in the overview in Fig. 5.1 is the formation of a staggered density-wave which spontaneously realizes one of two possible phases on top of the triangular lattice. It appears in a metastable regime where the atoms are Stark localized on the slope of the external confinement with its energy offset between neighboring lattice sites as the dominant energy scale and move back to the trap center within several hundred milliseconds. For the following analysis we use an energy offset of  $\Delta/h = 1.4$  kHz resulting from a  $15 \mu\text{m}$  shift of the external trap with respect to the atoms, whereas the tunnel coupling in the lattice is  $J/h = 13$  Hz.

### 5.2.1. Effective Model

In order to get a handle on the underlying physics leading to the observed formation of dynamical density-waves in the tilted triangular lattice of high occupation numbers, we, together with our theoretical collaborators from the group of Ludwig Mathey, developed an effective Hamiltonian to describe our system. The idea is to start from the Bose-Hubbard model and include the dominant energy offset from the strong tilt in a high-frequency approximation, leading to a center-of-mass conserving pair tunneling process to drive the emergence of the density-wave.

Our lattice system can be described by the Bose-Hubbard Hamiltonian with an additional summand to include the tilt:

$$\hat{H}_0 = -J \sum_{\langle jk \rangle} (\hat{b}_j^\dagger \hat{b}_k + \hat{b}_k^\dagger \hat{b}_j) + \frac{U}{2} \sum_j \hat{n}_j (\hat{n}_j - 1) + H_\Delta, \quad (5.1)$$

with

$$H_\Delta = \frac{\Delta}{a_{1D}} \sum_j x_j \hat{n}_j. \quad (5.2)$$

Here  $\hat{b}_j^\dagger$  ( $\hat{b}_j$ ) is the bosonic creation (annihilation) operator,  $\hat{n}_j = \hat{b}_j^\dagger \hat{b}_j$  is the occupation operator on site  $j$  and  $\langle jk \rangle$  restricts the summation to nearest neighbors. The energy offset  $\Delta$  is oriented perpendicular to one of the primitive lattice vectors, here along the  $x$ -direction. It is referring to the offset between neighboring lattice site columns, which are at a distance of  $a_{1D} = \sqrt{3}/2 a_{\text{lat}}$  and  $x_j$  gives the  $x$ -position of site  $j$ . In our system with  $\Delta \gg J, U$  the additional term is dominant and for the effective description we thus go to the interaction picture with respect to  $H_\Delta$ . As a result we obtain

$$\hat{H}_I = e^{i\hat{H}_\Delta t/\hbar} \hat{H}_0 e^{-i\hat{H}_\Delta t/\hbar} = \hat{H}_U + \hat{H}_J + \hat{H}_1 e^{-i\Delta t/\hbar} + \hat{H}_{-1} e^{i\Delta t/\hbar} \quad (5.3)$$

consisting of

$$\hat{H}_U = \frac{U}{2} \sum_j \hat{n}_j (\hat{n}_j - 1), \quad (5.4)$$

$$\hat{H}_J = -J \sum_{\langle jk \rangle_y} \hat{b}_j^\dagger \hat{b}_k + \hat{b}_k^\dagger \hat{b}_j, \quad (5.5)$$

$$\hat{H}_1 = -J \sum_{\langle jk \rangle_{x+}} \hat{b}_j^\dagger \hat{b}_k, \quad (5.6)$$

$$\hat{H}_{-1} = -J \sum_{\langle jk \rangle_{x-}} \hat{b}_j^\dagger \hat{b}_k. \quad (5.7)$$

Now  $\hat{H}_J$  is restricted to nearest neighbors along the  $y$ -direction  $\langle jk \rangle_y$  and  $\langle jk \rangle_{x\pm}$  describe those nearest neighbors oriented along  $x$  such that the potential energy due to the tilt on site  $k$  is higher (lower) than on site  $j$ . As it turns out, Eq. 5.3 is periodic with a frequency defined by  $\Delta$ , allowing to simplify the expression using a Magnus expansion [141–143]. This leads to the effective Hamiltonian

$$\hat{H}_{\text{eff}} = \hat{H}_{U,\text{eff}} + \hat{H}_{J_\perp} + \hat{H}_P \quad (5.8)$$

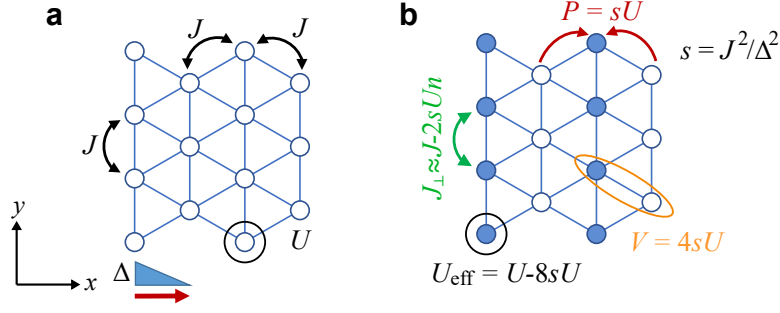


**Figure 5.2.: Effective Hamiltonian of the tilted lattice.** **a** Sketch of the triangular lattice with energy offset  $\Delta$  in  $x$ -direction per lattice site column in the Bose-Hubbard model, featuring a single particle tunneling  $J$  and an on-site interaction  $U$ . **b** Sketch of the respective effective model, which includes a renormalized single particle tunneling perpendicular to the tilt  $J_{\perp}$  and on-site interaction  $U_{\text{eff}}$  as well as nearest neighbor interaction  $V$  and pair tunneling  $P$ . Adapted from [26].

with

$$\hat{H}_{U,\text{eff}} = \left( \frac{U}{2} - 4sU \right) \sum_j \hat{n}_j (\hat{n}_j - 1) + 4sU \sum_{\langle jk \rangle_x} \hat{n}_j \hat{n}_k, \quad (5.9)$$

$$\hat{H}_P = -sU \sum_{\langle jkl \rangle_{\times}} \hat{b}_j^{\dagger} \hat{b}_j^{\dagger} \hat{b}_k \hat{b}_l + \hat{b}_l^{\dagger} \hat{b}_k^{\dagger} \hat{b}_j \hat{b}_j, \quad (5.10)$$

$$\begin{aligned} \hat{H}_{J_{\perp}} = & - \sum_{\langle jk \rangle_y} (J \hat{b}_j^{\dagger} \hat{b}_k + sU \hat{b}_j^{\dagger} \hat{n}_j \hat{b}_k + sU \hat{b}_j^{\dagger} \hat{n}_k \hat{b}_k + \text{h.c.}) \\ & + 2sU \sum_{\langle jkl \rangle_{\Delta}} (\hat{b}_j^{\dagger} \hat{n}_l \hat{b}_k + \hat{b}_k^{\dagger} \hat{n}_l \hat{b}_j). \end{aligned} \quad (5.11)$$

The sum of  $H_P$  runs over all pairs of bonds sharing a site  $j$  in the middle and with one bond up and one bond down the tilt, and  $\langle jkl \rangle_{\Delta}$  includes all triangular plaquettes of sites having  $j$  and  $k$  as nearest neighbors along the  $y$ -direction. The scaling factor  $s$  is given by the ratio of the bare tunneling  $J$  and the energy offset  $\Delta$  as  $s = (J/\Delta)^2$ .

This effective Hamiltonian features interesting non-standard terms whose strengths depends on the scaling parameter  $s$ . Most important is the aforementioned pair tunneling in Eq. 5.10 as the only tunneling term along the tilt direction, which describes a correlated tunneling of two atoms, either both towards or away from one lattice site with one lowering and the other one increasing its potential energy by  $\Delta$ . Additionally we find a nearest neighbor repulsion given by the second term of Eq. 5.9 as well as a density dependent tunneling perpendicular to the tilt given by the second term of Eq. 5.11. On top of that the lattice parameters from the unchanged Bose-Hubbard Hamiltonian get minor renormalizations, changing the interaction scaling to  $U - 8sU$  and the tunneling transverse to the tilt to  $J - 2sUn$ . The different processes are illustrated in a sketch in Fig. 5.2.

In order to test the effect of the pair tunneling process in a simplified way, we consider a simple 1D chain of lattice sites starting with homogeneous filling and

apply increasing numbers of pair tunneling events. Looking at the correlations of changes of the initial population, we indeed recover an increasing staggered pattern, with nearest neighbors having opposite changes in the population and next nearest neighbors having changes of the same sign (for more details see [26, 50]). Thus, the pair tunneling can indeed be associated with a density-wave formation as observed in the experiment, which also form reliably with a period of two lattice site columns along the tilt direction.

### 5.2.2. Numerical Modeling of the Dynamics

Additional to the derivation of an analytical model the system is also simulated numerically to get a direct comparison with the experimental data. This is done via a classical-field (*c*-field) method as described in [144]. The starting situation is again a Bose-Hubbard model, but the 1D tube character of the single lattice sites perpendicular to the lattice plane is included and instead of approximating the tilt by a homogeneous energy offset between neighboring columns the complete external harmonic trap potential is considered:

$$\hat{H} = - \sum_{\langle ij \rangle} J_{ij} (\hat{b}_i^\dagger \hat{b}_j + \hat{b}_i \hat{b}_j^\dagger) + \frac{\tilde{U}}{2} \sum_i \hat{n}_i^2 + \sum_i V_i \hat{n}_i. \quad (5.12)$$

Here  $V_i$  is the trap potential at site  $i$  and  $\tilde{U}$  is the on-site interaction energy. The tunneling energies  $J_{ij}$  depend on the direction of the bond, with tunnel couplings across the 2D lattice in the  $xy$ -plane given by the experimental value of  $J = 13$  Hz, whereas couplings along the  $z$ -direction are set to the much larger  $J_z = 27.9 J$  following from the chosen discretization length in  $z$ -direction of  $\ell_z = 0.4 \mu\text{m}$ . This also leads to a rescaling of the on-site interaction to  $\tilde{U} = g_{1D}/\ell_z = 17.6 J$  (see [145]), with the effective 1D interaction strength along the tubes  $g_{1D} = g_{3D}/(2\pi a_{\text{osc}}^2)$  and  $a_{\text{osc}}$  the oscillator length calculated using the lattice depth. As part of the *c*-field concept the operators  $\hat{b}$  in Eq. 5.12 and the equations of motion are replaced by complex numbers. To match the effects from the atom number the central tube population is chosen according to the experimental value, while the experimentally harder to confirm temperature of the atomic cloud is adjusted in the simulation to fit the experimental observations and stated individually in the following. It is used to determine the initial state of the system in a grand-canonical ensemble, which is then propagated via the classical equations of motion. Here the tilting is included by, at the start of the time propagation, quenching the position of the external harmonic trap by the same distance and in the same direction as in the experiment. The overall system in the simulation has a size between 50 and 100 sites in  $x$ - and  $y$ -directions and a fixed size in  $z$ -direction of 81 sites. Finally, as motivated in section 5.2.4, an additional atomic loss rate  $\gamma$ , drawn from the experimental data, is included.

An exemplary comparison of single shots from the experiment and  $c$ -field simulation is shown in Fig. 5.3, revealing their good qualitative agreement and allowing for quantitative comparisons as done in the following sections.

The simulation also offers the possibility to check the importance of the inhomogeneity of the tilt, which is due to the curvature of the magnetic trap used to generate the tilt in the experiment. Staying otherwise close to the experimental regime, we find a very similar behavior with the emergence of a staggered density-wave within tens of milliseconds using a homogeneous tilt. This helps to validate the analytical approach of approximating the tilt as a homogeneous energy offset and thus the importance of the pair tunneling process for the emergent density-wave.

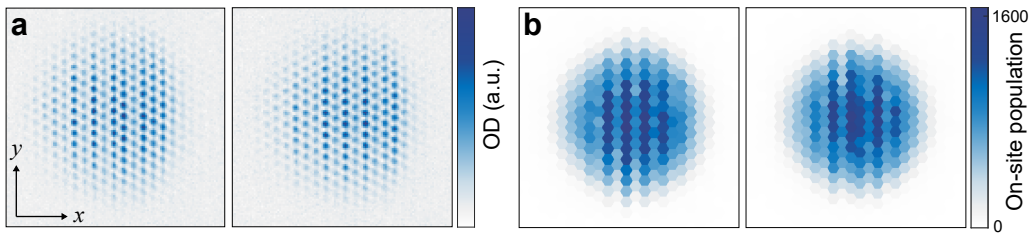


**Figure 5.3.: Comparison with  $c$ -field simulation.** **a** Two exemplary experimental images of the density-wave after a 60 ms hold time at energy offset per lattice site column of  $\Delta/h = 1.4$  kHz. **b** Atomic distributions for the same parameters using  $c$ -field simulation with  $T = 30J/k_B$ . Here the on-site populations are plotted, as the density modulation within lattice sites is not included in the model. Adapted from [26].

### 5.2.3. Spontaneous Symmetry Breaking

As introduced previously, the density-wave we find in the tilted system features a period of two lines of lattice sites of the underlying triangular lattice. Accordingly, there are two equally valid options for the position of this superlattice pattern, leading to a spontaneous realization of one of them. In order to quantitatively confirm the spontaneous nature, we extract the domains of the period two pattern of single realizations by comparing them to a staggered reference pattern. In this analysis the probabilistic appearance of defects in the period two pattern are interpreted as walls between domains in phase and out of phase with the reference pattern.

We use 132 repetitive measurements at the same parameters as stated in the previous section, i.e. after 60 ms hold time at a tilt leading to an energy offset between neighboring lines of  $\Delta/h = 1.4$  kHz. The analysis starts by extracting the single lattice site populations as explained in section 3.4. In order to get quantitative information on the domains, we calculate the difference of every site compared to a lattice population without the density-wave. This reference pattern is taken by averaging over all identically prepared images, since this washes out the arbitrarily positioned density-wave, already pointing to the spontaneous nature of the process. Another option

would be using systems without hold time at the tilt for the references. However, this proved to be not ideal, as despite the Stark localization at the slope there is a minor mass transport to the sides of the system along the highly populated lines and downwards along the tilt, leading to systematic errors in the residues. From the patterns of residues, the domains are assigned by element-wise multiplying them with a staggered reference pattern of alternating signs. The resulting staggered residues then have all positive values if the underlying density-wave has a perfect period of two without domain walls and is aligned with the reference pattern, all negative values if it has the other superlattice phase realized and domains of positive and negative values if the image featured domain walls. The calculation is visualized in Fig. 5.4a and a set of eight typical resulting staggered residue images is shown in Fig. 5.4b, usually consisting of one or two domains of random signs. To combine the information of the staggered residues of all measurements a histogram of the occurring staggered residues is plotted in Fig. 5.4c. The values used are limited to the lattice sites in a small circle around the center of the system as to reduce noise on the residues due to the significantly decreasing lattice site populations at the outer regions. Here the region of interest is set to a radius of three lattice sites as marked by the dashed circle in Fig. 5.4b. The histogram has a clear symmetric double peak structure, confirming the spontaneousness of the symmetry breaking, with equal probability for both domain signs. Performing the same analysis on results from  $c$ -field simulations at the experimental parameters, with very similar statistics and a cloud temperature of  $T = 250J/k_B$ , leads to very good agreement with the experimental histogram (dashed line in Fig. 5.4c).

To verify that the phase of the density-wave really is independent of the starting situation, we have to include the random lattice position with respect to the external confinement of the magnetic trap to the analysis. This lattice phase is already determined for every shot as it is necessary to correctly overlap the grid of Wigner-Seitz cells with an image for the read-out of the lattice site populations. The mask positions are fitted with a single pixel accuracy. As we used a magnification leading to a lattice constant of around five pixels in the measurement, the lattice position was thus fitted for five lattice phases in each direction. Here only the different phases along the tilt are relevant, because using this tilt direction the domains of the density-wave extend across the entire system perpendicular to the tilt. Consequently, we can differentiate between five relative positions between lattice and external trap. The resulting five histograms after this postselection are depicted in Fig. 5.5a. All of them clearly show a double-peak structure despite the now more limited statistics. This confirms that the density-wave indeed spontaneously breaks the translational symmetry, independent from the lattice phase. Additionally, the spontaneousness is checked via the spatial distribution of the domain walls across the system. If the density-wave forms randomly the probability for a domain wall should be constant along the tilt direction, which agrees well with the experimental observation (Fig. 5.5b). In this analysis, we again postselect the data via the lattice phase along the tilt direction and integrate the staggered residues perpendicular to the tilt. From this the likelihood of

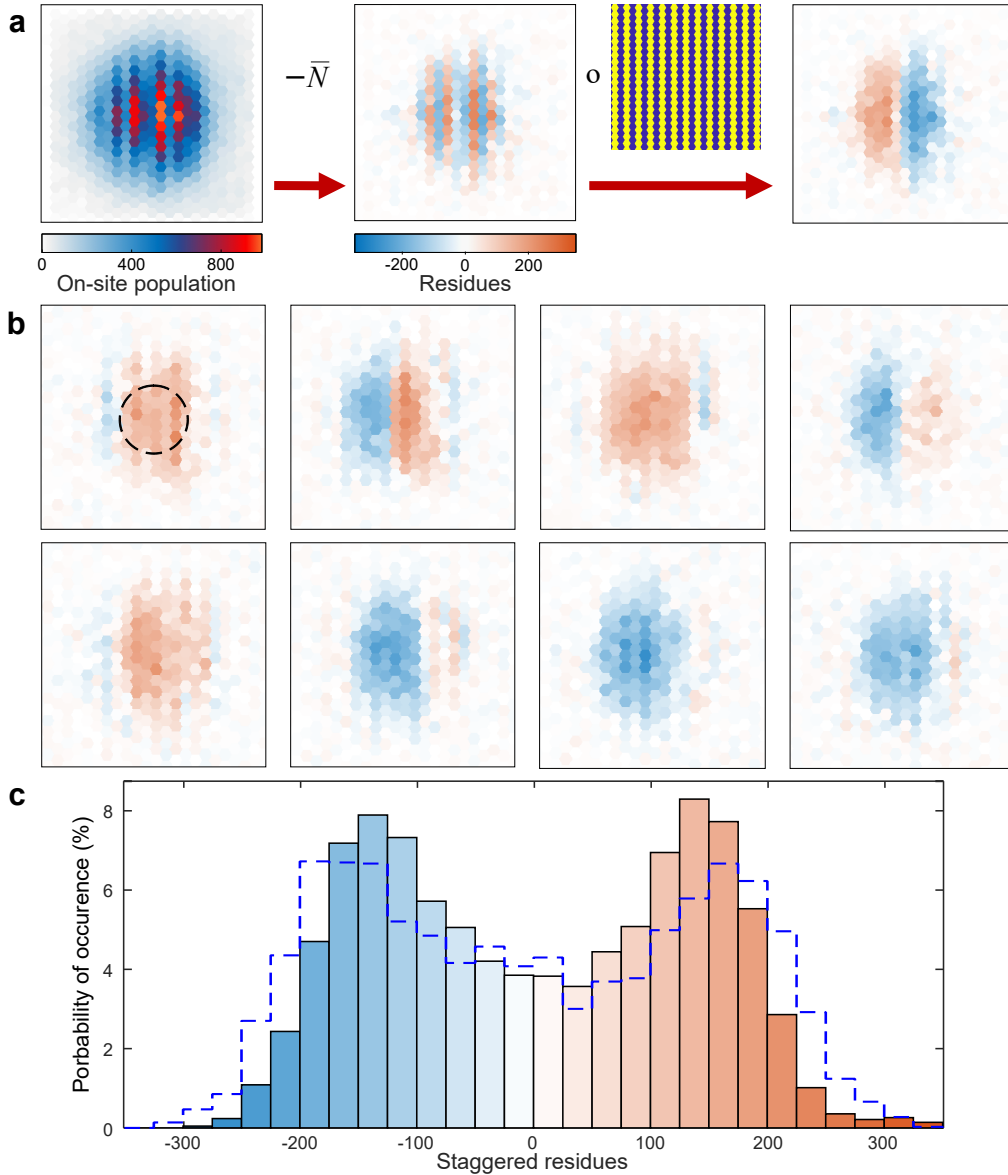


**Figure 5.4.: Spontaneous symmetry breaking.** **a** Calculation of the staggered residues of an exemplary density-wave. From the determined single site populations the residues are calculated by subtracting the mean of all repetitions taken at the same parameters. The staggered residues, which visualize the domains, follow by element-wise multiplication with a reference pattern of perfect period two. **b** Staggered residues for a set of representative single realizations of the density-wave. The atoms are held for 60 ms at a shifted position with energy offset  $\Delta/h = 1.4$  kHz. The dashed circle represents the region of interest used in the following. **c** Histogram of all staggered residues within the region of interest from all 132 individual realizations. The dashed line shows the same analysis on 130 distributions generated via  $c$ -field simulation with  $T = 250J/k_B$ . Adapted from [26].

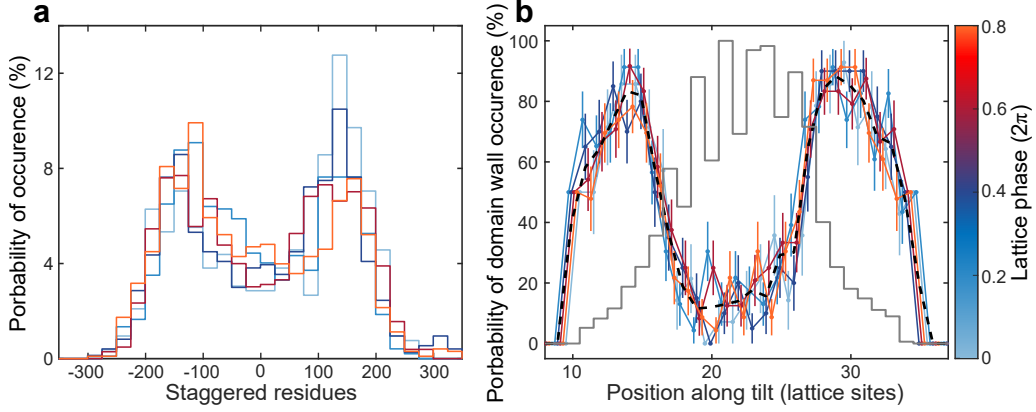


**Figure 5.5.: Lattice phase resolved spontaneous symmetry breaking.** **a** Histograms of the staggered residues as in Fig. 5.4c after postselection depending on the lattice phase (colors), i.e. the lattice position with respect to the external confinement. **b** Spatial distribution of domain walls after postselection on the lattice phase (colors) and the lattice phase independent average (black dashed line). Shown is the probability to find a domain wall at a given position along the tilt after integrating the signal in the perpendicular direction. For reference, an exemplary single-shot density-wave is plotted in gray. The error bars correspond to the 68% confidence interval. Adapted from [26].

a domain wall to appear at any  $x$ -position is calculated. The probabilities are within the experimental uncertainty compatible with a homogeneous distribution at values of around 15% within the central part of the populated region, with a small increase towards the right end of the central region. This we attribute to the onset of a pinning of the density-wave pattern down the slope due to self-trapping (see section 5.2.7). In the outer part the probability strongly rises, even above the uncorrelated expectation of 50%, which is due to the absence of a staggered pattern at the outer region of the system and increasing systematic errors in the analysis mostly from the density envelope.

The different checks all confirm the spontaneous nature of the observed symmetry breaking in the emergent density-wave.

#### 5.2.4. Evolution of the Density-Wave

So far we limited the considerations on measurements of the density-wave to hold times in the tilted system of 60 and 80 ms. In the following section the dynamic process from the emergence of the density-wave order to its very slow decay will be presented.

To quantify the dynamics, we calculate the power spectral density (PSD) of the density-wave after integrating the site populations along the emergent pattern, i.e.

along the y-direction (compare Fig. 5.2), leading to the 1D density  $n_x$ , since there is no systematic feature perpendicular to the tilt. The PSD is defined as

$$|n_k|^2 = \frac{|(\mathcal{F}n_x)(k)|^2}{N_{\text{tot}}^2}, \quad (5.13)$$

with the Fourier transform  $\mathcal{F}$  and normalized to the total atom number  $N_{\text{tot}}$ . The result is plotted logarithmically as function of the hold time at the tilt and wave vector  $k$  in Fig. 5.6a. As seen previously the density-wave emerges with a strongly dominant period of two, appearing here as a peak in  $|n_k|^2$  at  $ka_{1\text{D}}/(2\pi) = \pm 1/2$ , with  $a_{1\text{D}} = \sqrt{3}/2a_{\text{lat}}$ . Within around half a second the peak moves to roughly  $\pm 1/3$ , meaning the density-wave changes towards a period of three lattice rows. Due to the relatively small system size, we cannot meaningfully differentiate between a pattern of period two with an increasing number of domain walls and a pattern with period three. Exemplary density distributions from measurement ( $c$ -field simulation) after hold times of 1 (0), 60 (64) and 1600 ms (1560 ms) are shown in Fig. 5.6b illustrating the change in the density-wave during the dynamics. As overall measure of the contrast of the density-wave  $c$  we thus integrate the PSD from  $ka_{1\text{D}}/(2\pi) = 1/5$  to  $1/2$ , normalized by the entire range from 0 to  $1/2$ :

$$c = \frac{\int_{1/5}^{1/2} |n_k|^2 d(ka_{1\text{D}}/2\pi)}{\int_0^{1/2} |n_k|^2 d(ka_{1\text{D}}/2\pi)}. \quad (5.14)$$

It is depicted in Fig. 5.6c for three tilt strengths. The contrast emerges within few tens of milliseconds, most quickly for the weakest of the three tilts. Here the contrast stays mostly constant after the first 100 ms, while the density-wave slowly increases in period and the metastable cloud at the shifted position loses atoms, mostly tunneling to the trap center. For stronger tilts, the dynamics is slower, but reaches larger maximal density-wave contrasts. In all three cases, the contrast decay is very slow and compatible with moving towards a finite value. The experimental contrast is compared to the same measure calculated from  $c$ -field simulation. It agrees reasonably well with the initial formation, but shows a much quicker decay to an approximately vanishing density-wave contrast after around one second (dashed-dotted lines in Fig. 5.6c). However, the long-time dynamics is captured well by including the experimentally observed significant atom number losses from the system, mostly towards the external trap center, in the simulation (dashed lines in Fig. 5.6c). This can be explained by the pair tunneling term being density dependent, which leads to a freezing of the dynamics as the density drops. The individual loss rates of the different time series are set to each mimic the experimental data and thus increase with the tilt strength.

The dynamics of the  $c$ -field simulation without added atom losses also confirms the scaling expected from the effective Hamiltonian (Eq. 5.8). This is shown in Fig. 5.6d, where the contrast curves for different tilts collapse on each other after rescaling the time by the pair tunneling time  $t_p$  and the density-wave contrast by the energy offset

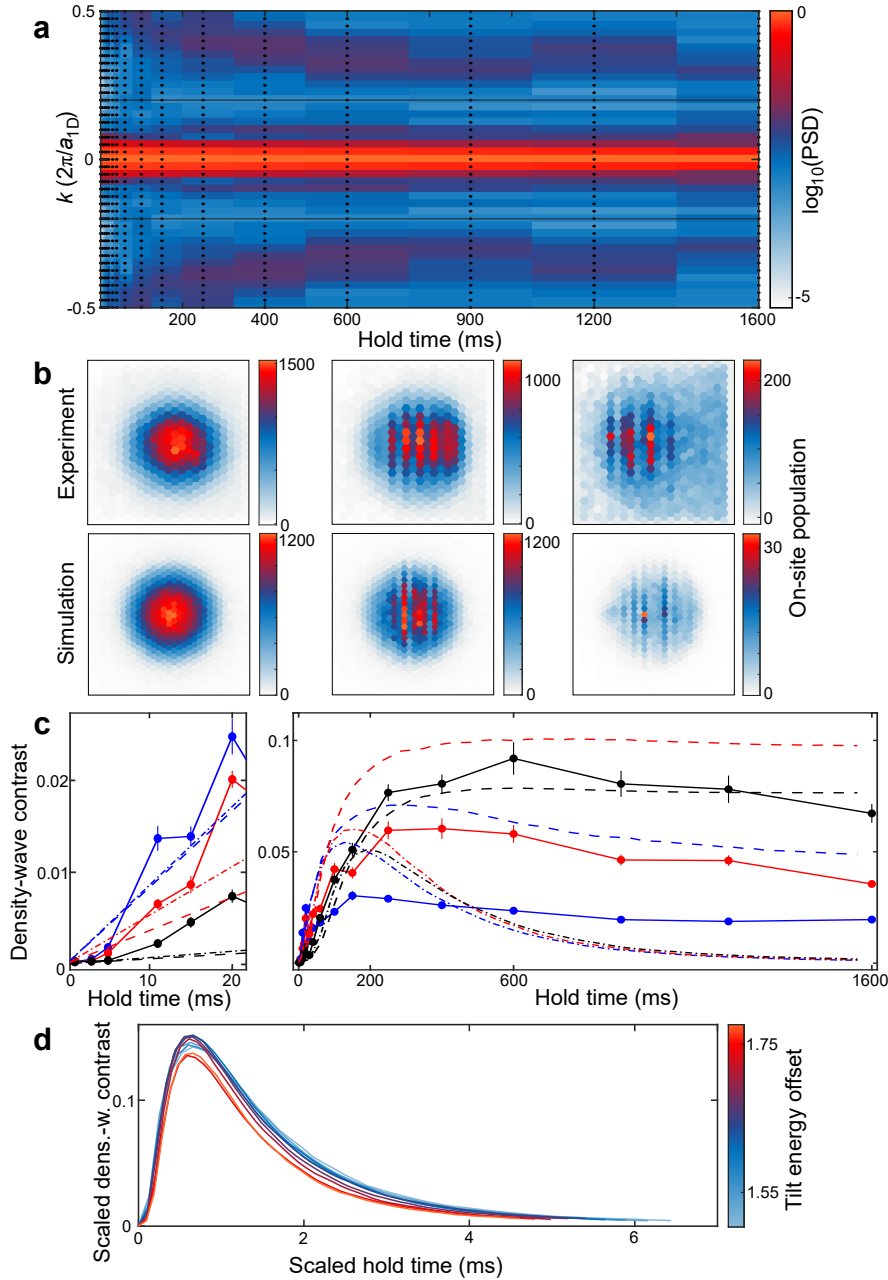


**Figure 5.6.: Dynamical evolution of the density-wave.** **a** Logarithm of the PSD as function of hold time and wave vector as defined in Eq. 5.13. The dots mark the exact parameters of the taken data, which had a constant energy offset from the tilt of  $\Delta/h = 1.4$  kHz. The gray solid lines mark  $ka_{1D}/(2\pi) = \pm 1/5$ . **b** Measured (simulated) exemplary site populations after hold times of 1 (0), 60 (64) and 1600 ms (1560 ms). **c** Evolution of the density-wave contrast  $c$  (Eq. 5.14) for energy offsets of  $\Delta/h = 1.1$  kHz (blue), 1.4 kHz (red) and 1.7 kHz (black). The symbols represent experimental data, the dashed-dotted (dashed) lines  $c$ -field simulation without (with) added atom losses as observed in the experiment and using a temperature  $T = 100J/k_B$ . The error bars correspond to the 68% confidence interval. **d** Scaled density-wave contrast from the simulation without atom losses for varying tilt strengths. By scaling the time with the pair tunneling time  $t_p$  and the contrast with the energy offset squared  $\Delta^2$  the different curves collapse on each other. Adapted from [26].

squared  $\Delta^2$ . Similarly, one recovers the interaction-driven nature of the density-wave formation by varying the total atom number in the system, which increases the atom number per site in the central region. This leads to a shortening of the time scale of the formation, consistent with the atom number dependence of the pair tunneling time. A quantitative comparison can be found in [26].

### 5.2.5. Role of the Transverse Tunneling

The density-wave investigated in the preceding sections always formed in a triangular lattice with the tilt perpendicular to one of the three primitive lattice vectors. Despite the very strong energy offsets from the tilt compared to the tunnel coupling in the lattice  $J$ , the system therefore had a significant tunneling perpendicular to the tilt, connecting 1D stripes within the system. In the following, this situation will be compared to the case of a tilt rotated by  $90^\circ$ , i.e. parallel to one of the lattice vectors. As a result, there are no 1st order tunneling processes unaffected by the tilt anymore, leading to a very strong suppression of transverse tunneling.

The couplings for both situations are schematically drawn in Fig. 5.7a and b. To more easily compare the two by having the tilt point in the same direction, the images in the second case are turned by  $90^\circ$  with respect to the orientation used otherwise throughout the thesis. The 1st order coupling along the tilt in Fig. 5.7b can be neglected, since it has twice the energy offset, slowing the dynamics by a factor four compared to the neighboring rows of lattice sites. Another difference is the smaller distance of these rows from each other amounting to only  $\frac{a_{\text{lat}}/2}{a_{\text{1D}}} \approx 0.58$  of the other tilt direction. This can be easily compensated though by increasing the shift distance accordingly, as on the outer part of the external potential its slope is to very good approximation linear. In total, this shows the strong similarities in the tight-binding descriptions in both cases, with the exception of the transverse tunneling. Nevertheless, we see a strong difference of the emergent density-waves, which already became apparent in Fig. 5.1a and c. Two examples each after read-out of the lattice site populations for the same energy offset between adjacent lines of 1.4 kHz are shown in Fig. 5.7c and d, with the density-wave having no transverse tunneling being much more irregular than the stripe-like patterns looked at so far. The visual impression is somewhat misleading though, as actually both cases have the same staggered pattern of more and less populated rows of lattice sites perpendicular to the tilt. However, with the tilt oriented along a lattice vector the nearest sites of different rows of the density pattern are closer together than the neighboring sites within single rows, which leads to the visual appearance of lines along the tilt.

For a quantitative comparison we calculate the density-density correlations for both cases in a region of interest around the center of the clouds of again three sites radius (dashed circle in Fig. 5.2.3b). To extract the density-wave we again start by computing the residues as in section 5.2.3. Then the covariance is computed between all sites within the region of interest according to

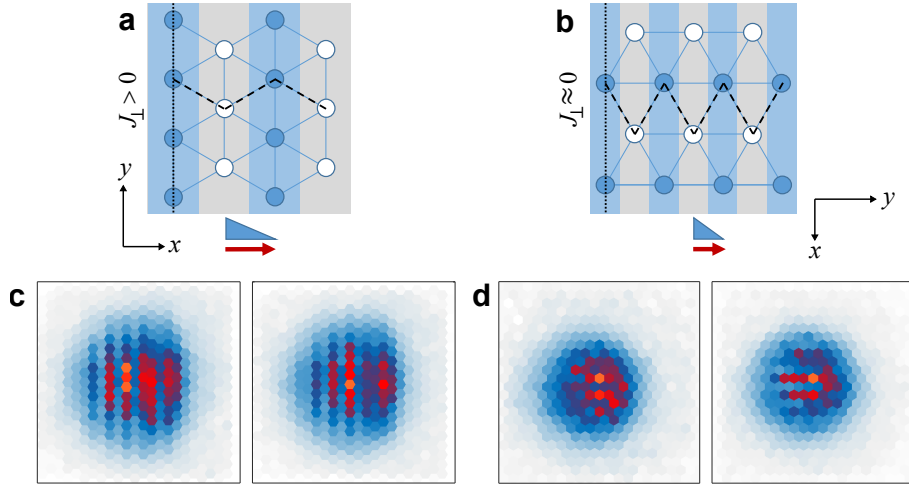


**Figure 5.7.: Importance of transverse tunneling for the density-wave.** **a** Sketch of the triangular lattice with blue and grey columns perpendicular to the tilt, which include a 1st order tunnel coupling. **a** Sketch of a system now rotated by  $90^\circ$  with a tilt again pointing to the left. The columns perpendicular to the tilt thus have almost no internal tunnel coupling. **c,d** Exemplary density distributions in the respective above lying orientations after a hold time of 60 ms at an energy offset between adjacent columns of  $\Delta/h = 1.4$  kHz and maximum initial atom numbers per tube of 900 and 850, respectively. Adapted from [26].

$$\text{cov}_{jkj'k'} = \frac{1}{N-1} \sum_{i=1}^N \delta N_{jk}^{(i)} \delta N_{j'k'}^{(i)}. \quad (5.15)$$

Here  $\delta N_{jk}^{(i)}$  is the residue at lattice site  $(j, k)$  of shot  $i$  and  $N$  the total number of shots. Finally, the results are averaged for all equal and exactly opposite distance vectors and normalized to the square of the mean initial highest single site population. The resulting density correlations as functions of the lattice site distances are shown in Fig. 5.8a and b. Indeed, we find a much stronger pattern for the tilt perpendicular to a lattice vector, reflecting the almost complete absence of domain walls perpendicular to the tilt in the case with transverse tunneling. Despite this, the difference in the staggered correlations along the tilt directions is actually very small (Fig. 5.8c-f). Fitting a heuristic staggered exponential decay  $c_d = c_0(-1)^d e^{-d/L_{\parallel}}$  with distance in sites  $d$  to both yields, within the errors, the same decay lengths  $L_{\parallel} = 2.1(7)$  and  $2.3(5)$  with and without transverse tunneling. Perpendicular to the tilt however, the decay lengths vary drastically. With transverse tunneling the density correlation function is heuristically described by a Gaussian with a width of around the system size, whereas without the transverse coupling its described by a monotone exponential decay  $c_d = c_0 e^{-d/L_{\perp}}$  yielding only short range order with  $L_{\perp} = 1.2(3)$ .

As a result, this shows the importance of the transverse tunneling for the alignment of the phase of the emergent density-wave perpendicular to the tilt, leading to long-

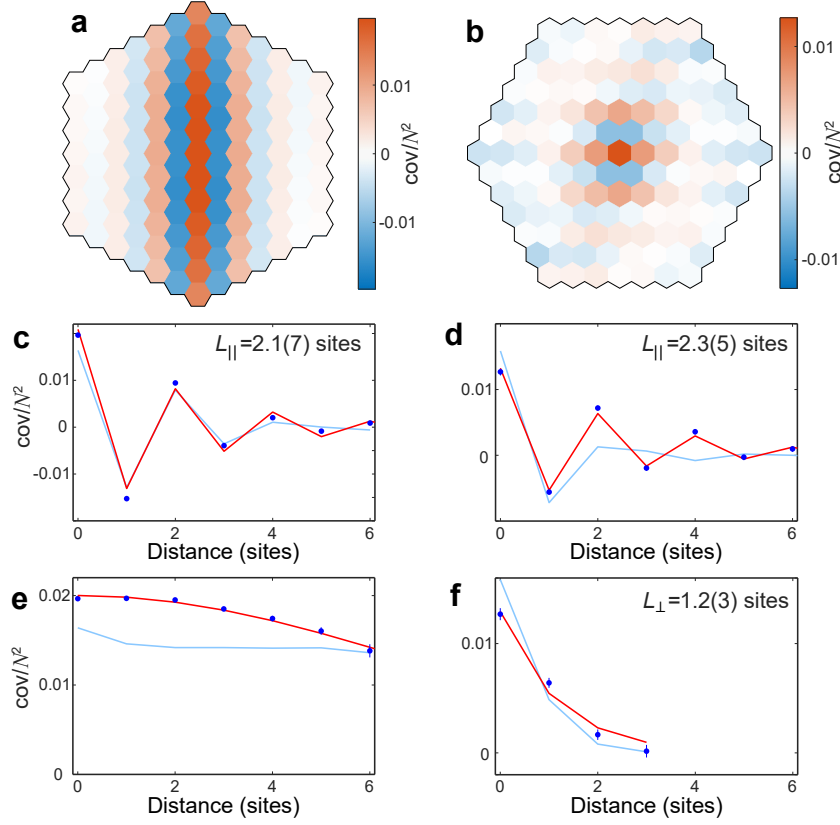


**Figure 5.8.: Importance of transverse tunneling for the correlations of the residues.** **a** Density correlations between different lattice sites as function of distance vector between the sites with transverse tunneling (Fig. 5.7a). **b** Density correlations without transverse tunneling (Fig. 5.7b). **c-f** Cuts through the respective above lying density correlations **a** and **b**. The red lines are fits to the data with functionalities as described in the main text, the blue lines result from the same analysis applied on images from *c*-field simulation at  $T = 50J/k_B$ . **c** Following a zigzag path (compare dashed line in Fig. 5.7a) starting from the center. **d** Following a zigzag path (compare dashed line in Fig. 5.7b) starting from the center. **e** Following a straight path (compare dotted line in Fig. 5.7a) starting from the center. **f** Following a straight path (compare dotted line in Fig. 5.7b) starting from the center. Adapted from [26].

range order across the entire system in the case with transverse tunneling and on average several domain walls perpendicular to the tilt without it. The staggered density signal however is independent of this, showing the same decay lengths in both cases.

### 5.2.6. Incommensurate Tilt Direction

Besides the two specific tilt directions, oriented either exactly orthogonal or parallel to one of the lattice vectors, we can also realize incommensurate tilt direction by shifting the magnetic trap under different angles. In a similar regime of energy differences, this mostly leads to the emergence of less regular density-waves. Applying a tilt closely to perpendicular to a lattice vector though leads to an interesting additional effect.

Already with the  $15^\circ$  rotation of the tilt direction in Fig. 5.1e we find parts of the atoms forming a regular period two density-pattern partially to the side of the initial cloud position. Going to a  $10^\circ$  angle to the perpendicular tilt direction and varying the hold time of the system, the effect becomes much more apparent as shown in Fig. 5.9. As illustrated by the arrows in the last panel, the force on the atomic cloud sitting at the slope of the magnetic potential can be decomposed into a component perpendicular and one parallel to a lattice vector. In the former the atoms are again Stark localized due to the large energy offsets along the tilt. In the latter though tunneling is not suppressed. This leads to the density-wave forming mostly outside

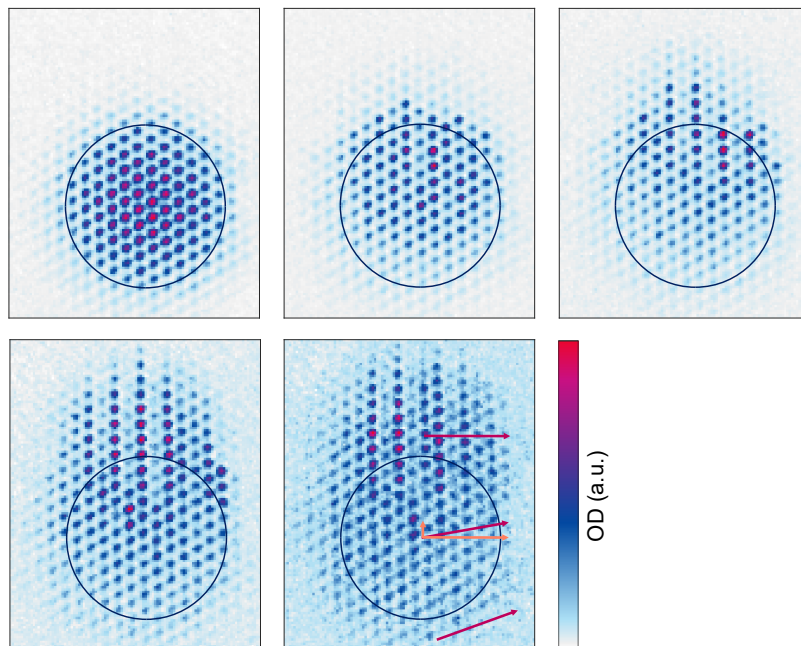


**Figure 5.9.: Incommensurate tilt direction.** The tilt is oriented  $10^\circ$  away from perpendicular to a lattice vector. The images show hold times from top left to bottom center of 1, 100, 300, 600 and 1200 ms. The initial cloud position is marked by the black ring. In the last panel the local orientation of the tilt is shown by the red arrows. At the initial position it can be decomposed into a part perpendicular to one lattice vector and a small part parallel to it (orange arrows). The latter vanishes at the shifted position of the emergent density-wave. Adapted from [26].

the starting position, with the tilt oriented in a commensurate direction and the component along the tilt vanishing. Interestingly, the shifted pattern shows a higher contrast than usual in the case of a perpendicular tilt, while the unmoved fraction of the cloud shows almost no density-wave. Since we know that coherence of the system is a necessary prerequisite for the density-wave to form, this points towards the shifted fraction being the initially condensed part of the atomic cloud. This is reminiscent of the distinct behaviors of the superfluid and the thermal parts of an atomic cloud in an array of Josephson junctions, where the former moves while the latter is mostly fixed in position [130, 146]. It might therefore be possible to make use of the observed separation to prepare a fully condensed sample at the slope.

### 5.2.7. Self-Trapping at the Edge of the System

Due to the dominance of the energy offset compared to the tunnel coupling, we only see a very small mass transport during the build-up of the density-wave. However, for longer hold times the single-particle tunneling, which contrary to the pair tunneling term can lead to a change in the center-of-mass, seems to play an increasing role. As shown in Fig. 5.10 we find an interesting pinning dynamic of the density-wave to the energetically lower end of the cloud. For the first around 100 ms of the dynamics the emergent density-wave is washed out in the averaged site populations integrated perpendicular to the tilt as discussed in section 5.2.3. However, there is a first change of the envelope from a symmetric Gaussian distribution to an increasing skewness, with the steeper slope pointing to the external trap center, which increases for longer hold times. This is most likely due to self-trapping, as observed in a 1D lattice in [139], meaning tunneling beyond the populated region is suppressed by the strong change in interaction energy. Following the formation of this steep slope, the averaged density increasingly shows the pattern of the underlying density-waves of the single-shot realizations from the energetically lower end inwards into the cloud. This increasing alignment or pinning of the patterns during the evolution points to a slow tunneling of the density-wave downwards within the system up to the self-trapping edge, which brings the different initial realizations of the staggered phase in phase with each other.

The same trapping of the atoms within the initial cloud size can also be observed outside the parameters of our effective Hamiltonian leading to a density-wave. For sufficient energy offsets between lattice sites a steep population wall forms from atoms tunneling down along the tilt direction (see Fig. 5.1f and Fig. 5.11a).

Another way of producing such patterns is to detune the lattice beams slightly to create running waves and let the atoms get transported upwards the magnetic potential slope by the moving optical lattice. In Fig. 5.11b-d are exemplary density distributions using a triangular lattice of similar depth, with more data series and observations provided in Appendix D. Here we also find the appearance of intriguing structures, from very clean accumulations at straight edges for slow shifts up to small energy offsets, to rows of lattice sites populated beyond this edge, stretching to the sides, i.e. perpendicular to the tilt. Furthermore, by sufficiently lowering the shift

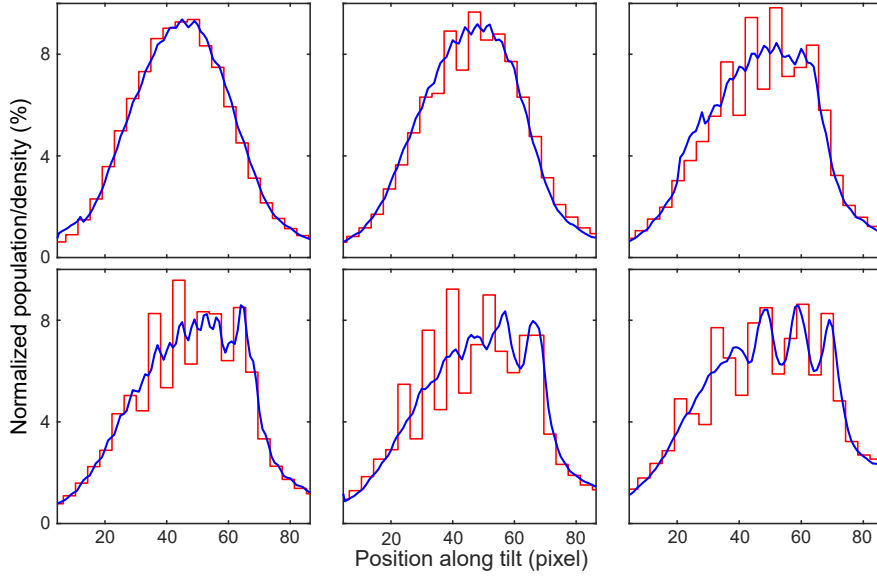


**Figure 5.10.: Pinning of the density-wave.** Shown are integrated density-waves for different hold times. The red lines are exemplary single-shot profiles of the site populations, the blue lines are averaged density profiles and both are normalized by the total atom number. The hold time from top left to bottom right is given by 5, 20, 60, 100, 150 and 400 ms, revealing the crossover from the initially spontaneous pattern to the pinning for longer times, which propagates from the edge with lower potential energy through the system. Adapted from [26].

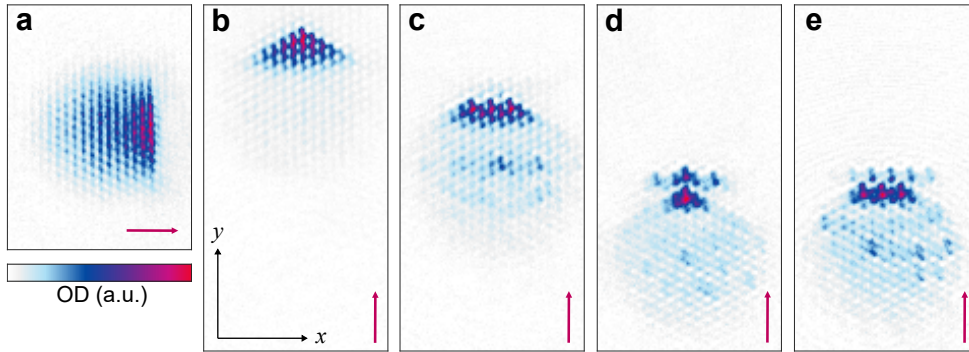


**Figure 5.11.: Self-trapping of the atoms at the systems edge.** **a** Density distribution after 80 ms hold time at an energy offset per column of around  $\Delta/h = 0.5$  kHz. **b-e** Density distribution, also in a triangular lattice, after transporting the atoms up the magnetic potential slope by moving the optical lattice. From left to right the lattice is shifted within 50, 45, 45, 40 ms by 17.5, 25, 32.5, 32.5  $a_{\text{lat}}$  and held constant for 60 ms at the final position. The transport is oriented along one of the lattice vectors and the atoms are not brought back to the trap center prior to imaging, leading to changes in the position and consequently sharpness. The tilt orientation is given by the red arrows. For more exhaustive data series see Appendix D.

velocity, the system undergoes a transition and no buildup of a density edge can be observed. More information on these preliminary measurements with dynamically increasing tilt strength is presented in Appendix D.

In conclusion, we find rich dynamics beyond the so far studied emergence of a spontaneous density-wave in different driving regimes of the lattice versus the external harmonic confinement. Finding precise descriptions of these effects is left for future work.

### 5.3. Transport in the Honeycomb Lattice

All the pattern formation experiments above are performed with a triangular lattice geometry. Here we set the geometry phase to the honeycomb lattice and study its effect on the dynamics by again applying a constant force to the atoms. This allows us to observe the emergence of a ring structure, with some atoms tunneling along equipotential lines at a constant distance to the center (Fig. 5.12a), as predicted for this lattice geometry [140].

In these experiments we suddenly shift the magnetic trap by approximately  $12 \mu\text{m}$  equivalent to  $17 a_{\text{lat}}$  and follow the subsequent transport dynamics in the lattice. The magnetic trap frequency is held constant at  $\omega_{\text{sys}} = \omega_{\text{ho}} = 2\pi \times 208 \text{ Hz}$ , leading to a magnification of 27 which corresponds to around 3 pixels per  $a_{1\text{D}}$ . With this the resulting energy offsets between adjacent A- and B-sites along the tilt are 1.8 kHz in the center of the cloud and thus only around 30% larger than in the previous measurements for the spontaneous density-wave. However, the tunnel coupling in the honeycomb lattice is much stronger. For a lattice depth of  $V = 2.5 E_{\text{rec}}$  it is approximately  $J = 330 \text{ Hz}$  which is only around a factor 5 smaller than the energy offset, compared to it only being around 1% of the energy offset in the triangular lattice for the density-wave. Consequently, single particle tunneling within the 2D plane plays a much more important role. Together with the buildup of a ring structure we see energy non-conserving movement down the potential slope, weakening the ring contrast and limiting the outer wings to around half a circle. The importance of heating for the movement to the center is clearly visible, since these atoms show a much weaker lattice contrast, pointing to excitations in higher bands with larger orbitals or beyond the optical lattice.

To gain qualitative understanding we integrate the atomic density in a region beyond the initial position, split in an outer part given by two ring segments for the atoms following equipotential lines and an inner part covering the central area of the external potential, as depicted in the 2nd image of Fig. 5.12a. From this, we compute the population in the ring segments compared to the entire masked region as a measure of the ring strength. It is shown for different hold times after the shift and different lattice depths in Fig. 5.12b. The ring strength maximizes for hold times of around 30 to 40 ms relatively independently of the lattice depth, with the fraction accumulating at the center getting more dominant for longer times. For fixed hold

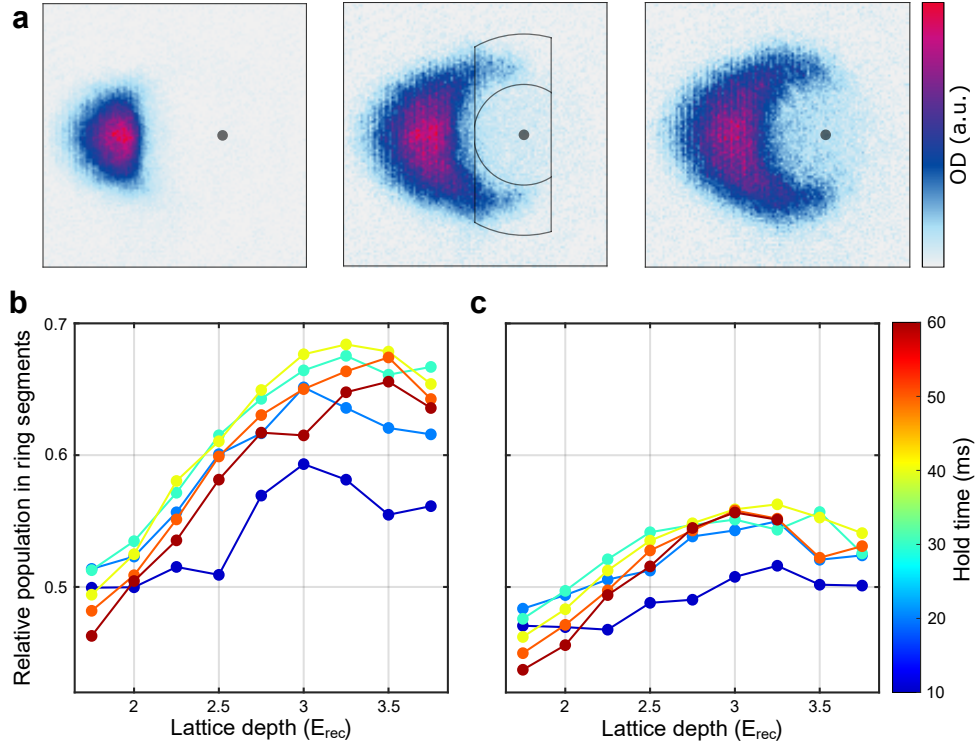


**Figure 5.12.: Ring structure due to transport in honeycomb lattice.** **a** Shown are the real space densities in a honeycomb lattice with  $V = 3.25 E_{\text{rec}}$  10, 40 and 60 ms after displacing the magnetic trap by  $17 a_{\text{lat}}$ . The new trap center is marked by the gray dots. To quantify the strength of the ring the atom number in two segments of an annulus is compared to the population including the inner circle. The masks are sketched in the 2nd image. **b** Relative strength of the outer ring as function of the lattice depth. The color denotes different hold times. **c** Same parameters as in **b**, but an independent 1D lattice with  $V = 6.8 E_{\text{rec}}$  is added perpendicular to the 2D lattice plane, which severely reduces the ring strength.

times the strength also features optimal depths, because for low depths the emerging ring is overshadowed by more atoms quickly moving down the slope, whereas deep lattices more strongly suppress tunneling along the ring. The full data is shown in Appendix E. To check the effect of the lattice sites being 1D tubes we compare this with a 3D lattice, consisting of the same 2D honeycomb lattice and an independent lattice in  $z$ -direction with  $\lambda = 826$  nm. We find this to both suppress the build-up of the ring structure as well as increase the accumulation at the center, leading to significantly smaller ring strengths (Fig. 5.12c). This might be explained by the larger energy offsets due to interactions in the 3D lattice, which make tunneling processes more off resonant. Additionally, our 3D system suffers from larger heating rates, reducing the time scale of the movement to the trap center.

In a next step we investigate the dependence of the ring formation on the geometry phase of the lattice (Fig. 5.13). We find an energy offset between A- and B-sites of the honeycomb lattice to again significantly lower the ring strength. Instead of a sizable fraction of the atoms following the equipotential lines, the form of the wave packet stays almost unchanged while it shifts down the slope. Of course, the geometry phase, by changing the energy difference between the sites, also impacts the tunneling strength within the lattice. To more directly target the dependence on the systems geometry, it would be interesting to vary the lattice depth such that the single particle tunneling  $J$  stays constant. For a larger change of the geometry phase this is very demanding though, given that the respective  $J$  differ by around three orders of magnitude when comparing a honeycomb lattice to a triangular lattice for  $V = 2.5 E_{\text{rec}}$ . Despite this change in  $J$  we can however already see the importance of the geometry in our data by comparing it to the measured dependence on the lattice depth in Fig. 5.12b. There we find the ring strength to increase between  $V = 2.5$  and  $3.5 E_{\text{rec}}$  for the same 50 ms hold time as used here, which leads to a reduction of  $J$ . By instead changing the geometry phase away from the honeycomb lattice we

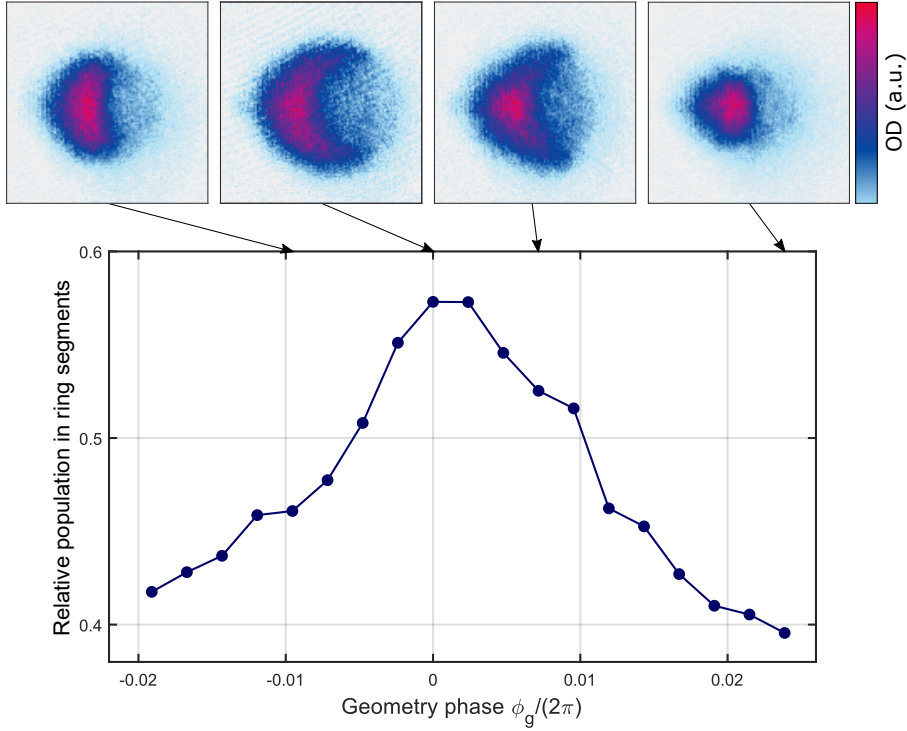


**Figure 5.13.: Ring structure as function of the geometry phase.** Honeycomb and boron nitride lattices with a lattice depth of  $V = 2.5 E_{\text{rec}}$  are displaced by 17 lattice sites relative to an external confinement of  $\omega_{\text{ho}} = 2\pi \times 208$  Hz and the following dynamic imaged after a 50 ms hold time. The relative ring strength is calculated using the masks from Fig. 5.12a on a single experimental run. The images in the top row show the situations at  $\phi_g/(2\pi) = -0.01, 0, 0.007$  and  $0.024$ .

make  $J$  increasingly off resonant. In this case, we conversely see a reduction of the ring strength. This is also reminiscent of the simulation in [140], where they instead compared a honeycomb to a square lattice of equal tunnel coupling and similarly found no tunneling along the equipotential lines.

With our high-resolution access and dynamic tuning possibilities it would be intriguing to further study the transport properties of graphene. One interesting option would be to mimic strained graphene by introducing an imbalance to the lattice beams [31, 102, 103] and study its anisotropic transport properties [147].

## 5.4. Conclusion and Outlook

In this chapter, we investigated different pattern formation in dc driven hexagonal optical lattices by using our quantum gas magnification to gain access to the real space density distribution of the system.

By going to a metastable regime on the slope of the external confinement with a strong energy offset between lattice sites compared to their tunnel coupling, we experimentally found the buildup of a density-wave on top of the underlying triangular lattice. As verified by extensive investigations, this density-wave spontaneously breaks the system's discrete translational symmetry. In cooperation with the theory group of Ludwig Mathey we were able to explain the dynamics in a Floquet picture via pair tunneling processes appearing in the effective Hamiltonian of the system. The observations also agree very well with a  $c$ -field simulation using the parameters of the experiment. Following the density evolution in the system after subjecting it to the strong driving, we found a freezing of the interaction-induced processes due to particle losses down the slope and thus very long lifetimes of the density-wave. Additionally, we varied the effective tight-binding description of the system to suppress tunneling transversely to the tilt direction. This leads to a density-wave, which still has the same staggered correlation length along the tilt direction, but only a very short correlation length perpendicular to it, leading to significantly more domain walls in the emerging pattern. The necessity of the pair tunneling process from the effective model for the description of the dynamics suggests that also dc driven systems [148, 149] might be an interesting approach for Floquet engineering of extended Hubbard models [150, 151]. In the future, by also adding an ac drive to break time reversal symmetry, topological states could be engineered, which might allow for the further study of, for example, topological band gap solitons [152] and Stark time crystals [153]. In our case the density-wave emerges as a nonequilibrium process, but by engineering stronger non-standard Hubbard terms, such effects could also be investigated in ground states [154, 155]. Since the magnifier in principle also enables the measurement of coherence properties, it would also be promising for the study of spontaneous symmetry breaking of phase patterns, engineered via driving of the lattices [156, 157] or for example the observation of twisted superfluids [158]

In another set of experiments, using the honeycomb optical lattice and again a strong driving applied to the system, a ring structure along the equipotential lines emerges. Its strength significantly decreases as a function of the lattice geometry, i.e. by introducing an energy offset between the A- and B-sites of the lattice. In the future, the parameter regime could be expanded to, for example, also simulate strained graphene via adding an imbalance to the optical lattice [31, 102, 103].

In the triangular lattice we further observed a bunching of the atoms at the edge of the populated region, both on the long time scale in the staggered density-wave regime, as well as even more pronounced for lower tilt strengths. This self-trapping [139] gets especially strong by dynamically increasing the tilt strength (Appendix D), with large fractions of the atoms accumulating at very few lattice sites. Here we see several interesting phenomena during the dynamics. To precisely map out and explain the underlying processes further work is necessary.

Beyond the examples shown in this thesis it would also be fascinating to study topological transport, like the recently demonstrated observation of chiral edge modes [159]. For the preparation of interesting topological systems, also our high lattice geometry tunability could be useful. The largest challenge for such realizations with our setup though would most likely be to engineer sufficiently sharp topological boundaries for the edge modes to stay localized.

In conclusion, the real space density access to new regimes of 3D systems via our quantum gas magnifier allows the observation of rich dynamics and further work regarding pattern formation and transport properties of such systems would be very interesting.

## Appendix A.

# Quantum Walk in Triangular Momentum Space Lattice

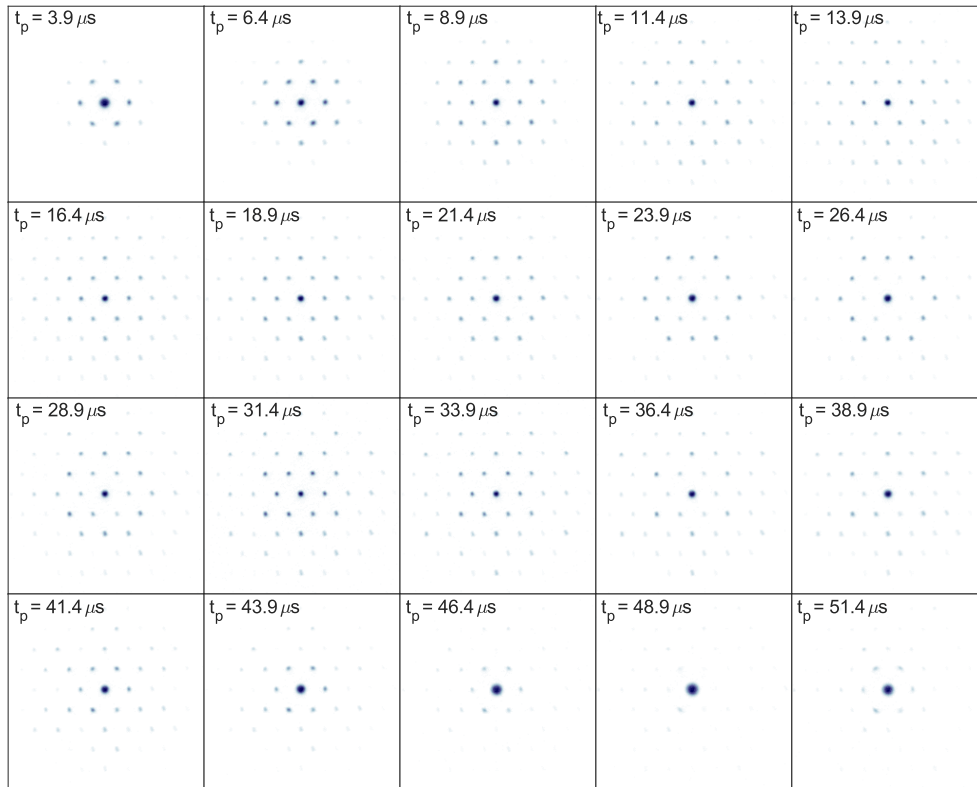


**Figure A.1.:** Quantum Walk in momentum space lattice with  $\phi_g = 0$ . Shown is a series of 20 pulse times in  $2.5 \mu\text{s}$  steps using a lattice depth of  $V = 6.5 E_{\text{rec}}$  and a geometry phase of  $\phi_g = 0$ . From these images the dark blue line in Fig. 4.13b is calculated. Adapted from [36].

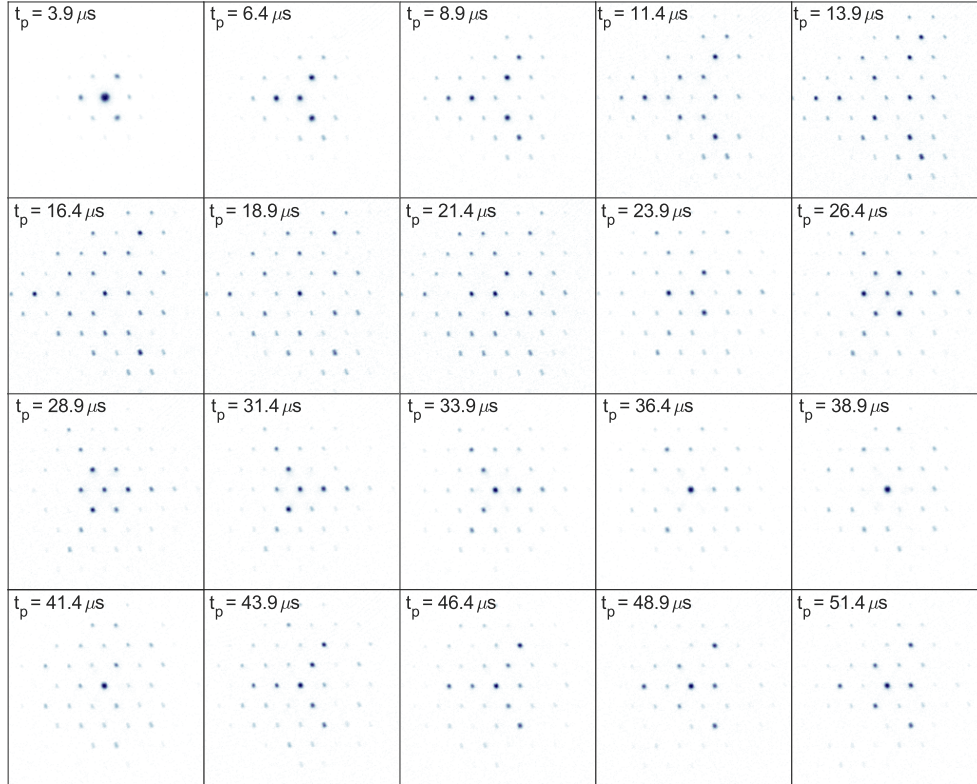


**Figure A.2.: Quantum Walk in momentum space lattice with  $\phi_g = \pi/2$ .**

Shown is a series of 20 pulse times in  $2.5 \mu\text{s}$  steps using a lattice depth of  $V = 6.5 E_{\text{rec}}$  and a geometry phase of  $\phi_g/(2\pi) = 0.25$ . From these images the middle blue line in Fig. 4.13b is calculated. Adapted from [36].

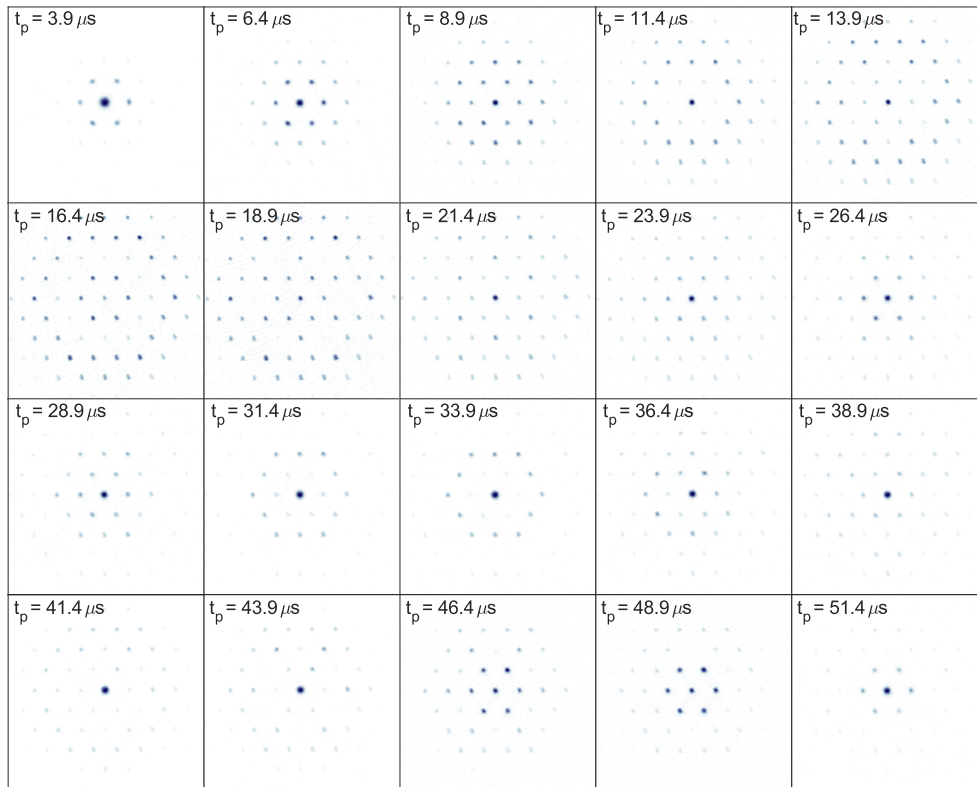


**Figure A.3.: Quantum Walk in momentum space lattice with  $\phi_g = \pi$ .** Shown is a series of 20 pulse times in  $2.5 \mu\text{s}$  steps using a lattice depth of  $V = 6.5 E_{\text{rec}}$  and a geometry phase of  $\phi_g/(2\pi) = 0.5$ . From these images the light blue line in Fig. 4.13b is calculated. Adapted from [36].



## Appendix B.

# PCA of Distorted Brillouin Zones

In the following I present our approach of getting an improved assignment of band mapping data to the different BZs via PCA, which is a useful tool for a wide range of applications [160], because it lowers the dimensionality of a data set. The problem arises from increasing distortions of the higher order BZs compared to the ideal ones as demonstrated in the three exemplary band mapping images in Fig. B.1a. We observe a shift along gravity, which is pointing downwards in the images, and deformations leading to washed-out contours in a reproducible way and independent of the modulation type used to excite the atoms to the given bands. This can be explained by a combination of multiple reasons, in particular by the external magnetic confinement, both in itself as well as through a possible mismatch between the potential trap center of the optical lattice and the magnetic confinement and also by gravity, acting on the atoms throughout the band mapping process. Instead of a combined numerical simulation using estimations of the different distortion sources, we reconstruct the distortions from the experimental findings themselves. For this we use the combined data set behind Fig. 4.16 from the three different modulation types, consisting of 147 images in total.

The PCA itself is done as described in [161] by first combining the data in a matrix  $D$  of size  $N \times P$ , where  $N$  is the total number of images and  $P$  the total number of pixels. It contains at  $D_{ji}$  the value of pixel  $j$  in image  $i$  after subtracting the average value of  $j$  of all images to center the data around 0. This allow to calculate the real and symmetric  $N \times N$  matrix  $\tilde{C} = DD^T/(N-1)$ . It features the same spectrum of up to  $N$  eigenvalues  $\lambda_i$  as the much larger  $P \times P$  covariance matrix  $C = D^T D/(N-1)$ . From the corresponding eigenvectors  $V_i$ , defined as  $\tilde{C}V_i = \lambda_i I_N V_i$  with the  $N \times N$  unit matrix  $I_N$ , the PCs follow as  $PC_i = D^T V_i / \sum_j (D^T V_i)$ . They are sorted in relevance by sorting their eigenvalues in decreasing order. The resulting nine most relevant PCs are depicted in Fig. B.1d.

In a next step we use the correlated regions found in the PCs to define masks for the distorted BZs. Since the distortions of the 1st and 2nd BZs are very small we stay with the ideal ones for them as shown by the orange and red regions in Fig. B.1b. The higher order BZs are constructed using those PCs with the strongest contrast to each other and to the outer region. For this we start with the 2nd PC and binarize it using as threshold the middle of the full range, visualized in the color map as white,

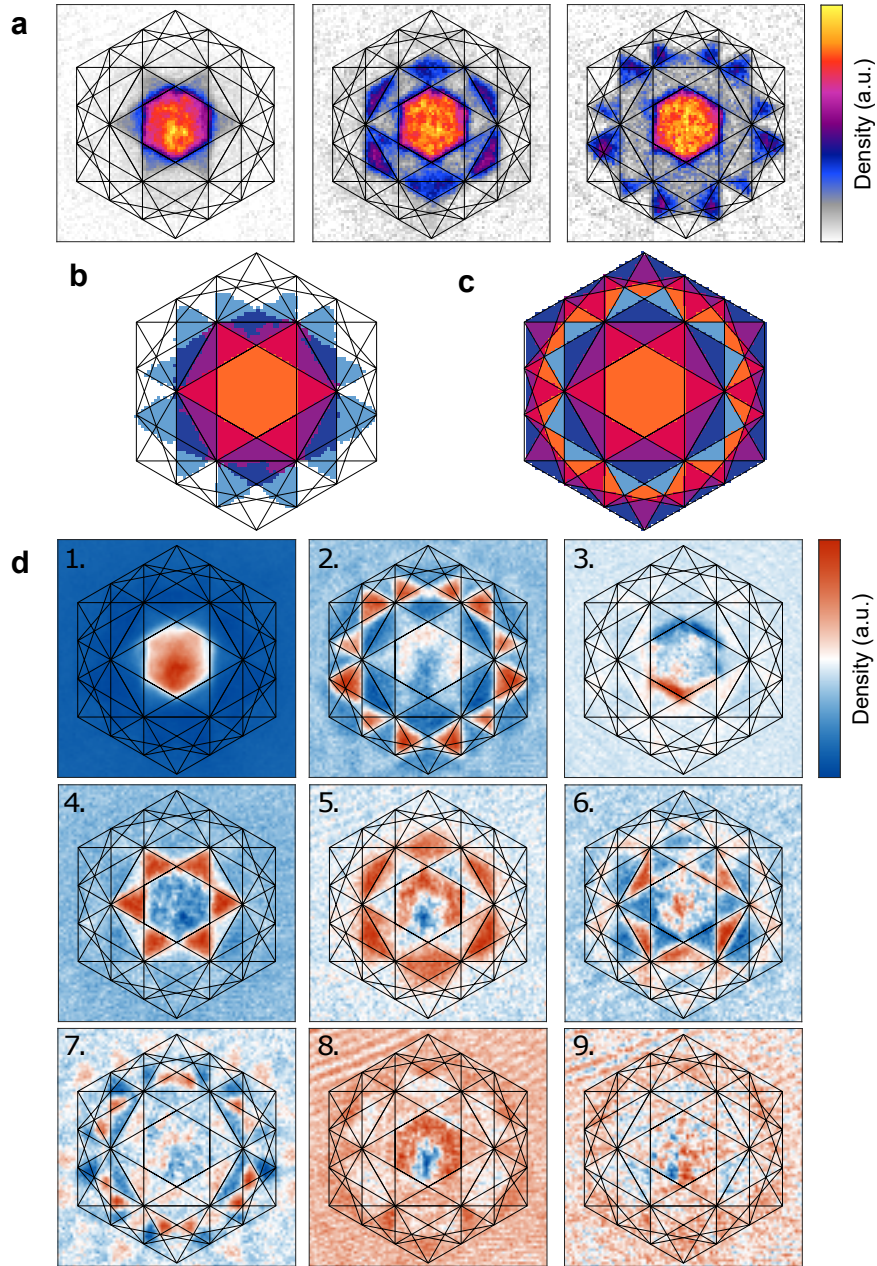


**Figure B.1.: PCA of distorted BZs.** **a** Exemplary band mapping images overlapped with the ideal BZs represented by the black lines. For higher BZs this demonstrates significant distortions. **b** Masks of the first six distorted BZs obtained via PCA. The outermost region gives the combined distorted 5th and 6th BZs. **c** The first nine ideal BZs in the same pixel resolution for comparison. The 6th BZ here is the outer orange region, instead of having the same color as the 5th BZ as in **a**. **d** The first nine PCs of the full data set of band mapping images. Some of which carry information on the experimentally distorted BZs. Adapted from [36].

meaning red regions are set to one and blue regions to zero. We identify the resulting mask as the distorted 5th+6th BZ. The reasoning is that these bands touch during the entire ramping of the lattice depth such that we do not expect to be able to distinguish between them and that the mask contains significant parts of both ideal BZs. This is also consistent with the extracted mask size being roughly twice as large as the ideal size of a single BZ. The combined mask is depicted in Fig. B.1b in light blue. With this outer mask combined with the known ideal masks for the 1st and 2nd BZs we also get the combined region of the 3rd and 4th distorted BZs. To best locate their border we use the sum of both the 4th and 6th PCs after normalizing each such that they span the same range of values and again use the middle of this range as threshold for the binarization. Additionally, pixels inside the already known masks are forced to be zero. Using only one of these PCs to identify the border between 3rd and 4th BZ yields very similar but slightly more fuzzy boundaries. Despite this there are still small islets of pixels which are clearly mislabeled between the two BZs. We correct for this by switching the assignment of all unconnected groups of less than ten pixels within large regions of opposite assignment, with the latter having sizes above 50 pixels. The resulting distorted 3rd and 4th BZs are shown in purple and dark blue in Fig. B.1b.

These distorted BZs are used for the read-out of the different relative band populations in Fig. 4.16.



## Appendix C.

# Derivation of Resonant Excitation Strengths

Here I will describe the derivation of the resonant excitation strengths to higher bands via amplitude modulation, sublattice modulation and circular lattice shaking. The results are used for the calculations shown in Fig. 4.17. For each method, the quasimomentum dependent excitation rates are approximated in time-dependent perturbation theory. The derivation follows closely our presentation in [36].

First, the rate for balanced amplitude modulation is derived. Here the perturbation consists of a periodic modulation of the intensity  $I_i$  of every lattice beam  $i$  with equal frequency  $\omega/(2\pi)$  and equal strength  $\epsilon_{\text{am}}$ . The time periodic intensities are thus given by

$$I_i(t) = I_{i,0} + \epsilon_{\text{am}} I_{i,0} \sin(\omega t). \quad (\text{C.1})$$

Since we also restrict the measurement to modulations of balanced lattices the situation simplifies to  $I_{1,0} = I_{2,0} = I_{3,0}$ . The resulting total lattice potential, starting from Eq. 4.1 and omitting constant terms, then is

$$\begin{aligned} V_{\text{am}}(\mathbf{r}, \phi_g, t) &= 2V(1 + \epsilon_{\text{am}} \sin(\omega t)) \sum_i \cos\left(\mathbf{b}_i \cdot \mathbf{r} + \frac{\phi_g}{3}\right) \\ &= V_{\text{pot}}(\mathbf{r}, \phi_g) + \sin(\omega t) V_{\text{pot}}'(\mathbf{r}, \phi_g), \end{aligned} \quad (\text{C.2})$$

with the time-independent perturbation operator

$$V_{\text{pot}}'(\mathbf{r}, \phi_g) = \epsilon_{\text{am}} V_{\text{pot}}(\mathbf{r}, \phi_g). \quad (\text{C.3})$$

The resonant excitation strength of this time-dependent potential is calculated using time-dependent perturbation theory. According to Fermi's golden rule, the excitation rate  $\Gamma_{B,B'}^{q,q'}$  from an initial quasimomentum  $\mathbf{q}$  in  $B = 1$  to a final quasimomentum  $\mathbf{q}'$  in band  $B'$  is given by

$$\Gamma_{B,B'}^{qq'} \propto \left| \int d^3r \psi_B^q(\mathbf{r}) V_{\text{pot}}'(\mathbf{r}) \psi_{B'}^{q'*}(\mathbf{r}) \right|^2. \quad (\text{C.4})$$

The corresponding states  $\psi_{B^{(\prime)}}^{\mathbf{q}^{(\prime)}}$  are eigenstates of the static lattice Hamiltonian  $\hat{H}$  and can thus be expressed as a Fourier series of Bloch waves

$$\psi_{B^{(\prime)}}^{\mathbf{q}^{(\prime)}}(\mathbf{r}) = e^{-i\mathbf{q}^{(\prime)} \cdot \mathbf{r}} \sum_u c_u^{\mathbf{q}^{(\prime)}, B^{(\prime)}} e^{-i\mathbf{k}_u \cdot \mathbf{r}}. \quad (\text{C.5})$$

Here  $c_u^{\mathbf{q}, B}$  are the Bloch coefficients and  $\mathbf{k}_u$  are integer linear combinations of the reciprocal lattice vectors  $\mathbf{b}_i$ .

In order to calculate the excitation strength we now plug in Eq. C.3 and Eq. C.5 into Eq. C.4. In a first step we only take into consideration the first summand,  $V_1' = \epsilon_{\text{am}} 2V \cos(\mathbf{b}_1 \mathbf{r} + \phi_g/3)$ , of the perturbation operator  $V_{\text{pot}}'$  for the sake of clarity. This results in

$$\begin{aligned} \int d^3r \psi_B^{\mathbf{q}} V_1' \psi_{B'}^{\mathbf{q}'*} &= \epsilon_{\text{am}} V \int d^3r e^{-i(\mathbf{q}-\mathbf{q}') \cdot \mathbf{r}} \left( \sum_u c_u^{\mathbf{q}, B} e^{-i\mathbf{k}_u \cdot \mathbf{r} + i\mathbf{b}_1 \cdot \mathbf{r} + i\phi_g/3} \right) \left( \sum_{u'} c_{u'}^{*\mathbf{q}', B'} e^{i\mathbf{k}_{u'} \cdot \mathbf{r}} \right) \\ &+ \epsilon_{\text{am}} V \int d^3r e^{-i(\mathbf{q}-\mathbf{q}') \cdot \mathbf{r}} \left( \sum_u c_u^{\mathbf{q}, B} e^{-i\mathbf{k}_u \cdot \mathbf{r} - i\mathbf{b}_1 \cdot \mathbf{r} - i\phi_g/3} \right) \left( \sum_{u'} c_{u'}^{*\mathbf{q}', B'} e^{i\mathbf{k}_{u'} \cdot \mathbf{r}} \right) \\ &= \epsilon_{\text{am}} V \delta_{\mathbf{q}, \mathbf{q}'} \sum_{u, u'} \left( e^{i\phi_g/3} \delta_{\mathbf{k}_u + \mathbf{b}_1, \mathbf{k}_{u'}} + e^{-i\phi_g/3} \delta_{\mathbf{k}_u - \mathbf{b}_1, \mathbf{k}_{u'}} \right) c_u^{\mathbf{q}, B} c_{u'}^{*\mathbf{q}', B'} \\ &= \epsilon_{\text{am}} V \delta_{\mathbf{q}, \mathbf{q}'} \left( \sum_u c_u^{*\mathbf{q}, B'} \left( c_{\mathbf{k}_u + \mathbf{b}_1}^{\mathbf{q}, B} e^{-i\phi_g/3} + c_{\mathbf{k}_u - \mathbf{b}_1}^{\mathbf{q}, B} e^{i\phi_g/3} \right) \right). \end{aligned} \quad (\text{C.6})$$

Including all three summands of Eq. C.3 leads straightforwardly to the excitation rate as

$$\begin{aligned} \Gamma_{B, B'}^{\mathbf{q} \mathbf{q}'} &\propto \delta_{\mathbf{q}, \mathbf{q}'} \epsilon_{\text{am}}^2 V^2 \left| \left( \sum_u c_u^{*\mathbf{q}, B'} \left( c_{\mathbf{k}_u + \mathbf{b}_1}^{\mathbf{q}, B} e^{-i\phi_g/3} + c_{\mathbf{k}_u - \mathbf{b}_1}^{\mathbf{q}, B} e^{i\phi_g/3} \right) \right) \right. \\ &\quad \left. + \left( \sum_u c_u^{*\mathbf{q}, B'} \left( c_{\mathbf{k}_u + \mathbf{b}_2}^{\mathbf{q}, B} e^{-i\phi_g/3} + c_{\mathbf{k}_u - \mathbf{b}_2}^{\mathbf{q}, B} e^{i\phi_g/3} \right) \right) + \left( \sum_u c_u^{*\mathbf{q}, B'} \left( c_{\mathbf{k}_u + \mathbf{b}_3}^{\mathbf{q}, B} e^{-i\phi_g/3} + c_{\mathbf{k}_u - \mathbf{b}_3}^{\mathbf{q}, B} e^{i\phi_g/3} \right) \right) \right|^2. \end{aligned} \quad (\text{C.7})$$

In combination with our band structure calculation, giving the needed Bloch coefficients for the different band indices  $B = 1, B' = 2, \dots, 7$  and discretized quasimomenta throughout the 1st BZ  $\mathbf{q} = \mathbf{q}'$ , the relative excitation rates can be calculated for each quasimomentum. To approximate the total excitation strengths shown in Fig. 4.17 these results are summed up over the entire 1st BZ. This will tend to overestimate the influence of higher quasimomenta, since condensed bosons would be found around the  $\Gamma$  point. However, during the spectroscopy we find the atoms to already be distributed over the 1st BZ and thus use the integrated excitation rate for a qualitative comparison with our measurement.

Next, the excitation rates for sublattice modulation are derived. Here the 1D lattice phases  $\phi_i$  are periodically modulated with equal frequency and amplitude  $A_{\text{sm}}$ , which keeps the lattice position fixed and changes the geometry phase  $\phi_g$  by  $3A_{\text{sm}}$  (4.19). The time-dependent lattice potential is therefore

$$\begin{aligned}
V_{\text{sm}}(\mathbf{r}, \phi_g, t) &= 2V \left( \sum_i \cos\left(\mathbf{b}_i \cdot \mathbf{r} + \frac{\phi_g}{3} + \frac{A_{\text{sm}}}{3} \sin(\omega t)\right) \right) \\
&= 2V \left( \sum_i \cos\left(\mathbf{b}_i \cdot \mathbf{r} + \frac{\phi_g}{3}\right) \cos\left(\frac{A_{\text{sm}}}{3} \sin(\omega t)\right) - \right. \\
&\quad \left. \sin\left(\mathbf{b}_i \cdot \mathbf{r} + \frac{\phi_g}{3}\right) \sin\left(\frac{A_{\text{sm}}}{3} \sin(\omega t)\right) \right) \\
&\approx 2V \left( \sum_i \cos\left(\mathbf{b}_i \cdot \mathbf{r} + \frac{\phi_g}{3}\right) + \sin\left(\mathbf{b}_i \cdot \mathbf{r} + \frac{\phi_g}{3}\right) \frac{A_{\text{sm}}}{3} \sin(\omega t) \right) \\
&= V_{\text{pot}}(\mathbf{r}, \phi_g) + 2V \cos\left(\mathbf{b}_i \cdot \mathbf{r} + \frac{\phi_g}{3} + \frac{\pi}{2}\right) \frac{A_{\text{sm}}}{3} \sin(\omega t) \\
&= V_{\text{pot}}(\mathbf{r}, \phi_g) + V_{\text{pot}}(\mathbf{r}, \phi_g - \pi/2) \epsilon_{\text{sm}} \sin(\omega t) \\
&= V_{\text{pot}}(\mathbf{r}, \phi_g) + \sin(\omega t) V_{\text{pot}}'(\mathbf{r}, \phi_g - \pi/2), \tag{C.8}
\end{aligned}$$

with  $\epsilon_{\text{sm}} = A_{\text{sm}}/3$ . The approximation in the 3rd line consists of restricting the Taylor series of sine and cosine of  $\left(\frac{A_{\text{sm}}}{3} \sin(\omega t)\right)$  to their first order, because the perturbation is kept very small. Including also higher order terms leads to the appearance of terms modulated with multiples of  $\omega$ . In first order, the perturbation operator for sublattice modulation compared to amplitude modulation only acquires an additional phase and has a different prefactor. Plugging it into Eq. C.4 thus results in

$$\begin{aligned}
\Gamma_{B, B'}^{qq'} &\propto \delta_{\mathbf{q}, \mathbf{q}'} \epsilon_{\text{sm}}^2 V^2 \left| \left( \sum_u c_u^{*\mathbf{q}, B'} \left( c_{u+\mathbf{b}_1}^{\mathbf{q}, B} e^{-i(\phi_g/3+\pi/2)} + c_{u-\mathbf{b}_1}^{\mathbf{q}, B} e^{i(\phi_g/3+\pi/2)} \right) \right) \right. \\
&\quad + \left( \sum_u c_u^{*\mathbf{q}, B'} \left( c_{u+\mathbf{b}_2}^{\mathbf{q}, B} e^{-i(\phi_g/3+\pi/2)} + c_{u-\mathbf{b}_2}^{\mathbf{q}, B} e^{i(\phi_g/3+\pi/2)} \right) \right) \\
&\quad \left. + \left( \sum_u c_u^{*\mathbf{q}, B'} \left( c_{u+\mathbf{b}_3}^{\mathbf{q}, B} e^{-i(\phi_g/3+\pi/2)} + c_{u-\mathbf{b}_3}^{\mathbf{q}, B} e^{i(\phi_g/3+\pi/2)} \right) \right) \right|^2. \tag{C.9}
\end{aligned}$$

Last, the excitation rates for circular lattice shaking are determined. The modulation in this case is done by periodically modulating the frequencies of two of the three lattice beams with amplitude  $\Delta\nu$ :

$$\begin{aligned}
\delta\nu_1(t) &= 0 \\
\delta\nu_2(t) &= 2\Delta\nu \left( \cos(\omega t) + \sqrt{3} \sin(\omega t) \right) \\
\delta\nu_3(t) &= 2\Delta\nu \left( -\cos(\omega t) + \sqrt{3} \sin(\omega t) \right).
\end{aligned} \tag{C.10}$$

This can be equivalently stated as detunings of the sideband frequencies and thus as the detunings of the individual 1D lattices making up our lattice. The corresponding detunings of the sideband frequencies  $\nu_{\alpha,\beta,\gamma}$  are

$$\begin{aligned}
\delta\nu_\alpha(t) &= \delta\nu_1 - \delta\nu_2 = -2\Delta\nu \left( \cos(\omega t) + \sqrt{3} \sin(\omega t) \right), \\
\delta\nu_\beta(t) &= \delta\nu_2 - \delta\nu_3 = 4\Delta\nu \cos(\omega t), \\
\delta\nu_\gamma(t) &= \delta\nu_3 - \delta\nu_1 = -2\Delta\nu \left( \cos(\omega t) - \sqrt{3} \sin(\omega t) \right).
\end{aligned} \tag{C.11}$$

The detunings to all times add up to zero,  $\sum_i \delta\nu_i = 0$ , showing that indeed only the position of the lattice changes, while its geometry stays constant. The detunings are connected to the 1D lattice phases via their time derivatives,  $\dot{\phi} = 2\pi\delta\nu_i$ , which leads to

$$\begin{aligned}
\phi_\alpha &= A_{\text{cs}} \left( \sin(\omega t) - \sqrt{3} \cos(\omega t) \right), \\
\phi_\beta &= 2A_{\text{cs}} \sin(\omega t), \\
\phi_\gamma &= A_{\text{cs}} \left( \sin(\omega t) + \sqrt{3} \cos(\omega t) \right),
\end{aligned} \tag{C.12}$$

with modulation amplitude  $A_{\text{cs}} = 4\pi\Delta\nu/\omega$ . These phases are added to the lattice potential in order to get the time-dependent potential for circular shaking:

$$\begin{aligned}
V_{\text{cs}}(\mathbf{r}, \phi_g, t) &= 2V \left( \cos\left(\mathbf{b}_1 \cdot \mathbf{r} + \frac{\phi_g}{3} - A_{\text{cs}}\left(\sin(\omega t) - \sqrt{3}\cos(\omega t)\right)\right) \right. \\
&\quad + \cos\left(\mathbf{b}_2 \cdot \mathbf{r} + \frac{\phi_g}{3} + 2A_{\text{cs}}\sin(\omega t)\right) \\
&\quad \left. + \cos\left(\mathbf{b}_3 \cdot \mathbf{r} + \frac{\phi_g}{3} - A_{\text{cs}}\left(\sin(\omega t) + \sqrt{3}\cos(\omega t)\right)\right) \right) \\
&\approx 2V \left( \cos\left(\mathbf{b}_1 \cdot \mathbf{r} + \frac{\phi_g}{3}\right) + \cos\left(\mathbf{b}_1 \cdot \mathbf{r} + \frac{\phi_g}{3} - \frac{\pi}{2}\right) A_{\text{cs}}\left(\sin(\omega t) - \sqrt{3}\cos(\omega t)\right) \right. \\
&\quad + \cos\left(\mathbf{b}_2 \cdot \mathbf{r} + \frac{\phi_g}{3}\right) + \cos\left(\mathbf{b}_2 \cdot \mathbf{r} + \frac{\phi_g}{3} + \frac{\pi}{2}\right) 2A_{\text{cs}}\sin(\omega t) \\
&\quad \left. + \cos\left(\mathbf{b}_3 \cdot \mathbf{r} + \frac{\phi_g}{3}\right) + \cos\left(\mathbf{b}_3 \cdot \mathbf{r} + \frac{\phi_g}{3} - \frac{\pi}{2}\right) A_{\text{cs}}\left(\sin(\omega t) + \sqrt{3}\cos(\omega t)\right) \right) \\
&= V_{\text{cs}}(\mathbf{r}, \phi_g) + \epsilon_{\text{cs}} 2V \left( \frac{1}{2} \cos\left(\chi_1 - \frac{\pi}{2}\right) \left(\sin(\omega t) - \sqrt{3}\cos(\omega t)\right) \right. \\
&\quad \left. + \cos\left(\chi_2 + \frac{\pi}{2}\right) \sin(\omega t) + \frac{1}{2} \cos\left(\chi_3 - \frac{\pi}{2}\right) \left(\sin(\omega t) + \sqrt{3}\cos(\omega t)\right) \right). \tag{C.13}
\end{aligned}$$

The corresponding modulation strength in this case is given by  $\epsilon_{\text{cs}} = 2A_{\text{cs}}$  and in the last expression  $\chi_i = \mathbf{b}_i \cdot \mathbf{r} + \phi_g/3$  is used. The approximation again results from limiting the sine and cosine functions with  $\sin(\omega t)$  in the argument to the 1st order. Finally, the modulated part of  $V_{\text{cs}}(\mathbf{r}, \phi_g, t)$  is plugged into Eq. C.4, yielding

$$\begin{aligned}
\Gamma_{B,B'}^{\mathbf{q}\mathbf{q}'} &\propto \delta_{\mathbf{q},\mathbf{q}'} \epsilon_{\text{sm}}^2 V^2 \left| \left( \frac{1}{2} + \frac{i\sqrt{3}}{2} \right) \left( \sum_u c_u^{*\mathbf{q},B'} \left( c_{u+\mathbf{b}_1}^{\mathbf{q},B} e^{-i(\phi_g/3-\pi/2)} + c_{u-\mathbf{b}_1}^{\mathbf{q},B} e^{i(\phi_g/3-\pi/2)} \right) \right) \right. \\
&\quad + \left( \sum_u c_u^{*\mathbf{q},B'} \left( c_{u+\mathbf{b}_2}^{\mathbf{q},B} e^{-i(\phi_g/3+\pi/2)} + c_{u-\mathbf{b}_2}^{\mathbf{q},B} e^{i(\phi_g/3+\pi/2)} \right) \right) \\
&\quad \left. + \left( \frac{1}{2} - \frac{i\sqrt{3}}{2} \right) \left( \sum_u c_u^{*\mathbf{q},B'} \left( c_{u+\mathbf{b}_3}^{\mathbf{q},B} e^{-i(\phi_g/3-\pi/2)} + c_{u-\mathbf{b}_3}^{\mathbf{q},B} e^{i(\phi_g/3-\pi/2)} \right) \right) \right|^2. \tag{C.14}
\end{aligned}$$



## Appendix D.

# Dynamic Increase of the Tilt Strength in the Triangular Lattice

In this section, I present an overview of different transport effects measured in the triangular lattice geometry with a dynamically increasing tilt strength. Contrary to the approach in chapter 5 where the tilt was initialized by suddenly quenching the external magnetic confinement, resulting in an immediate constant driving force applied to the atoms, here the lattice beams are detuned with respect to each other leading to a constant movement of the optical lattice upward the magnetic potential slope. For a sufficient lattice depth the atoms are dragged along, which in turn dynamically increases the tilt strength experienced by them.

As exemplified in Fig. 5.11 this can result in very strong accumulations of the atoms at the energetically lower side of the system. In the correct parameter regime, the relatively slow movement of the lattice upward the slope allows for most of the atoms to tunnel downwards the slope, minimizing their increase in potential energy. Tunneling downwards outside of the populated region however is suppressed due to the large change in interaction energy. This nonlinear self-trapping [139, 162] restricts the movement of the atoms along the tilt direction, leading to accumulations of a large fraction of the atoms on very few lattice sites at the edge of the initial system. For these measurements we used a lattice depth of  $V \approx 1.5 E_{\text{rec}}$ , corresponding to a tunnel coupling of  $J \approx 3 \text{ Hz}$ , and varied the shift velocity and duration of the optical lattice as well as the subsequent hold time at the slope after the detuning is turned off. To give a more conclusive picture of the density evolution in this system Fig. D.1, D.2 and D.3 each show a series of increasing shift velocities. Going to the higher velocities depicted here, we find a fascinating phenomenon of atoms tunneling to lattice sites beyond the self-trapping bulges. Initially this happens only from the center and then the feature extends to the sides, i.e. along equipotential lines, as visible when comparing single images from Fig. D.1 and D.2 which only differ in the hold time after the detuning of 10 and 60 ms. Furthermore, the images feature density modulations within the atomic cloud, possibly pointing towards standing waves building up in the system due to reflections at the edges. More work is needed here to identify the underlying processes leading to this tunneling across the self-trapping bulge and the density-waves. It should be noted that in these measurements the atomic cloud was

not shift back to the center of the magnetic trap for the matter wave optics. This here results in distortions of the real space distribution most likely due to the Talbot effect (see [58, 63] for more details). Specifically, for most of the final positions imaged in these measurements, we see the inverse lattice structure, probably arising from an inverse Talbot revival due to anharmonic aberrations slightly changing the necessary time for sharp imaging. With the distortions, the atomic signal is found on the edges of hexagons. For the read-out of the overall atomic distribution, this is no problem, since the signal coming from a certain lattice site is still reliably found within one lattice site. However, its shape gets strongly deformed which for example leads to the single lattice sites in the lines beyond the self-trapping edge featuring two local maxima despite each only arising from single sites as evidenced by the corresponding lattice constant known from the matter wave protocol, which is illustrated in Fig. D.4.

Using very slow shift velocities the emerging edge gets increasingly wider and starts to encircle the trap center, forming ring structures along equipotential lines as dis-

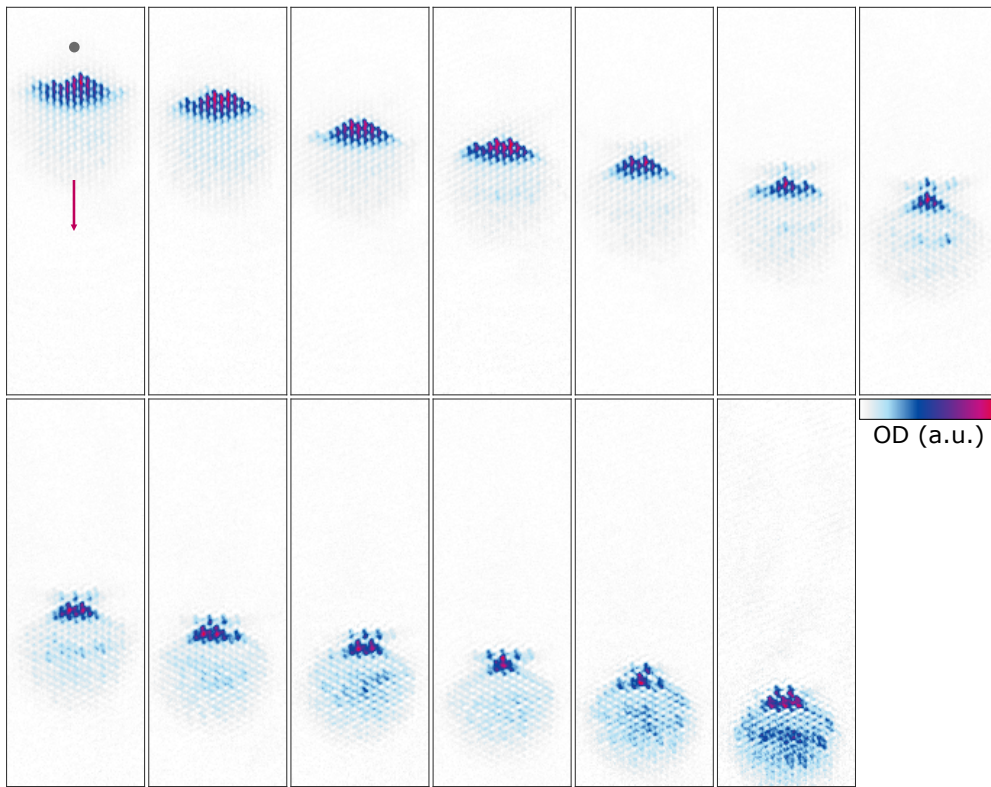


**Figure D.1.: Density in a shifted triangular lattice.** The lattice beam detuning is varied in 50 Hz steps from 250 to 850 Hz with constant detuning times of 50 ms resulting in shift distances between  $12.5$  and  $42.5 a_{\text{lat}}$ . Afterwards the atoms are held at the external trap slope for 10 ms. The lattice depth is  $V \approx 1.5 E_{\text{rec}}$ . In the first panel the trap center is marked by a gray dot and the movement direction specified by an arrow

cussed in section 5.3. This effect is strongest close to the trap center and for long hold times in the system, shown in Fig. D.5. By comparing the density distribution 120 ms after the shift up the slope (D.5a) with the situation after 500 ms (D.5b) we further see a pour out of the atoms from behind the self-trapping edge to the trap center, completely erasing the edge and resulting in a symmetric population around the trap center. The more atoms surpass the barrier the smaller the barrier becomes, speeding up the process, which leads to a depletion of the self-trapping bulge. Additionally, for very slow lattice velocities combined with short hold times following the shift, as depicted in Fig. D.6, we again do not reliably observe self-trapping. Actually, the different realizations of the same experimental parameters plotted within the columns of Fig. D.6 show distinctly different behavior. Sometimes we find a sharp self-trapping edge and in other shots the atoms are situated in the trap center. Considering the much shorter final hold times than in D.5, the atoms in the latter case probably did not form a self-trapping edge during the dynamics. This might point towards a regime below some critical velocity, underneath which the atoms have enough time to simply follow the changing position of the trap center. The effect might be connected

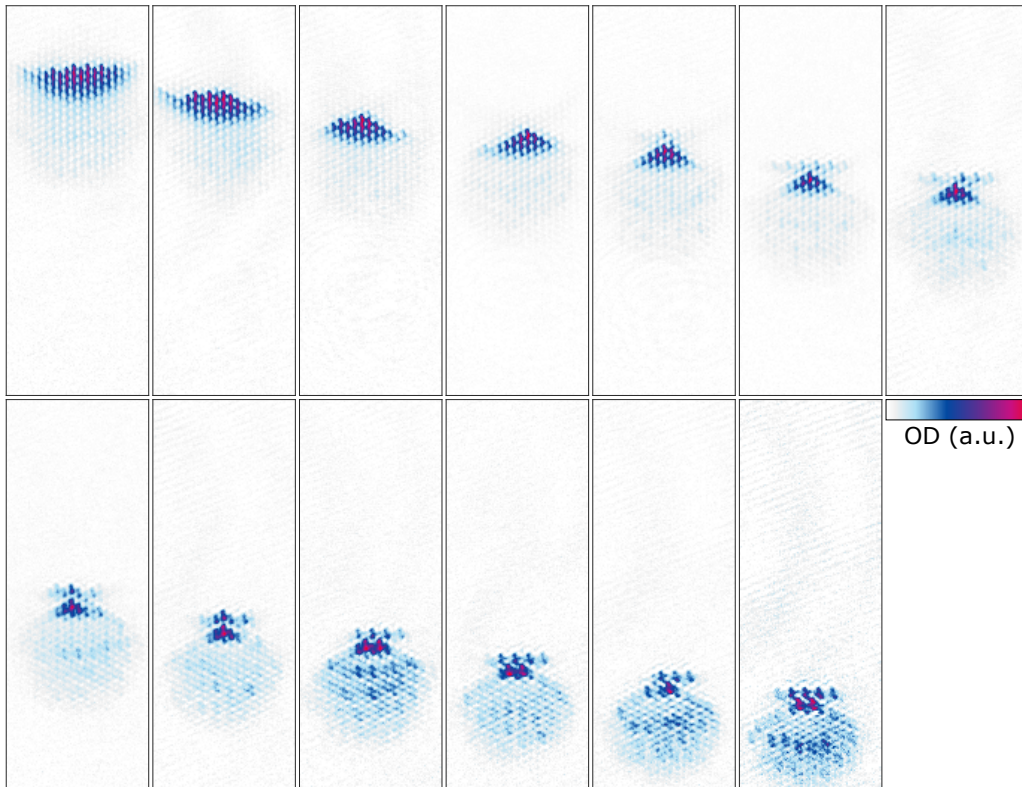


**Figure D.2.: Density in a shifted triangular lattice.** The lattice beam detuning is varied in 50 Hz steps from 250 to 850 Hz with constant detuning times of 50 ms resulting in shift distances between  $12.5$  and  $42.5 a_{\text{lat}}$ . Afterwards the atoms are held at the external trap slope for 60 ms. The lattice depth is  $V \approx 1.5 E_{\text{rec}}$ .

to the critical velocity observed in [146] by displacing a 1D chain of BECs from the trap center, which separates a superfluid and an incoherent regime. For more conclusive results it would be helpful to continue the measurements for even slower shift velocities than so far. Similarly, the seemingly broken determinism in the resulting distribution that might suggest a fluctuation dependent buildup of the self-trapping edge should be studied more in detail.

In total we find a rich behavior of the density distribution when dragged upward the external potential slope, which would be very interesting to investigate more in

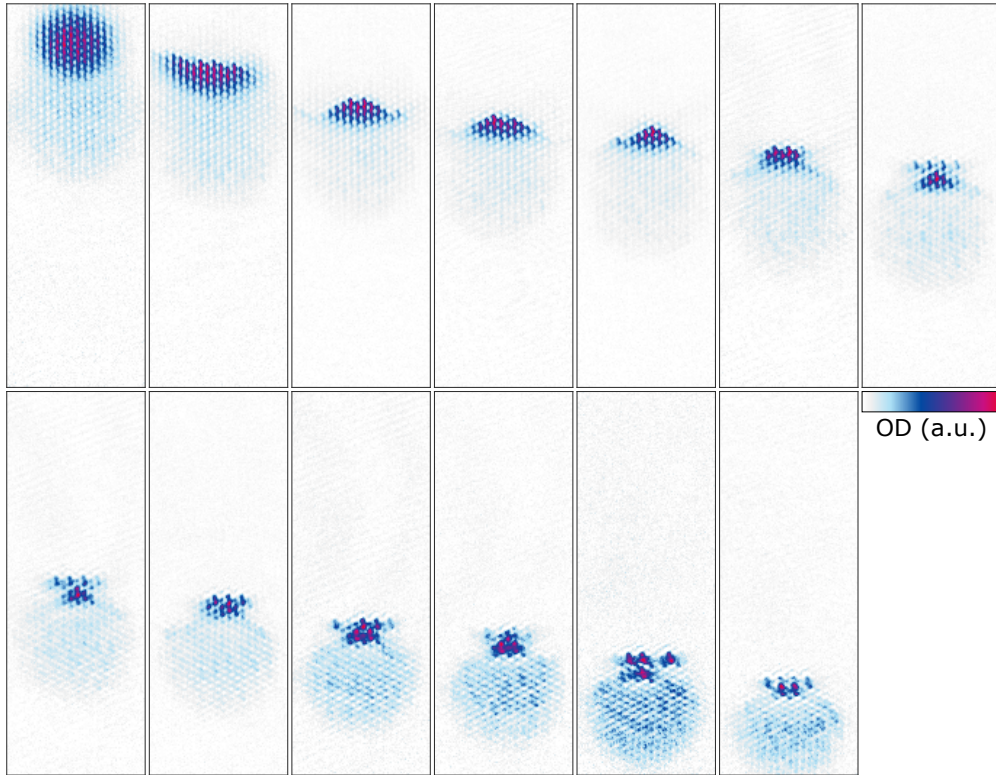


**Figure D.3.: Density in a shifted triangular lattice.** The lattice beam detuning is varied in 33 Hz steps from 167 to 567 Hz with constant detuning times of 75 ms resulting in shift distances between  $12.5$  and  $42.5 a_{\text{lat}}$ . Afterwards the atoms are held at the external trap slope for 120 ms. The lattice depth is  $V \approx 1.5 E_{\text{rec}}$ .

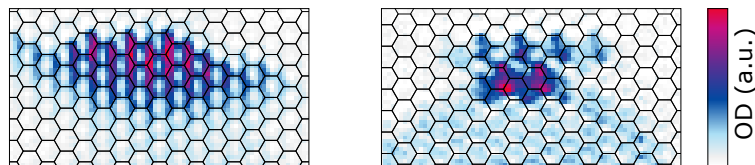


**Figure D.4.: Visualization of the imaging aberration.** Two exemplary images are overlapped with grids of Wigner-Seitz cells, positioned to illustrate the deformations. The signal from the triangular lattice is found on edges of hexagons.

depth in the future. The same protocol could then also be applied to honeycomb and boron nitride optical lattices.

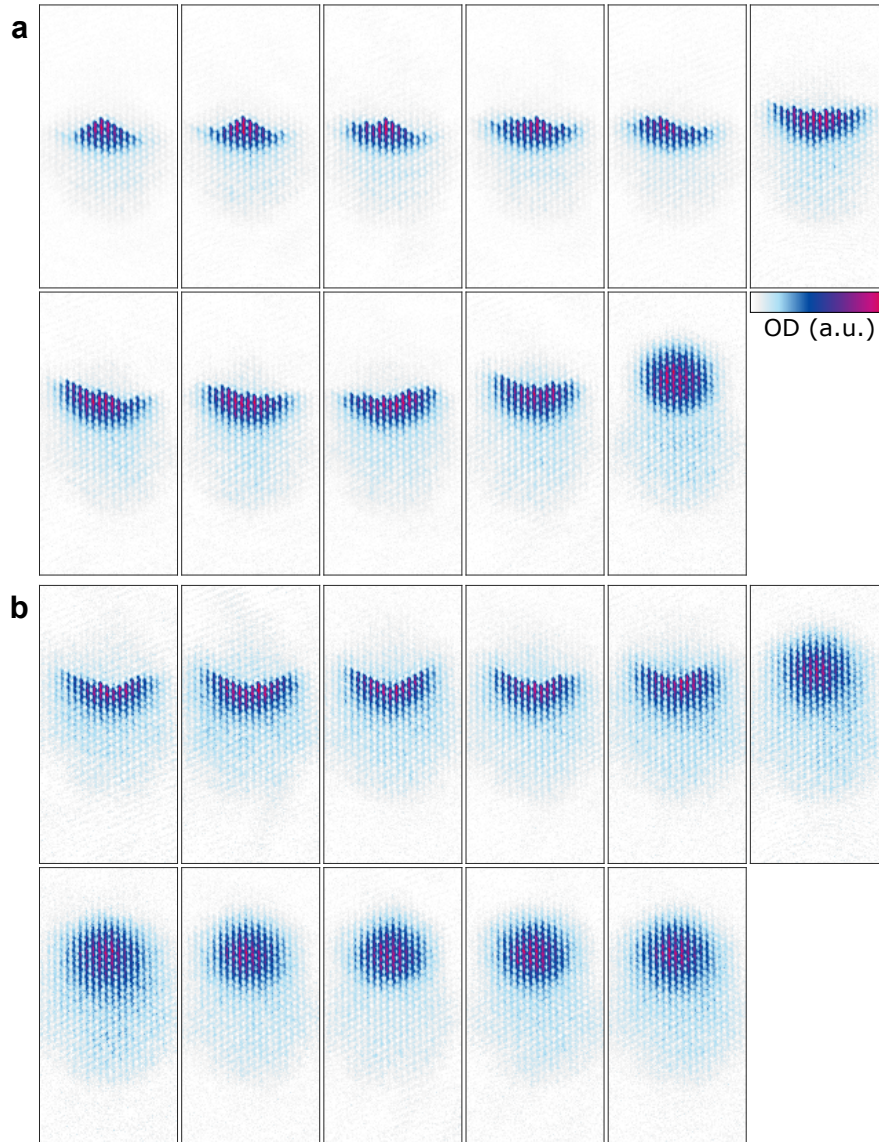


**Figure D.5.: Density in the shifted triangular lattice as function of the shift velocity.** The triangular lattice of depth  $V \approx 1.5 E_{\text{rec}}$  is shifted by  $12.5 a_{\text{lat}}$ . In both subfigures the shift duration is varied from top left to bottom right from 25 to 75 ms in 5 ms steps. Subsequently the atoms are held at the slope for 120 ms (**a**) and 500 ms (**b**).

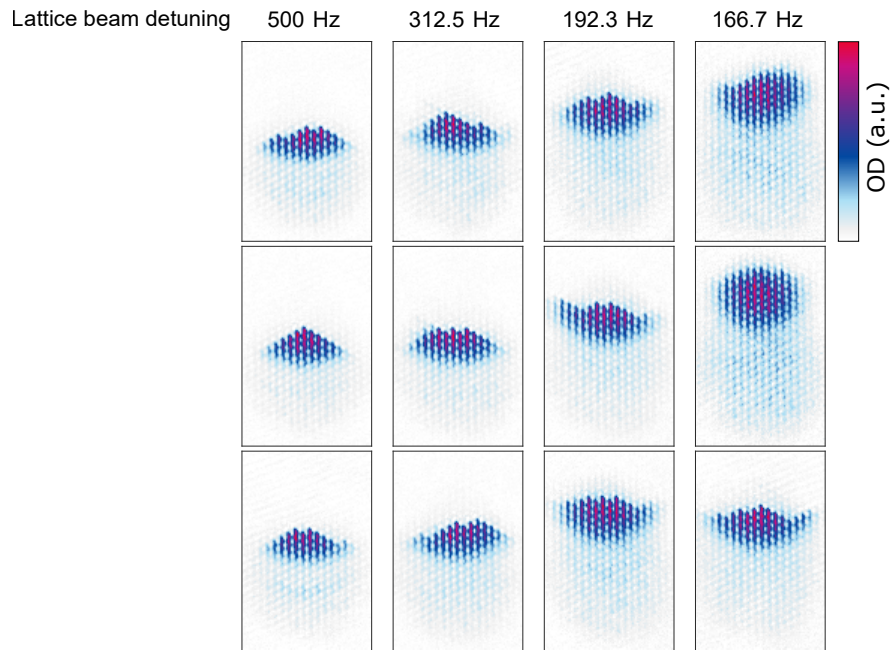


**Figure D.6.:** Density in the shifted triangular lattice as function of the **shift velocity**. The triangular lattice of depth  $V \approx 1.5 E_{\text{rec}}$  is shifted by  $12.5 a_{\text{lat}}$ . The shift duration is increased from left to right, using 25, 40, 65 and 75 ms. Within every column repetitions of the same experimental parameters are shown. Following the shift upwards the atoms are held for 10 ms at the slope.

## Appendix E.

### Transport in the Honeycomb Lattice

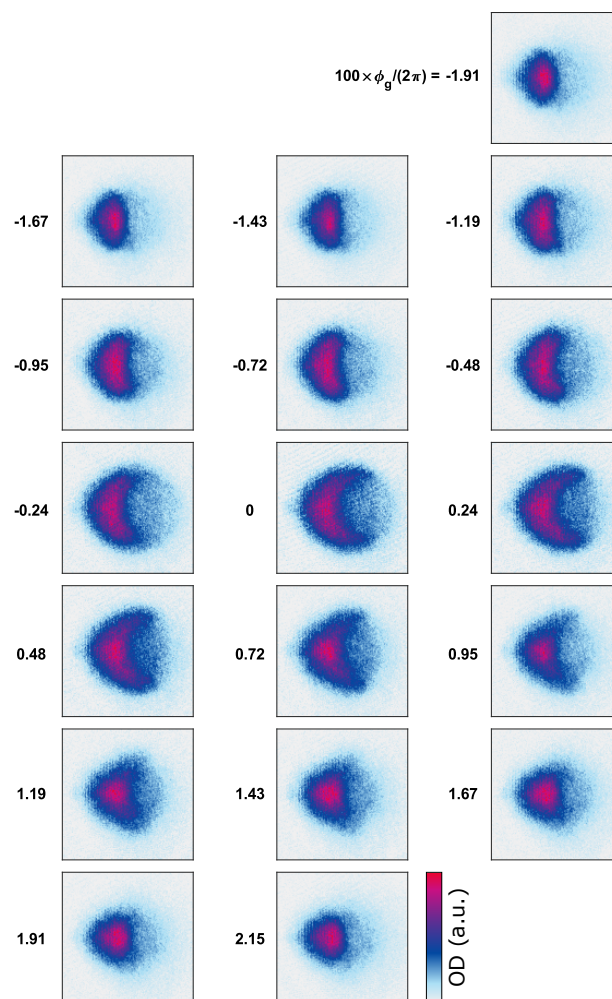


**Figure E.1.: Varying the geometry phase.** The images show the density distribution 50 ms after shifting the atoms  $12 \mu\text{m}$  from the trap center using a lattice depth of  $V = 2.5 E_{\text{rec}}$ . From these images the relative population in the ring segments in Fig. 5.13 is read out.

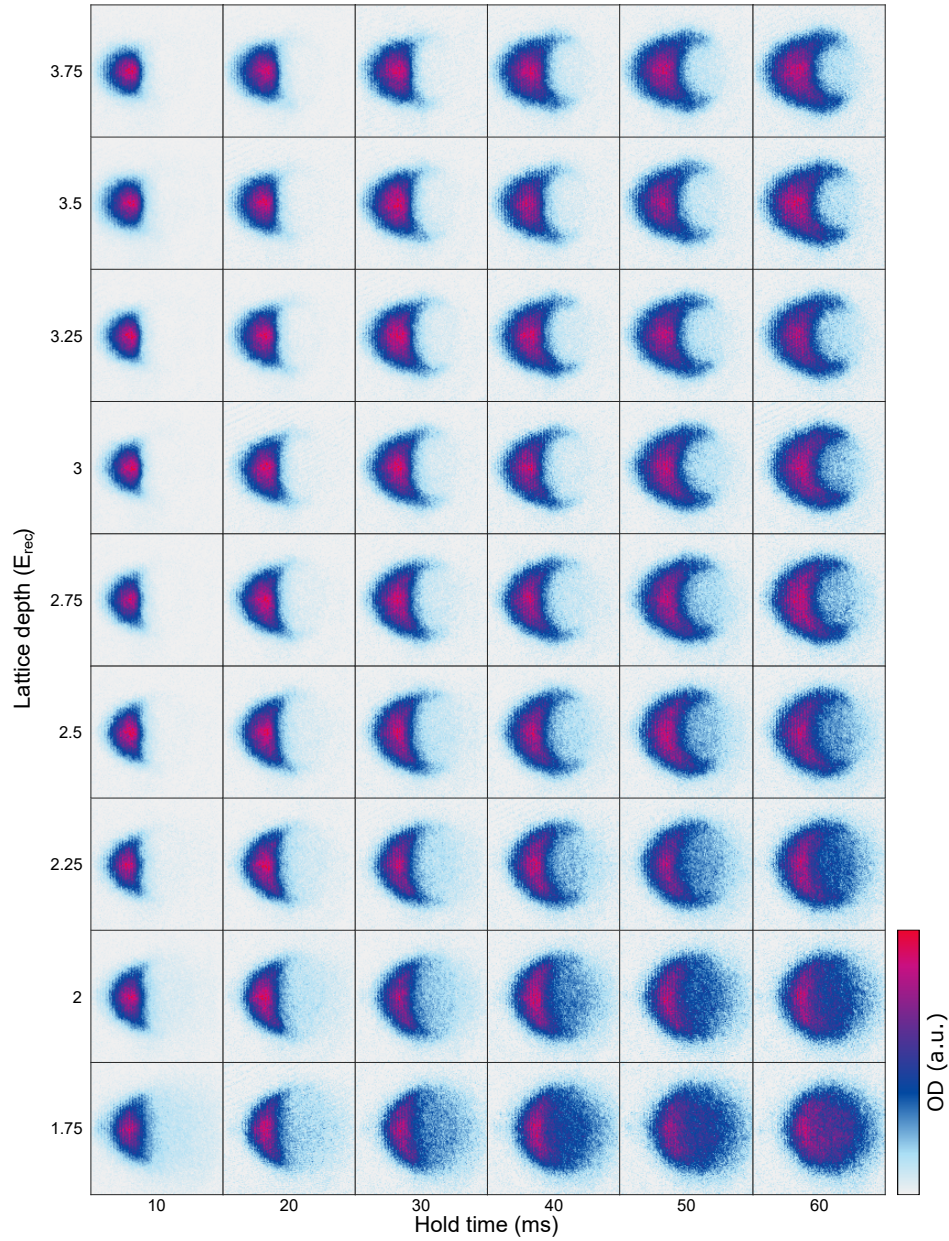


**Figure E.2.: Following the transport dynamics in the honeycomb lattice.**

The images show the density distribution for different lattice depths and hold times after shifting the atoms  $12 \mu\text{m}$  from the trap center. From these images the relative population in the ring segments in Fig. 5.12b is read out.

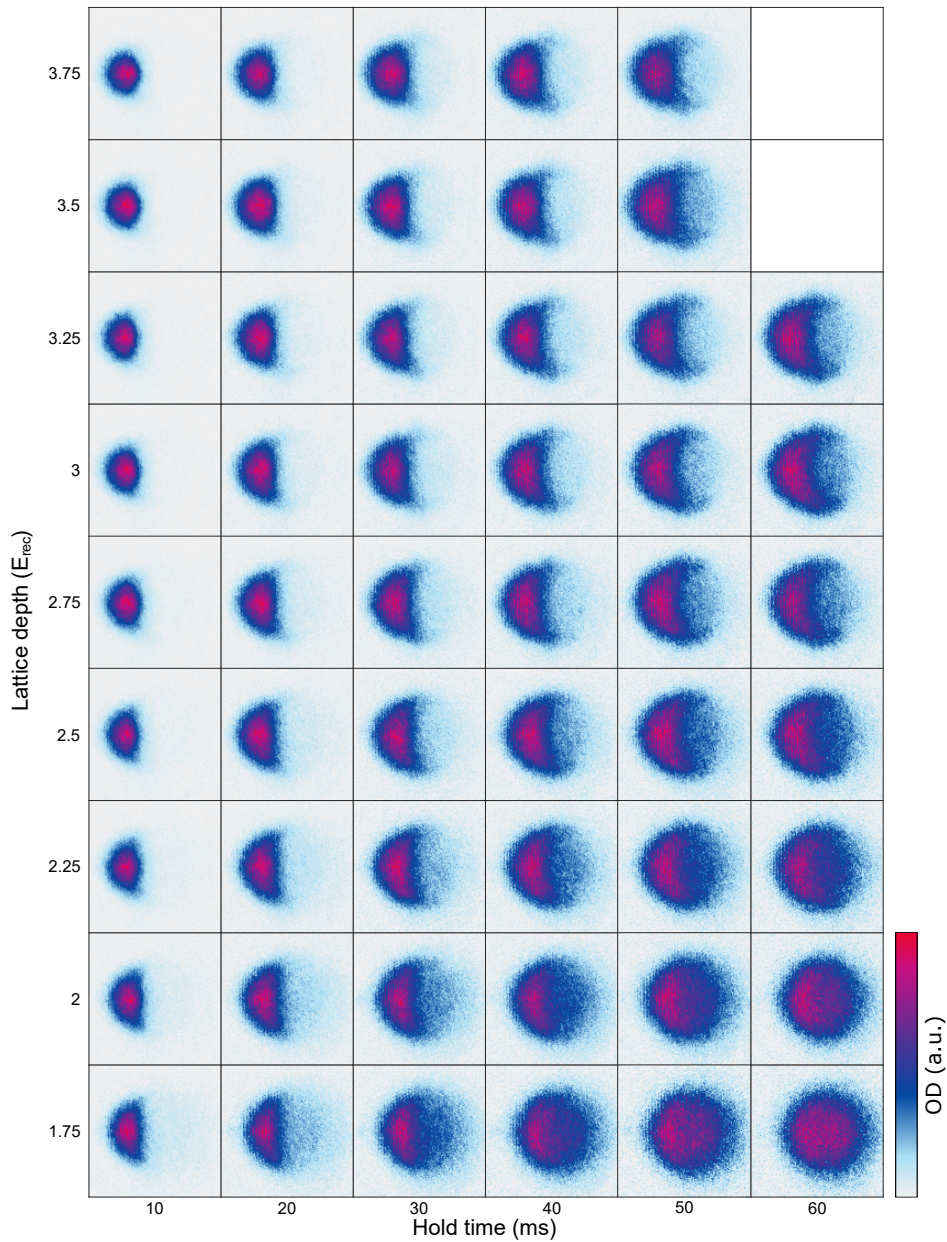


**Figure E.3.: Following the transport dynamics in 2D honeycomb lattice planes.** The images show the density distribution for different 2D lattice depths and hold times after shifting the atoms  $12\ \mu\text{m}$  from the trap center. Perpendicular to the 2D lattice a 1D lattice from retroreflection with  $\lambda = 826\ \text{nm}$  and  $V = 6.8 E_{\text{rec}}$  is added. From these images the relative population in the ring segments in Fig. 5.12c is read out.



---

## Bibliography

- [1] R. P. Feynman: “Simulating physics with computers”, *International Journal of Theoretical Physics* **21** (6-7), 467–488 (1982). 1
- [2] I. Bloch, J. Dalibard and S. Nascimbène: “Quantum simulations with ultracold quantum gases”, *Nature Physics* **8** (4), 267–276 (2012). 1
- [3] M. H. Anderson, J. R. Ensher, M. R. Matthews, C. E. Wieman and E. A. Cornell: “Observation of Bose-Einstein Condensation in a Dilute Atomic Vapor”, *Science* **269** (5221), 198–201 (1995). 1
- [4] C. C. Bradley, C. A. Sackett, J. J. Tollett and R. G. Hulet: “Evidence of Bose-Einstein Condensation in an Atomic Gas with Attractive Interactions”, *Phys. Rev. Lett.* **75**, 1687–1690 (1995).
- [5] K. B. Davis, M. O. Mewes, M. R. Andrews, N. J. Van Druten, D. S. Durfee, D. M. Kurn and W. Ketterle: “Bose-Einstein condensation in a gas of sodium atoms”, *Physical Review Letters* **75** (22), 3969–3973 (1995). 1
- [6] B. DeMarco and D. S. Jin: “Onset of Fermi degeneracy in a trapped atomic gas”, *Science* **285** (5434), 1703–1706 (1999). 1
- [7] I. Bloch, J. Dalibard and W. Zwerger: “Many-body physics with ultracold gases”, *Rev. Mod. Phys.* **80**, 885–964 (2008). 1
- [8] P. Törmä and K. Sengstock: *Quantum Gas Experiments*, Imperial College Press (2014).
- [9] C. Gross and I. Bloch: “Quantum simulations with ultracold atoms in optical lattices”, *Science* **357** (6355), 995–1001 (2017). 1
- [10] I. Bloch: “Ultracold quantum gases in optical lattices”, *Nature Physics* **1** (1), 23–30 (2005). 1
- [11] M. Lewenstein, A. Sanpera, V. Ahufinger, B. Damski, A. Sen(De) and U. Sen: “Ultracold atomic gases in optical lattices: mimicking condensed matter physics and beyond”, *Advances in Physics* **56** (2), 243–379 (2007). 1, 43
- [12] J. Hubbard: “Electron correlations in narrow energy bands”, *Proc. R. Soc. Lond. A* **276**, 238–257 (1963). 1

- 
- [13] D. Jaksch, C. Bruder, J. I. Cirac, C. W. Gardiner and P. Zoller: “Cold Bosonic Atoms in Optical Lattices”, *Phys. Rev. Lett.* **81**, 3108–3111 (1998). 1
- [14] C. Chin, R. Grimm, P. Julienne and E. Tiesinga: “Feshbach resonances in ultracold gases”, *Rev. Mod. Phys.* **82**, 1225–1286 (2010). 1
- [15] J. F. Sherson, C. Weitenberg, M. Endres, M. Cheneau, I. Bloch and S. Kuhr: “Single-atom-resolved fluorescence imaging of an atomic Mott insulator”, *Nature* **467** (7311), 68–72 (2010). 2, 13
- [16] W. S. Bakr, A. Peng, M. E. Tai, R. Ma, J. Simon, J. I. Gillen, S. Fölling, L. Pollet and M. Greiner: “Probing the Superfluid-to-Mott Insulator Transition at the Single-Atom Level”, *Science* **329** (5991), 547–550 (2010). 2, 13
- [17] L. Asteria, H. P. Zahn, M. N. Kosch, K. Sengstock and C. Weitenberg: “Quantum gas magnifier for sub-lattice-resolved imaging of 3D quantum systems”, *Nature* **599** (7886), 571–575 (2021). 2, 3, 13, 19, 29, 30, 31, 33, 34, 36, 39
- [18] D. McKay, M. White and B. DeMarco: “Lattice thermodynamics for ultracold atoms”, *Physical Review A* **79** (6), 063605 (2009). 2
- [19] S. Trotzky, L. Pollet, F. Gerbier, U. Schnorrberger, I. Bloch, N. V. Prokof’ev, B. Svistunov and M. Troyer: “Suppression of the critical temperature for superfluidity near the Mott transition”, *Nature Physics* **6** (12), 998–1004 (2010).
- [20] H. Cayla, C. Carcy, Q. Bouton, R. Chang, G. Carleo, M. Mancini and D. Clément: “Single-atom-resolved probing of lattice gases in momentum space”, *Physical Review A* **97** (6), 061609 (2018). 2
- [21] M. McDonald, J. Trisnadi, K. X. Yao and C. Chin: “Superresolution Microscopy of Cold Atoms in an Optical Lattice”, *Physical Review X* **9** (2), 021001 (2019). 2, 13
- [22] S. Subhankar, Y. Wang, T. C. Tsui, S. L. Rolston and J. V. Porto: “Nanoscale Atomic Density Microscopy”, *Physical Review X* **9** (2), 021002 (2019). 2, 13
- [23] H. Ott, E. de Mirandes, F. Ferlaino, G. Roati, G. Modugno and M. Inguscio: “Collisionally Induced Transport in Periodic Potentials”, *Phys. Rev. Lett.* **92**, 160601 (2004). 2
- [24] N. Strohmaier, Y. Takasu, K. Günter, R. Jördens, M. Köhl, H. Moritz and T. Esslinger: “Interaction-Controlled Transport of an Ultracold Fermi Gas”, *Phys. Rev. Lett.* **99**, 220601 (2007).
- [25] U. Schneider, L. Hackermüller, J. P. Ronzheimer, S. Will, T. Braun, Simon Best, I. Bloch, E. Demler, S. Mandt, D. Rasch and A. Rosch: “Fermionic transport and out-of-equilibrium dynamics in a homogeneous Hubbard model with ultracold atoms”, *Nature Physics* **8**, 213–218 (2012). 2

- [26] H. P. Zahn, V. P. Singh, M. N. Kosch, L. Asteria, L. Freystatzky, K. Sengstock, L. Mathey and C. Weitenberg: “Formation of Spontaneous Density-Wave Patterns in dc Driven Lattices”, *Physical Review X* **12** (2), 021014 (2022). 2, 3, 94, 96, 97, 98, 100, 101, 103, 104, 105, 106, 107, 109
- [27] M. C. Cross and P. C. Hohenberg: “Pattern formation outside of equilibrium”, *Reviews of Modern Physics* **65** (3), 851–1112 (1993). 2
- [28] M. Anderlini, P. J. Lee, B. L. Brown, J. Sebby-Strabley, W. D. Phillips and J. V. Porto: “Controlled exchange interaction between pairs of neutral atoms in an optical lattice”, *Nature* **448** (7152), 452–456 (2007). 2
- [29] S. Trotzky, P. Cheinet, S. Fölling, M. Feld, U. Schnorrberger, A. M. Rey, A. Polkovnikov, E. A. Demler, M. D. Lukin and I. Bloch: “Time-resolved observation and control of superexchange interactions with ultracold atoms in optical lattices”, *Science* **319** (5861), 295–299 (2008). 2
- [30] C. Becker, P. Soltan-Panahi, J. Kronjäger, S. Dörscher, K. Bongs and K. Sengstock: “Ultracold quantum gases in triangular optical lattices”, *New Journal of Physics* **12** (6), 065025 (2010). 2, 43
- [31] L. Tarruell, D. Greif, T. Uehlinger, G. Jotzu and T. Esslinger: “Creating, moving and merging Dirac points with a Fermi gas in a tunable honeycomb lattice”, *Nature* **483** (7389), 302–305 (2012). 43, 78, 113, 114
- [32] N. Fläschner, B. S. Rem, M. Tarnowski, D. Vogel, D.-S. Lühmann, K. Sengstock and C. Weitenberg: “Experimental reconstruction of the Berry curvature in a Floquet Bloch band”, *Science* **352**, 1091–1094 (2016). 2, 43, 74, 75, 77, 78, 79, 88
- [33] S. Taie, H. Ozawa, T. Ichinose, T. Nishio, S. Nakajima and Y. Takahashi: “Coherent driving and freezing of bosonic matter wave in an optical Lieb lattice”, *Science Advances* **1** (10), e1500854 (2015). 2
- [34] G.-B. Jo, J. Guzman, C. K. Thomas, P. Hosur, A. Vishwanath and D. M. Stamper-Kurn: “Ultracold Atoms in a Tunable Optical Kagome Lattice”, *Phys. Rev. Lett.* **108**, 045305 (2012). 2
- [35] K. Viebahn, M. Sbroscia, E. Carter, J.-C. Yu and U. Schneider: “Matter-Wave Diffraction from a Quasicrystalline Optical Lattice”, *Phys. Rev. Lett.* **122**, 110404 (2019). 2, 83
- [36] M. N. Kosch, L. Asteria, H. P. Zahn, K. Sengstock and C. Weitenberg: “Multi-frequency optical lattice for dynamic lattice-geometry control”, *Phys. Rev. Res.* **4**, 043083 (2022). 2, 3, 9, 43, 44, 48, 52, 55, 56, 57, 59, 61, 62, 64, 66, 72, 73, 84, 85, 87, 115, 116, 117, 120, 123

- 
- [37] P. Hauke, M. Lewenstein and A. Eckardt: “Tomography of band insulators from quench dynamics”, *Phys. Rev. Lett.* **113**, 045303 (2014). 2, 74, 77, 88
- [38] S. Ospelkaus-Schwarzer: “Quantum Degenerate Fermi-Bose Mixtures of  $^{40}\text{K}$  and  $^{87}\text{Rb}$  in 3D Optical Lattices”, Ph.D. thesis, Universität Hamburg (2006). 5
- [39] C. Ospelkaus: “Fermi-Bose mixtures – From mean-field interactions to ultracold chemistry”, Ph.D. thesis, Universität Hamburg (2006). 5, 6, 93
- [40] E. L. Raab, M. Prentiss, A. Cable, S. Chu and D. E. Pritchard: “Trapping of Neutral Sodium Atoms with Radiation Pressure”, *Phys. Rev. Lett.* **59** (23), 2631–2634 (1987). 5
- [41] J. Dalibard and C. Cohen-Tannoudji: “Laser cooling below the Doppler limit by polarization gradients: simple theoretical models”, *J. Opt. Soc. Am. B* **6** (11), 2023–2045 (1989). 5
- [42] W. Ketterle and N. J. van Druten: “Evaporative cooling of trapped atoms”, *Advances in Atomic, Molecular, and Optical Physics* **37** (23), 181–236 (1996). 5
- [43] M. Kottke: “Magnetfallen und Signaturen der Eindimensionalität für Bose-Einstein-Kondensate”, Ph.D. thesis, Universität Hannover (2004). 6
- [44] R. Dinter: “Aufbau und Charakterisierung einer Magnetfalle zur simultanen Speicherung von K und Rb”, Diplomarbeit, Universität Hamburg (2004). 6, 7, 93
- [45] M. Erhard: “Experimente mit mehrkomponentigen Bose-Einstein-Kondensaten”, Ph.D. thesis, Universität Hamburg (2004). 6
- [46] R. Grimm, M. Weidemüller and Y. B. Ovchinnikov: “Optical Dipole Traps for Neutral Atoms”, *Advances In Atomic, Molecular, and Optical Physics* **42**, 95–170 (2000). 8, 89
- [47] O. Morsch and M. Oberthaler: “Dynamics of Bose-Einstein condensates in optical lattices”, *Rev. Mod. Phys.* **78**, 179–215 (2006). 8, 91
- [48] M. Langbecker: “Tunable Interactions and Lattice Geometries in Fermionic Quantum Gases”, Masterarbeit, Universität Hamburg (2013). 8
- [49] N. Fläschner: “Ultracold Fermions in Tunable Hexagonal Lattices: From High-Precision Spectroscopy to the Measurement of Berry Curvature”, Ph.D. thesis, Universität Hamburg (2016). 8, 9, 11, 49, 74
- [50] H. Zahn: “Observation of spontaneous density-wave patterns using a quantum gas magnifier”, Ph.D. thesis, University of Hamburg (2022). 10, 29, 31, 41, 94, 97

- [51] W. Ketterle, D. S. Durfee and D. M. Stamper-Kurn: “Making, probing and understanding Bose-Einstein condensates”, arXiv e-prints cond-mat/9904034 (1999). 10
- [52] F. Bloch: “Über die Quantenmechanik der Elektronen in Kristallgittern”, *Zeitschrift für Physik* **52** (7-8), 555–600 (1929). 11
- [53] D. Vogel: “Measuring Geometry and Topology of Floquet-Bloch States in and out of Equilibrium with ultracold fermions”, Ph.D. thesis, Universität Hamburg (2018). 11, 52, 74
- [54] M. Endres, M. Cheneau, T. Fukuhara, C. Weitenberg, P. Schauß, C. Gross, L. Mazza, M. C. Bañuls, L. Pollet, I. Bloch and S. Kuhr: “Observation of correlated particle-hole pairs and string order in low-dimensional mott insulators”, *Science* **334** (6053), 200–203 (2011). 13
- [55] A. Mazurenko, C. S. Chiu, G. Ji, M. F. Parsons, M. Kanász-Nagy, R. Schmidt, F. Grusdt, E. Demler, D. Greif and M. Greiner: “A cold-atom Fermi-Hubbard antiferromagnet”, *Nature* **545** (7655), 462–466 (2017). 13
- [56] T. Gericke, P. Würtz, D. Reitz, T. Langen and H. Ott: “High-resolution scanning electron microscopy of an ultracold quantum gas”, *Nature Physics* **4** (12), 949–953 (2008). 13
- [57] C. Veit, N. Zuber, O. A. Herrera-Sancho, V. S. Anasuri, T. Schmid, F. Meinert, R. Low and T. Pfau: “Pulsed Ion Microscope to Probe Quantum Gases”, *Physical Review X* **11** (1), 011036 (2021). 13
- [58] L. Asteria, H. P. Zahn, M. N. Kosch, K. Sengstock and C. Weitenberg: “Quantum gas magnifier for sub-lattice-resolved imaging of 3D quantum systems, *Supplementary information*”, *Nature* **599** (7886), 571–575 (2021). 16, 17, 18, 21, 22, 24, 26, 28, 40, 41, 130
- [59] P. A. Murthy, D. Kedar, T. Lompe, M. Neidig, M. G. Ries, A. N. Wenz, G. Zürn and S. Jochim: “Matter-wave Fourier optics with a strongly interacting two-dimensional Fermi gas”, *Physical Review A* **90** (4), 43611 (2014). 17
- [60] S. Tung, G. Lamporesi, D. Lobser, L. Xia and E. A. Cornell: “Observation of the presuperfluid regime in a two-dimensional bose gas”, *Physical Review Letters* **105** (23), 230408 (2010).
- [61] K. Hueck, N. Luick, L. Sobirey, J. Siegl, T. Lompe and H. Moritz: “Two-Dimensional Homogeneous Fermi Gases”, *Physical Review Letters* **120** (6), 060402 (2018). 17

- [62] B. Santra, C. Baals, R. Labouvie, A. B. Bhattacharjee, A. Pelster and H. Ott: “Measuring finite-range phase coherence in an optical lattice using Talbot interferometry”, *Nature Communications* **8** (1), 1–8 (2017). 18, 41
- [63] L. Asteria: “Quantum Gas Magnifier for imaging of ultracold Atoms in highly tunable optical Lattices”, Ph.D. thesis, Universität Hamburg (2022). 18, 41, 130
- [64] S. Giorgini, L. P. Pitaevskii and S. Stringari: “Condensate fraction and critical temperature of a trapped interacting Bose gas”, *Physical Review A* **54** (6), R4633–R4636 (1996). 30
- [65] J. R. Ensher, D. S. Jin, M. R. Matthews, C. E. Wieman and E. A. Cornell: “Bose-einstein condensation in a dilute gas: Measurement of energy and ground-state occupation”, *Physical Review Letters* **77** (25), 4984–4987 (1996). 30
- [66] R. P. Smith, R. L. Campbell, N. Tammuz and Z. Hadzibabic: “Effects of interactions on the critical temperature of a trapped bose gas”, *Physical Review Letters* **106** (25) (2011). 30
- [67] C. Weitenberg, M. Endres, J. F. Sherson, M. Cheneau, P. Schau, T. Fukuhara, I. Bloch and S. Kuhr: “Single-spin addressing in an atomic Mott insulator”, *Nature* **471** (7338), 319–325 (2011). 34
- [68] P. Würtz, T. Langen, T. Gericke, A. Koglbauer and H. Ott: “Experimental demonstration of single-site addressability in a two-dimensional optical lattice”, *Physical Review Letters* **103** (8), 080404 (2009). 34
- [69] P. M. Preiss, R. Ma, M. E. Tai, A. Lukin, M. Rispoli, P. Zupancic, Y. Lahini, R. Islam and M. Greiner: “Strongly correlated quantum walks in optical lattices”, *Science* **347** (6227), 1229–1233 (2015). 34
- [70] M. Karski, L. Förster, J. M. Choi, A. Steffen, N. Belmechri, W. Alt, D. Meschede and A. Widera: “Imprinting patterns of neutral atoms in an optical lattice using magnetic resonance techniques”, *New Journal of Physics* **12** (6), 065027 (2010). 34
- [71] J. Y. Choi, S. Hild, J. Zeiher, P. Schauß, A. Rubio-Abadal, T. Yefsah, V. Khemani, D. A. Huse, I. Bloch and C. Gross: “Exploring the many-body localization transition in two dimensions”, *Science* **352** (6293), 1547–1552 (2016). 37
- [72] K. D. Nelson, X. Li and D. S. Weiss: “Imaging single atoms in a three-dimensional array”, *Nature Physics* **3**, 556–560 (2007). 38
- [73] R. Bücker, A. Perrin, S. Manz, T. Betz, C. Koller, T. Plisson, J. Rottmann, T. Schumm and J. Schmiedmayer: “Single-particle-sensitive imaging of freely

- propagating ultracold atoms”, *New Journal of Physics* **11** (10), 103039 (2009). 41
- [74] A. Bergschneider, V. M. Klinkhamer, J. H. Becher, R. Klemt, G. Zürn, P. M. Preiss and S. Jochim: “Spin-resolved single-atom imaging of  ${}^6\text{Li}$  in free space”, *Physical Review A* **97** (6), 063613 (2018). 41
- [75] P. A. Murthy and S. Jochim: “Direct imaging of the order parameter of an atomic superfluid using matterwave optics”, arXiv preprint 1911.10824 (2019). 41
- [76] P. Windpassinger and K. Sengstock: “Engineering novel optical lattices”, *Rep. Prog. Phys.* **76** (8), 086401 (2013). 43
- [77] K. I. Petsas, A. B. Coates and G. Grynberg: “Crystallography of optical lattices”, *Physical Review A* **50** (6), 5173–5189 (1994). 43, 85, 87
- [78] J. Struck, C. Ölschläger, R. Le Targat, P. Soltan-Panahi, A. Eckardt, M. Lewenstein, P. Windpassinger and K. Sengstock: “Quantum simulation of frustrated classical magnetism in triangular optical lattices”, *Science* **333** (6045), 996–999 (2011). 43
- [79] M. Weinberg, C. Staarmann, C. Ölschläger, J. Simonet and K. Sengstock: “Breaking inversion symmetry in a state-dependent honeycomb lattice: artificial graphene with tunable band gap”, *2D Materials* **3** (2), 024005 (2016). 43
- [80] X. Q. Wang, G. Q. Luo, J. Y. Liu, W. V. Liu, A. Hemmerich and Z. F. Xu: “Evidence for an atomic chiral superfluid with topological excitations”, *Nature* **596** (7871), 227–231 (2021). 43, 65, 67, 88
- [81] J.-Y. Liu, G.-Q. Luo, X.-Q. Wang, A. Hemmerich and Z.-F. Xu: “Experimental realization of a high precision tunable hexagonal optical lattice”, *Opt. Express* **30** (25), 44375–44384 (2022). 43
- [82] C. D. Brown, S. W. Chang, M. N. Schwarz, T. H. Leung, V. Kozii, A. Avdoshkin, J. E. Moore and D. Stamper-Kurn: “Direct geometric probe of singularities in band structure”, *Science* **377** (6612), 1319–1322 (2022). 46
- [83] A. Kerkmann: “A novel Apparatus for Quantum Gas Microscopy of Lithium Atoms”, Ph.D. thesis, University of Hamburg (2019). 52
- [84] P. Soltan-Panahi, J. Struck, P. Hauke, A. Bick, W. Plenkers, G. Meineke, C. Becker, P. Windpassinger, M. Lewenstein and K. Sengstock: “Multi-component quantum gases in spin-dependent hexagonal lattices”, *Nature Phys.* **7**, 434–440 (2011). 53

- 
- [85] C. K. Thomas, T. H. Barter, T.-H. Leung, S. Daiss and D. M. Stamper-Kurn: “Signatures of spatial inversion asymmetry of an optical lattice observed in matter-wave diffraction”, *Phys. Rev. A* **93**, 063613 (2016). 63
- [86] M. Weinberg, O. Jürgensen, C. Ölschläger, D.-S. Lühmann, K. Sengstock and J. Simonet: “Symmetry-broken momentum distributions induced by matter-wave diffraction during time-of-flight expansion of ultracold atoms”, *Phys. Rev. A* **93**, 033625 (2016). 63, 65
- [87] B. Gadway: “Atom-optics approach to studying transport phenomena”, *Phys. Rev. A* **92**, 043606 (2015). 63
- [88] E. J. Meier, F. A. An and B. Gadway: “Atom-optics simulator of lattice transport phenomena”, *Phys. Rev. A* **93**, 051602 (2016). 63
- [89] F. A. An, E. J. Meier and B. Gadway: “Direct observation of chiral currents and magnetic reflection in atomic flux lattices”, *Science Advances* **3** (4), e1602685 (2017). 63
- [90] P. Lauria, W.-T. Kuo, N. R. Cooper and J. T. Barreiro: “Experimental Realization of a Fermionic Spin-Momentum Lattice”, *Phys. Rev. Lett.* **128**, 245301 (2022). 63
- [91] G. Wirth, M. Ölschläger and A. Hemmerich: “Evidence for orbital superfluidity in the P-band of a bipartite optical square lattice”, *Nature Physics* **7**, 147–153 (2011). 65
- [92] M. Ölschläger, G. Wirth and A. Hemmerich: “Unconventional Superfluid Order in the  $F$  Band of a Bipartite Optical Square Lattice”, *Phys. Rev. Lett.* **106**, 015302 (2011).
- [93] T. Kock, M. Ölschläger, A. Ewerbeck, W.-M. Huang, L. Mathey and A. Hemmerich: “Observing Chiral Superfluid Order by Matter-Wave Interference”, *Phys. Rev. Lett.* **114**, 115301 (2015).
- [94] M. Hachmann, Y. Kiefer, J. Riebesehl, R. Eichberger and A. Hemmerich: “Quantum Degenerate Fermi Gas in an Orbital Optical Lattice”, *Phys. Rev. Lett.* **127**, 033201 (2021). 65
- [95] S. Jin, W. Zhang, X. Guo, X. Chen, X. Zhou and X. Li: “Evidence of Potts-Nematic Superfluidity in a Hexagonal  $sp^2$  Optical Lattice”, *Phys. Rev. Lett.* **126**, 035301 (2021). 65
- [96] K. Loida, J.-S. Bernier, R. Citro, E. Orignac and C. Kollath: “Probing the Bond Order Wave Phase Transitions of the Ionic Hubbard Model by Superlattice Modulation Spectroscopy”, *Phys. Rev. Lett.* **119**, 230403 (2017). 74

- [97] S. V. Rajagopal, T. Shimasaki, P. Dotti, M. Račiūnas, R. Senaratne, E. Anisimovas, A. Eckardt and D. M. Weld: “Phasonic Spectroscopy of a Quantum Gas in a Quasicrystalline Lattice”, *Phys. Rev. Lett.* **123**, 223201 (2019). 74, 83
- [98] N. Fläschner, D. Vogel, M. Tarnowski, B. S. Rem, D.-S. Lühmann, M. Heyl, J. C. Budich, L. Mathey, K. Sengstock and C. Weitenberg: “Observation of dynamical vortices after quenches in a system with topology”, *Nature Physics* **14** (3), 265–268 (2018). 74
- [99] M. Tarnowski, F. N. Ünal, N. Fläschner, B. S. Rem, A. Eckardt, K. Sengstock and C. Weitenberg: “Measuring topology from dynamics by obtaining the Chern number from a linking number”, *Nature Communications* **10** (1), 1728 (2019). 74, 75, 79, 88
- [100] C.-R. Yi, J. Yu, H. Yuanv, R.-H. Jiao, Y.-M. Yang, X. Jiang, J.-Y. Zhang, S. Chen and J.-W. Pan: “Extracting the Quantum Geometric Tensor of an Optical Raman Lattice by Bloch State Tomography”, arXiv preprint 1911.10824 (2023). 74
- [101] S.-L. Zhu, B. Wang and L.-M. Duan: “Simulation and Detection of Dirac Fermions with Cold Atoms in an Optical Lattice”, *Phys. Rev. Lett.* **98**, 260402 (2007). 78
- [102] L. Duca, T. Li, M. Reitter, I. Bloch, M. Schleier-Smith and U. Schneider: “An Aharonov-Bohm interferometer for determining Bloch band topology”, *Science* **347** (6219), 288–292 (2015). 78, 113, 114
- [103] M. Tarnowski, M. Nuske, N. Fläschner, B. Rem, D. Vogel, L. Freystatzky, K. Sengstock, L. Mathey and C. Weitenberg: “Observation of Topological Bloch-State Defects and Their Merging Transition”, *Phys. Rev. Lett.* **118**, 240403 (2017). 78, 113, 114
- [104] G. Jotzu, M. Messer, R. Desbuquois, M. Lebrat, T. Uehlinger, D. Greif and T. Esslinger: “Experimental realization of the topological Haldane model with ultracold fermions”, *Nature* **515** (7526), 237–240 (2014). 80, 88
- [105] M. Aidelsburger, M. Lohse, C. Schweizer, M. Atala, J. T. Barreiro, S. Nascimbène, N. R. Cooper, I. Bloch and N. Goldman: “Measuring the Chern number of Hofstadter bands with ultracold bosonic atoms”, *Nature Physics* **11** (2), 162–166 (2015). 80
- [106] L.-J. Lang, X. Cai and S. Chen: “Edge States and Topological Phases in One-Dimensional Optical Superlattices”, *Phys. Rev. Lett.* **108**, 220401 (2012). 80
- [107] Y. E. Kraus, Y. Lahini, Z. Ringel, M. Verbin and O. Zeitler: “Topological States and Adiabatic Pumping in Quasicrystals”, *Phys. Rev. Lett.* **109**, 106402 (2012). 80, 83

- 
- [108] T. A. Corcovilos and J. Mittal: “Two-dimensional optical quasicrystal potentials for ultracold atom experiments”, *Appl. Opt.* **58** (9), 2256–2263 (2019).
- [109] M. A. Bandres, M. C. Rechtsman and M. Segev: “Topological Photonic Quasicrystals: Fractal Topological Spectrum and Protected Transport”, *Phys. Rev. X* **6**, 011016 (2016). 83
- [110] D. Johnstone, P. Öhberg and C. W. Duncan: “Mean-field phases of an ultracold gas in a quasicrystalline potential”, *Phys. Rev. A* **100**, 053609 (2019). 85
- [111] D. Johnstone, P. Ohberg and C. W. Duncan: “The mean-field Bose glass in quasicrystalline systems”, *Journal of Physics A: Mathematical and Theoretical* **54** (39), 395001 (2021). 85, 89
- [112] V. Khemani, D. N. Sheng and D. A. Huse: “Two Universality Classes for the Many-Body Localization Transition”, *Phys. Rev. Lett.* **119**, 075702 (2017). 85
- [113] B. Yan and C. Felser: “Topological Materials: Weyl Semimetals”, *Annual Review of Condensed Matter Physics* **8** (1), 337–354 (2017). 85
- [114] Z.-Y. Wang, X.-C. Cheng, B.-Z. Wang, J.-Y. Zhang, Y.-H. Lu, C.-R. Yi, S. Niu, Y. Deng, X.-J. Liu, S. Chen and J.-W. Pan: “Realization of an ideal Weyl semimetal band in a quantum gas with 3D spin-orbit coupling”, *Science* **372** (6539), 271–276 (2021). 85
- [115] W. A. Benalcazar, B. A. Bernevig and T. L. Hughes: “Quantized electric multipole insulators”, *Science* **357** (6346), 61–66 (2017). 85
- [116] F. Schindler, A. M. Cook, M. G. Vergniory, Z. Wang, S. S. P. Parkin, B. A. Bernevig and T. Neupert: “High-order topological insulators”, *Science Advances* **4** (6), eaat0346 (2018). 85
- [117] B. Huang, V. Novičenko, A. Eckardt and G. Juzeliūnas: “Floquet chiral hinge modes and their interplay with Weyl physics in a three-dimensional lattice”, *Phys. Rev. B* **104**, 104312 (2021). 85, 89
- [118] T. H. Barter, T.-H. Leung, M. Okano, M. Block, N. Y. Yao and D. M. Stamper-Kurn: “Spatial coherence of a strongly interacting Bose gas in the trimerized kagome lattice”, *Phys. Rev. A* **101**, 011601 (2020). 86
- [119] L. Z. Cai, X. L. Yang and Y. R. Wang: “Formation of three-dimensional periodic microstructures by interference of four noncoplanar beams”, *J. Opt. Soc. Am. A* **19** (11), 2238–2244 (2002). 87
- [120] O. Toader, T. Y. M. Chan and S. John: “Photonic Band Gap Architectures for Holographic Lithography”, *Phys. Rev. Lett.* **92**, 043905 (2004). 87

- 
- [121] X. Li and W. V. Liu: “Physics of higher orbital bands in optical lattices: a review”, *Reports on Progress in Physics* **79** (11), 116401 (2016). 88
- [122] C. Wu: “Orbital Analogue of the Quantum Anomalous Hall Effect in  $p$ -Band Systems”, *Phys. Rev. Lett.* **101**, 186807 (2008). 88
- [123] A. Ilin: “Orbital condensates in higher Bloch bands of an optical boron-nitride lattice”, Ph.D. thesis, Universität Hamburg (2022). 88
- [124] A. Eckardt: “Colloquium: Atomic quantum gases in periodically driven optical lattices”, *Rev. Mod. Phys.* **89**, 011004 (2017). 88
- [125] T. Boulier, J. Maslek, M. Bukov, C. Bracamontes, E. Magnan, S. Lellouch, E. Demler, N. Goldman and J. V. Porto: “Parametric Heating in a 2D Periodically Driven Bosonic System: Beyond the Weakly Interacting Regime”, *Phys. Rev. X* **9**, 011047 (2019). 88
- [126] K. Wintersperger, C. Braun, F. N. Únal, A. Eckardt, M. D. Liberto, N. Goldman, I. Bloch and M. Aidelsburger: “Realization of an anomalous Floquet topological system with ultracold atoms”, *Nature Physics* **16** (10), 1058–1063 (2020). 88
- [127] M. Nuske, L. Mathey and E. Tiesinga: “Sudden-quench dynamics of Bardeen-Cooper-Schrieffer states in deep optical lattices”, *Phys. Rev. A* **94**, 023607 (2016). 88
- [128] J.-H. Zheng, B. Irsigler, L. Jiang, C. Weitenberg and W. Hofstetter: “Measuring an interaction-induced topological phase transition via the single-particle density matrix”, *Phys. Rev. A* **101**, 013631 (2020). 88
- [129] M. Boll, T. A. Hilker, G. Salomon, A. Omran, J. Nespolo, L. Pollet, I. Bloch and C. Gross: “Spin- and density-resolved microscopy of antiferromagnetic correlations in Fermi-Hubbard chains”, *Science* **353** (6305), 1257–1260 (2016). 89
- [130] F. S. Cataliotti, S. Burger, C. Fort, P. Maddaloni, F. Minardi, A. Trombettoni, A. Smerzi and M. Inguscio: “Josephson junction arrays with Bose-Einstein condensates”, *Science* **293** (5531), 843–846 (2001). 91, 108
- [131] J. Mun, P. Medley, G. K. Campbell, L. G. Marcassa, D. E. Pritchard and W. Ketterle: “Phase Diagram for a Bose-Einstein Condensate Moving in an Optical Lattice”, *Phys. Rev. Lett.* **99**, 150604 (2007).
- [132] D. McKay, M. White, M. Pasienski and B. DeMarco: “Phase-slip-induced dissipation in an atomic Bose-Hubbard system”, *Nature* **453**, 76–79 (2008). 91

- [133] J. Simon, W. S. Bakr, R. Ma, M. E. Tai, P. M. Preiss and M. Greiner: “Quantum simulation of antiferromagnetic spin chains in an optical lattice”, *Nature* **472** (7343), 307–312 (2011). 91
- [134] R. Ma, M. E. Tai, P. M. Preiss, W. S. Bakr, J. Simon and M. Greiner: “Photon-assisted tunneling in a biased strongly correlated bose gas”, *Physical Review Letters* **107** (9), 095301 (2011).
- [135] F. Meinert, M. J. Mark, E. Kirilov, K. Lauber, P. Weinmann, M. Gröbner, A. J. Daley and H.-C. Nägerl: “Observation of many-body dynamics in long-range tunneling after a quantum quench”, *Science* **344** (6189), 1259–1262 (2014).
- [136] H. Bernien, S. Schwartz, A. Keesling, H. Levine, A. Omran, H. Pichler, S. Choi, A. S. Zibrov, M. Endres, M. Greiner, V. Vuletic and M. D. Lukin: “Probing many-body dynamics on a 51-atom quantum simulator”, *Nature* **551** (7682), 579–584 (2017). 91
- [137] E. Guardado-Sanchez, A. Morningstar, B. M. Spar, P. T. Brown, D. A. Huse and W. S. Bakr: “Subdiffusion and Heat Transport in a Tilted Two-Dimensional Fermi-Hubbard System”, *Physical Review X* **10** (1), 011042 (2020). 91
- [138] S. Scherg, T. Kohlert, P. Sala, F. Pollmann, B. Hebbe Madhusudhana, I. Bloch and M. Aidelsburger: “Observing non-ergodicity due to kinetic constraints in tilted Fermi-Hubbard chains”, *Nature Communications* **12** (1), 1–8 (2021). 91
- [139] T. Anker, M. Albiez, R. Gati, S. Hunsmann, B. Eiermann, A. Trombettoni and M. K. Oberthaler: “Nonlinear self-trapping of matter waves in periodic potentials”, *Physical Review Letters* **94** (2) (2005). 93, 108, 114, 129
- [140] M. Snoek and W. Hofstetter: “Two-dimensional dynamics of ultracold atoms in optical lattices”, *Phys. Rev. A* **76**, 051603 (2007). 93, 110, 113
- [141] W. Magnus: “On the exponential solution of differential equations for a linear operator”, *Communications on Pure and Applied Mathematics* **7** (4), 649–673 (1954). 95
- [142] S. Blanes, F. Casas, J. A. Oteo and J. Ros: “The Magnus expansion and some of its applications”, *Physics Reports* **470** (5-6), 151–238 (2009).
- [143] B. Zhu, T. Rexin and L. Mathey: “Magnus expansion approach to parametric oscillator systems in a thermal bath”, *Zeitschrift für Naturforschung A* **71** (10), 921–932 (2016). 95
- [144] V. P. Singh, W. Weimer, K. Morgener, J. Siegl, K. Hueck, N. Luick, H. Moritz and L. Mathey: “Probing superfluidity of Bose-Einstein condensates via laser stirring”, *Physical Review A* **93** (2), 023634 (2016). 97

- [145] C. Mora and Y. Castin: “Extension of Bogoliubov theory to quasicondensates”, *Phys. Rev. A* **67**, 053615 (2003). 97
- [146] F. S. Cataliotti, L. Fallani, F. Ferlaino, C. Fort, P. Maddaloni and M. Inguscio: “Superfluid current disruption in a chain of weakly coupled Bose-Einstein condensates”, *New Journal of Physics* **5**, 71 (2003). 108, 132
- [147] B. Real, O. Jamadi, M. Milićević, N. Pernet, P. St-Jean, T. Ozawa, G. Montambaux, I. Sagnes, A. Lemaître, L. Le Gratiet, A. Harouri, S. Ravets, J. Bloch and A. Amo: “Semi-Dirac Transport and Anisotropic Localization in Polariton Honeycomb Lattices”, *Phys. Rev. Lett.* **125**, 186601 (2020). 113
- [148] I. Dimitrova, N. Jepsen, A. Buyskikh, A. Venegas-Gomez, J. Amato-Grill, A. Daley and W. Ketterle: “Enhanced Superexchange in a Tilted Mott Insulator”, *Phys. Rev. Lett.* **124**, 043204 (2020). 113
- [149] A. Bohrdt, L. Homeier, I. Bloch, E. Demler and F. Grusdt: “Atom-optics approach to studying transport phenomena”, *Nature Physics* **18**, 651–656 (2022). 113
- [150] O. Dutta, M. Gajda, P. Hauke, M. Lewenstein, D. S. Lühmann, B. A. Malomed, T. Sowiński and J. Zakrzewski: “Non-standard Hubbard models in optical lattices: a review”, *Reports on Progress in Physics* **78** (6), 066001 (2015). 113
- [151] C. Weitenberg and J. Simonet: “Tailoring quantum gases by Floquet engineering”, *Nature Physics* **17**, 1342–1348 (2021). 113
- [152] S. Mukherjee and M. C. Rechtsman: “Observation of Floquet solitons in a topological bandgap”, *Science* **368** (6493), 856–859 (2020). 113
- [153] A. Kshetrimayum, J. Eisert and D. M. Kennes: “Stark time crystals: Symmetry breaking in space and time”, *Physical Review B* **102** (19), 195116 (2020). 113
- [154] S. Baier, M. J. Mark, D. Petter, K. Aikawa, L. Chomaz, Z. Cai, M. Baranov, P. Zoller and F. Ferlaino: “Extended Bose-Hubbard models with ultracold magnetic atoms”, *Science* **352** (6282), 201–205 (2016). 113
- [155] F. Meinert, M. J. Mark, K. Lauber, A. J. Daley and H.-C. Nägerl: “Floquet Engineering of Correlated Tunneling in the Bose-Hubbard Model with Ultracold Atoms”, *Phys. Rev. Lett.* **116**, 205301 (2016). 113
- [156] J. Struck, M. Weinberg, C. Ölschläger, P. Windpassinger, J. Simonet, K. Sengstock, R. Höppner, P. Hauke, A. Eckardt, M. Lewenstein and L. Mathey: “Engineering Ising-XY spin-models in a triangular lattice using tunable artificial gauge fields”, *Nature Physics* **9** (11), 738–743 (2013). 113

- 
- [157] C. V. Parker, L. C. Ha and C. Chin: “Direct observation of effective ferromagnetic domains of cold atoms in a shaken optical lattice”, *Nature Physics* **9** (12), 769–774 (2013). 113
- [158] D. S. Lühmann: “Twisted superfluid phase in the extended one-dimensional Bose-Hubbard model”, *Physical Review A* **94** (1), 011603 (2016). 113
- [159] C. Braun, R. Saint-Jalm, A. Hesse, J. Arceri, I. Bloch and M. Aidelsburger: “Real-space detection and manipulation of topological edge modes with ultracold atoms”, arXiv preprint 1911.10824 (2023). 114
- [160] I. T. Jolliffe: *Principal Component Analysis*, Springer International Publishing, New York (2002), ISBN 0-387-95442-2. 119
- [161] R. Dubessy, C. De Rossi, T. Badr, L. Longchambon and H. Perrin: “Imaging the collective excitations of an ultracold gas using statistical correlations”, *New Journal of Physics* **16**, 122001 (2014). 119
- [162] A. Trombettoni and A. Smerzi: “Discrete Solitons and Breathers with Dilute Bose-Einstein Condensates”, *Phys. Rev. Lett.* **86**, 2353–2356 (2001). 129

## Danksagung

An dieser Stelle möchte ich mich bei all jenen bedanken, die mich auf dem Weg zur Fertigstellung dieser Arbeit unterstützt haben.

Zunächst gilt mein Dank Klaus, der mir ermöglicht hat meine Doktorarbeit in seiner Forschungsgruppe anzufertigen. Vielen Dank für die interessanten Diskussionen und die hilfreichen Vorschläge. Ich habe die angenehmen Rahmenbedingungen in deiner Forschungsgruppe sehr genossen. Weiterhin danke ich Christof für seine sehr engagierte Betreuung unseres Projekts und die zahlreichen guten Hinweise im Arbeitsalltag. Auch für das viele Korrekturlesen meiner Arbeit bin ich sehr dankbar. Ein großer Dank gilt auch meinen beiden Mitdoktoranden, Luca und Henrik, für die allzeit angenehme Atmosphäre im Labor und Büro und die sehr hilfreiche Unterstützung und Einarbeitung in das BFM-Experiment. Danke auch an Luca für das Korrekturlesen meiner Arbeit.

Darüber hinaus möchte ich mich bei der gesamten Forschungsgruppe für die gegenseitige Unterstützung und das freundliche Miteinander bedanken. Insbesondere beim Lithium Team für die stete Hilfs- und Leihbereitschaft und bei Ortwin für seine Betreuung verschiedener experimenteller Probleme. Außerdem möchte ich mich beim administrativen und technischen Personal am ILP bedanken für die positiven Rahmenbedingungen, die mir erlaubt haben, mich ganz auf unsere Experimente zu konzentrieren. Henning Moritz danke ich für die freundliche Übernahme des Zweitgutachtens.

Ein ganz besonderer Dank gilt darüber hinaus meinen Eltern und meiner ganzen Familie, die mich stets unterstützt und begleitet haben.

